

CRANFIELD UNIVERSITY

**SAMIR ESHATI**

**AN EVALUATION OF OPERATION AND CREEP LIFE OF  
STATIONARY GAS TURBINE ENGINE**

SCHOOL OF ENGINEERING  
DEPARTMENT OF POWER AND PROPULSION

PhD  
Academic Year: 2011 - 2012

Supervisors: Dr. Panagiotis Laskaridis  
Professor Pericles Pilidis

March, 2012



CRANFIELD UNIVERSITY

SCHOOL OF ENGINEERING  
DEPARTMENT OF POWER AND PROPULSION

PhD

Academic Year 2011 - 2012

**SAMIR ESHATI**

**AN EVALUATION OF OPERATION AND CREEP LIFE OF  
STATIONARY GAS TURBINE ENGINE**

Supervisors: Dr. Panagiotis Laskaridis  
Professor Pericles Pilidis

March, 2012

This thesis is submitted in partial fulfilment of the requirements for  
the degree of degree of Doctor of Philosophy

© Cranfield University 2012. All rights reserved. No part of this  
publication may be reproduced without the written permission of the  
copyright owner.



## *ABSTRACT*

During operation, gas turbine components undergo various types of time-dependent degradation due to high temperatures and mechanical loading. In the case of stationary GT engines for mechanical power, creep failure mechanism problems are a very common cause of mechanical failure that significantly reduces component life. The magnitude of the adverse effect is highly dependent on the operating conditions and design parameter of the components. Against this background, the research programme was aimed at achieving a better scientific understanding of the major reasons for creep failure. This would allow mechanical equipment to keep running free creep problem for longer. Therefore, the *aim* of this research was to develop an analytical life model capable of assessing the influence of humidity on the turbine blade heat transfer and cooling processes considering the engine design parameters, operating conditions and working environment which, in turn, affect blade creep life.

The whole cooled blade row is regarded as heat exchanger with convective/film cooling and a thermal barrier coating. The approach is based on an engine performance model, heat transfer models and the change of properties of moist air as a function of water to air ratio (WAR). The changes of fluid properties due to the presence of water vapour were not only considered through a variation of the specific heat, the ratio of major specific heats and gas constant, but also with the variation of density, Reynolds number, Nusselt number and other related parameters.

The effect of different parameters including radial temperature distortion factor, material properties, cooling effectiveness and turbine entry temperatures is investigated. The results show that different design parameters combined with a change in operating conditions can significantly effect the creep life of the HPT blade and the location along the span of the blade where the failure occur. Results show that with increasing WAR from 0 to 0.10, the blade inlet coolant temperature reduced at the blade mean from 825K to 807K respectively. Also, the blade metal temperature at each section is reduced (at blade mean, 1025K

for WAR=0 and 1012K for WAR=0.10), which in turn increased the blade creep life from 2.22  $L_f/L_{fR}$  to 4.88  $L_f/L_{fR}$  respectively. Different operating points are also evaluated at different WAR and ambient temperature to identify the effect of WAR on the creep life at the blade mean. The results show that an increase in WAR increases the blade creep life even if  $T_{amb}$  is increased. At an operating TET of 1460K, an increase in WAR from 0.008 ( $T_{amb}=288.15K$ ) to 0.10 ( $T_{amb}=313.15K$ ), gives a corresponding increase in blade creep life factor from 2.6 fold to 4.3 fold. Thus, the effect of the increase in the WAR on heat transfer is more significant than the increase in the ambient temperature. Moreover, the results show that at turbine entry temperatures above the turbine entry temperature reference the blade creep life improves with increase in WAR.

A 3-D Finite element model is used to calculate the thermal stresses using the nodal temperature distributions and the maximum engine rotational speed as boundary conditions. Finite element analysis is coupled with a creep lifing model (Larson-Miller parameter to predict the evolution of metal temperature, stress and the critical areas susceptible to creep are identified and visualized. It is observed that the blade creep life increases with increase in WAR from the root to the tip at the leading edge. This is in contrast to a similar critical point (root) in the trailing edge, where the creep life decreases significantly from root to the tip. The thermal stress analysis with the mechanical stress analysis will yield more valuable information about the actual magnitudes of overall stresses encountered by the turbine blade.

The model developed is capable of assessing the main parameters that influence blade cooling performance, such as cooling methods, alternative cooling fluids, blade geometry, heat transfer coefficients, gas properties, material and thermal barrier coatings. In addition, the method will assist users in the selection of the most cost effective engine and will help them to make appropriate inspection and/or maintenance decisions, to minimise operating cost while giving the best engine availability.



*All gratefulness and praises be to Allah, the god of Adam, Abraham, Moses, Jesus and  
Mohammad. Peace be upon them all.*

## **ACKNOWLEDGEMENTS**

I wish to express my sincere thanks and gratitude to my supervisor Dr Panagiotis Laskaridis for his support, valuable and continuous advice, guidance, thoughtfulness and assistance throughout the duration of this PhD research. Also, I would like to thank Dr Ken Ramsden and Professor Pericles Pilidis for their support, advice and assistance. Many thanks to all the staff in the Department of Power and Propulsion at Cranfield University.

My thanks also go to the Libyan government for the provision of the scholarship and financial support for the duration of my study at Cranfield University. Special thanks and appreciation is due to Osama Lotfi, Firoz Khan, Sreejith Babu and Abu Abdullahi Obonyegba, for their help and advice.

My gratitude belongs to my father, mother, wife, sisters and all my family, whose love, encouragement, support and faith meant a very great deal to me. I would like to express my appreciation for all the kind support they have offered. May Allah bless all of my family because without their prayers, encouragement, understanding and patience, it would have been impossible for me to finish this work. A very special thanks goes to my brothers Anwar and Salem for their support, encouragement and assistance in doing this work.

Finally, but no means least, I would like to thank all my friends at Cranfield for their support during my study at Cranfield University.

***To my beloved daughters, Nusiaba and Shaden***





## Publications

- S. Eshati, A. O. Abu, P. Laskaridis, F. Khan, "Influence of Water Air Ratio on the Heat Transfer and Creep Life of High Pressure GAS Turbine Blade", Applied Thermal Engineering, No-ATE-2012-2470
- A. O. Abu, S. Eshati, E.S. Najafi, P. Laskaridis, A. Haslam, " Physics Based Approach For Life Assessment of Gas Turbine Blades" Proceedings of ASME 2012-Gas Turbine India Conference December 1, 2012, Mumbai, Maharashtra, India, GT 2012-9638 (Draft)
- S, Eshati, P. Laskaridis, A. Haslam, P. Pilidis, "The Influence of Humidity on the Creep Life of A High Pressure Gas Turbine Blade: Part I Heat Transfer Model", ASME Turbo Expo 2012, Copenhagen, Denmark, GT2012-69455
- S, Eshati, P. Laskaridis, A. Haslam, P. Pilidis, "The Influence of Humidity on the Creep Life of A High Pressure Gas Turbine Blade: Part II Case study", ASME Turbo Expo 2012, Copenhagen, Denmark, GT2012-69462
- Samir Eshati, Abdullahi Abu, Panagiotis Laskaridis, Anthony Haslam, "Investigation Into The Effects of Operating Conditions and Design Parameters on The Creep Life of High Pressure Turbine Blades in A Stationary Gas Turbine Engine" Journal of mechanics and mechanical engineering, Vol. 15, No. 3 (2011) 237-247
- W. Mohamed, S, Eshati, P. Pillids, S. Ogaji, P. Laskaridis, A. Nasir, "A Method to Evaluate the Impact of Power Demand on HPT Blade Creep Life", ASME Turbo Expo 2011, Vancouver, Canada, GT2011-45092
- S. Eshati, M.F.Abdul Ghafir, P. Laskaridis, Y.G.Li, "Impact of Operating Condition and Design Parameters on Gas Turbine Hot Section Creep Life", ASME Turbo Expo 2010, Glasgow, UK, 2010, GT2010-22334



# TABLE OF CONTENTS

<i>ABSTRACT</i> .....	i
<i>ACKNOWLEDGEMENTS</i> .....	iii
LIST OF FIGURES.....	xi
LIST OF TABLES .....	xvi
LIST OF SYMBOLS .....	xvii
ABBREVIATIONS .....	xxi
<i>Chapter one</i> .....	1
1 INTRODUCTION.....	1
1.1 Brief introduction.....	1
1.2 Background.....	3
1.3 Research focus.....	5
1.4 Research aim and objectives.....	6
1.5 Research contribution .....	7
1.6 Thesis structure .....	8
<i>Chapter two</i> .....	11
2 GT DEGRADATION, FAILURE MECHANISMS AND LIFING APPROACHES .....	11
2.1 Engine degradation.....	11
2.2 Common failures in gas turbines.....	12
2.2.1 Fatigue.....	15
2.2.2 Corrosion and oxidation .....	16
2.2.3 Creep.....	17
2.2.3.1 Creep characteristics.....	18
2.2.3.2 Creep driving factors .....	19
2.3 Turbine blade cooling.....	22
2.4 Humid air and blade cooling.....	29
2.5 Parametric methods.....	31
2.5.1 Orr-Sherby-Dorn parameter (OSDP): .....	32
2.5.2 Goldhoof-Sherby parameter (GSP).....	33
2.5.3 Mason-Haferd parameter (MHP):.....	34
2.5.4 Manson-Succop's parameter (MSP):.....	34
2.5.5 Larson Miller parameter (LMP) .....	35
2.6 Parameter selection .....	36
2.7 State of the art in creep life modelling.....	37
2.8 Creep life estimation approaches.....	38
2.8.1 Design approach.....	40
2.8.1.1 Life-based model for creep life estimation.....	40
2.8.1.2 Creep life estimation using the strain based model.....	42
2.8.1.3 Creep life estimation using the damage based model.....	43
2.8.2 Service-based approach .....	46

2.8.2.1	Remaining life assessment using non-destructive testing .....	47
2.8.2.2	Remaining life assessment using DT techniques .....	48
2.8.3	Statistical/probabilistic approach.....	49
2.9	Chapter Conclusions.....	51
	<i>Chapter three</i> .....	55
3	METHODOLOGY .....	55
3.1	Engine performance simulation .....	57
3.2	Blade sizing model.....	58
3.3	Analytical creep life model .....	59
3.4	Heat transfer model .....	61
3.5	3-D finite element model .....	62
3.6	Chapter Conclusion .....	63
	<i>Chapter four</i> .....	65
4	HUMIDITY .....	65
4.1	The effect of humidity.....	65
4.2	Coolant gas properties in presence of water vapour.....	70
4.3	Coolant gas properties at different values of WAR .....	71
4.4	The engine performance for different values of WAR .....	73
4.5	Hot gas properties in presence of water vapour .....	75
4.5.1	Natural gas properties for different values of WAR .....	77
4.6	Chapter Conclusions.....	84
	<i>Chapter five</i> .....	87
5	MECHANICAL STRESS MODEL.....	87
5.1	Stresses model .....	88
5.1.1	Centrifugal stress model.....	89
5.1.2	Gas bending stress model.....	90
5.1.3	Momentum bending moment model .....	95
5.1.4	Maximum stress acting on the blade .....	96
5.2	Chapter Conclusions.....	98
	<i>Chapter sixe</i> .....	101
6	HEAT TRANSFER MODEL.....	101
6.1	Heat Transfer Model and Application.....	102
6.1.1	Coolant Side Heat Transfer.....	104
6.1.1.1	Coolant Density .....	105
6.1.1.2	Cooling Configuration .....	106
6.1.1.3	Viscosity and Thermal Conductivity of Humid Air .....	107
6.1.1.4	Coolant Reynolds Number, Nusselt Number and Heat Transfer Coefficient .....	109
6.1.2	Hot Side Heat Transfer.....	110
6.1.2.1	Gas Recovery Temperature .....	111
6.1.2.2	Radial Distribution of Gas Temperature.....	111
6.1.2.3	Hot Gas Reynolds Number .....	114

6.1.2.4 Stanton Number and Hot Side Heat Transfer Coefficient .....	114
6.1.2.5 Adiabatic Effectiveness.....	115
6.1.2.6 Thermal Barrier Coating and Wall Biot Numbers.....	116
6.1.2.7 Blade Metal Temperatures .....	117
6.2 Creep model .....	118
6.3 Chapter Conclusions.....	119
<i>Chapter seven</i> .....	121
7 FINITE ELEMENT MODELLING DESCRIPTION.....	121
7.1 Mechanical and Thermal Stress Modelling .....	122
7.1.1 Abaqus CATPart Module.....	122
7.1.2 Property Module .....	124
7.1.3 Mesh module.....	126
7.1.4 Assembly module .....	128
7.1.5 Step module .....	128
7.1.6 Interaction .....	129
7.1.7 Constraints .....	130
7.1.8 Load .....	131
7.1.9 Boundary conditions.....	131
7.2 Thermal Modelling .....	133
7.3 Chapter Conclusions.....	134
<i>Chapter eight</i> .....	137
8 FINITE ELEMENT RESULTS.....	137
8.1 Mechanical stresses .....	137
8.2 Heat transfer analysis .....	140
8.3 Thermal stress analysis .....	145
8.4 Model validation.....	151
8.5 Chapter Conclusions.....	153
<i>Chapter nine</i> .....	155
9 CASE STUDIES.....	155
9.1 Analytical results: effect of operating conditions and design parameters on the blade creep life .....	155
9.1.1 The effect of RTDF on creep life .....	155
9.1.2 The effect of cooling effectiveness on creep life .....	158
9.1.3 The effect of TET on creep life.....	161
9.1.4 Effect of compressor degradation on creep life.....	163
9.2 The effect of WAR on the HP turbine blade creep life.....	165
9.2.1 Heat transfer and creep life distribution along the blade span ..	166
9.2.2 Different location and operating point .....	172
9.3 Finite element results: effect of humidity on the blade creep life.....	177
9.4 Chapter Conclusions.....	183
<i>Chapter ten</i> .....	187
10 CONCLUSIONS AND RECOMMENDATION FOR FUTURE WORK..	187

10.1	Conclusions .....	187
10.2	Recommendations .....	194
	REFERENCES .....	197
	APPENDICES .....	211
	Appendix A Blade sizing model .....	211
	Appendix B Humidity.....	225
	Appendix C Gas absolute velocity .....	230

## LIST OF FIGURES

Figure 1-1: Increase in TET with implementation of new blade materials and cooling technologies [2].....	1
Figure 2-1: Major sources of failure mechanisms in hot section components [30] .....	15
Figure 2-2: Schematic illustration of fatigue characteristics [39].....	16
Figure 2-3: Regimes of high temperature environmental attack [45].....	17
Figure 2-4: Four stages of creep failure mechanisms [46; 49].....	19
Figure 2-5: Creep curves dependence on stress and temperature [52; 54] .....	21
Figure 2-6: Stress to produce creep rupture in 100h in various alloys [47].....	22
Figure 2-7: Cooling architecture of HP turbine blade [57].....	23
Figure 2-8: Cooling technology performance curve [56].....	24
Figure 2-9: schematic explanation of iso-stress lines in $\log t_f$ vs. $(1/T_m)$ [37; 62; 63].....	33
Figure 2-10: Iso-stress lines for $\log t_f$ vs. $1/T_m$ .....	33
Figure 2-11: Iso-stress lines for $\log t_f$ vs. $T_m$ .....	34
Figure 2-12: Iso-stress lines in $\log t_f$ vs. $T_m$ using MSP [37].....	35
Figure 2-13: Schematic illustration of plot of $\log t_f$ vs $1/T_m$ .....	35
Figure 2-14: Creep Life span of hot section components due deformation [70; 71].....	38
Figure 2-15: Creep life estimation methodologies [72; 73] .....	39
Figure 2-16: Creep damage classification [118; 119] .....	47
Figure 2-17: Correlation between creep damage classification and life fraction of 1Cr-0.5Mo [119] .....	48
Figure 3-1: Research methodology flow diagram .....	56
Figure 3-2: General layout of the gas turbine engine .....	58
Figure 3-3: High pressure turbine blade design process flow diagram.....	59
Figure 3-4: Creep model life assessment flow diagram [72].....	60
Figure 3-5: Heat transfer model flow diagram .....	62
Figure 4-1: Variation of gas properties with water vapour content (Walsh and Fletcher).....	66
Figure 4-2: Water air ratio as function of altitude and deviation from ISA temperature [22].....	67
Figure 4-3: Effects of humidity on engine performance [141] .....	68
Figure 4-4: injected WAR in LP compressor in hot day enhance the power and reduce blade inlet temperature ( $T_3$ ) [145].....	69
Figure 4-5: Variation of gas properties for different values of WAR at 473K ....	72
Figure 4-6: Variation of gas properties for different values of WAR at 573K ...	72
Figure 4-7: Variation of gas properties for different values of WAR at 673K ....	73
Figure 4-8: Engine performance parameters at ambient temperature 288.15K for different values of WAR (RH levels 0%-100%) .....	74

Figure 4-9: Engine performance parameters at ambient temperature 308.15K for different values of WAR (RH levels 0%-100%) .....	74
Figure 4-10: Engine performance parameters at ambient temperature 318.15K for different values of WAR (RH levels 0%-100%) .....	75
Figure 4-11: Hot gas specific heat at constant pressure for natural gas for WAR=0 and FAR=0, 0.04, 0.05 and 0.06.....	78
Figure 4-12: Hot gas specific heat at constant pressure for natural gas for WAR= 0.08 and FAR=0, 0.04, 0.05 and 0.06.....	78
Figure 4-13: Hot gas specific heat at constant pressure for natural gas for WAR= 0.10 and FAR=0, 0.04, 0.05 and 0.06.....	79
Figure 4-14: Hot gas isentropic coefficient ( $\gamma$ ) for natural gas for WAR=0 and FAR=0, 0.04, 0.05 and 0.06 .....	80
Figure 4-15: Hot gas isentropic coefficient ( $\gamma$ ) for natural gas for WAR=0.8 and FAR=0, 0.04, 0.05 and 0.06 .....	80
Figure 4-16: Hot gas isentropic coefficient ( $\gamma$ ) for natural gas for WAR=0.1 and FAR=0, 0.04, 0.05 and 0.06 .....	81
Figure 4-17: Gas constant for hot natural gas for WAR=0 and FAR=0, 0.04, 0.05 and 0.06 .....	81
Figure 4-18: Gas constant for hot natural gas for WAR=0.08 and FAR= 0.04, 0.05 and 0.06 .....	81
Figure 4-19: Gas constant for natural gas for WAR=0.1 and FAR= 0.04, 0.05 and 0.06 .....	82
Figure 4-20: Comparison of no-dissociation $C_p$ as a function of T, WAR and FAR at $p=20\text{atm}$ .....	82
Figure 4-21: Comparison of no dissociation $\gamma$ as a function of T, WAR and FAR at $p=20\text{atm}$ .....	83
Figure 4-22: Comparison of no dissociation R as a function of T, WAR and FAR at $p=20\text{atm}$ .....	83
Figure 5-1: Blade sections.....	88
Figure 5-2: Blade stress model flow chart .....	89
Figure 5-3: Blade centrifugal forces.....	90
Figure 5-4: Bending moment at root due to static pressure difference and momentum change .....	91
Figure 5-5: Diagram illustrating the mixing between the core flow and exit cooling.....	93
Figure 5-6: Schematic diagram of the blade and gas flow directions [66]. .....	97
Figure 6-1: Temperature profile through the blade with film cooling and thermal barrier coating. ....	102
Figure 6-2: Simplified flow diagram of the heat transfer model.....	103
Figure 6-3: Flow chart of process calculating coolant heat transfer coefficient and blade sections .....	105



Figure 6-4: process calculating heat transfer of hot side and outlet cooling temperature.....	110
Figure 6-5: Typical average radial temperature profile at inlet stage turbine rotor blade [169] .....	112
Figure 7-1: Abaqus three stages .....	122
Figure 7-2: Blade CAD model using CATIA software .....	123
Figure 7-3: Blade finite element model using Abaqus .....	124
Figure 7-4: Young's modulus, Poisson's ratio, expansion coefficient and material density .....	125
Figure 7-5: Section and section assignment for whole blade .....	125
Figure 7-6: Section and section assignment for contact surfaces .....	126
Figure 7-7: Point mesh convergence curve .....	126
Figure 7-8: Element type and mesh control.....	127
Figure 7-9: Geometry mesh density .....	128
Figure 7-10: Specification of type of stress analysis in the step module .....	129
Figure 7-11: Surface to surface contact in the tip and root surface .....	130
Figure 7-12: Tie constraint to the contacts using a surface to surface discretization method load.....	130
Figure 7-13: Pressure and centrifugal loads applied on the blade.....	131
Figure 7-14: Firtree faces constrained normal to contact face.....	132
Figure 7-15: Firtree constrained – axial direction .....	132
Figure 7-16: Firtree – restrained to circumferential direction .....	133
Figure 7-17: FE Hot temperature and hot heat gas transfer coefficient.....	134
Figure 7-18: FE Coolant air temperature and coolant heat transfer coefficient .....	134
Figure 8-1: Von Mises stress at PCN=1 (a), 0.98 (b), PCN=0.94 (c) and PCN=0.92 (d).....	139
Figure 8-2: HP turbine blade 3-D finite element model.....	141
Figure 8-3: TET 1480K and WAR=0.0.....	142
Figure 8-4: TET 1480K and WAR=0.04.....	142
Figure 8-5: TET 1480K and WAR=0.08.....	142
Figure 8-6: TET 1480K and WAR=0.1.....	142
Figure 8-7: Blade metal distribution across the chord wise of the blade at root, mean and tip for different WAR=0.0 (dry) and 0.1.....	143
Figure 8-8: Blade metal distribution on the coolant and hot side of the blade airfoil for WAR=0.0 (dry) and 0.1.....	144
Figure 8-9: Cross-sectional blade metal temperature K distribution for different coolants ( $h_c=1000, 2000$ and $3000 \text{ W/m}^2\text{K}$ ) .....	145
Figure 8-10: Thermal stress (Von Mises) for WAR=0.0.....	146
Figure 8-11: Thermal stress (Von Mises) for WAR=0.04.....	146
Figure 8-12: Thermal stress (Von Mises) for WAR=0.08.....	146
Figure 8-13: Thermal stress (Von Mises) for WAR=0.1.....	146

Figure 8-14: Thermal-stress at the blade LE, nodes 7682 (Root), 9169 (Mean) and 9758 (Tip) for different WAR .....	148
Figure 8-15: Thermal stress on the blade chord (25% blade span) at different WAR.....	149
Figure 8-16: Thermal stress FE model on the blade chord (25% blade span) at WAR=0.0 and 0.1.....	149
Figure 8-17: Cross-sectional blade thermal-stress distribution (50% blade span) for different coolant schemes ( $h_c=1000, 2000$ and $3000 \text{ W/m}^2\text{K}$ ).....	150
Figure 8-18: Variation of the mechanical stress along the blade span using analytical model (A) and finite element model (B).....	151
Figure 8-19: Variation of metal temperature distribution along the blade span using analytical model (A) and finite element model (B) .....	152
Figure 9-1: Turbine Blade Inlet Temperature Profile along the span of the blade at different values of RTDF .....	156
Figure 9-2: Maximum Stress Distribution along the span of the blade at different values of RDTF .....	156
Figure 9-3: Turbine blade creep life along the span of the blade at RTDF=0.10 .....	157
Figure 9-4: Turbine blade creep life along the span of the blade at RTDF=0.15 and 0.20 .....	158
Figure 9-5: Turbine blade inlet temperature profile along the span of the blade at different reductions in cooling effectiveness.....	159
Figure 9-6: Maximum stress distribution along the span of the blade at different reductions in cooling effectiveness.....	159
Figure 9-7: Turbine blade creep life along the span of the blade at different reductions in cooling effectiveness.....	160
Figure 9-8: Inlet temperature profile along the span of the turbine blade at different TETs.....	161
Figure 9-9: Maximum stress distribution along the span of the blade at different TETs .....	162
Figure 9-10: Creep life along the span of the turbine blade at different TETs	162
Figure 9-11: Blade creep life for compressor degradation at $T_{amb}=288.15\text{K}$ ...	164
Figure 9-12: Combustor outlet temperature distribution for compressor degradation at $T_{amb} = 288$ .....	165
Figure 9-13: Blade metal temperature for compressor degradation at $T_{amb}=288.15\text{K}$ .....	165
Figure 9-14: Blade inlet cooling temperature along blade span at WAR = dry (0.0), 0.06, 0.08 and 0.10.....	167
Figure 9-15: Coolant air density and viscosity along the blade span at WAR = dry (0.0), 0.06, 0.08 and 0.10.....	168
Figure 9-16: Coolant Reynolds Number along the blade span at WAR = dry (0.0), 0.06, 0.08 and 0.10.....	169

Figure 9-17: Coolant heat transfer coefficient along the blade span at WAR = dry (0.0), 0.06, 0.08 and 0.10 .....	169
Figure 9-18: Blade metal temperatures and stress distribution along blade span at WAR = dry (0.0), 0.06, 0.08 and 0.10.....	170
Figure 9-19: Blade creep life ( $L_f/L_{fR}$ ) long the span relative to the blade root at WAR = dry (0.0), 0.06, 0.08 and 0.10.....	171
Figure 9-20: Creep life at the blade mean for different operating points, WAR (dry (0.0), 0.008, 0.01) and $T_{amb}=288.15K$ .....	173
Figure 9-21: Creep life at the blade mean for different operating points, WAR (dry (0.0), 0.04, 0.055) and $T_{amb}=208.15K$ .....	173
Figure 9-22: Creep life at the blade mean for different operating points, WAR (dry (0.0), 0.08, 0.10) and $T_{amb}=313.15K$ .....	174
Figure 9-23: Creep life at the blade mean for different $T_{amb}$ , TET and.....	174
Figure 9-24: Creep life at the blade mean for different $T_{amb}$ , TET and WAR=0.008, 0.035, 0.055 and 0.10.....	175
Figure 9-25: Creep life at blade mean for different TET at WAR= dry (0.0), 0.008, 0.01. $T_{amb}$ 288.15K .....	176
Figure 9-26: Creep life at blade mean for different TET and WAR=0.0, 0.08, 0.10. $T_{amb}= 313.15K$ .....	177
Figure 9-27: LE metal temperature and stress sensitivity of creep life along the blade span.....	181
Figure 9-28: TE metal temperature and stress sensitivity of creep life along the blade span.....	181

## LIST OF TABLES

Table 2-1: Severity of failures of gas turbine applications [33] .....	14
Table 2-2: Common failure in gas turbine components [34] .....	14
Table 2-3: Lifting approaches .....	39
Table 3-1: Engine performance parameters .....	57
Table 4-1: Engine performance parameter for injected steam in the combustion .....	70
Table 4-2: Components natural gas and Jet-A (kerosene) and their formulae .	76
Table 4-3: Coefficients for the calculation of the gas properties of UK Natural Gas. ....	77
Table 6-1: Cooling system data .....	104
Table 6-2: Coefficients for the calculation of the thermal conductivities of dry air and water vapour .....	109
Table 7-1: HP turbine blade dimensions .....	123
Table 8-1: Lifting limiting factor-mechanical stresses .....	140
Table 9-1: Creep life ratio at different values of $\varepsilon$ .....	160
Table 9-2: Creep life ratio at different TET .....	163
Table 9-3: Mass flow capacity and efficiency for different levels of fouling....	164
Table 9-4: Reference point input data .....	166
Table 9-5: Effect of WAR on various parameters along the span.....	170
Table 9-6: Blade creep life with different values of WAR at $T_{am} = 318.15K$ ....	172
Table 9-7: Cp coolant at TET1460K and different WAR.....	175
Table 9-8: FE model LE blade metal temperature, stress, and creep life for WAR=0.....	178
Table 9-9: FE model LE blade metal temperature, stress, and creep life for WAR=0.06.....	178
Table 9-10: FE model LE blade metal temperature, stress, and creep life for WAR=0.08.....	178
Table 9-11: FE model LE blade metal temperature, stress, and creep life for WAR=0.10.....	179
Table 9-12: FE model TE blade metal temperature, stress, and creep life for WAR=0.0.....	180
Table 9-13: FE model TE blade metal temperature, stress, and creep life for WAR=0.06.....	180
Table 9-14: FE model TE blade metal temperature, stress, and creep life for WAR=0.08.....	180
Table 9-15: FE model TE blade metal temperature, stress, and creep life for WAR=0.10.....	181
Table 9-16: Blade creep life at critical location for WAR=0.....	182
Table 9-17: Blade creep life at critical location for WAR=0.10.....	183

## LIST OF SYMBOLS

$A_{AnSec}$	<i>blade section annulus area</i>
$A_{CsAv}$	<i>Average cross sectional area</i>
$A_{In}$ and $A_{Out}$	<i>Inlet and outlet annulus area</i>
$A_{ch}$	<i>Channel cross-sectional area</i>
$A_{cs}$	<i>Wetted heat transfer areas of coolant flow single blade</i>
$A_g$	<i>Gas cross-section area</i>
$A_{gs}$	<i>Wetted heat transfer areas of gas flow single blade</i>
$BMP_{Sec}$	<i>Pressure bending moment at specific section</i>
$BMV_{Axsec}$	<i>Axial momentum bending moment at specified section</i>
$BMV_{Tansec}$	<i>Tangential momentum bending moment at specified section</i>
$C_c$	<i>Cold steam thermal capacity</i>
$C_g$	<i>Hot steam thermal capacity</i>
$C_p$	<i>Specific heats at constant pressure</i>
$C_{pd}$	<i>Specific heat for dry air</i>
$C_{pd_w}$	<i>Specific heat for water</i>
$C_{pfac}$	<i>Ratio of <math>C_p</math> for moist air to that for dry air</i>
$D_h$	<i>Cooling hydraulic diameter</i>
$D_{LDA}$	<i>Damage parameter used in LDA theory</i>
$D_m$	<i>Mean blade row diameter</i>
$D_{root}$	<i>Blade root diameter</i>
$D_{tip}$	<i>Blade tip diameter</i>
$I_{max}$	<i>Maximum second moment of inertia</i>
$I_{min}$	<i>Minimum second moment of inertia</i>
$L_F$	<i>Life fraction</i>
$L_f$	<i>Calculated life</i>
$L_{fR}$	<i>Reference life</i>
$MW_a$	<i>Molecular weights of dry air=28.96</i>
$MW_w$	<i>Molecular weights of water=18.015</i>
$M_{xx}$	<i>Resulting bending moment about the X-X direction</i>
$M_{yy}$	<i>Resulting bending moment about the Y-Y direction</i>
$NGV_{mass\ frac}$	<i>NGV mass fraction of coolant flow</i>
$N_b$	<i>Number of blade</i>
$N_u$	<i>Nusselt number</i>
$P_{NGV}$	<i>Turbine inlet stagnation pressure</i>
$P_{Out}$	<i>Turbine outlet stagnation pressure</i>
$P_{OutStage}$	<i>Outlet static pressure for turbine stage</i>
$P_o$	<i>Gas stagnation pressure</i>
$P_{oNGV}$	<i>Turbine inlet stagnation pressure</i>
$R_c$	<i>Specific gas constant for humid air</i>
$R_d$	<i>Gas constant of dry air, 287.058 J/(kg·K)</i>
$R_e$	<i>Reynold's number</i>
$R_{fac}$	<i>Ratio of R for moist air to that for dry air</i>
$R_o$	<i>The universal gas constant 8.31 kJ/mole K</i>
$R_v$	<i>gas constant for water vapor, 461.495 J/(kg·K)</i>

$T_{75\%}$	<i>Inlet gas temperature at 75% distance of the blade root</i>
$T_M$	<i>Metal temperature</i>
$T_{NGV}$	<i>Turbine inlet stagnation temperature</i>
$T_{OutStage}$	<i>Outlet static temperature for turbine stage</i>
$T_{REF}$	<i>Temperature rise of the burner</i>
$T_{amb}$	<i>Ambient temperature</i>
$T_b$	<i>Blade metal temperature</i>
$T_{cin}$	<i>Inlet coolant temperature</i>
$T_{co}$	<i>Outlet coolant temperature</i>
$T_f$	<i>Film coolant temperature</i>
$T_{gr}$	<i>Rotor inlet gas recovery temperature</i>
$T_{gst}$	<i>Gas static temperature</i>
$T_{gtot}$	<i>Gas total temperature</i>
$T_{in}$	<i>Inlet coolant temperature</i>
$T_{inj}$	<i>Film injection temperature=<math>T_{cin}</math></i>
$T_{io}$	<i>Reference temperature</i>
$T_m$	<i>Milting temperature</i>
$T_{ma}$	<i>Temperature constant</i>
$T_{max}, T_{min}$	<i>Maximum and minimum gas temperatures</i>
$T_{mixing}$	<i>NGV exit temperature</i>
$T_o$	<i>Gas stagnation temperature</i>
$V_1$	<i>Blade inlet relative velocity</i>
$V_2$	<i>Blade outlet relative velocity</i>
$V_3$	<i>Blade exit absolute velocity</i>
$V_{Abs}$	<i>Gas absolute velocities</i>
$V_{Ax}$	<i>Gas axial velocity</i>
$VF_{AxSec}$	<i>Momentum force at axial direction at specified section</i>
$VF_{TanSec}$	<i>Momentum force at tangential direction at specified section</i>
$V_{Tan}$	<i>Gas tangential velocity</i>
$V_{W2}$	<i>Blade whirl outlet velocity</i>
$V_{Wo}$	<i>Blade inlet whirl velocity</i>
$V_o$	<i>Blade inlet absolute velocity</i>
$V_{w1}$	$V_{Wo} - U$
$V_{w3}$	<i>Outlet whirl velocity</i>
$WAR_{molar}$	<i>Ratio of water to dry air by number of moles.</i>
$W_{Tan}$	<i>Gas relative tangential velocity</i>
$a_c$	$A_{cs}/A_{gs}$
$b_w$	<i>Blade well</i>
$c_g$	<i>Centre gravity</i>
$k_{MG} \text{ \& } m_{MG}$	<i>Monkman--Grant constant</i>
$m_{cb}$	<i>Blade mass flow</i>
$m_{cc}$	<i>Channel mass flow</i>
$m_g$	<i>Gas mass flow</i>
$n_{Ha}$	<i>Moles of the mixture of humid air</i>
$n_{ch}$	<i>Number of coolant channels</i>
$n_v$	<i>Moles of water vapor</i>

$p_d$	Partial pressure of dry air, Pa
$p_{sat}$	saturation vapour pressure, Pa
$p_v$	Pressure of water vapor, Pa
$r_{cg}$	distance between the rotation axis and the section centre of gravity
$r_f$	Reference
$t_{Lif}$	Remaining life
$t_a$	Time constant
$t_f$	Time to failure
$t_{fi}$	Time to failure under condition $i$
$t_i$	Time spent under condition $i$
$t_r$	Rupture time
$t_{spent}$	Life spent in service
$h$	Heat transfer coefficient
$E$	Young's modulus
$Bi$	Biot number
$C$	Chord
$CF$	Centrifugal force
$Ext$	External surface
$FAR$	Fuel air ratio
$GPa$	Gigapascal
$GSP$	Goldhoof-Sherby Parameter
$H$	Blade height
$LMP$	Larson-Miller Parameter
$M$	Mach number
$MHP$	Mason-Haferd Parameter
$MPa$	Megapascal
$MSP$	Manson-Succop's Parameter
$MW$	Molecular weight of moist air
$Mc$	Coolant bleed %
$N$	Number of cycles
$NGV$	Nozzle guide vane
$OSDP$	Orr-Sherby-Dorn Parameter
$PCN$	Relative compressor speed
$PF$	Pressure force
$Pr$	Prandtl number
$Q$	Representation of term $m\sqrt{T_o}/(AP_o)$
$RTDF$	Radial temperature distribution factor
$S$	Surface per unit length (perimeter, subscripts $g$ and $c$ for gas and coolant)
$Sec$	Section
$St$	Stanton number
$T$	Temperature, K
$TBC$	Thermal barrier coating
$TET$	Turbine entry temperature
$U$	Total heat transfer coefficient
$UTS$	Ultimate Tensile Strength

$V$	Velocity
$V/U$	Flow coefficient
$WAR$	Ratio of water to dry air by mass.
$X$	Molar fraction
$X$ and $Y$	distances between the corresponding location to the section CG
$b$	Axial chord
$c$	Coolant
$d$	Dry air.
$e$	Surface curvature at throat
$g$	Hot gas
$k$	Thermal conductivity
$m$	Inlet mass flow
$q$	Rate of heat transferred, $W/m^2K$
$r$	Recovery temperature factor
$t$	Thickness
$w$	Wet/water
$\%T_{drop}$	Temperature drop percentage of each turbine stage
$m^*/W^*$	Dimensionless coolant mass flow rate

## Greek

$\dot{\epsilon}_C$	Creep strain rate
$\dot{\epsilon}_{CS}$	Secondary creep strain rate
$\Delta V_{TanSec}$	Average tangential velocity difference at specified section
$\Delta V_{axialSec}$	Average axial velocity difference at specified section
$\Delta p_{AvSec}$	average section static pressure
$d_{CGsec}$	distance of the section CG
$\Gamma_p$	Stage pressure ratio
$\Delta V_w$	Total whirl velocity
$\Delta H/U^2$	Stage load
$v_{CDM}$	Constant used in CDM general equation
$\alpha_1$	Blade inlet flow angle
$\alpha_2$	Blade outlet angle
$\alpha_3$	Whirl exit angle
$\alpha_o$	NGV outlet angle
$\beta_2$	Blade outlet angle
$\gamma_{fac}$	Ratio of $\gamma$ for moist air to that for dry air
$\gamma_w, \gamma_d$	Ratio of specific heats for water and dry air
$\epsilon_C$	Creep strain
$\eta_P$	polytropic efficiency
$\eta_{ad}$	Adiabatic film effectiveness
$\eta_{con}$	Convection efficiency
$\eta_{ist}$	Turbine isentropic efficiency
$\theta_{ind}$	Induced incidence
$\sigma_{BMsec}$	bending moment stress
$\sigma_{CF}$	Centrifugal stress
$\sigma_{TotSec}$	Total stress at each blade section
$\sigma_{eff}$	Effective stress



$\psi_T$	Zweifel loading coefficient
$\psi_d$	Channel shape factor
$\omega_{CDM}$	Damage state variable in continuum damage mechanics
$\Omega$	non-dimensional stage work done factor
$\gamma$	Isentropic coefficient (Gamma)
$\delta$	Deviation angle
$\varepsilon$	Cooling effectiveness
$\mu$	Viscosity, kg/m/s
$\nu$	Poisson's ratio
$\xi$	stagger angle
$\rho$	Density, Kg/m <sup>3</sup>
$\sigma$	Stress
$\phi$	Percentage of air cooling
$\omega$	angular speed

## ABBREVIATIONS

0-D	Zero dimensional
1-D	One dimensional
2-D	Two dimensional
3-D	Three dimensional
ANN	Artificial neural networks
CAD	Computer aided design
CAE	Complete Abaqus environment
CDM	Continuum damage mechanics
CEA	Chemical equilibrium with application
CFD	Computational fluid dynamics
CG	Centre of gravity
DP	Design point
DT	Destructive test
FE	Finite element
FEA	Finite element analysis
GT	Gas turbine
HCF	High cycle fatigue
HP	High pressure
ISA	International standard atmosphere
LCF	Low cycle fatigue
LDA	Linear damage accumulation
LE	Leading edge
NDT	Non-destructive test
ODP	Off-design point
OEM	Original equipment manufacturers
RH	Relative humidity
RS	Response surface
SFC	Specific fuel consumption
STIG	Steam injected gas turbine
TE	Trailing edge
TET	Turbine entry temperature
TMF	Thermal mechanical fatigue
Z	Cooling technology level
N	Number of cycles



# Chapter one

## 1 INTRODUCTION

### 1.1 Brief introduction

Improvement in engine performance has been a key factor in gas turbine (GT) design, manufacture and operation, since the GT engine entered service in the late 1940's and, as a result, technological development has progressed rapidly [1]. The drive for better engine performance and efficiency will continue to require engine components which are exposed to extreme mechanical and thermal load. For example, increases in HP turbine inlet temperature beyond the melting point of present blades may be achieved by using new composite materials for blade coatings and introducing advanced technologies and air cooling capabilities for the component parts of the turbine. Figure 1-1 shows the trend of firing temperature and blade metal capability [2].

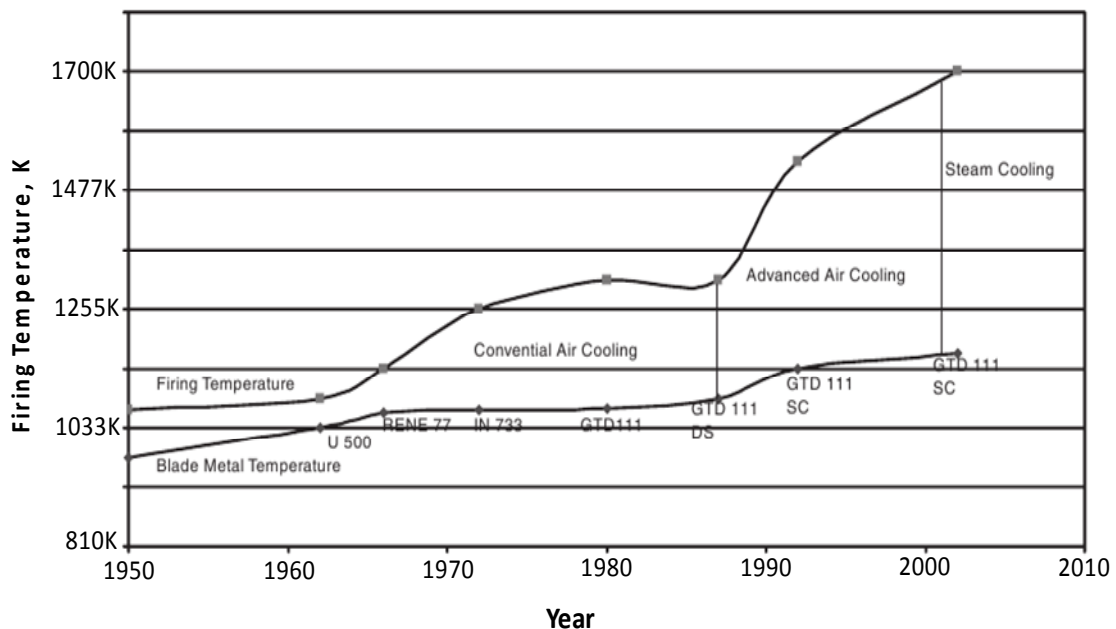


Figure 1-1: Increase in TET with implementation of new blade materials and cooling technologies [2]

High turbine inlet temperature provides a challenging environment for turbine blades which are subject to a variety of damage mechanisms, including thermo-mechanical fatigue, oxidation, corrosion and creep. Gas turbine manufacturers must make compromises between the engine thermodynamic performance requirement, component lifing, and running cost for end users.

In the case of stationary GT engines creep is one of the most common failure mechanisms that significantly reduce component life. The effect of creep is highly dependent on the operating conditions of the engine, its mode of operation and also the design parameters and details of the critical hot section components in question. Cooling technologies and processes used in blade cooling also have significant effect on the blade life since the creep is a function of temperature and stresses acting on the blade from the root to the tip. However, the determining factors such as operating conditions and working environment that limit serviceable life of high pressure (HP) turbine blades vary significantly from one component to another and consideration should be given to the possible interaction between these factors upon the creep life of hot section components. The original equipment manufacturer will have estimated component life based on the design envelope of the expected base load, calculated component stresses and temperatures, and the expected response of the material to those conditions. However, a substantial safety factor will have been included to ensure failure free operation, due to which most components will be discarded while still retaining residual life [3].

The life of turbine components and the factors that limit their life vary significantly from operator to operator due to a combination of the engine design, application, working environments and operating conditions. These factors have significant effect on the hot section component life during operation. Therefore, a lifing assessment method is needed to assess the life of the component in order to avoid discarded components which retain significant useful life. The limitations of existing lifing techniques do not cover all lifing consumption elements, are very complicated to apply, give inaccurate results,

and are based on data not easy to access. Therefore, a comprehensive lifing technique which is simple to implement is needed.

Prospects of success in this respect lie in improving the depth of knowledge and understanding of the failure mechanisms. As part of this there is a need to develop an analytical model to investigate the influence of humidity on the HP turbine blade heat transfer and cooling processes which affect blade creep life.

## **1.2 Background**

The cooling of high temperature GTs has been the subject of intensive work over the past few decades. There are three well known methods for the design the first stage of a HP turbine blade; un-cooled, convection cooled and film cooled. In the case of film cooling, air is used as a barrier between the hot gas and the blade metal. In the early 80's the GT industry developed a turbine blade using both convection and film cooled methods with a thermal barrier coating to reduce the blade metal temperature [4]. The analysis of the temperatures of the cooled blades requires the solution of equations governing heat flow through the solid blade given the internal and external distributions of the boundary gas temperature and heat transfer coefficients [5]. Although analytical solutions are nowadays used for detailed blade design, in earlier years engine companies relied on practical methods for determining the amount of cooling flow required to maintain blade temperature within prescribed metallurgical limits [6]. The determination of the rate of heat transfer from the turbine blade in a cross flow is important in hot section GT life assessment. For design purposes, the rate of heat transfer is normally fixed by semi-empirical correlations expressing the Nusselt number in terms of Reynolds and Prandtl numbers. The implementation of such correlations requires knowledge of fluid properties such as density, viscosity, thermal conductivity and specific heat, all which depend on temperature. For gases these properties are normally available only for the dry state, thus the possible effect of the water vapour content of the gas has been overlooked [7].

Research has been carried in last three decades to investigate the process of cooling of the HP turbine blade. The researches were based on fundamental equations for heat transfer process and assuming constant inlet gas temperature along the blade span and chord, where the blade metal temperature was constant along the chord and through the blade walls. That means the blade metal temperature increases in the span-wise direction and reaches a maximum at the end of the blade [1; 5; 8-14]. Where, Torbidoni [6; 15] and Horlock and Torbidoni [16] developed a new analytical model, based on Consonni's [1] and Ainley's [8] previous work. The new model allowed for chord-wise variations of coolant flow, blade temperature, mainstream gas and coolant temperature, heat transfer coefficients, finite blade wall thickness, TBC and multi-pass channels.

It must be noted that all the work mentioned above used the properties of dry air and neglected the effect of air humidity, possibly because many GTs operate in environments in which air humidity is very low and therefore has little influence on GT performance. But humidity becomes more important when large variations in ambient absolute humidity are expected, especially in hot and humid climates [17]. Also, the introduction of a spray of water inside the compressor has become a popular approach to achieve increased power and efficiency, and most research work carried out in the last few years has focused on the effects of water injection on the engine performance [17-21]. In aviation GTs, the effect of humidity and water ingestion on the engine performance has been investigated and presented in AGARD [22]. Amell et al [23] investigated the influence of relative humidity (RH) on the atmospheric air cooling thermal load. Still et al [7] investigated experimentally the influence of humidity on the convective heat transfer from a small cylinder at low air temperatures and found that for molar fractions of water vapour up to 0.27, the heat transfer rate increased with increasing humidity. The convective cooling of GT blades using air or steam as the coolant medium in open and closed loop steam cooling was investigated under different operating conditions by Albeirutty et al. [24]. The study compared the performance of different blade cooling schemes. A general

heat transfer model was developed for the analysis using the mean blade temperature at the mid-blade height.

However, none of these approaches has attempted to evaluate the long term effects of air humid on the GT blade cooling process and creep life. Assessing how an existing GT operates, its working environment and the adoption of possible alternative coolant and working media are of interest for innovative cycles. Based on a review of the open literature, there has not been a great deal of work done to model the effect of humidity on the heat transfer and cooling processes (film and convective cooling) of a HP turbine blade of an industrial GT which, in turn, affect the HP turbine blade creep life. This investigation can be carried by evaluating the influence of changing coolant fluid composition on the analysis of the cooling process in the HP turbine blade as result of presence of water vapour. Therefore, in this work an analytical model has been developed in order to investigate the influence of humidity on the HP turbine blade heat transfer and cooling processes taking into account change of gas properties of moist air as a function of temperature and water air ratio (WAR). Also, the temperature variation due to the heat transfer along the metal blade span is considered. Such a model provides the end user with a flexible creep life methodology with which to perform a feasibility study of the effects of presence of water vapour and other contributing factors on the blade creep life. Also, this will help the user to select the most cost-effective engine and make the right inspection and/or maintenance decisions, to help minimise operating cost while giving best engine availability.

### **1.3 Research focus**

Temperature related damage to hot section components are one of the largest factors causing unscheduled engine removals and maintenance costs for GT engines. Original equipment manufacturers (OEM) always calculate the life of such equipment based on the design point of the expected base load and a substantial safety factor will have been included to ensure failure free operation, this leads to many components being discarded while still retaining substantial residual life. In order to assess the life of hot section components of GTs, the

operating conditions, working environment and design parameters should be taken into account when making the lifing assessment. It is common practice in lifing assessments to narrow the scope of the process to a specific engine part by highlighting the following [25]:

- Life criticality of the part,
- Levels of assessment,
- Data available, and
- The importance of the part on the overall operation of the engine or plant.

The GT engine is divided into rotational mechanical equipment, accessory equipment and thermodynamic gas path elements, and this research will focus on exploring the life of the rotational equipment such the HP turbine blades. The decision is taken to identify the parts that operate in the harshest environments within the engine and to consider a part where all possible lifing factors converge.

The blades are subjected to aerodynamic and centrifugal loads on top of the thermal loading (highest temperatures and stresses). Also, failures of HP turbine blades have very serious consequence on the general performance, availability and reliability of GT engines. The working environment and operating conditions of the engine including ambient temperature ( $T_{am}$ ), air humidity, rotational speed (RPM), cooling effectiveness ( $\epsilon$ ) and firing temperatures are important because they are factors that affect turbine blade creep life. The study carried out in this thesis is focused on the creep life of hot section component considering operating conditions, working environment and design parameters. An important addition to existing methods found in the open literature is the effect of humidity in terms of engine performance and creep life.

#### **1.4 Research aim and objectives**

The aim of this research is to develop an analytical life model capable of assessing the influence of humidity on the heat transfer and cooling processes on a HP turbine blade taking into account the engine design parameters, operating conditions and working environment which affect blade creep life.

The following objectives have been defined:



- To execute engine performance simulation by modelling a stationary GT engine using Turbomatch software (DP&ODP), calculations performed considering the variation of humidity.
- To develop and implement a generic component sizing model: a constant nozzle inlet angle method is used with data of the engine performance to size the first stage HP turbine blade.
- To develop and implement a thermal and stress model: the Larson Miller Parameter (LMP) time temperature approach is used to estimate the remaining life of the hot section component at different design parameters and operating conditions.
- To determine the effect of humidity on the creep life of hot section components: investigate the change in gas properties by changing the water air ratio (WAR - the ratio of water to dry air by mass) and investigate the impact of humidity on the heat transfer coefficient.
- A 3-D finite element model (FE) is used to identify critical areas and, perform a feasibility study and facilitate the creep life estimation model.

Finally, the model will be developed for possible use across a range of engine types and operating conditions in different geographical area.

## **1.5 Research contribution**

The major contribution to knowledge in this work includes:

- The focus of this work to develop creep life methodology that is able to provide good creep life prediction for gas turbine high pressure turbine blade's creep life under various gas turbine operating and environmental conditions.
- The main contribution to knowledge of the current work will be the consideration of the effects of the humidity on the HP turbine blade cooling processes and, subsequently, its impact on the performance and blade creep life of GT engines.
- In the case of the performance, the effect of humidity will be considered in term of changes in operating temperature, mass flow, power output and the

relative rotational speed (PCN). In creep lifing consumption the effect of humidity is considered in terms of changes in the operating condition (obtained by performance analysis) as well as modelling the effect of humidity on the heat transfer and cooling process.

## **1.6 Thesis structure**

The thesis includes ten chapters; a brief overview of these chapters is described hereafter:

- **Chapter 1, “introduction”**

The first chapter provide the overall of the research while defining its aim, objectives and scopes of the researcher.

- **Chapter 2, “GT Component Failure And Lifing Approaches”**

This chapter gives some background of engine degradation, common failure mode in gas turbine engine. The creep characteristics and its driving factors are explained. This chapter also summarises the previous research work conducted to calculate the heat transfer in blade cooling and effect of other cooling fluid on the engine performance and blade cooling process. It further discusses the lifing approaches alongside parametric methods.

- **Chapter 3, “Modelling Approach”**

The creep life methodology used in this study is explained in this chapter, which also includes the lifing sub-models. The software model used in the performance simulation with the engine specification is presented. Also, the sizing sub-model of the first stage of HP turbine blade using constant nozzle method is presented. The creep life model is presented in three stages; stage A includes the creep life model to investigate the effect of operating conditions, design parameters and working environment. Stage B includes the heat transfer sub-model in the creep life model to investigate the impact of humidity change on the heat transfer coefficient and blade cooling process. Stage C shows how the analytical creep life model is integrated with 3-D FE model to identify the critical region on the HP turbine blade.

- **Chapter 4, “Humidity”**

This chapter provides a thorough explanation of the method used to calculate the effect of humidity (WAR) on air coolant transport properties. The change of the air coolant properties with water content at different temperature is presented. The use of the NASA CEA programme to calculate the changed in gas properties due to the presence of humidity for different FAR, T and P in the main hot gas stream is explained. The multi regression equation developed for the gas properties of natural gas from the multi-dimensional fluid model data tables using NASA CEA programme is presented. The hot gas properties (natural gas) predicted for different values of WAR is reported.

- **Chapter 5, “Mechanical Stress Model”**

The stress in the blade at each section obtained using 2-D developed stress model is presented. In this study the model developed considers the centrifugal stress and the gas bending stress from the blade root to the tip. The model takes the input data from the performance simulation results and blade sizing model. The centrifugal stress and the resulting bending moment stress acting on the blade sections were calculated at different operating condition and different values of WAR along the blade span.

- **Chapter 6, “Blade Cooling And Heat Transfer”**

Detail of the heat transfer model with the influence of humidity on the blade coolant heat transfer coefficient and non-dimensional parameters is presented in this chapter. The main equations and assumptions made to calculate the rate of heat transfer as well as fluid properties such as density, viscosity, thermal conductivity and specific heat are discussed. The structure of heat transfer model is presented in term of two main sub-models: (i) coolant heat transfer model and (ii) hot heat transfer model.

- **Chapter 7, “Finite Element Modelling Description”**

This chapter provide full details of the stress and thermal models of first stage HP turbine in 3-D FE using Abaqus software. The procedure used to model the mechanical stress and heat transfer from the hot gas to the coolant air through

the blade metal, from which the blade metal temperature distribution is obtained. All the boundary condition, element, material properties, type of mesh, load, constraint, etc used in the thermal and mechanical model are presented in this chapter.

- **Chapter 8, “Finite Element Results”**

This chapter provides the linear static analysis results obtained from the blade 3-D FE model which was conducted to investigate the effects of humidity on the heat transfer and thermal stress, and to identify the critical location of the blade creep life. In first part the mechanical stresses result from centrifugal loads and pressure load is given. Then the results of the blade metal temperature distribution which calculated as function of WAR and also the result using different coolant schemes are presented. Finally the chapter provides the thermal stress result in the form of contour maps and figures in order to identify the effect of dry and humid air on the temperature gradient and critical area.

- **Chapter 9, “Case Studies”**

This chapter provides the results of the integrated creep lifing model including the effect of operating condition, design parameter and working environment. In addition the result of the creep life obtained from the 3-D FE model in terms of blade metal temperature and mechanical stress as used in the LMP are presented.

- **Chapter 10, “Conclusions and Recommendations for Future Work”**

The final chapter of this thesis provides the conclusions of the work presented in each chapter. Also, the limitations of the model and recommendations to improve the creep life model are made for further work.

## *Chapter two*

### **2 GT DEGRADATION, FAILURE MECHANISMS AND LIFING APPROACHES**

#### **2.1 Engine degradation**

Gas turbines (GTs) can be found in many applications in such critical industries as aviation, power generation, oil and gas production and process plant as well as smaller related industries and even domestically. The power generation applications include offshore platforms and marine use where minimizing weight is a major consideration and the GTs used are usually aero-derivative engines. With land-based industries GTs can be used for either direct drive or mechanical drive application.

Normally operation for GTs in aviation is about 2000h before inspection of turbine components, and often more than 5000h before overhaul. GTs for power applications can operate for considerably longer periods before inspection and maintenance due to the difference in safety factors between aviation and industrial/marine applications [26]. Depending on the manner of operation and the working environment, GT components are subjected to different temperature and stress levels, and these differences cause different GT components to fail in different ways: e.g. creep, oxidation, corrosion or fatigue.

During service; industrial, marine or aero, engine failures can exist individually or in combination, and vary with application. Although life techniques for hot section components have been studied for the last three decades [27], understanding failure mechanisms with related driving factors in order to estimate the lifing of hot section component requires further attention.

Failure of a GT engine component is defined as any change in the size, shape and/or mechanical properties of the component that makes it unable to continue to satisfactorily perform its design functions. Failure mode is defined as a

physical or chemical process which singly or in combination produces component failure.

GT engine performance degradation is one of the most important concerns for manufacturers and operators. There are different types of component degradation mechanisms such as fouling, erosion and corrosion. The physical degradation of components and the consequences for the engine performance and life will vary. For example, sand particles deposited on the compressor blades can cause compressor fouling and erosion, though erosion is probably more of a problem for aero engine application, since the state of the art filtration system used for industrial and marine application will invariably eliminate large particles. Fouling will change blade and annulus dimensions causing reduction in mass flow, blade erosion will change blade geometry, boundary layer and aerodynamic profile and, through metal loss, will result in a drop in the compressor efficiency [28; 29].

GT degradation results in lower component efficiencies and reduction of available power which usually requires higher fuel flows and increased Turbine Inlet Temperature (TET) to maintain the required thrust or power. However, due to the limitations of the materials used and air cooling technologies available the TET cannot exceed a certain point. Increasing the TET with given operating conditions and working environment will quickly detract from the life of the hot section components.

## **2.2 Common failures in gas turbines**

During service in a corrosive environment under high stress and high temperature, turbine components such as NGV, blade and discs suffer from cumulative damage. This gradually degrades their mechanical properties, and may cause component failure. Indeed, new failure modes are being discovered with the increasing demand for modern engines to operate at higher temperature and stresses, combined with the use of new materials and new cooling technology systems [31]. Most of the turbine hot section components

are classified as critical components because the consequences of failure could be catastrophic to machine and personnel.

Naturally, those GT engine parts operating under the most extreme conditions of temperature and stress show the most failures, see Table 2-1. Understanding these failure mechanisms and their driving factors are very important in evaluating the life of hot section components. Table 2-1 shows different GT engine applications and their different influences on damage mechanisms. Land based GT engines for the majority of their time are operated at known conditions and therefore can operate for long periods of constant load (speed) coupled with a high operating temperature. For this reason, land based engines are more susceptible to creep than fatigue or oxidation. On the other hand, helicopter engines with frequent start-up and shut-down cycles, and change of flight profiles, makes fatigue more dominant. Marine engines work in an environment where the air ingested into the engine contains higher concentrations of salt and during combustion sulphur from the fuel reacts with the sodium chloride to form sodium sulphate which will then be deposited on the hot section components resulting in accelerated corrosion attack [32].

Three types of damage mechanisms affect turbine blades and cause mechanical damage through creep, fatigue and high temperature corrosion and oxidations. Table 2-2 from [34] shows the GT critical parts and their dominated failure. Table 2-2 shows High Cycle Fatigue as making a significant contribution to failure in turbine and compressor blades but, in fact, HCF failures are uncommon in industrial GTs unless some external factor initiates the fault, e.g. a manufacturing defect is present in a rotating part [26]. This could be because with the new materials and technologies used in modern turbine engines fatigue is almost eliminated at the design stage. Turbine blade life is primarily limited by thermal-mechanical fatigue (TMF), creep and surface degradation due to oxidation and corrosion. In peak load applications involving frequent start-up and shut-down, TMF is the dominate failure mode. In a base loaded combined cycle, oxidation and corrosion will control the component life [35].

**Table 2-1: Severity of failures of gas turbine applications [33]**

	Creep	Oxidation	Hot Corrosion	Thermal-Fatigue
<b>Aero-engines</b>	↔	↑	↔	↑
<b>Industrial engines</b>	↑	↔	↑	↓
<b>Marine engines</b>	↔	↔	↑	↔

Severe ↑, moderate ↔, and light ↓.

**Table 2-2: Common failure in gas turbine components [34]**

← Design criteria and life expenditure effects →							
<b>Components</b>	Yield strength/ stiffness	Time dependent life expenditure			Cyclic life expenditure		
		<i>Oxidation Corrosion Erosion</i>	<i>Wet Corrosion Erosion</i>	<i>Creep</i>	<i>LCF</i>	<i>HCF</i>	<i>Crack propagation</i>
<b>Turbine blade</b>	●	■	●	■	■	■	●
<b>Compressor blade</b>	■	●	■	●	■	■	●
<b>Inner casing</b>	●	■	●	■	■	□	●
<b>Rotor parts</b>	■	●	●	●	■	●	■
<b>Pressure casing</b>	■	●	●	●	■	●	●

■ Significant contribution; □ Affect only local; ● Irrelevant

Naeem et al. [30] have summarised the effects of major three sources of failure for hot section components in GTs (see Figure 2-1) and shown that at temperatures below 800°C, mechanical fatigue is usually the dominant cause of failure, but in the intermediate temperature range (800-1000°C) any of creep, mechanical fatigue and thermal fatigue can be dominant, depending on component design, cooling technology, material used and engine cycle employed.



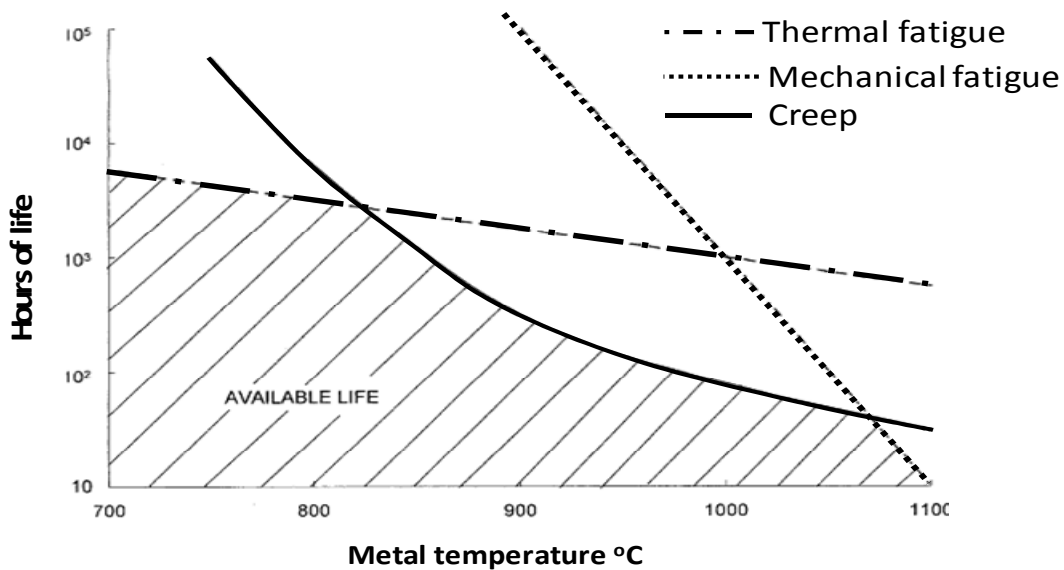


Figure 2-1: Major sources of failure mechanisms in hot section components [30]

### 2.2.1 Fatigue

A metal subjected to repetitive or fluctuating load will fail at a stress magnitude much lower than that required for failure on a single application of load. Fatigue due to cyclic load fluctuation, known as mechanical and thermal fatigue, will lead to crack initiation and propagation which leads to fracture. The mechanical fatigue can be classified into two types of fatigue as shown in Figure 2-2: high cycle fatigue (HCF) and low cycle fatigue (LCF). LCF occurs at high stress and a low number of cycles ( $N < 10^4$ ) and typically is of concern when there is significant cyclic plasticity [36]. HCF results from cracking or fracture phenomenon at stress levels much lower than stresses associated with steady loading. An important distinction between LCF and HCF is that with HCF most of the fatigue life is spent in crack initiation, whereas in LCF most of the life is spent in crack propagation [37; 38].

TMF usually occurs due to the combined effects of cyclic temperature and cyclic stress. Although the stress or strain that caused fatigue is often produced mechanically, it is perhaps even more usual to find the cyclic strain produced by a cyclic thermal field. If the natural thermal expansions and contractions of a part are either wholly or partially constrained as often happens when a thermal gradient is applied to the component, then cyclic strains and stresses result. These cyclic strains produce fatigue failure just as if an external mechanical

loading were applied. Component cracking can be induced not only mechanically but also thermally, and combined will accelerate the cracking. Most LCF problems at high temperatures involve TMF processes. For simplification, in the past, thermal fatigue traditionally has been treated as being synonymous with isothermal LCF at the maximum temperature of the thermal cycle. However, isothermal life prediction techniques are often not applicable to TMF because different damage mechanisms can arise under extreme temperature conditions. Using finite element (FE) analysis, it is possible to analyse complex thermal cycles and to conduct thermal mechanical fatigue under controlled conditions.

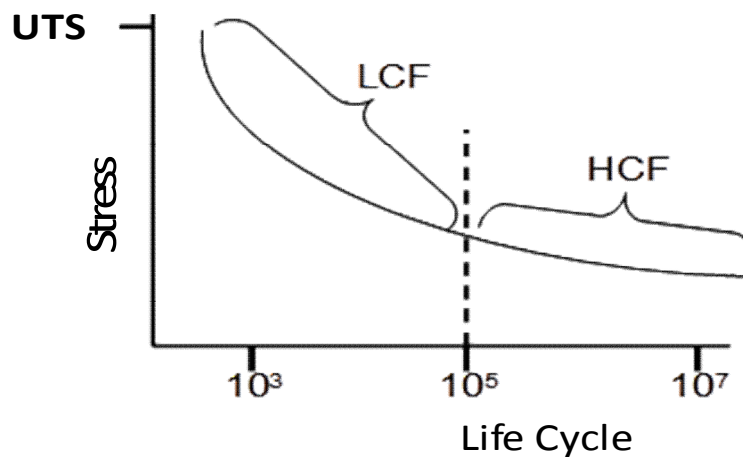


Figure 2-2: Schematic illustration of fatigue characteristics [39]

### 2.2.2 Corrosion and oxidation

In oil and gas, marine, chemical and power generation industries hot section components can be affected not only by corrosion and oxidation because of the range of operating temperatures experienced but will also depend on the working environment. Hot corrosion is the accelerated attack of materials caused by elevated temperatures in the presence of salt contaminants and deposits of ash. Many materials that experience hot corrosion are exposed to high heat fluxes and temperature gradients, e.g. turbine blades. The hot corrosion can be described by the dissolution of a protective metal oxide into the fused salt and the subsequent precipitation of the metal oxide in a non-protective form. Hot corrosion can be classify into two types; high temperature

hot corrosion (type I), which occurs at metal temperatures between 815°C to 955°C and low temperature hot corrosion (type II), occurs at temperatures between 595°C to 815°C. These temperatures regimes and their severities are shown in Figure 2-3 [40-42].

Oxidation is a thermo-chemical process and usually occurs at high temperatures by formation of a thin oxide layer on the alloy surfaces. Oxidation is a temperature, time and strain dependent phenomenon. The growth rate of the oxidation is depending on the diffusion through the oxide layer at that surface. The oxidation failure can be estimated based on the oxidation growth rate. One of the most common consequences of the oxidation failure is wear of the hot section components [43]. Oxidation phenomenon also has significant influence on crack growth. During fracture mode the oxygen reduces the grain boundary energy in such a way that the crack growth path becomes intergranular. In this case, plastic deformation can exist within the grain, and slip bands work as diffusion paths for oxygen to reach the grain boundaries [22; 44].

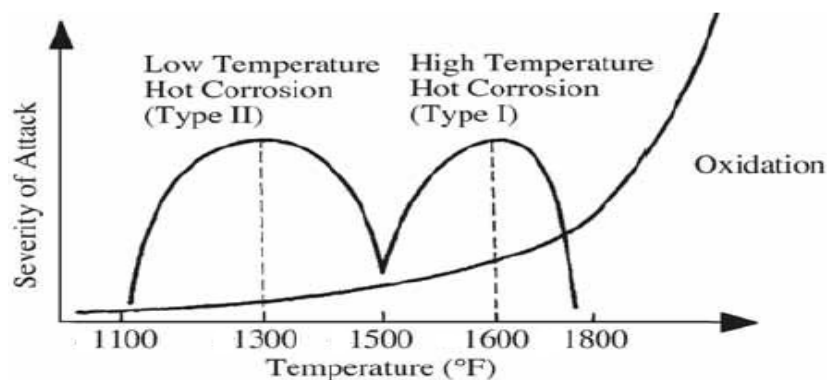


**Figure 2-3: Regimes of high temperature environmental attack [45]**

Coating techniques are essential and are now widely used to protect hot section components from a wide range of temperature and working environment attacks. However, corrosion and oxidation are unavoidable in high temperature environments contaminated with e.g. harmful fuel.

### **2.2.3 Creep**

Creep is slow plastic deformation (strain) that occurs in a component under the influence of stress and metal temperature over a period of time. Deformation or

creep is governed by the material properties, time, temperature, and load conditions. The deformation that occurs is made up of an elastic deformation and an inelastic or permanent deformation which is not recoverable. Typically creep occurs at temperature above about 40% to 60% of the absolute melting temperature according to the material [37; 46; 47].

Creep behaviour is one of the most critical factors determining the integrity of elevated temperature components, because such components can slowly and continuously deform under constant stress over a period of time. This deformation is the result of slip occurring in the crystal structure together with flow of the grain boundary layer. Because of such deformation, unacceptable dimensional changes and distortions take place, ending in final rupture of the component (see Chapter 5). Creep is the largest potential problem in applications involving high temperatures and high stress.

Creep in polycrystalline materials occurs as a result of the motion of dislocations within grains, grain boundary sliding, cavitation and diffusion processes. Increase in metal temperature can give an atom enough thermal energy to jump from its original position at to another while transmitting energy to adjacent atoms. This results in diffusion which, in turn, alters the atomic arrangement and forces the grain to extend with time [47; 48].

### **2.2.3.1 Creep characteristics**

The typical characteristics of high temperature creep can be explained in term of strain versus time. The gradient of the curve shown in Figure 2-4 is the creep rate. The strain axis is the total of initial elastic and inelastic strain. Incubation period is the region of initial elastic deformation, which occurs immediately after the full load is applied. In single crystal or highly oriented materials it is usually observed at relatively low stress and high temperature. This stage is followed by the primary stage of creep behaviour in which the initial creep rate reduces rapidly until a constant creep rate is attained as dislocations build up and material hardening processes dominate. This is followed by the second phase or steady state region of creep deformation. It is frequently the longest portion and corresponds to a period of constant creep rate where there is a balance

between work hardening and thermally activated recovery processes, the behaviour here can be described as a function of stress and temperature. Finally in the tertiary stage the creep rate increases rapidly until fracture or stress rupture occurs. It can be due to a number of factors including; (i) mechanical instability, such as the occurrence of necking (localized reduction in cross-sectional area), (ii) microstructural instability, including grain growth or recrystallization with single-phase material or the gradual loss of creep strength as over-ageing occurs during creep of precipitation-hardened alloys, (iii) the nucleation and growth of internal micro cracks which develop until the number and sizes of the micro cracks are sufficient to cause the creep rate to increase.

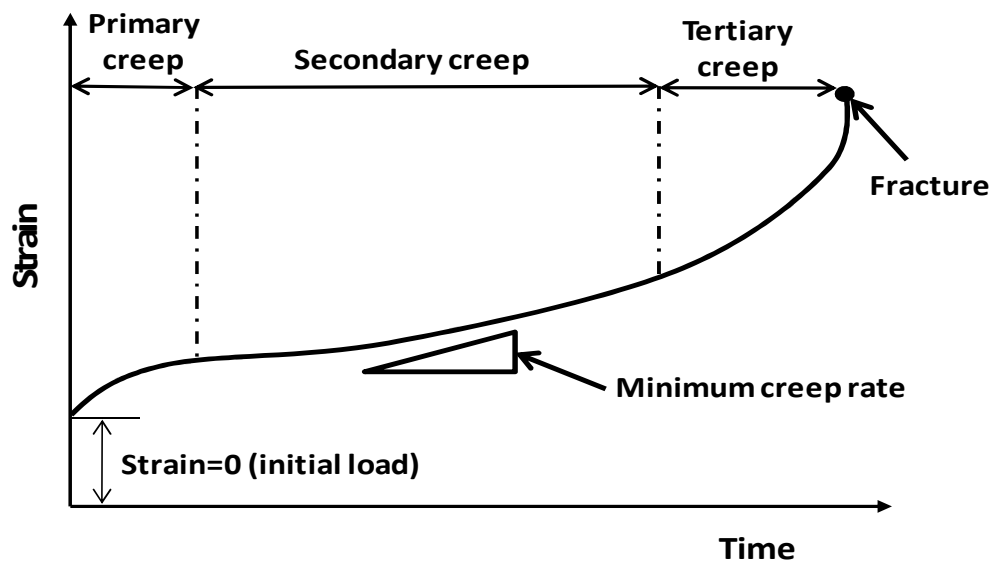


Figure 2-4: Four stages of creep failure mechanisms [46; 49]

The creep behaviour of materials is obtained through testing of specimens at constant temperature and stress. The initial assessment of creep capability is made using stress rupture data that determines the time to failure [39]. But the limitation of this technique is that it does not give any information on the shape of the creep curve rather giving useful data for initial life assessment in a new design.

### 2.2.3.2 Creep driving factors

Creep characteristics depend on several driving factors in hot section components; temperature, stress, time and material properties. However, for

engineering applications the most important factors are stress and temperature [26; 31; 37; 43; 50; 51].

**Temperature:** Figure 2-5 shows the variation of creep strain against time, the influence of temperature on creep rate can also be observed. As temperature increases the gradient of the creep strain rate in the primary region also increases as does the secondary creep rate, and the point at which the acceleration into the tertiary phase occurs is earlier resulting in a reduced life to stress rupture [52]. At the highest temperature  $T > 0.4$  melting point temperature ( $T_m$ ) the mobility of atoms increases rapidly with temperature and so can cause material diffusion which can also help dislocation. At lower temperatures diffusion still can occur but only in limited local areas such as grain boundaries and phase interfaces. A temperature which is considered high for creep in one material might not be so in another [53].

**Stress:** Creep rate is also sensitive to the applied load and load state. In Figure 2-5, the variation of creep strain against time and the influence of stresses on creep rate are shown. The initial creep strain rate in the primary region is higher the higher the stress. The secondary creep rate also increases with stress and the acceleration into the tertiary phase occurs earlier the higher the stress, resulting in a reduced life to stress rupture. In other word, with increase in applied stress, the primary and secondary stages are shortened or even eliminated and the tertiary stage predominates in the creep process [52; 53].

From the creep curves shown in Figure 2-5 similar behaviour is observed for constant stress and different temperatures. This means both parameters significantly affect creep behaviour. It can also be seen that all stages of creep are accelerated with increase in stress or temperature. Webster [47] stated that the shape of the curve was different depending on the time and/or temperature. For  $T > 0.4T_m$  it is likely that secondary and tertiary creep will be most pronounced and for  $T < 0.6 T_m$  primary creep will predominate. This behaviour can be partly attributed to the different stresses needed at each temperature to cause failure in the same time.

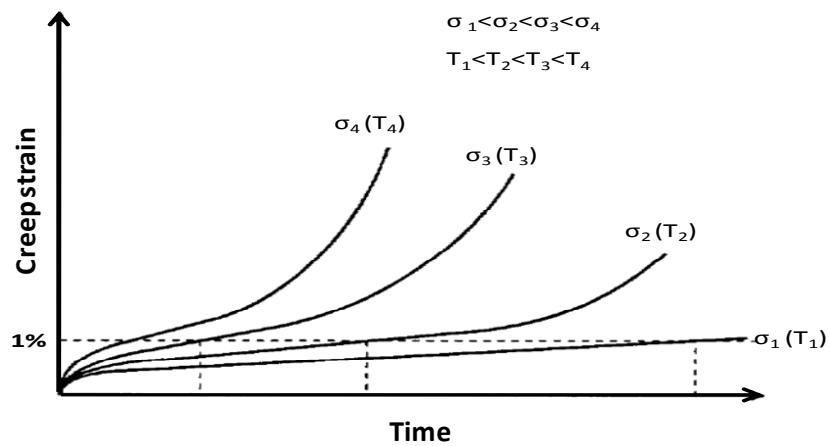
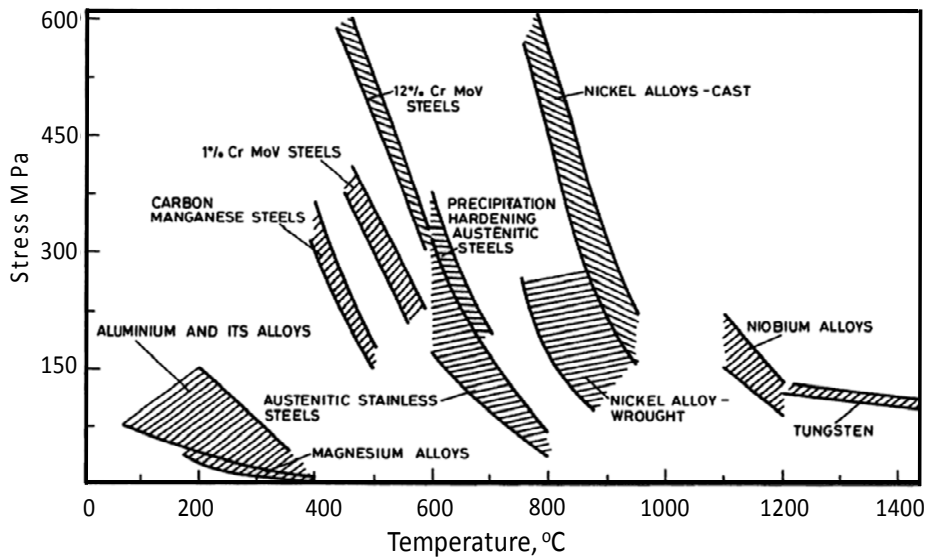


Figure 2-5: Creep curves dependence on stress and temperature [52; 54]

**Microstructure:** Creep properties of materials are intrinsically determined by the microstructure of the materials. Grain size affects creep rate in all three creep stages. These microstructural effects can be superimposed and can affect creep properties of materials in a number of complex ways. At constant stress and temperature, the increase of grain size increases the steady state creep rate of one material and decreases it in another. Li and Dasgupta [53] classified the microstructural deformation mechanisms in creep into two types; intragranular and intergranular. Intragranular creep deformation involves creep deformation within single crystals and individual grains of polycrystal. The mechanisms of intragranular creep deformation including slip (stress decrease or temperature increase, slip spacing increases for most materials) and subgrain formation (during the primary stage of creep). While intergranular creep deformation involves deformation occurring in grain boundaries of polycrystals. The mechanisms of intergranular creep deformation including grain boundary sliding, creep cavity, fold formation and grain boundary migration. These two types of deformation illustrate the relation between the microstructural effects and the creep properties of materials.

Creep in polycrystalline materials is sensitive to grain size, alloying additions, initial condition of the material and heat treatment. It indicates that improvements in creep strength that can be gained by alloying additions to steel to produce a material which can be used for the highest temperature application

such as turbine blades. Figure 2-6 compares the creep resistance properties of a range of engineering alloys.



**Figure 2-6: Stress to produce creep rupture in 100h in various alloys [47]**

Figure 2-6 shows tungsten and niobium alloys have high temperature resistance but lower stress resistance. 12% CrMoV steels, in contrast, have better stress resistance but fail at lower temperatures. Cobalt base superalloys are primarily used for blade vanes because of their good weldability and Nickel base superalloys are used for turbine blades to achieve greater strength. Both these metals can be subject to microstructural changes. Material microstructural changes lead to decrease in strength of the grain boundaries and the matrix, thus leading to the deterioration of the mechanical properties and a decrease in the rupture time and creep strength. Also, the residual life of all materials decreases with increasing service life due to microstructural changes [45; 55].

### 2.3 Turbine blade cooling

The technology of cooling GT HP turbine blades using internal convective coolant has developed over the years from simple smooth cooling passages to very complex geometries involving many different surfaces, architectures and fluid-surface interactions. The aim of such technology is to obtain the highest overall cooling effectiveness with the lowest possible penalty on the thermodynamic cycle performance [56]. Figure 2-7 show typical film-convective



cooling architecture of HP turbine blades. Figure 2-8 presents the generic cooling technology performance chart for a turbine blade airfoil. The cooling technology shown on this figure presents the heat loading parameter and airfoil cooling effectiveness, defined as non-dimensional quantities.

$$\text{cooling effectiveness, } \varepsilon = \frac{T_g - T_b}{T_g - T_{cin}} \quad 2-1$$

$$\text{heat loading parameter} = m_c * C_{p_c} / 2 * h_g * A_{gs} \quad 2-2$$

Where the heat loading parameter, is the ratio of the overall hot gas heat flux delivered to the blade against the overall coolant capability to absorb that heat.

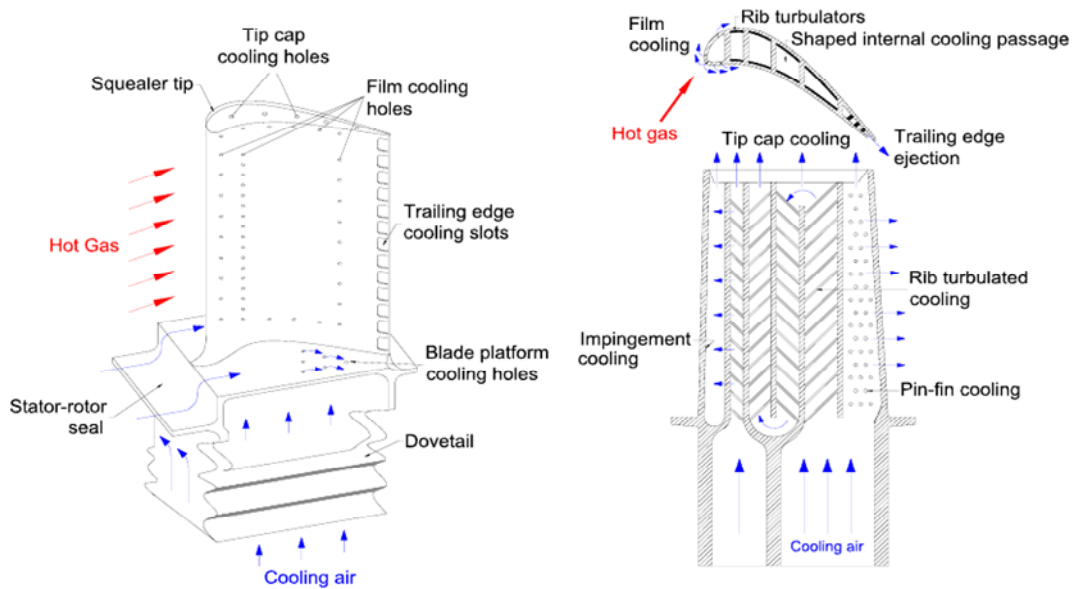


**Figure 2-7: Cooling architecture of HP turbine blade [57]**

Research has been carried out in last three decades to investigate the process of cooling of the HP turbine blade. Two conceptually different cooling models are reviewed, firstly a simple model that employs semi-empirical data established for air cooled conventional blade turbines. The purpose of the first model (standard blade) is to calculate the required mass flow of coolant to maintain blade temperature within prescribed metallurgical limits. A standard blade has uniform gas temperature and blade metal temperature along the blade span and chord, and infinite thermal conductivity. The second model

considers the influence of detailed cooled blade geometry for describing the cooling of the gas turbine blades. This model can consider the influence of cooling methods and internal geometry of the blade on the heat transfer.

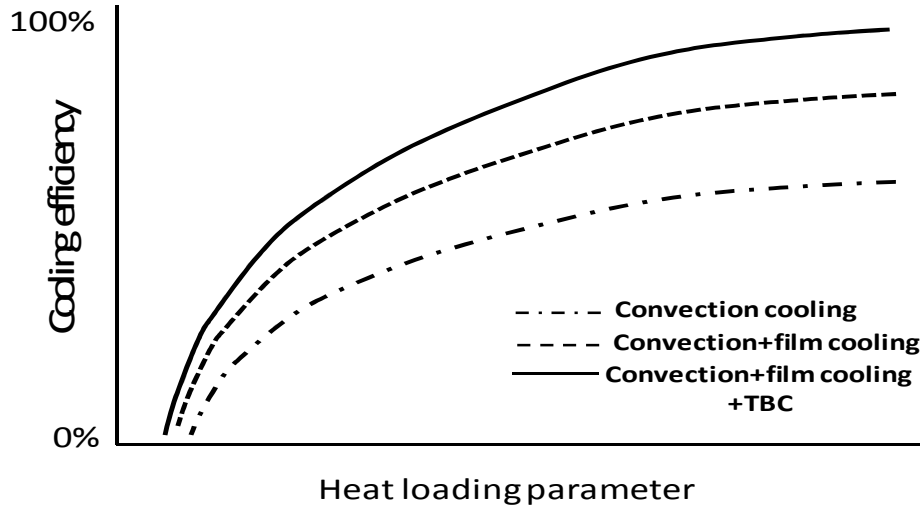


Figure 2-8: Cooling technology performance curve [56]

**Ainley** [8] presented basic equations for the heat transfer process and assumed constant inlet gas temperature ( $T_g$ ) along the span and chord, where the blade metal temperature was constant only along the chord and through the blade walls  $T_b=T_{bg}=T_{bc}$ , where  $T_{bg}$  is the blade metal temperature gas side,  $T_{bc}$  is the blade metal temperature coolant side. That means the blade metal temperature increases in the span-wise direction and reaches a maximum at the end of the blade.

Also, the external and internal wetted perimeters for the blade were constant along the span. The wet parameters of gas and coolant side ( $S_g$  and  $S_c$ ) are constant along the span. Ainley stated the basic equation for the heat transferred from hot gas to the coolant per unit span ( $q$ ) as:

$$q = k_{bw}A_{bw} \frac{d^2T_b}{dy^2} + h_g S_g (T_g - T_b) = h_c S_c (T_b - T_{cl}) \quad 2-3$$

$$q = m_c C p_c \frac{dT_{cl}}{dy} + h_c S_c (T_{cl} - T_b) \quad 2-4$$

Where  $T_{cl}$  is coolant temperature,  $k_{bw}$  is the metal conductivity and  $A_{bw}$  is the metal area in a blade cross-section.

Ainley rewrote these equations in terms of the parameters as presented in [6; 16] and obtained the blade metal temperature and outlet coolant temperature at  $y=H$ :

$$T_{bmax} = T_g - (T_g - T_{cl})Xe^{-k}/(1 + X) \quad 2-5$$

$$T_{co} = T_g - (T_g - T_{cl})e^{-k} \quad 2-6$$

Where  $x = h_c S_c / h_g S_g$ ,  $k = X / [(1 + X)w^+]$ ,  $w^+ = (m_c C_{p_c}) / h_g S_g H$  and  $H$  is the blade height.

**Halls [9] and Holland and Thake [5]** used convectively cooled blades and defined cooling effectiveness based on constant inlet gas temperature and blade metal temperature along the span and chord (standard blade). They assumed constant coolant inlet temperature in the chord-wise direction with uniform metal wall temperature (constant through the blade wall  $T_b = T_{bg} = T_{bc}$ ). The heat transfer from the gas stream to the coolant side, under the assumption of the perfect gas and uniform heat transfer coefficient, is given by the heat balance equation:

$$h_g A_{gs} (T_g - T_b) = m_{cstandard} C_{p_c} (T_b - T_{cin}) \quad 2-7$$

Consider the external wetted area to the product of the airfoil perimeter and span, the energy balance for the blade is given by:

$$h_g S_g H (T_g - T_b) = m_c C_{p_c} (T_{co} - T_{cin}) \quad 2-8$$

With the three temperatures  $T_g$ ,  $T_b$  and  $T_{cin}$ , known or specified the cooling effectiveness can be obtained using the following equation:

$$\varepsilon = (T_g - T_b) / (T_g - T_{cin}) \quad 2-9$$

Also, the cooling efficiency can defined as the ratio of the actual temperature rise ( $T_{co} - T_{in}$ ) to the maximum temperature ( $T_b - T_{cin}$ ), the details of their approach for a blade with convective cooling, film cooling, finite thickness of the metal wall and thermal barrier coating (TBC) is presented in [6; 11; 16; 58].

**Consonni** [1] followed the Ainley approach in terms of determining the heat transfer coefficient and descriptions of the internal blade geometry using the Z parameter (technology level); he assumed that the hot gas external temperature was constant and the blade temperature increases along the span but allowed for finite metal and TBC thickness using the Biot number. He also introduced film cooling to the blade cooling model. Thus, the coolant outlet temperature was obtained by equating the heat fluxes at the outlet section:

$$h_g(T_g - T_{bg})k_{bw}(T_{bg} - T_{bc})/t_{bw} = h_c(T_{bc} - T_{co}) \quad \mathbf{2-10}$$

Where  $t_{bw}$  is the blade metal Biot number.

Consonni's analysis and calculation were based on estimating the cooling flow required over the chord of the blade, using mean temperatures and heat transfer coefficients.

**Horlock** [10] investigated the operation of a counter-flow heat exchanger with a large surface area, with water injection to the cold side and increase in the thermal capacity of the cold gas stream for both reversible and irreversible flows. The thermal capacity of the cold stream is  $C_c$  and the hot stream is  $C_g$ . The mole flow rate is  $n$  and the mole heat capacity is  $C_p$ , thus the  $C_c = n \cdot C_p$ . With no external heat loss, the heat transferred calculated using:

$$C_g(T_{g1} - T_{g2}) = C_c(T_{c1} - T_{c2}) \quad \mathbf{2-11}$$

Where the 1 and 2 are the stations in and out.

The exchanger effectiveness ( $\varepsilon$ ) is defined in [59] as the ratio of the actual heat transferred to the maximum heat that can be absorbed. Horlock et al [11] also studied the effect of cooling air flow rate (external film cooling and internal convective cooling) on the GT performance (thermal efficiency). For convective cooled blade only, the simple heat balance is given by Equation 2-12 and when film cooling is used the heat transfer is calculated using Equation 2-13:

$$q = m_c C_{p_c}(T_{co} - T_{cin}) = m_g C_{p_g}(T_{gin} - T_{gout}) = h_g A_{sg}(T_{gin} - T_w) \quad \mathbf{2-12}$$

$$q = A_{sg} h_{fg} (T_{aw} - T_b) = m_c C p_c (T_{co} - T_{cin}) \quad \mathbf{2-13}$$

The  $T_{aw}$  is the adiabatic wall temperature, which in absence of film cooling equals the mainstream temperature and  $h_{fg}$  is the heat transfer coefficient under film cooling conditions ( $h_g = h_{fg}$ ). The film cooling effectiveness is defined by:  $\varepsilon_f = (T_g - T_{aw}) / (T_g - T_{co})$ , and  $T_{aw}$  is obtained as shown in Chapter 6.

They found the most important effects of turbine blade cooling were reducing the inlet stagnation temperature to the first rotor and a pressure loss resulting from mixing the cooling air with the mainstream.

**Jordal et al** [12] combined two conceptually different cooling models to estimate the behaviour of a convective cooled blade and defined the coolant mass flow. The first, simpler, model used semi-empirical data for air cooled GTs and the fundamental equations for cooling are presented in [5]. The limitation of the first model is that it cannot use alternative coolant or working media ( $m_c$ ,  $C p_c$ ), also it cannot assess the effect of internal geometry ( $Z$  parameter) on the cooling process. The second model used more a detailed analytical approach, relied on a large number of geometrical parameters and was based on the work of Consonni [1]. The second model requires significantly input data, however it gives more information about coolant pressure losses and indicates required changes in the blade internal geometry to keep the desired blade metal temperature.

**Young and Wilcock** [13; 14] developed a framework for modelling air cooled GT cycles based on Holland's approach, including supplementing the film cooling with convective cooling for finite thickness of the metal wall and for thermal barrier coating. They assumed a temperature distribution in the cross direction through the blade wall and coating (not standard blade), with the assumption that such temperatures are constant in the chord direction ( $T_{TBC} \geq T_{bg} \geq T_{bc}$ ). Also, the inlet gas temperature was assumed to be constant along both the span and chord. The heat transfer rates for the coolant side are given by:

$$q = m_c C p_c (T_{co} - T_{cin}) \quad \mathbf{2-14}$$

The calculation of the  $T_{co}$  required the knowledge of the mean internal heat transfer coefficient and was obtained by introducing an internal flow cooling efficiency (typical values 0.6-0.8) as presented in [58]. The mainstream flow heat transfer rate can also be expressed by:

$$q = h_g A_{gs} (T_{aw} - T_{TBC}) \quad \mathbf{2-15}$$

The dimensionless coolant mass flow rate  $m^*$  and, the TBC and blade metal Biot numbers are calculated using:

$$m^* = m_c C_{p_c} / h_g A_{gs} = (T_{aw} - T_{TBC}) / (T_{co} - T_{cin}) \quad \mathbf{2-16}$$

$$Bi_{tbc} = h_g t_{tbc} / k_{tbc} = (T_{TBC} - T_{bg}) / (T_{aw} - T_{TBC}) \quad \mathbf{2-17}$$

$$Bi_{bw} = h_g t_{bw} / k_{bw} = (T_g - T_{bc}) / (T_{aw} - T_{TBC}) \quad \mathbf{2-18}$$

Thus, the overall cooling effectiveness is obtained by using:

$$\varepsilon = (T_g - T_{bg}) / (T_g - T_{cin}) \quad \mathbf{2-19}$$

**Torbidoni** [6; 15] developed a new analytical model, based on Consonni's [1] and Ainley's [8] previous work, to calculate the cooling flow required for the turbine blade first stage of a high temperature GT, with given gas and coolant inlet temperatures. The method considered the heat flux through an elementary cross-sectional area of the blade, at given height and chord position. The effect of the internal blade geometry on the cooling performance was considered through the cooling system technology parameter  $Z$ . Torbidoni assumed that the inlet gas temperature is constant along both the span and the chord and the blade metal temperature is constant only along the chord, but varies in the span-wise direction and also through the blade walls and coating. The presence of TBC reduces the convective heat transfer through the blade. The overall energy equation for the heat flux transfer is therefore as follows:

$$dq = U_g dA_{cs} (T_{gr} - T_{cin}) \quad \mathbf{2-20}$$

$$U_g = [a_s (1/h_g + t_{TBC}/k_{TBC} + t_{bw}/k_{bw}) + 1/h_c]^{-1} \quad \mathbf{2-21}$$

Where  $U_g$  is the overall heat transfer coefficient and  $a_s$  is the ratio of the wetted heat transfer area of coolant flow single blade to the wetted heat transfer area of gas flow single blade.

Horlock and Torbidoni [16] analytically re-examined Ainley's work in order to overcome some of the limitations of Ainley's cooling approach. The new model allowed for chord-wise variations of coolant flow, blade temperature, mainstream gas and coolant temperature, heat transfer coefficients, finite blade wall thickness, TBC and multi-pass channels.

It must be noted that all the work mentioned above used the properties of dry air and neglected the effect of air humidity, possibly because many GTs operate in environments in which air humidity is very low and therefore has little influence on GT performance.

## **2.4 Humid air and blade cooling**

Many gas turbines operate in environments in which air humidity is very low and therefore has little influence on gas turbine performance. This is the reason why ambient humidity effects have not received much attention in industrial gas turbines. But humidity becomes more important when large variations in ambient absolute humidity are expected, especially in hot and humid climates [17]. In aviation gas turbines the effect of humidity has been investigated and presented in AGARD [22]. Amell et al [23] investigated the influence of the relative humidity on the atmospheric air cooling thermal load. The result shows that at high relative humidity the cooling thermal load increased to almost twice that when the relative humidity is low. Mathioudakis and Tsalavouts [17] investigated the impact of ambient humidity on the performance of industrial gas turbines and examined the effect of humidity on methods used for engine condition assessment and fault diagnostics. It was found that humidity has significant effect (especially at higher ambient temperatures) on component health parameters and such parameters could exhibit apparent deviations if humidity is not taken in account.

The spraying of water inside the compressor is a popular approach to achieving increased power and efficiency, and much research has focused on this effect

[18-21], but no attempt has been made to evaluate the long term effects of air humidity on the GT blade cooling heat transfer and creep life.

James [60] investigate the feasibility of using water injection and evaporation into the turboshaft engine to allow increased power output and decrease in air cooling temperature. This decrease in cooling temperature can offset the effect of increased gas temperature and increased shaft speed and thus keep turbine blade stress rupture life constant. The analysis utilized the NASA Navy Engine Program (NNEP) to model the thermodynamic performance of a typical helicopter engine in order to study the effect of inject water on the air cooling temperature and the rate of TBC transient heat conduction. The increased turbine speed and gas temperature were used in a stress repute model to determine the blade metal temperature required to give constant stress rupture life. The thermal properties of the coolant air were ignored, since claimed that the thermal properties of steam are more favourable for heat transfer process. The study was considered only the effect of water injection on the gas side heat transfer and TBC.

Still et al. [7] experimentally investigated the influence of humidity on the convective heat transfer from a small cylinder at low air temperatures. For molar fractions of water vapour up to 0.27, the heat transfer rate increased with increasing humidity. They proposed a correction factor if humid air is used in the heat transfer equation in terms of a Nusselt number expressed as a function of Reynolds and Prandtl numbers.

Cleeton et al. [61] studied the blade cooling optimization of a humidified air turbine (HAT) and a steam injected gas turbine (STIG) cycles. The blade cooling model used was that presented in Yound and Wilcock [14]. It was found that in HAT, using the humidified or post-aftercooled coolant reduced the coolant demand but increased compression work. Optimising the choice of coolant bleeds in STIG, the bleeding steam for cooling purposes reduced the steam available for power augmentation and thus compromised work output.

The convective cooling of gas turbine blades using air or steam as the coolant medium in open and closed loop steam cooling was investigated under different



operating conditions by Albeirutty et al. [24]. The study compared the performance of different blade cooling schemes. A general heat transfer model was developed for the analysis using the mean blade temperature at the mid-blade height. The result showed that steam was a better cooling medium than air, when employed in an open circuit and a closed loop scheme. Also, the use steam or water as alternative cooling fluids is feasible and practicable for stationary turbine, where the added weight and complication of the fluid supply system are not major concerns.

There has not been a great deal of work done to model the effect of humidity on the heat transfer and cooling processes (film and convective cooling) of a HP turbine blade. The aim of this study is to present an analytical model to investigate the influence of humidity on the turbine blade heat transfer and cooling processes which, in turn, affect blade creep life of industrial gas turbines. The work presented here considers gas properties of moist air as a function of temperature and relative humidity, to investigate the effect of humidity on the high pressure turbine blades' heat transfer coefficient and creep life. Also, the temperature variation due to the heat transfer along the metal blade span is considered. The model is flexible and capable of assessing the main parameters that influence the blade cooling performance, such as cooling methods, alternative cooling fluids, blade geometry, heat transfer coefficients, gas properties and material and thermal barrier coating. The whole cooled blade row is regarded as a heat exchanger subjected to a mainstream hot gas flow from the combustion chamber.

## **2.5 Parametric methods**

Component life assessment based on data collected from creep curve and experimental creep laws do not always provide accurate life estimation. Although experiments can provide accurate life estimation, data are often insufficient to cover different loads and temperatures and extrapolation or interpolation to the stresses and temperatures of interest need to be performed. Also, creep laws require suitable constants to be obtained before the model can

be used. When these constants change with temperature the calculated life becomes inaccurate.

There are alternative methods based on time and temperature. Many parametric techniques have been proposed in the literature and it is not possible to discuss all of them here; the most widely accepted are the Orr-Sherby-Dorn parameter (OSDP), Goldhoof-Sherby parameter (GSP), Manson-Haferd parameter (MHP), Manson-Succop parameter (MSP) and Larson Miller parameter (LMP). The requirement for these models is that a full range of temperature and stress can be covered that may require extrapolation to high or low temperature and to high stresses beyond where test data exists. The limitation to the extrapolation on temperature is set by the material melting point (40% of absolute melting temperature). Limits to the stress are linked to the tensile properties such that the ultimate tensile strength at the temperature of interest presents an upper limit to the applied load [52]

### **2.5.1 Orr-Sherby-Dorn parameter (OSDP):**

Using Equation 2-22, creep data obtained from for different values of stress and different temperatures can be superimposed and plotted on  $\log t_f$  versus  $1/T_M$  to build iso-stress lines will be parallel to each other as shown in Figure 2-9. The value of the OSDFP is the intercept on the  $\log t_f$  axis. Satisfactory agreement is usually found for pure metals and dilute alloys at  $T > 0.5T_m$  but not in other circumstances [47; 62].

The OSDP presupposes parallel iso-stress evolution lines with the same gradient, A, and no intersection points (assumes activation energy is constant) as shown in Figure 2-9. The parameter is given by:

$$OSDP = \log(t_f) - A/T \quad \mathbf{2-22}$$

Where  $A=Q/R_0$ , Q is a characteristic activation energy and  $R_0$  is the universal gas constant.

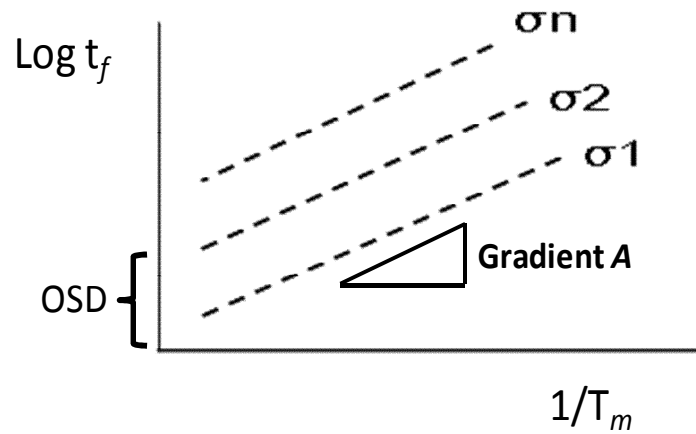


Figure 2-9: schematic explanation of iso-stress lines in  $\log t_f$  vs.  $(1/T_m)$  [37; 62; 63]

Once the value of the OSDP for different stresses is obtained, a creep rupture curve can be plotted. Using Equation 2-22 with the value of OSDP at any stress but different metal temperature can be interpolated or extrapolated to determine the component creep life.

### 2.5.2 Goldhoof-Sherby parameter (GSP)

This method is based on the convergence of the iso-stress evolution lines at a point with coordinates  $1/T_m$  and  $\log t_f$ , located below the region of the experimental data (see Figure 2-10). The parameter given by [37; 62]:

$$GSP = \frac{(\log(t_f) - \log(t_a))}{\left(\frac{1}{T_m} - 1/T_{ma}\right)} \quad 2-23$$

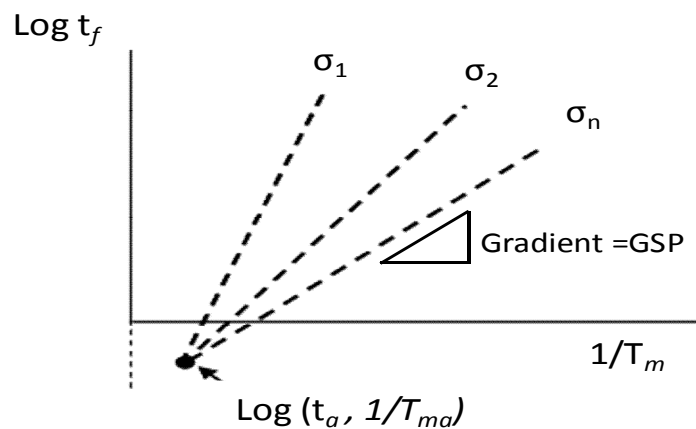


Figure 2-10: Iso-stress lines for  $\log t_f$  vs.  $1/T_m$

### 2.5.3 Mason-Haferd parameter (MHP):

This parameter is slightly different from LMP and OSDP, the iso-stress plots are of  $\log t_f$  vs  $T$  instead of  $\log t_f$  vs  $1/T_m$ , and all the lines pass through a common point  $(T_m, \log t_f)$  as shown in Figure 2-11. MHP assume that the convergence of the iso-stress lines located above the region of the experimental data with the parameter given by [39; 62]:

$$MHP = \frac{(T_m - T_{ma})}{(\log(t_f) - \log(t_a))} \quad 2-24$$

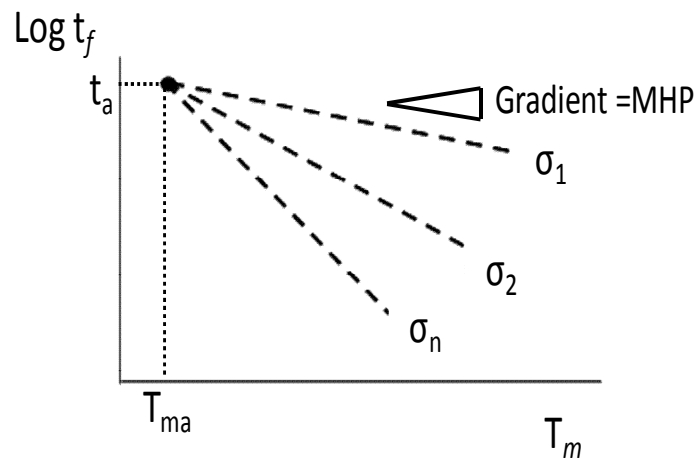


Figure 2-11: Iso-stress lines for  $\log t_f$  vs.  $T_m$

### 2.5.4 Manson-Succop's parameter (MSP):

The MSP is similar to the Manson-Haferd in that temperature is used as the predictor of  $\log t_f$ , however, no intersection of the iso-stress lines is allowed. In that sense MSP is similar to the OSDP. The MSP assumes that parallel iso-stress line can be achieved when graph  $\log t_f$  is plotted against  $T_m$  and the gradient is equal to B, see Figure 2-12 [37; 62; 63]. The MSP equation can be written as:

$$MSP = \log(t_f) - BT_m \quad 2-25$$

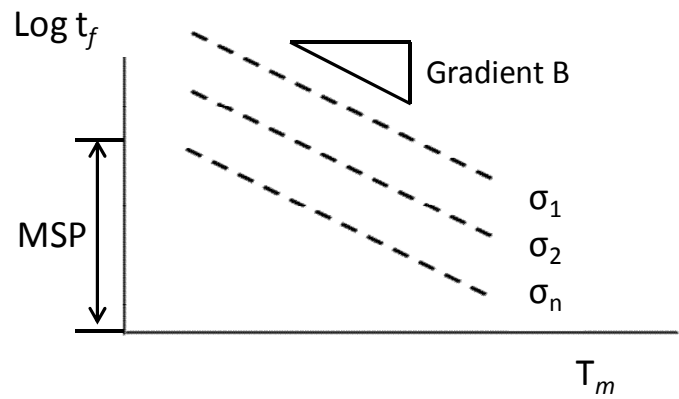


Figure 2-12: Iso-stress lines in  $\log t_f$  vs.  $T_m$  using MSP [37]

### 2.5.5 Larson Miller parameter (LMP)

The LMP approach has been a useful tool in predicting low stress, long time rupture behaviour in the handling of creep rupture data. LMP combines temperature and creep life data and is a useful analytical technique for evaluating the effects of stress on creep life over a range of temperatures. The success of LMP lies on the fortuitous elimination of the one of the two independent variables that can be controlled during a creep test namely absolute temperature and applied stress with time. The power of the LMP lies in the elimination of the temperature dependence and allows one to construct master rupture curves [64; 65].

$$LMP = \frac{T}{1000} (\log t_f + C) \quad 2-26$$

Where C is material constant and  $t_f$  = time-to-failure

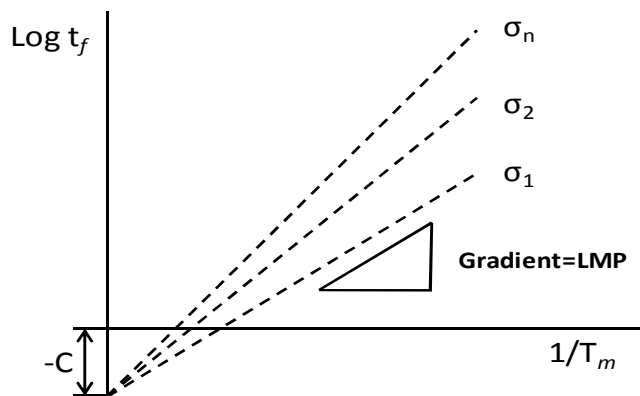


Figure 2-13: Schematic Illustration of plot of  $\log t_f$  vs  $1/T_m$

The constant  $C$  is often taken as 20 in industrial applications but it can vary according to the application. Any combination of temperature and time-to-failure will give equivalent values for LMP and for creep stress. The LMP approach has been extended to cover rupture strength in which case it would represent the life time to reach fracture due to either strain or rupture, depending on operating conditions. Therefore, by dividing the real time of operation by the total life to failure, life fractions can be determined [66]. The LMP assumes the convergence of the iso-stress evolution lines in a point located at  $-C$  on the  $\log t_f$  axis as shown in Figure 2-13 [37; 62; 63].

## 2.6 Parameter selection

A critical decision for accurate life calculation is selection of the most appropriate parameter for the assessment because suitability of the parameter depends on the temperature or/and stress range, the type of materials used and relevant failure mechanisms. Here the different parameters used to fit creep data are compared.

Marahleh et al. [55] claim LMP gives accurate predictions for materials subjected to long periods at high temperatures in those cases where no microstructural changes take place. When microstructural change does occur, the extrapolated values are greater than the test results.

Bueno and Sordi [63] compared the performance of OSDP, GSP, MHP, MSP and LMP applied to Fe-Mn-Al steel creep data. Good results were obtained from MSP, LMP and OSDP, though MSP was slightly better than the other two. Bueno and Sordi also, compared the relation between hot tensile behaviour and creep of Cr-Mo steel for different stress levels and temperatures. In order, the best results were given by MHP, OSDP, MSP, LMP and GSP. It was suggested that the relative success of MHP was due the range of high temperatures used for the material testing. The good results for of OSDP were due to the good fit of the Monkman-grant relationship to the creep and hot tensile results.

Eno et al. [62] evaluated the commonly used parameters OSDP, MHP, MSP, LMP and the Mandelson-Roberts-Manson parameter (MRMP), using creep data

for Haynes 230 alloy and nickel chromium alloy 617. The parameters were assessed for their ability to fit stress-temperature creep behaviour data. The best fit for the nickel chromium alloy 617 was achieved using MRMP, followed by LMP. The best fit for the Haynes 230 alloy was achieved using MRMP, closely followed by MHP and LMP.

The research results presented above indicate that the individual parameters should be considered as particular cases within a common framework with LMP the most useful because its ease of use over a wide variety of applications.

## 2.7 State of the art in creep life modelling

Creep behaviour is usually approached in one of three ways [54]. First is the study of **empirical relations** between temperature stress, time and creep rate. The aim is to derive formulae to estimate structural behaviour under creep conditions. Component time-dependent deformation and life times are predicted using experimental data and such extrapolation techniques as the Monkman-Grant relation [67].

**Materials science modelling** derives equations for the creep rate by characterising and simulating creep behaviour using microstructural rearrangements including assumed values of transport processes on the microscale (e.g. void growth, glide of dislocations, diffusion of vacancies, crack initiation and propagation). Depending on the assumptions made concerning damage mechanisms, deformation and specific temperature and stress values will depend on the form of the resulting specific rate equation. This approach aims to correlate quantities characterizing the material behaviour and quantities characterising the micro-structure and processes involved (e.g. grain size, types of hardening).

**Continuum mechanics modelling** investigates creep in ideal 3-D solids using balance equations for elemental volumes of the material. Depending on the assumptions made regarding the kinematics of deformation and motion allow creep behaviour to be described by constitutive equations (mechanical equation of state) which relate stresses to the resulting deformation processes. Recently

numerical solutions using FE and time-step integration techniques have been developed to simulate time dependent structural behaviour to critical state of failure. This approach needs a large amount of experimental data for the creep behaviour of materials over a relevant range of temperatures and stresses.

## 2.8 Creep life estimation approaches

A lifing model defines the relation between loading level and component lifetime. In generally calculates total time to failure and the major division in lifing models is between total life models and crack growth models [68]. In service the useful life of hot section components decreases progressively due to creep deformation because both deformation and fracture are time-dependent, see Figure 2-14. The rate at which useful life is consumed will be a function of the operating conditions of the specific GT and how well the material resists creep deformation. The material will degrade faster, and consume its useful life more quickly the more extreme the operating conditions. The material will degrade progressively due to crack formation which begins even in the primary stage. Betten et al. [69] have described how micro-cracks begin on the surface and propagate until they link into macro-cracks and become visible at the tertiary stage of creep.

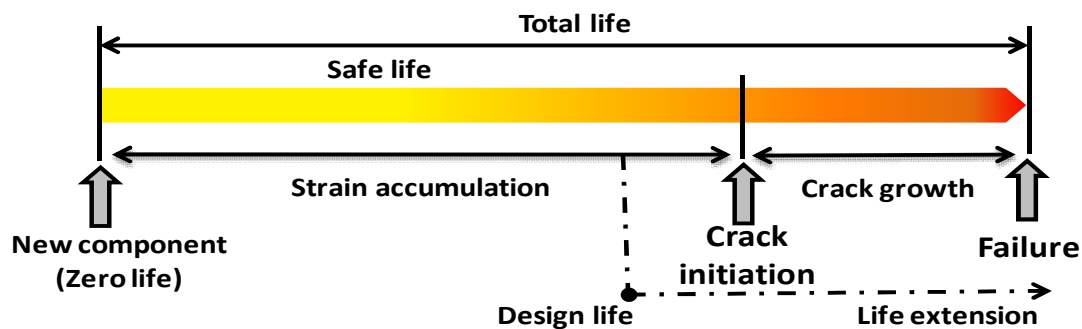


Figure 2-14: Creep Life span of hot section components due deformation [70; 71]

There are several methods for estimating creep life. In general, the life methodologies may be classed into three distinct approaches as shown in Figure 2-15 [72; 73]:

- **Design approach**
- **Post-service approach**



• **Statistical/probabilistic approach**

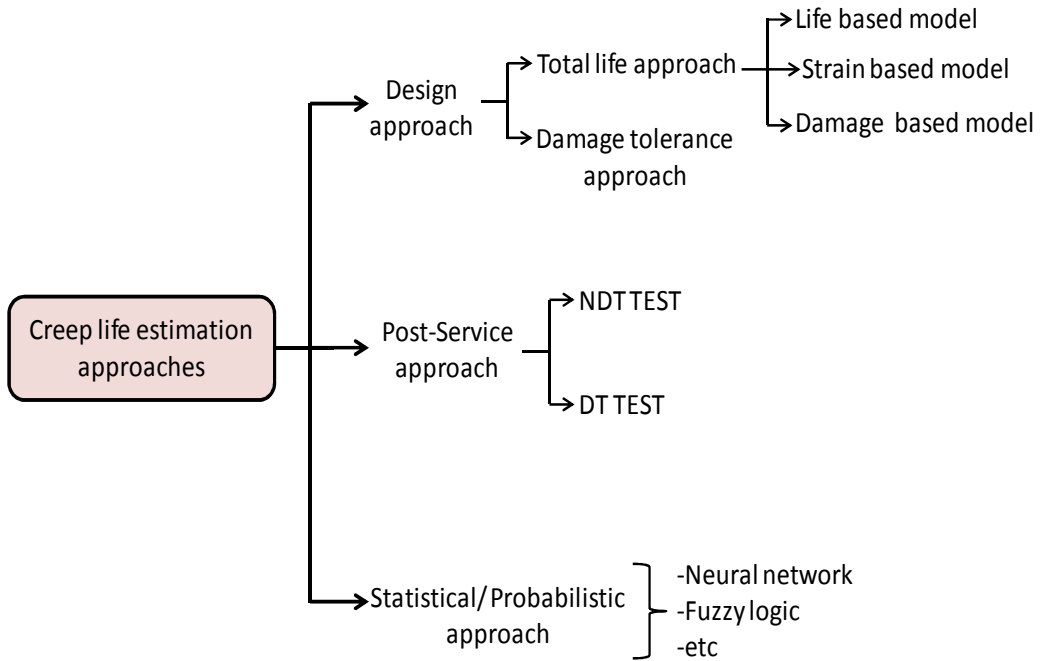


**Figure 2-15: Creep life estimation methodologies [72; 73]**

**Table 2-3: Lifting approaches**

	Design approach	Post-service approach	Statistical approach
<b>Methods</b>	<ul style="list-style-type: none"> <li>▪Analytical method.</li> <li>▪Empirical method.</li> <li>▪Numerical method.</li> </ul>	<ul style="list-style-type: none"> <li>▪Non-Destructive test</li> <li>▪Destructive test</li> </ul>	<ul style="list-style-type: none"> <li>▪Statistical tools</li> <li>▪Probabilistic tools</li> <li>▪Artificial intelligent methods</li> <li>▪Others</li> </ul>
<b>Advantages</b>	<ul style="list-style-type: none"> <li>▪Life estimation can be performed at design stage.</li> <li>▪Low cost if low fidelity model is used.</li> </ul>	<ul style="list-style-type: none"> <li>▪Identifies the components that need to be monitored.</li> <li>▪Offers different techniques for both destructive and non-destructive test</li> </ul>	<ul style="list-style-type: none"> <li>▪Reduced complexity.</li> <li>▪Fast computing.</li> <li>▪Identifies driving factors.</li> <li>▪Tackle the uncertainties.</li> </ul>
<b>Disadvantages</b>	<ul style="list-style-type: none"> <li>▪Based on empiric data to build the model.</li> <li>▪High complexity to achieve.</li> <li>▪High cost.</li> </ul>	<ul style="list-style-type: none"> <li>▪Needs prior techniques to estimate life at design stage.</li> <li>▪Performed during maintenance.</li> <li>▪Inaccurate if un-calibrated.</li> <li>▪Device used.</li> </ul>	<ul style="list-style-type: none"> <li>▪Requires prior models.</li> <li>▪The factors may vary according to the nature of the research.</li> </ul>

The techniques outlined in this section are used for different applications and at different stages of component failure so there can be no comparable accuracy and reliability. Table 2-3, summarized the three lifing approaches and gives the general advantages and disadvantages of each technique.

### **2.8.1 Design approach**

The design approach calculates the component's remaining creep life using analytical and empirical data, and/or numerical models. Information such as component geometry, properties of the component material and likely engine operating conditions are required to estimate component life. Wood [74] has claimed that when the life fraction is greater than 0.5, conventional non-destructive testing (NDT) and destructive testing (DT) techniques should be carried out.

The design approach can further sub-divided into the damage tolerance approach and the total life approach. The damage tolerance approach emphasises the modelling of crack initiation and the propagation processes. The total life approach effectively predicts the time at which failure is likely to occur, which is the same thing as the life span of the component to failure. This section discusses only the total life approach as the author's integrated creep life prediction model is based on this.

The total life approach estimates creep life using a damage-based model, a strain-based model, or a life-based model.

#### **2.8.1.1 Life-based model for creep life estimation**

Given the stress and metal temperature the life-based model predicts the time-to-failure of the component directly. This is done using time-temperature parameters, an empiric method first established some sixty years ago. Usually the empirically determined parameters are incorporated into a thermal/stress model to estimate creep life based on given operating and health conditions.

Dedikin, [75] introduced the LMP into a non-linear FE code to compute time-to-failure of a turbine blade. He first used a Computational fluid dynamics (CFD) package to define boundary conditions at the internal and external surfaces of

the cooled turbine blades, then the FE code calculated the temperatures and stresses in the blade. By incorporating the LMP into the FE code, the blade time-to-failure could be automatically computed, and then using a linear damage parameter an assessment could be made of current damage due to creep deformation.

DiCristoforo et al. [76] also used the LMP when investigating second stage turbine blade design of the GE MS6001. The purpose of the investigation was to lower stress distributions in high temperature regions. Here, an attempt was made to reduce creep deformation by redesign of the airfoils using an iterative process to shift the centre of gravity of the blade and reduce the radial bending moments imposed at high temperature locations. Heat transfer and resulting thermal stresses in the blade were obtained using a parametric 3-D FE model which produced a computed time-to-failure for each design based on LMP.

Naeem, [77]; Cerri, [78]; Assoul et al. [79]; Eshati, [72] and Ghafir, [80] also developed creep life prediction models using the LMP. In each case the input data for stress and thermal analysis were supplied by a GT performance simulation model. In Assoul et al. [79], the gas pressure and temperature pressure were found using the thermodynamics relations of a Brayton cycle. Simplified 0-D [77; 80] and 1-D models [72; 78; 80; 81] were used to predict the bulk metal temperature of the individual components and temperature variations across the blade span. Naeem, [77]; Eshati, [82] consider centrifugal stress as the main contributing factor, but Eshati, [72]; Abdul Ghafir, [80] include consideration of both bending moment and centrifugal stress.

Hagmeijer [83] and Tinga [84] have proposed an integrated lifing model incorporating GT performance simulation, CFD and FE packages, and in-flight engine data acquisition and capture. The data acquired was collected in a 1-D performance simulation software package which analysed transient behaviour and aero-thermal characteristics to produce a history of stress, strain and temperature distribution from the flight profile using CFD and FE models, before the remaining life was estimated.

Rosario et al. [85] used the Windows-based standalone Creep-Fatigue Pro3 developed by the Electrical Power Research Institute for creep life assessment in power plants. The model is composed of three sub-models: the first receives measured plane data and from that estimates component stress, the second uses LMP to predict time to failure on the basis of a linear damage accumulation model, and the third is a calculates fatigue crack growth.

### 2.8.1.2 Creep life estimation using the strain based model

Strain based models predict the life span of the material/component by direct calculation of the time-to-failure (using creep strain rate and creep strain ( $\dot{\epsilon}_C/\epsilon_C$ )). The classic empirical relation of Monkman-Grant [67] allows the time-to-failure to be calculated using the secondary creep strain rate ( $\dot{\epsilon}_{CS}$ ) obtained for a specific metal component of known stress and temperature. Monkman-Grant assumed that as the secondary creep strain rate decreased the time-to-failure ( $t_f$ ) increased linearly, see Equation 2-27, where  $k_{MG}$  and  $m_{MG}$  are the experimentally determined Monkman-Grant constants. Having found both constants,  $t_f$  can be estimated for any secondary creep strain rate for any given temperature and stress.

$$t_f = \frac{k_{MG}}{\dot{\epsilon}_{CS}^{m_{MG}}} \quad \text{2-27}$$

Aghaie-Khafri and Hajjavady, [86]; Aghaie-Khafri and Noori, [87]; Kaftelen and Baldan, [88], carried out experimental work on the nickel based superalloys IN738C, Rene 80, and MAR-M-002 at different temperatures and stresses. For each combination of temperature and stress, creep tests were performed and the time-to-failure, creep strain, etc, were measured. The findings show that the Monkman-Grant relation is suitable for creep life assessment.

The Omega method and Theta projection model are examples of empirical curve fitting models that have been successfully used for prediction of component creep. Evans, [89], Ibanez et al. [90], Bagnoli et al. [91] and Baldan et al. [92] have all recently evaluated the ability of the Theta projection model to provide accurate creep predictions for the NI100 and GTD111 superalloys and

1CrMoV rotor steel. It was found that for all combination of metal temperatures and stresses in the ranges investigated the time-to-failure for any creep test can be accurately predicted. Also, a strain-based model that considers the properties of individual phases has been developed to reduce the use of empirical properties (i.e. stacking fault energy, material constants, and modulus) to perform creep life estimation. Miodownik et al. [93] used JMatPro (Java-based Materials Properties) developed by Sente Software to obtain the secondary creep strain rate and time-to-failure for commercially available multi-component nickel based alloys. In this work, the component's overall properties were computed by integrating the particular properties (e.g. mechanical, thermal stacking fault energy etc.) of each individual phase. The calculations of the parameters needed to compute the time-to-failure were self-consistent because of the access to the properties at the individual phases.

Harrison et al. [31] and Shepherd et al. [94] have reported the development of a more advanced strain-based model which takes into account micro-level creep deformation. This was achieved by developing a strain-based numerical model that models the creep deformation at slip system levels by determining local shear creep strain accumulation and resolved shear stress by taking into account the material's anisotropic behaviour. The total creep strain was found by determining the individual shear creep strain contributions along the modal axis for each slip system, which were then summed.

### **2.8.1.3 Creep life estimation using the damage based model**

Creep deformation is often presented as progressive damage taking place in a material which can lead to material failure. The two most important theories using this approach are the Linear Damage Accumulation (LDA) theory developed by Robinson [95] and the classical Continuum Damage Mechanics (CDM) theory developed by Kachanov and Rabotnov [54]. Both are often used in models for predicting component lifing.

The LDA theory assumes damage,  $D_{LDA}$ , accumulates linearly from zero for undamaged material to unity when the material fails. Robinson [98] defines  $D_{LDA}$  as:

$$D_{LDA} = \sum \frac{t_i}{t_{fi}} \quad \mathbf{2-28}$$

Where  $t_i$  is the actual time spent under condition  $i$  and  $t_{fi}$  is the time-to-failure under condition  $i$ .

Robinson assumed that each particular fraction of the life span which contributes to  $D_{LDA}$ , is independent of and has no influence on any of the other fractions [95]. The  $t_{fi}$  can be found from experimental creep rupture data, life-based models or strain-based models. Researchers as such as Cunha, [96]; Naeem, [77]; Dedekind, [75]; Hagmeijer, [83]; Tinga, [84]; Rosario, [85]; Rinaldi, [97] have incorporated the LDA in their component creep life assessment.

In the CDM theory a damage state variable,  $\omega_{CDM}$  is introduced that assesses the irreversible accumulation of material damage with time. As in the LDA theory,  $\omega_{CDM}$  is assumed to progress from zero for undamaged material to unity at failure. CDM theory has found widespread application in the analysis of stress rupture and creep and time-to-failure is found using [98];

$$\omega_{CDM} = 1 - \left(1 - \frac{t}{t_f}\right)^{\frac{1}{v_{CDM}+1}} \quad \mathbf{2-29}$$

Where  $\omega_{CDM}$  is damage state variable,  $v_{CDM}$  is a constant of the constitutive equation,  $t$  is time,  $t_f$  is time-to-failure.

The CDM approach to creep life prediction has evolved considerably, generally along the lines of re-formulation of the original CDM equations to simultaneously include a number of damage mechanisms and the development of complex 3-D FE computer analyses which consider the anisotropic behaviour of the material. Recent work on creep life modelling and life estimation is presented below.

Betten et al, [69] extended the CDM theory to polycrystalline materials with parallel flat micro-cracks. This work developed a 3-D creep damage model based on the assumption that for such materials creep damage is related to degradation of surface discontinuities when parallel planar micro-cracks also exist. A damage vector was introduced as a function of  $\omega_{CDM}$ , where  $\omega_{CDM}$  was defined as the integral with time of the product of the equivalent stress and equivalent creep strain rate.

Qi et al. [99] developed a 3D model for anisotropic creep damage for face-centred cubic single crystals. The model was further developed and tested for multi-dimensional non-proportional loading conditions using a single SRR99 crystal and reported in [100]. To describe the anisotropic nature of the material the scalar form of  $\omega_{CDM}$  is converted into a damage tensor. The model has been applied to monotonous creep tests at elevated temperatures and different orientations. The results show that the proposed model is capable of describing both the strong orientation dependence and the non-linearity with respect to the applied load of the entire creep process. The model accounts for the initial anisotropy of the crystal in the evolution function of the creep and damage variables, and the crack-opening/closure behaviour due to micro-voids and micro-cracks via the activation and deactivation mechanism of the damage.

MacLachlan et al. [101; 102] have investigated the creep behaviour of a single crystal of superalloy. Their model adapted the Kachanov-Rabotnov damage mechanics and strain rate functions to include the ultimate tensile strength and claimed that the stress rupture data could accurately modelled. The work of MacLachlan has been used by Karaivanov et al. [103] when they developed a 3-D FE damage mechanism creep model for advanced hydrogen fired turbine systems. They used the commercial codes Fluent and ANSYS for the thermo-mechanical analyses and development of a creep user routine, respectively. The latter incorporated the MacLachlan model. A code was developed which simulated the individual and combined evolution of damage equivalent stress, creep strain and damage parameter. The model was used to identify critical regions and creep damage distributions for various projected operating times.

Vladimirov et al. [104] extended the single crystal plastic model of Meric and Cailletaud [105] into a FE slip system-based damage mechanism creep model and introduced  $\omega_{CDM}$  for each slip system to obtain accurate anisotropic creep modelling at all three creep stages. MacLachlan et al. [106; 107] who also used single crystal plasticity theory incorporated  $\omega_{CDM}$  in the effective stress ( $\sigma_{eff}$ ) formulation while Vladimirov et al. [104] included,  $\omega_{CDM}$  in the resolved shear stress formulation for each slip system.

Recognising the presence of in-service microstructural material degradation, Ashby and Dyson [108] introduced a physically-based CDM using knowledge available in the public domain relating to the mechanism of microstructural degradation. Dyson [109] argued that if it is possible to categorise the material damage on the basis of the kinetics of the damage evolution, then certain broad categories will emerge: (a) strain induced damage (such as the mechanism of grain boundary cavitation), sub-grain coarsening and mobile dislocation; (b) thermally induced damage such as particle coarsening and solid solution elements; and (c) environmentally induced damage in which the damage rate follows either the strain induced or thermally induced damage with the addition of chemical interaction with containment fluids.

### **2.8.2 Service-based approach**

The service-based approach requires component damage evaluation and assessment of the remaining life of the component, both of which need direct access to the specific components. The status of the component (obtained either by directly measuring its material properties or assessing the extent of its damage as a result of actual service) is compared to standard scatter bands which provide a refined prediction [51].

Assessment of the remaining life will involve both non-destructive and destructive testing.



### 2.8.2.1 Remaining life assessment using non-destructive testing

NDT techniques suitable for qualitative and quantitative assessment of anomalies in GT blades relating levels of microstructural damage to life usage are reported in [110]. These include internal visual inspection using a fibrescope, or borescope, surface crack inspection using dye penetrant testing, eddy currents methods for crack detection and sizing, ultrasonic crack detection techniques, and radiographic techniques using radioscopy, X-ray diffraction, X-ray and neutron tomography and neutron radiography [111-115]. NDT also includes metallographic analysis using replication technique to assess the microstructural degradation of metals [116; 117].

Neubuer and Wedel [118] have categorized creep damage due to creep cavitation into six separate stages (undamaged, A, B, C, D and damaged), as shown in Figure 2-16. For each stage specific remedial action is prescribed. Non-destructive metallographic analysis categorises the four levels of observed damage as A, B, C or D and corresponding remedial action is taken. Viswanathan [119] claims that the damage classification of Neubauer and Wedel correlates with the component life fraction ( $L_f$ ). An example of this correlation can be seen in Figure 2-17, between cavity classification and life fraction in the case of 1Cr-0.5Mo tested at 570°C.

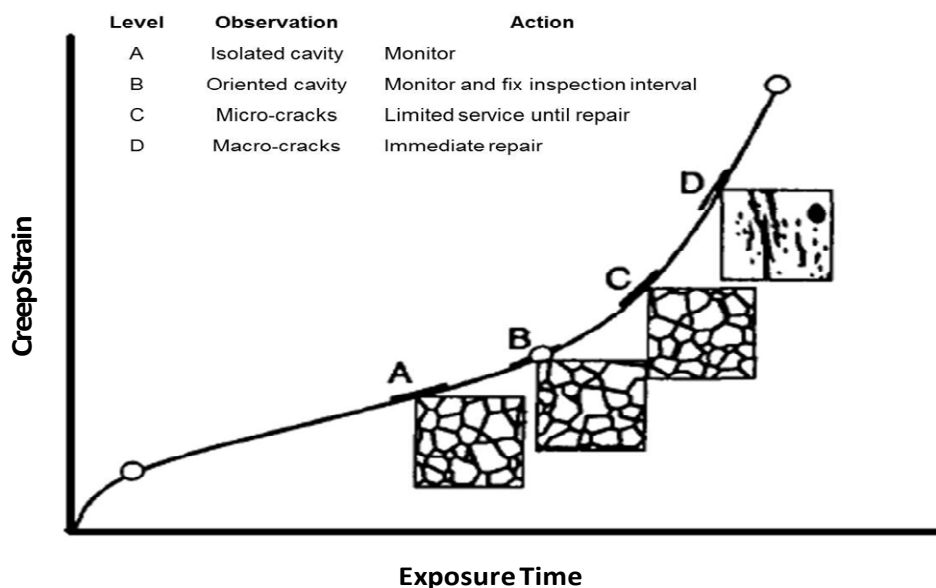
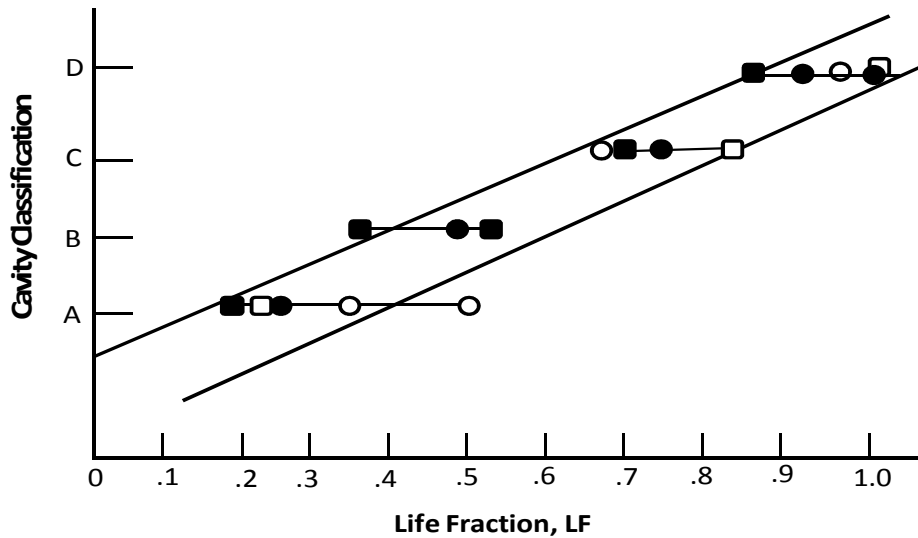


Figure 2-16: Creep damage classification [118; 119]



**Figure 2-17: Correlation between creep damage classification and life fraction of 1Cr-0.5Mo [119]**

Non-destructive metallographic analysis can determine  $Lf$ , and hence the remaining life of the component,  $t_{Lif}$  can be readily calculated from Equation 2-12.

$$t_{Lif} = t_{spent} \left( \frac{1}{LF} - 1 \right) \quad 2-30$$

Where  $t_{spent}$  is the time already spent in service.

Other techniques have been used to correlate other microstructural degradations with  $LF$ , temperature exposure time and/or service duration [120; 121].

### 2.8.2.2 Remaining life assessment using DT techniques

NDT techniques can provide valuable evidence regarding the condition of a component, however direct testing of material/components removed from service is more reliable [120]. Typically a creep specimen of standard size will be removed from the component and tested using a standard DT technique, these will include: metallographic tests to identify coating degradation, cracks and grain boundary carbide particles; tensile tests to assess degradation of strength and/or ductility; impact tests to assess toughness degradation; and

hardness, stress rupture and creep tests. In this way the component's remaining life will be determined.

Maraleh et al. [55] carried out creep life prediction assessment of five turbine blades of nickel-based superalloy IN738. The blades were a reference sample which had not seen service and four blades which had seen 30,000, 45,000, 60,000 and 80,000 hours of service, respectively. A stress rupture test was carried out at 850°C. The residual life of each turbine blade was calculated from the test data using LMP and the life fraction rule.

Similar work was performed by Vaezi and Solaymani [122] who investigated the remaining life in an ABB-130 GT blade which had seen 61,000 hours of service. First, a hardness test, a creep test and a metallographic assessment were used to assess the damage to the blade. Then  $t_f$  was found using LMP. It was estimated that the remaining life of the blade after 61,000 hours in service was approximately 32,000 hours.

### **2.8.3 Statistical/probabilistic approach**

With this approach creep life is predicted using statistical methods, often through the application of artificial intelligence techniques. The objective is to construct a relationship between the driving factors and the resulting creep life. For example, Zhimin et al. [123] by limiting their work to the engine rotational speed and hot flow temperature were able, using the statistical response surface (RS) approach, to develop an explicit relationship between creep life and these two parameters. Later, Zhimin et al. [124] extended their investigation and added a further six parameters to the RS equation.

Wallace et al. [125] extended the work of Zhimin to 16 parameters using FE and CFD techniques combined with the OSDP. Mechanical and thermal analyses were carried out and creep life calculated on the basis of the Graham-Walles theory. Using statistical design of experiment methods the most important five parameters were identified and used to improve the accuracy of the RS equation. More recently Zhao et al. [126] introduced a model to predict

in-service creep rupture life based on the Z parameter [127]. The duration of the creep rupture life and the changes in service conditions are combined using Monte Carlo probabilistic methods to evaluate reliability. Harris [128] has investigated the uncertainty in creep response to real in-service conditions by introducing fuzzy logic methods.

Koul et al. [129] performed a life data analysis (also known as a Weibull analysis) to investigate the variation in the microstructural parameters: grain size, inter-particle spacing and grain boundary precipitate size. A deterministic analysis was carried out using a damage-based creep model, before conducting the probabilistic analysis, in order to obtain the critical nodes [129]. A three-parameter Weibull distribution was obtained and the critical nodal creep lives at a cumulative probability failure of 0.1% estimated. Later Koul et al. [130] integrated their probabilistic analysis with a 3-D FE damage-based model which combined creep and oxidation damage, to determine fracture critical locations and estimate the combined creep life at these locations to a cumulative probability failure of 0.1%.

Liu et al. [131; 132] in an attempt to reduce the complexity and computational burden of current creep life assessment prediction methods, proposed a simplified model using the statistical-based RS method. Log (creep life) was taken as the response, ( $R$ ) with, initially, gas temperature and rotational speed as the independent variables [131]. However, in Liu et al. [132], four variables were considered as independent variables. A relationship between these four independent variables and creep life was developed using a RS equation. A value for the creep life was obtained using 3-D FE based creep models. Once the RS equation was established, probabilistic analysis was by Monte Carlo simulation [132]. Lui et al. [133] extended this technique to develop a computationally efficient probabilistic assessment of creep-fatigue life by summing the component's operational history and predicting its future operating profile. For each element of the operational profile, probabilistic distributions of independent variables were used as input data into the RS equation and accumulative probabilistic distribution of  $R$  was computed. Other research using

the RS method and Monte Carlo simulation for probabilistic analysis of GT blades can be found in [125; 133].

Frolova et al. [134] and Gupta et al. [135] also used a multilayer feedforward back propagation neural network to predict the likely creep behaviour of a rotating composite disc. They developed a model of steady state creep behaviour to generate the input-output samples with which to train and test the network. Tangential and radial stress and strain rates were chosen as network outputs, and operating temperature, particle size and radial distance were the network inputs. A 4-30-30-4 network was designed, constructed and trained using the samples obtained from the model. The trained network was tested against unseen samples and the output from the network compared to the mathematical model's predictions. Excellent agreement was found, particularly near the inner radius of the disc. The maximum differences were found in the radial and tangential strains and these reached 13 to 16%. Artificial Neural Networks (ANNs) have been used not only to predict the  $t_f$  of a material for a given set of inputs but also to predict the most important parameter(s) prior to creep assessment [136].

## 2.9 Chapter Conclusions

During operation, industrial gas turbine components undergo various types of time-dependent degradation due to high temperatures and mechanical loading. These conditions make the components susceptible to such failure mechanisms as low cycle fatigue, high cycle fatigue, thermal fatigue, environmental attack and creep. In the case of stationary gas turbine engines creep is one of the most common failure mechanisms (under high stresses and temperatures) that significantly reduce component life. The effect of creep is highly dependent on the operating conditions of the engine, its mode of operation and also the design parameters and details of the critical hot section components in question. The design parameters of such components are affected and determined by both aerodynamic and structural characteristics. A proper consideration must be given during the design stage to the possible interaction

between these parameters and intended operating condition upon the creep life of hot section components.

A better understanding of the lifing factors of the failure mechanisms and their interactions will help designers in the trade-off between different design options and will also help operators to make wise maintenance decisions. However, the determining factors that limit serviceable life vary significantly from one component to another and because of uncertainties in these factors and variations between the operating conditions and working environment of specific engines, the original equipment manufacturer will have estimated component life based on the design envelope of the expected base load, calculated component stresses and temperatures, and expected response of the material to those conditions. However, a hefty safety factor will have been added to ensure failure free operation, due to which most of components will be discarded while still retaining residual life.

Time-temperature parameters can provide the simplest method for creep life estimation and as the parameter master curves are readily available in the open literature this method remains widely used. The challenge is to develop external numerical and/or analytical models (e.g. thermal, stress, performance, diagnostic) which can be coupled to form an integrated lifing assessment framework. With analytical models performing stress or thermal analyses, the accuracy generally depends on whether the analysis is performed in 1-D, 2-D or 3-D. It also depends on how many parameters are included in the model (e.g. bending, thermal and centrifugal stresses, cooling technology, uniform or non-uniform gas temperatures, etc.). The greater the number of parameters included, the more complex the model and the greater amount of information required. Both the analytical and numerical models used for stress and/or thermal analyses need inputs from a performance simulation model. Input for the latter may be from either a computerised data acquisition system or input manually.

For this project the most important conclusion is how little research has been carried out into the effects of humidity on the heat transfer and cooling

processes which, in turn, affect the blade creep life of GTs. The overwhelming emphasis of current research is on the cooling processes of the hot section components. Model creation for creep behavioural representation and life prediction can be divided into two sub-approaches: total life and damage tolerance.

A simple form of creep failure based life assessment is provided by the Linear Damage Accumulation theory, but is considered rather crude because its underlying principle does not take into account the history of the damage as it progresses so the damage calculation is less accurate. Continuum Damage Mechanics gives a better damage-based life assessment because it considers the evolution of the damage. The CDM approach has been improved by the modification made to the classical CDM constitutive equations at both a micro and a macro level. These modifications include 3-D Finite Element (FE) analysis of in-service microstructural degradation and different creep damage mechanisms, and re-formulating CDM theory by determining damage evolution based on accumulated creep strain rather than time.

A service-based approach to life assessment needs hands-on access to the component – through either DT or NDT. DT techniques are usually considered the most reliable creep life prediction method, but requires removing the relevant components from service and performing one or more of a number of destructive tests; the remaining life is then found using a parametric method such as life fraction rule or LMP. NDT techniques to detect anomalies in GT blades include dye penetrant testing, eddy current testing, visual inspection and radiographic testing. Metallographic analysis using a replication technique is another way to assess microstructural damage. By using a correlated component life fraction, the remaining life of the component can be assessed.

Another approach to the assessment of creep rupture data is the use of statistical and probabilistic models derived from either time-temperature parameters or existing algebraic models. The statistical RS method is also used to simplify complex existing models by deriving a relationship between the creep life and system parameters. This statistical/probabilistic theory (Weibull

and log-normal distributions, Monte Carlo simulations) has also been used to explain changes in the microstructural parameters and how they affect prediction of creep life. Recently the applications of fuzzy logic and Artificial Neural Networks techniques have added another dimension to creep modelling and life estimation.



## *Chapter three*

### **3 METHODOLOGY**

In GTs the first stage rotor blade is a high temperature component subject to severe operating conditions in a gas stream where the temperature exceeds 1000°C [137]. To achieve life assessment it is necessary to develop a life prediction method for the blades. This is usually based on stress/strain and temperature distributions under varying operating conditions. In this chapter the methodology implemented in this study to meet the research aim and objectives will be described and is shown in Figure 3-1. The research starts with developing a simple creep life model (A) to investigate the effect of different operating conditions and working environments. Presented in (B) is an explanation regarding the research work to upgrade the creep life model - which includes the effect of change in humidity on the heat transfer coefficient in the blade cooling processes. The factors that drive creep life in hot section components will be investigated using this model [72]. Finally in (C) the creep life model and heat transfer model are integrated with the finite element 3-D first stage HP turbine blade model to identify the maximum mechanical/ thermal stress and metal temperature of the turbine blade.

The analytical creep life model considers the change of stress along the blade span, blade trailing and leading edges and back of the blade. However, the blade metal temperature was considered along the blade span only. The model was upgraded to include the change of blade metal temperature through the blade TBC and blade wall. However, in this model the thermal stress was not considered, thus the 3-D finite element model was developed to calculate the thermal stress model of the blade as result of the change of the WAR and heat transfer coefficient.

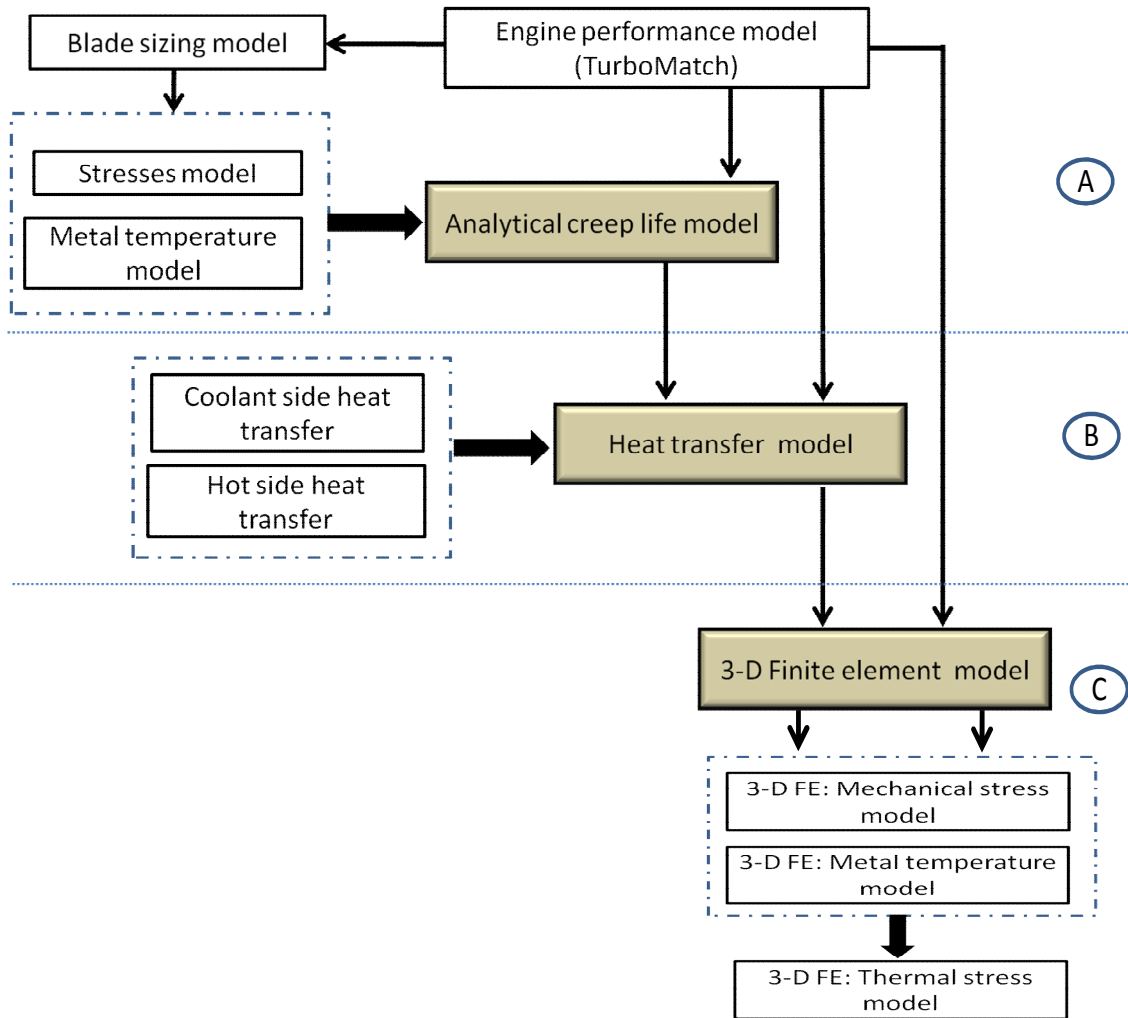


**Figure 3-1: Research methodology flow diagram**

Before the analytical creep life model was developed, several important assumptions were made in order to include the effect of humidity on the blade coolant heat transfer:

- The inlet gas temperature is varied along the blade span and constant in the chordwise direction.
- The blade metal temperature is constant along the blade chord and varies in the spanwise direction and through the blade wall and TBC.
- Any single blade has a number of internal uniform circular cooling channels with constant cross-sectional area.
- The blade cooling system is defined by its internal geometry and the cooling flow.

- The fluid properties of the coolant flow are function of temperature and WAR only.
- Whole blade coolant is considered as a heat exchanger subjected to the main steam gas temperature.

### 3.1 Engine performance simulation

Based on the engine configuration shown in Figure 3-2, an engine performance model was created using Turbomatch which is an existing component based engine performance tool developed at Cranfield University. Turbomatch was used to develop and run representative thermodynamic models of the engine investigated. This tool has the ability to simulate different thermodynamic cycles and processes while analysing the overall performance of the engine including among other things, the effects of cooling flows, air and gas mixing, component degradation, variable geometry ( including compressors, turbines and exhaust nozzles) as well as extraction of bleed air and shaft power off takes. Turbomatch has the ability to perform steady-state engine performance calculations at both design point (DP) and off-design point (ODP) conditions. The simple cycle engine selected for this study consisted of a compressor, combustor, HP turbine and free power turbine. The engine performance parameters are listed in Table 3-1. The simulation procedure was conducted as proposed in the Turbomatch manual [138]. Typical output data from the engine performance model such as temperature, pressure, mass flow rate and engine rotational speed for each component at inlet and outlet were then used as inputs for the next stage during the blade sizing process, thermal stress model, creep model and finite element analysis (FEA) model.

**Table 3-1: Engine performance parameters**

<b>Parameter</b>	<b>Value</b>
Pressure ratio	23:1
Power output	30.2 MW
Exhaust gas flow rate	82.5 kg/s
Thermal efficiency	28-40%

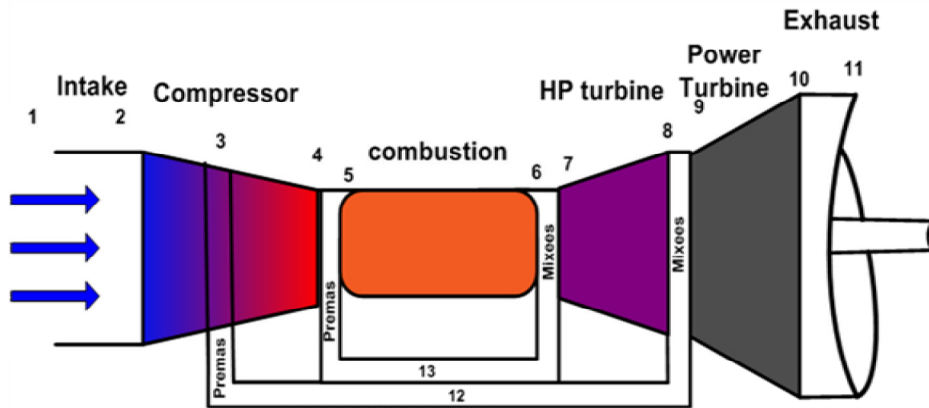
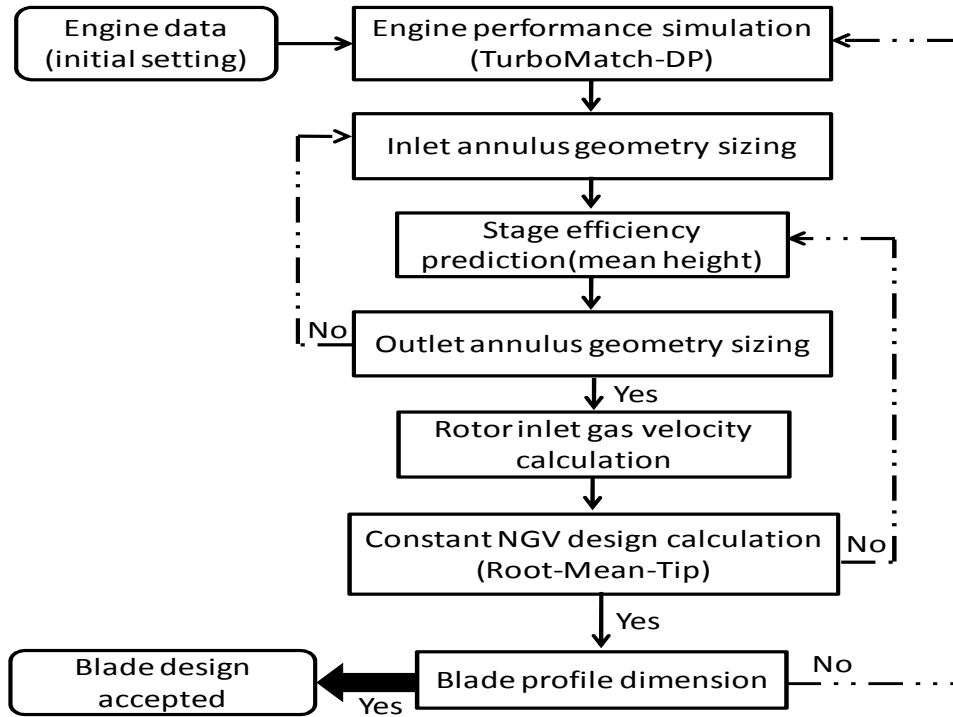


Figure 3-2: General layout of the gas turbine engine

### 3.2 Blade sizing model

The first stage of the HP turbine blade was sized using the constant nozzle inlet angle method [139; 140]. The aim of the constant nozzle design method is to satisfy the radial equilibrium condition and at the same time meet the condition of constant mass flow per unit area at all the blade radii. Also, it avoids the necessity of having a large twisted blade which could cause fabrication problems (e.g. the cooling system within the blade) and bending stresses. The blade sizing process starts with a given turbine specification at the DP that includes gas stagnation temperature and pressure at inlet and outlet, mass flow or turbine power output, and shaft speed. Then the velocity diagrams at the blade mean diameter are determined, this step will include a selection of the number of stages to be used.

The design process as shown in Figure 3-3 consisted of initial engine performance simulation, inlet/outlet annulus geometry sizing, stage efficiency prediction, rotor inlet velocity calculation and detailed blade design at the root, mean and tip. Although the turbine is two-stage, only the first stage blade was considered during the design process. The initial data used to design the process was selected based on a literature study, values previously used by other researchers and engineering judgement. From the simulation made by Turbomatch, the inlet and outlet gas path values at the DP were obtained. The detail sizing process is presented and illustrated in Appendix B.



**Figure 3-3: High pressure turbine blade design process flow diagram**

The inlet Mach number value (0.211) used in this study was to minimize pressure losses in upstream ducting and to ensure that the gas flow will accelerate at all points along the NGV surface. The blade inlet root relative Mach number was less than 0.7 to ensure that there is acceleration relative to the blade all the way through the blade passage. The NGV exit angle should be between  $65^{\circ}$  and  $73^{\circ}$  [141].

The degree of reaction which expresses the fraction of the stage expansion that occurs in the rotor is defined in terms of ratio of the static enthalpy drop to the total enthalpy drop that occurs across the rotor blade. The degree of reaction varies through the blade span, being small at the root and highest at the tip. For best efficiency pitch line reaction should be 50% at the mean, especially for gas generator turbines since high kinetic energy flow remains for the subsequent stage [140; 141].

### 3.3 Analytical creep life model

In this study, a creep life model has been developed and used with the HP turbine first stage rotor blade of a typical stationary GT [72]. Figure 3-4 shows

the methodology used for blade creep life assessment using a creep life model which consists of sub-models; performance, sizing, stress, thermal and creep. The model presented in Figure 3-4 consists of a 2-D stress model and a 1-D metal temperature distribution model. The model based on input data from the engine performance model and other secondary input data such as geometry data, material properties and cooling effectiveness and cooling technology used. The engine performance was simulated using Turbomatch.

The cooling effectiveness assumed was based on the turbine entry temperature (TET) and the material data defined by the user. The blade maximum stresses and metal temperature will be identifying along the blade span by combining the data from the engine performance and secondary data. Change in the design parameters or the engine operating condition and the creep life can be calculated using LMP. However, in this model the heat transfer coefficient of the hot side and the coolant side was not considered. Film cooling and TBC were taken into account in this simple model by specifying the overall cooling effectiveness based on the TET.

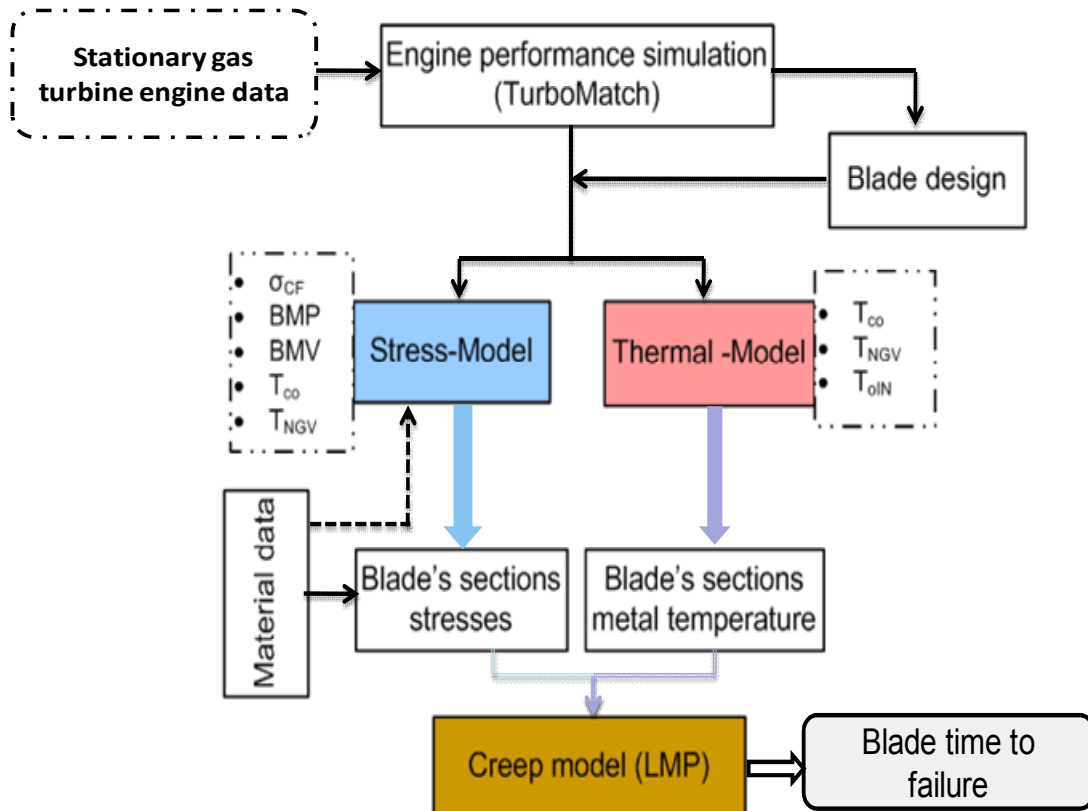


Figure 3-4: Creep model life assessment flow diagram [72]

### 3.4 Heat transfer model

The determination of the rate of heat transfer from the turbine blade in a cross flow is important in hot section GT life assessment. The rate of heat transfer is normally fixed by semi-empirical correlations expressing the Nusselt number in terms of Reynolds and Prandtl numbers. The implementation of such correlations requires knowledge of fluid properties such as density, viscosity, thermal conductivity and specific heat. For gases these properties are normally available only for the dry state, thus the possible effect of the water vapour content of the gas has been overlooked.

The effect of heat transfer on the blade creep life is investigated by developing a model to consider the change of heat transfer on the coolant side and hot side as function of change the fluid gas properties. The change of fluid properties of the coolant side due to the presence of water vapour was modelled through variation of the specific heat at constant pressure ( $C_p$ ), the ratio of the major specific heats ( $\gamma$ ), density ( $\rho$ ), viscosity ( $\mu$ ), Reynolds number ( $Re$ ), Nusselt number ( $Nu$ ), gas constant ( $R$ ) and other related parameters. The change of hot side fluid properties ( $C_p$ ,  $\gamma$ ,  $\rho$ , etc.) can be calculated using data from the NASA computer program Chemical Equilibrium with Applications (CEA) [142; 143].

The model presented in Figure 3-5 consists of two main sub-models (i) coolant heat transfer model and (ii) hot heat transfer model. The models receive the aero thermal input from the Turbomatch engine performance software, gas properties with presence of WAR from the gas property model, and the geometrical and material data as defined by the user. The temperature variation due to the heat transfer along the metal blade span and through the thermal barrier coating and blade metal are considered. The whole cooled blade row is regarded as a heat exchanger subjected to a mainstream hot gas flow from the combustion chamber. The developed model identifies the location of critical points along the span of the blade. The output of the model is the blade metal temperature and stress distribution along the blade span which will be used as input to calculate the blade creep life. Also, some data will be used in the finite

element model to calculate the mechanical stress, metal temperature and thermal stress spanwise and chordwise along the blade.

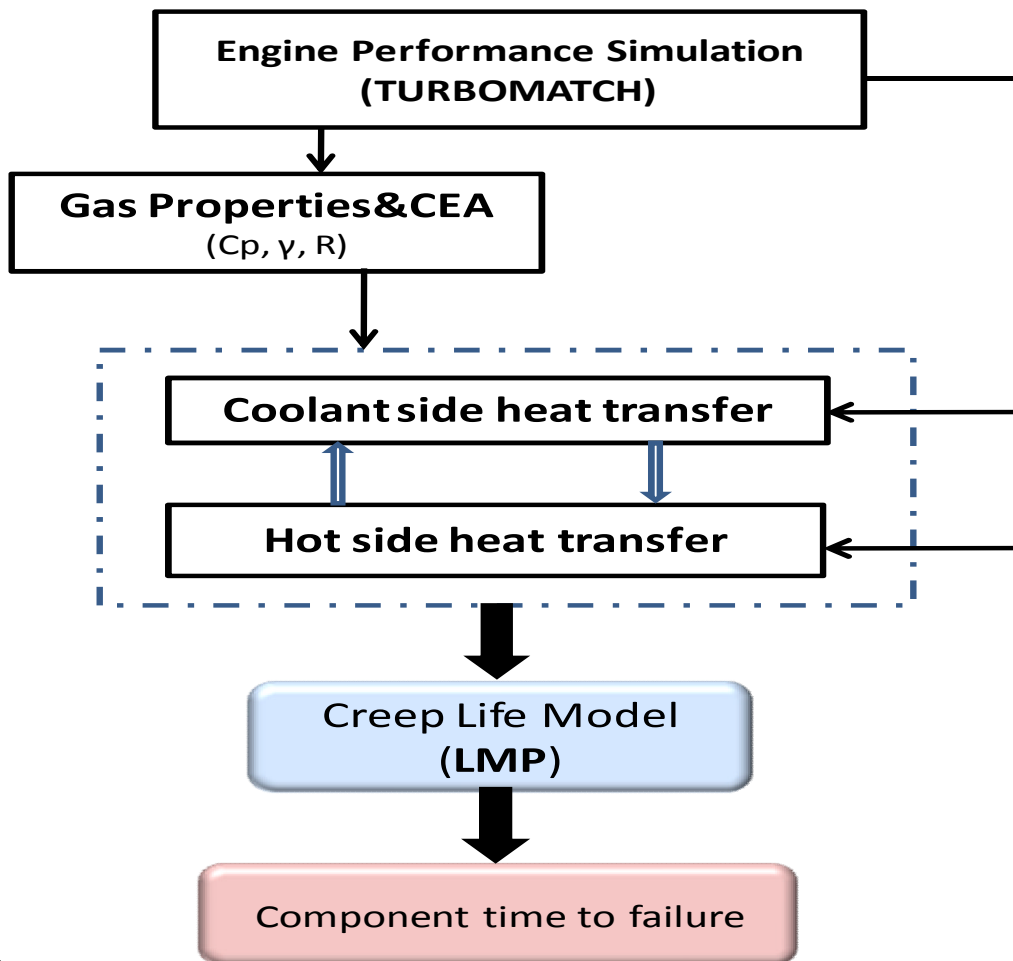


Figure 3-5: Heat transfer model flow diagram

### 3.5 3-D finite element model

The first stage of HP turbine blade dimension was obtained from the blade sizing model. The blade geometry designed using CATIA V5R19 software and the file saved as .CATPart in order to export to the ABAQUS 6.9-3 finite element software to carry out the structural analysis (stress and thermal). The internal blade cooling system was also included in the CATI model and the boundary conditions of the coolant flow were applied in Abaqus model. The blade model was created without a shroud and then modified to include the shroud in order to see the effect of the presence of the shroud on the thermal stress and critical regions.



All details of the boundary conditions, mesh, materials and loads can be found in Chapter 7. The main gas path boundary conditions were extracted from the Turbomatch performance model. The distribution of temperature and heat transfer coefficients for the hot and coolant sides were mapped on the blade following a similar procedure as for the data coming from the analytical heat transfer model. Other data used in the FE model was specified by the author using expertise and advice from staff at Cranfield University.

Data used in the stress and thermal assessments must be derived from the use of good quality refined 3-D finite element models of the turbine blade. Mesh detail is determined by the degree of accuracy required for the temperature and stress prediction of the component. Temperatures, pressures and other boundary conditions should be based on best available data and should originate from refereed sources. Blade gas and coolant temperatures are a key input for the analysis and will be supplied by the Turbomatch analytical model.

### **3.6 Chapter Conclusion**

This chapter has outlined the methodology to be used in this study to meet the research aim and objectives and was designed based on the research idea. The project will begin by running the engine performance model and the results produced will be used as input to the blade sizing model, the analytical creep life model, the heat transfer model and the FE model, see Figures 3-3, 3-4 and 3-5. A description of each model and major task is given later in this thesis.



## *Chapter four*

### **4 HUMIDITY**

Water ingested by a GT can be due to ambient humidity, water or steam injection and ice [144]. A common approach to increasing power output and efficiency of GTs is to spray water into the compressor, and there has been much research in the last few years on the effects of water injection on engine performance [18]; [20]. However, there has been no systematic attempt to evaluate the likely long term effects of humid air on the GT blade cooling processes and failure mechanisms such as creep. The work presented here investigates the effect of humidity of the intake coolant air on the HP turbine blades' heat transfer coefficient which in turn affects the blade metal temperature and creep life.

#### **4.1 The effect of humidity**

Humid air contains an amount of water vapour depending on the degree of saturation and air temperature. Humidity has less effect on engine performance than either ambient temperature and/or pressure but its effects are not negligible. Humidity changes the inlet air's specific heat ( $C_p$ ), the ratio of major specific heats ( $\gamma$ , isentropic exponent) and gas constant ( $R$ ), see Figure 4-1, and so should be included when considering GT performance, especially where the ambient temperature is high and the amount of water vapour in the atmosphere can increase substantially [22].

With the presence of water vapour in the inlet air  $C_p$  and  $R$  increase, while  $\gamma$  diminishes more slowly, see Figure 4-1, these changes have a significant impact upon the thermodynamic processes throughout the GT engine. When the mass fraction of water vapour is less than 10%, which is usually the case when it is due to ambient humidity alone, then for performance calculations the air mixture may be considered a perfect gas. All calculations of GT thermodynamic processes use gas properties ( $C_p$ ,  $\gamma$  and  $R$ ) for the working

medium which should be considered a mixture of air and water vapour. The water content is taken into account through the absolute humidity (WAR) and is defined as the ratio of mass of water ( $m_w$ ) to dry air mass ( $m_d$ ):

$$WAR = \frac{m_w}{m_d} \quad (4-1)$$

The water mass fraction of the humid air mixture (specific humidity) is given by [22] as:

$$x = \frac{WAR}{1 + WAR} \quad (4-2)$$

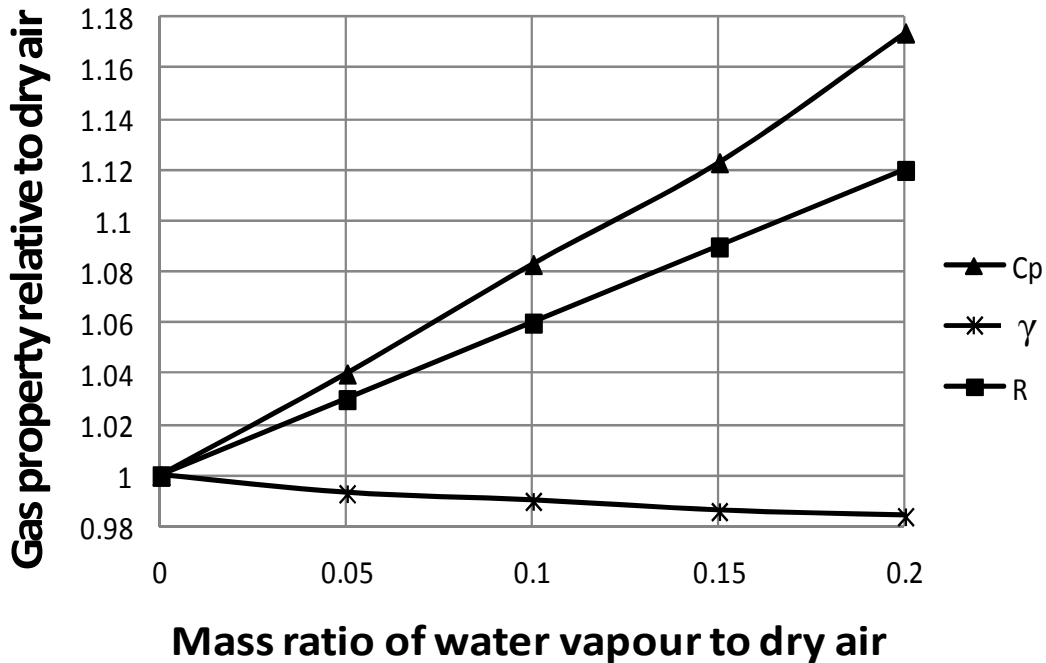
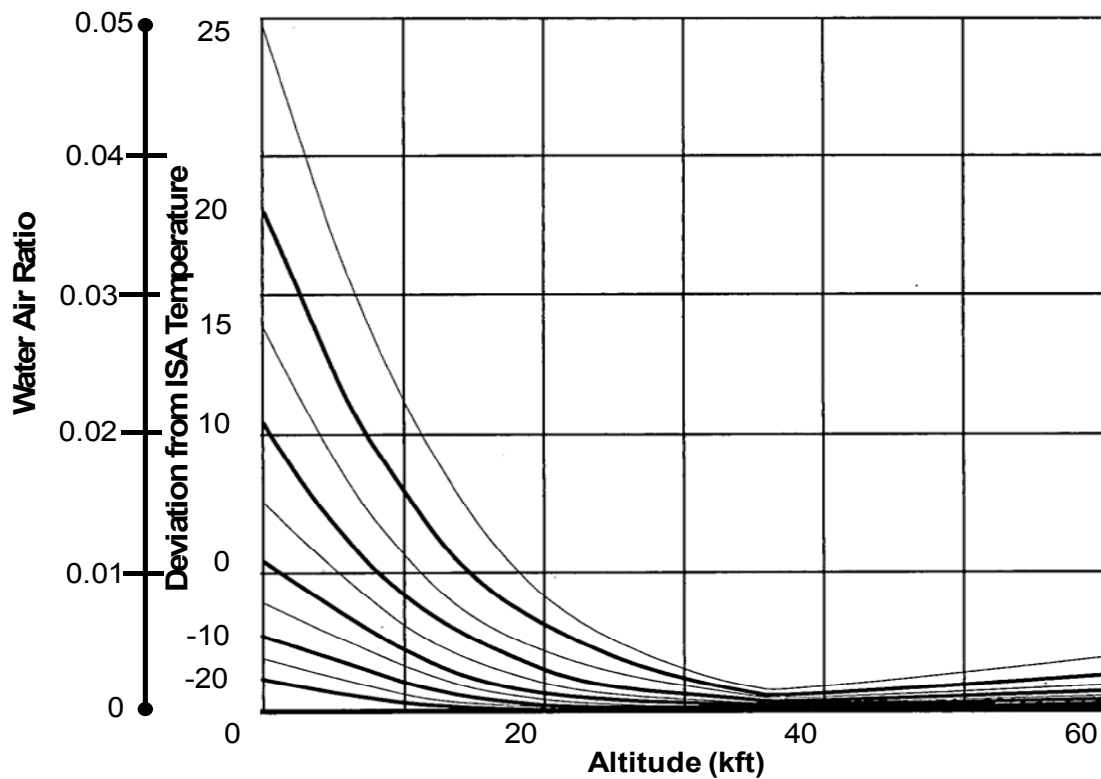


Figure 4-1: Variation of gas properties with water vapour content (Walsh and Fletcher)

The maximum amount of water vapour in the atmosphere increases with temperature, see Figure 4-2, at altitudes above 6000m the very small water air ratio causes a noticeable change in the performance of aircraft engines compared to ISA conditions [22]. Some industrial GT engines are based in relatively hot climates where the humidity is high and has a significant effect on the characteristics of the engine working fluid.



**Figure 4-2: Water air ratio as function of altitude and deviation from ISA temperature [22]**

Figure 4-3 shows the major effect of variations in these properties on GT engine performance [141]. In the compressor, at constant non-dimensional speed ( $N/\sqrt{T}$ ) and pressure ratio, the presence of water vapour causes a reduction in the non-dimensional mass flow ( $W\sqrt{T}/P$ ). This is because  $R$  increases more rapidly than  $\gamma$  decreases, and the quantity  $\sqrt{(\gamma RT)}$  increases with increase in humidity and the dimensionless group for speed,  $N/\sqrt{(\gamma RT)}$ , is reduced relative to its value for dry air. At this lower dimensionless speed the compressor passes a lower dimensionless flow,  $(W\sqrt{T\gamma R}/P)$ . Also, at this lower dimensionless flow, the  $(W\sqrt{T}/P)$  is further reduced, again by the increased  $R$ .

Injected water into the compressor inlet improves the power and/or thrust of GT engines by reducing the compressor inlet/outlet temperature rather than the additional mass flow due to the presence of the water. For GTs the presence of water vapour produces a small change in  $W\sqrt{T}/P$  at constant  $N/\sqrt{(T)}$  and  $\Delta H/T$ .

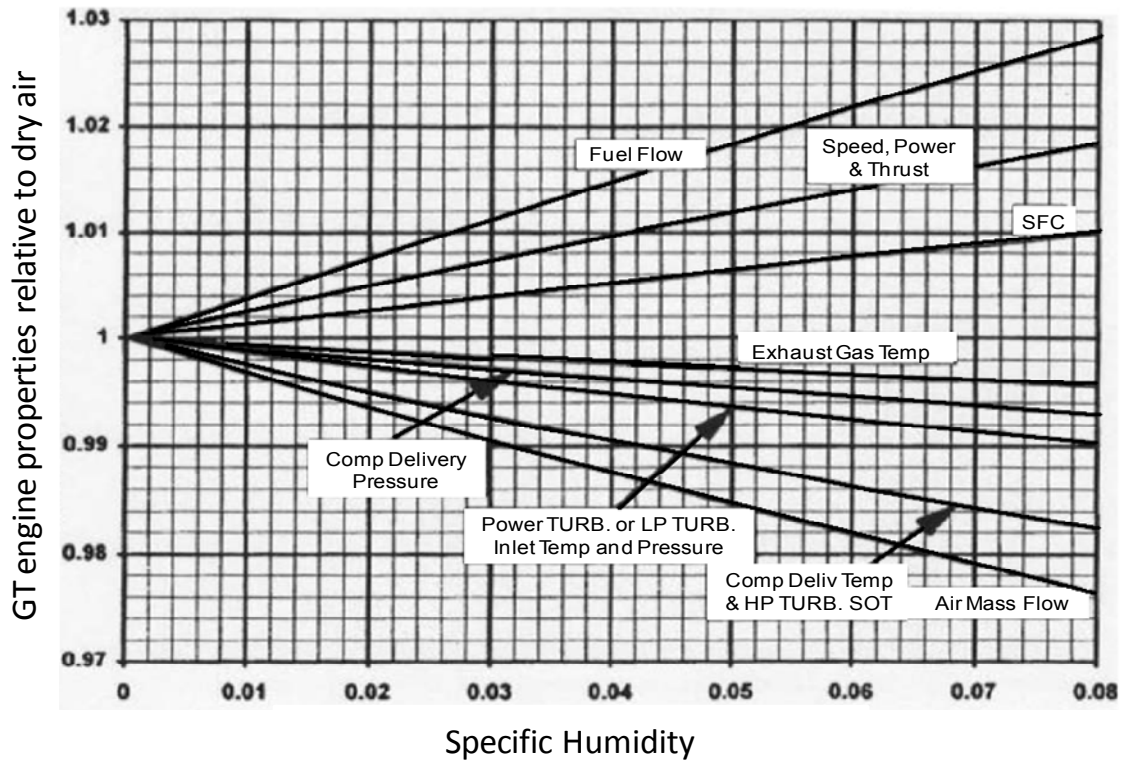


**Figure 4-3: Effects of humidity on engine performance [141]**

The injected water in industrial engine is primarily intended to increase the power output on hot days. It does this by lowering the TET, which allows increased fuel flow, bringing the power back to normal cool day. At a  $T_{amb}$  of 305K, a 20% increase in power is achieved by injected a rate of 0.87% WAR into the engine core. This drops to a 5% increase at 288K for an injection rate of 0.53%. As shown in Figure 4-4, the power output is increased with decreases in the SFC, NOx and compressor exit temperature which used in the HP turbine blade cooling [145].

The results in Figure 4-3 were obtained by considering all the full non-dimensional parameter groups to be constant at a given operating condition. The results show increases in the engine power and specific fuel consumption (SFC) by increase in the specific humidity. Note, however, that compressor outlet temperature and turbine inlet temperature were reduced by around 1.8% and 1% respectively. But the precise impact depends on the engine cycle and other operating factors.

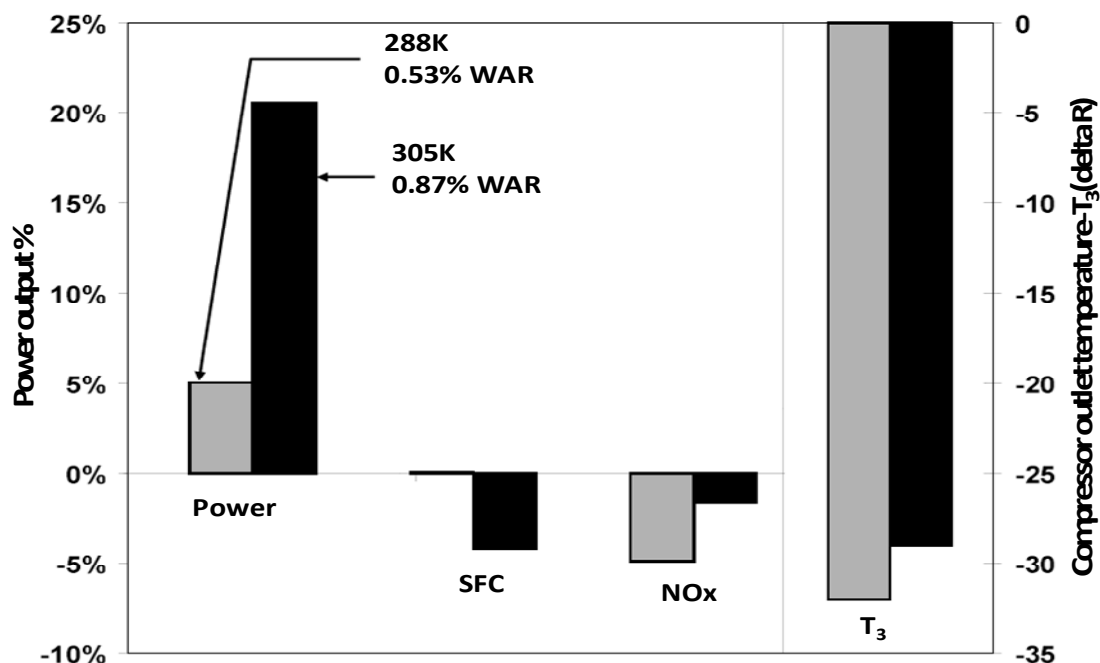


**Figure 4-4: injected WAR in LP compressor in hot day enhance the power and reduce blade inlet temperature ( $T_3$ ) [145]**

Injecting water into the combustor (steam injection) increases the mass flow through the turbine which in turn increases the HPT rotational speed. Since the compressor and the HPT are coupled on one shaft, the rotational speed of the compressor is increased. Also, by increased the PCN and turbine mass flow, the pressure ratio is increased which results in an increase in the compressor discharge pressure and temperature. The positive effect of the increased compressor exit temperature is off-set by a rise in fuel flow due to the heat required to raise the injected steam to the combustor outlet temperature. The coolant temperature is also affected since the bleed is taken from the compressor exit. This will affect the cooling effectiveness and can impact on the HP turbine NGV and blade. However, a rise in coolant mass flow by steam injection increases the internal heat transfer coefficient. Moreover, steam injection increases the power output due to the flow in the turbine exceeding the flow in the compressor and the  $C_p$  of the flow in the turbine being increased by the water. SFC is worse due to the significant amount of heat required to evaporate the water. The quantity of steam injected in the combustion is controlled by the control system in order to avoid flame out and surge. Work carried as a part of this research has presented details of the effect of steam

injection on engine performance, gas transport properties and blade creep life presented in [146]. The effect of injected steam (WAR= 0 to 0.1) on the engine performance parameter is presented in Table 4-1.

**Table 4-1: Engine performance parameter for injected steam in the combustion**

WAR increased from 0 to 0.1		
Parameter	Unit	Status
<b>Mass flow</b>	<b>kg/s</b>	Increased
<b>Power</b>	<b>MW</b>	Increased
<b>Compressor exit temperature</b>	<b>K</b>	Increased
<b>Compressor exit pressure</b>	<b>atm</b>	Increased
<b>Coolant flow</b>	<b>kg/s</b>	Increased
<b>SFC</b>	<b>Kg/kW/hr</b>	Decreased
<b>PCN</b>		Increased

## 4.2 Coolant gas properties in presence of water vapour

When moist air data are not available, it is common practice to use data for dry air in heat transfer calculations. However, the dry air assumption may lead to errors in predicted heat fluxes, mainly because of the relatively low molar mass of water vapour [147]. Thus, the present analysis is based on the properties of humid air (dry air and water vapour) using existing procedures in the literature [141; 148]. A number of analytical methods and correlations were reviewed and used with gas mixture component properties as input parameters to derive the temperature and humidity dependence of specific heat capacity, ratio of major specific heat and gas constant ( $C_p$ ,  $\gamma$  and  $R$ ) see Equations 4-3 to 4-7 and also of mixture density, thermal conductivity, viscosity, Reynolds number, Nusselt number and other related parameters. The water content is considered through the magnitude of the absolute humidity (WAR).

$$\begin{aligned}
 & \text{Specific heat factor for moist air, } Cp_{fac} \\
 & = \frac{[WAR_{molar} * Cp_w + (1 - WAR_{molar}) * Cp_d]}{Cp_d} \quad (4-3)
 \end{aligned}$$



$$WAR_{molar} = WAR * \frac{M_{W_d}}{M_{W_w}} \quad (4-4)$$

Where,  $C_{p_{fac}}$  is the ratio of  $C_p$  for moist air to that for dry air,  $WAR_{molar}$  is the molar ratio of water to dry air,  $C_{p_w}$  and  $C_{p_d}$  are the specific heats at constant pressure of water and air,  $WAR$  is the ratio of water to dry air by mass (18.015, 28.96 are the molecular masses of water and dry air respectively).

$$\text{Gas constant factor for moist air, } R_{fac} = \frac{R_o}{(M_w * R_A)} \quad (4-5)$$

$$\text{Molecular weight of moist air, } MW = \frac{1}{\left\{ \left( \frac{WAR}{M_{W_w}} \right) + \left[ \frac{(1 - WAR)}{M_{W_d}} \right] \right\}} \quad (4-6)$$

Where,  $R_{fac}$  is the ratio of  $R$  for moist air to that for dry air,  $R_o=8.31\text{kJ/mol K}$  and  $R_A$  is the gas constant of dry air,  $0.28705\text{kJ/kg K}$ .

$$\begin{aligned} &\text{Gamma factor for moist air, } \gamma_{fac} \\ &= \frac{[(WAR_{molar} * \gamma_w) + (1 - WAR_{molar}) * \gamma_d]}{\gamma_d} \end{aligned} \quad (4-7)$$

Where,  $\gamma_{fac}$  is the ratio of  $\gamma$  for moist air to that for dry air,  $WAR_{molar}$  is the molar ratio of water to dry air and  $\gamma_w$ ,  $\gamma_d$  are the ratio of specific heats for water and dry air respectively.

For the gases of interest,  $C_p$  - specific heat at constant pressure - is a function only of gas composition and static temperature. For performance calculations total temperature can be used up to a Mach number of 0.4. The gas constant extensively relating pressure and temperature changes for an individual gas is the universal gas constant divided by the molecular weight of the gas.  $\gamma$  is the ratio of the specific heat at constant pressure to that at constant volume and is a function of gas composition and static temperature [141].

### 4.3 Coolant gas properties at different values of WAR

Figures 4-5 to 4-7 show the change of the gas properties with water content at three temperatures, 473K, 573K and 673K. It is clear that the  $R$  increases relatively rapidly with increase in either temperature or  $WAR$ ,  $C_p$  increases in

value with both WAR and temperature but only marginally, and  $\gamma$  decreases slightly with increase in either WAR and/or temperature. This because the molecular weight of water is less than that for dry air. Increase in the temperature for the same RH will increase the WAR, which in turn increases the  $C_p$  of the gas flow as shown in these figures. The result will be used to demonstrate the effect of the WAR on the heat transfer and blade creep life.

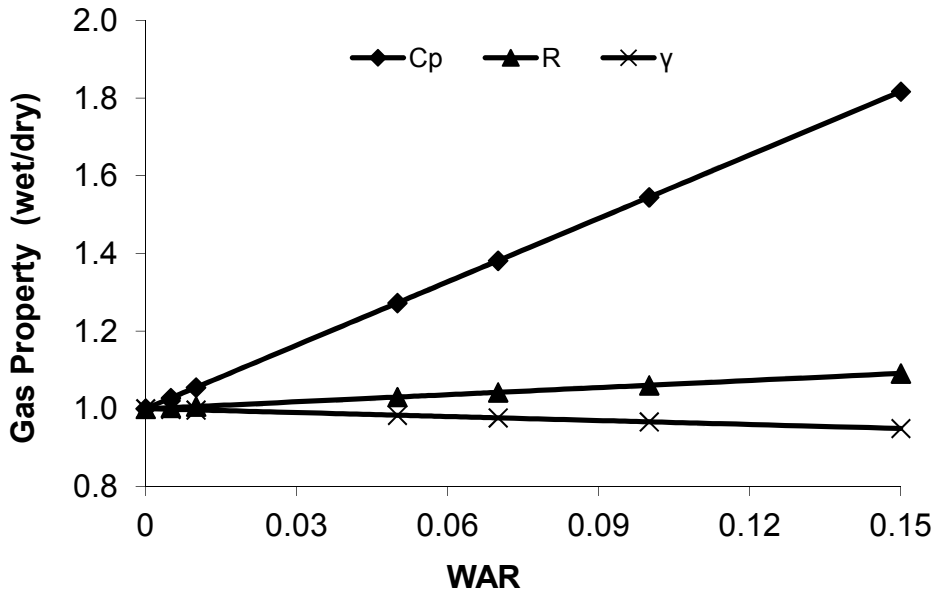


Figure 4-5: Variation of gas properties for different values of WAR at 473K

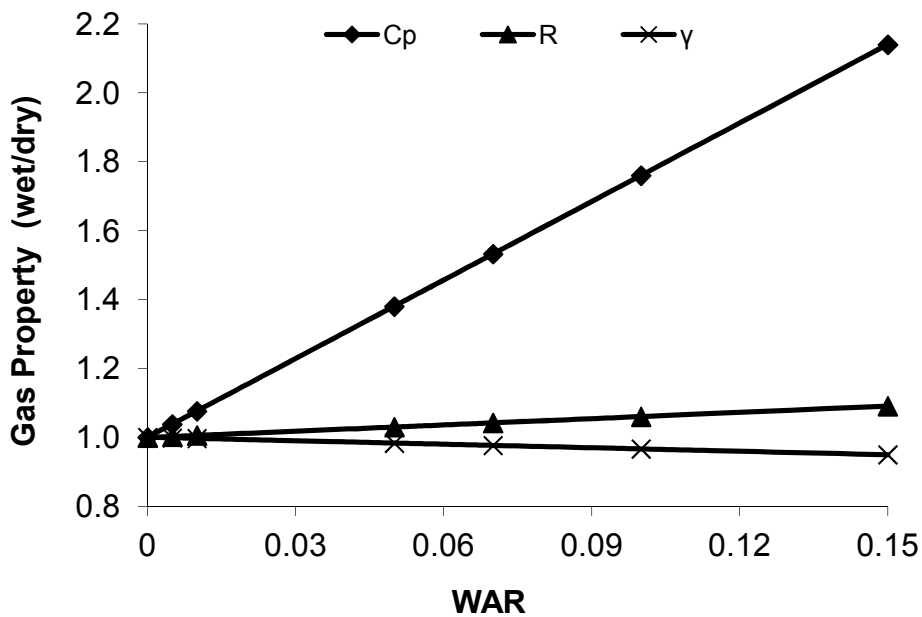


Figure 4-6: Variation of gas properties for different values of WAR at 573K

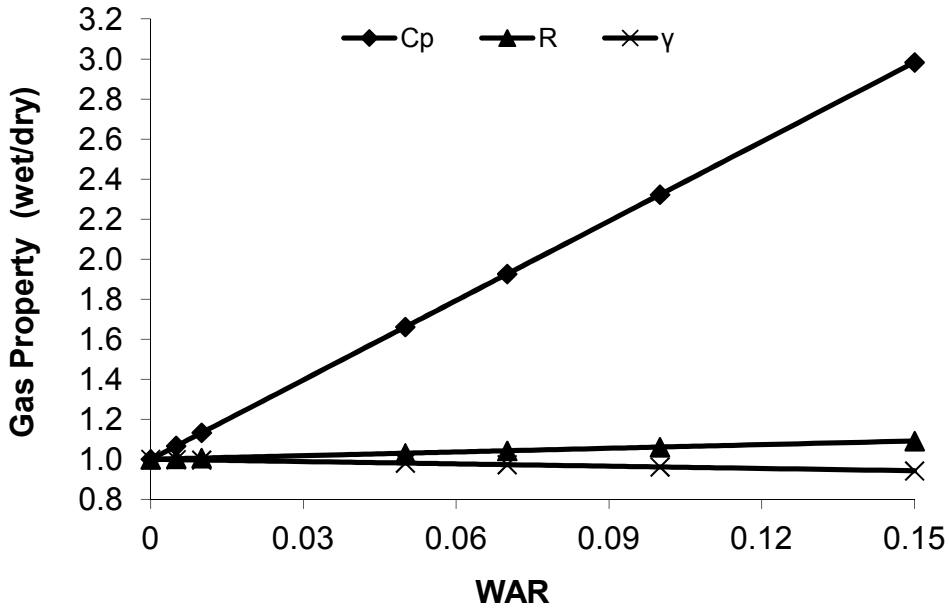


Figure 4-7: Variation of gas properties for different values of WAR at 673K

#### 4.4 The engine performance for different values of WAR

In this section the effect of different levels of WAR (different levels of RH. 0% to 100%) on key engine performance parameters is investigated at ambient temperatures 288.15K, 308.15K and 318.15K to better study blade creep life duration. Figure 4-8 shows the change of engine performance parameters such as PCN, inlet mass flow, TET, etc., relative to the reference operating point (0% humidity and 288.15K). It is clear that the effect of change in RH, from 0% to 100%, at 288.15K was small as result of the small change in value of the WAR; at RH 100% WAR=0.01069. The greatest changes were in SFC and fuel flow; the compressor delivery pressure and temperature dropped less than 0.5% compared to the reference operating point.

Figure 4-9 and 4-10 show the effect of WAR on engine performance at higher ambient temperatures. At RH = 100% the WAR at 308.15K was 0.037, and at 318.15K was 0.065. Some aspects of engine performance changed remarkably when changing RH from 0% to at 100% RH. At 308.15K, compressor pressure and temperature dropped around 2% and 1.5% respectively, while SFC increased by about 1.02%, see Figure 4-9. At ambient temperature 318.15K,

the compressor pressure and temperature dropped around 3.4% and 2.3% respectively, but SFC increased by about 1.2%, see Figure 4-10.

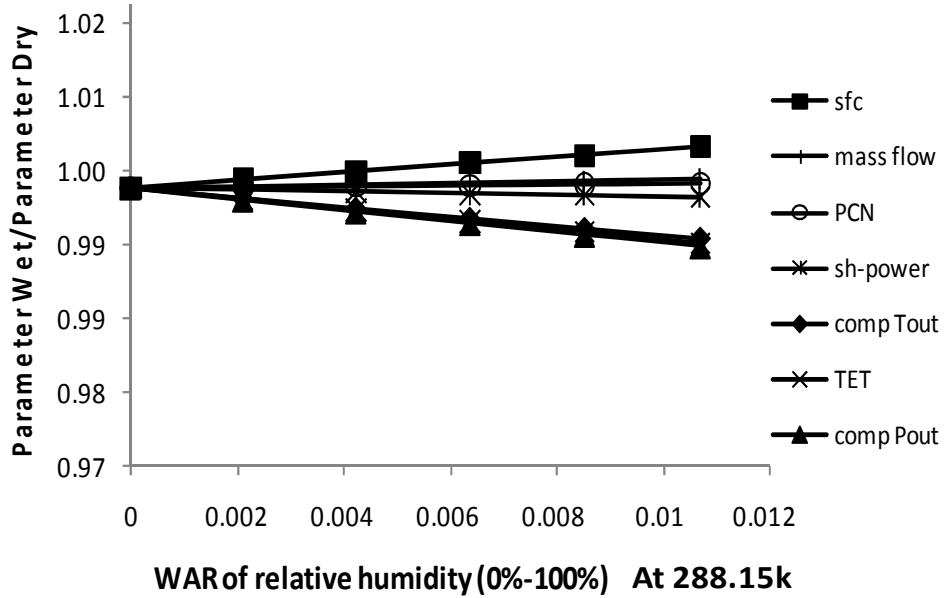


Figure 4-8: Engine performance parameters at ambient temperature 288.15K for different values of WAR (RH levels 0%-100%)

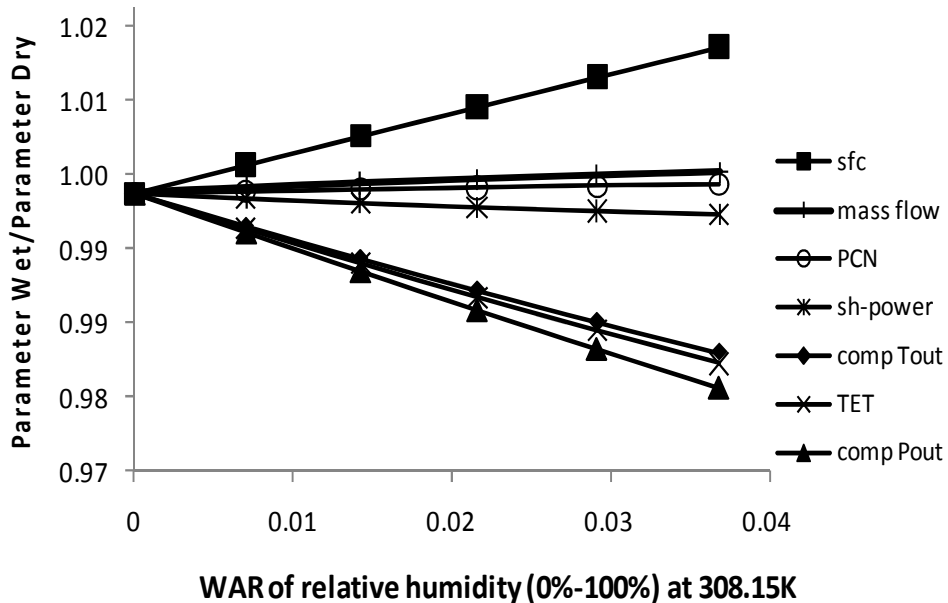
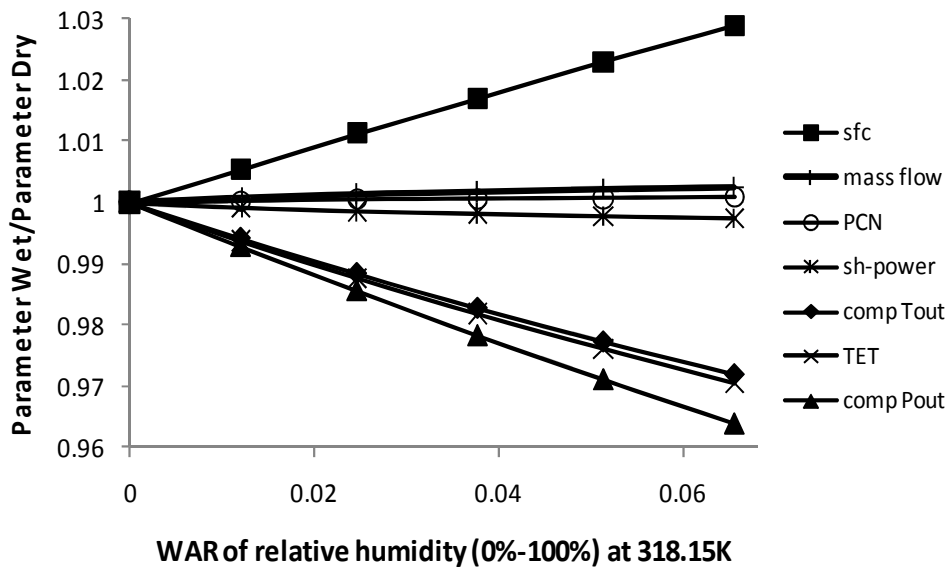


Figure 4-9: Engine performance parameters at ambient temperature 308.15K for different values of WAR (RH levels 0%-100%)



**Figure 4-10: Engine performance parameters at ambient temperature 318.15K for different values of WAR (RH levels 0%-100%)**

As mentioned earlier change in WAR will affect the gas properties which in turn affect the engine performance. The drop in compressor delivery pressure results from the change in inlet mass flow (increased air density). Mixing air with water causes the compressor temperature to drop and if the amount of water exceeded the amount that can be evaporated within the compressor, the water will enter the combustion and cause an effect similar to reducing the TET.

#### 4.5 Hot gas properties in presence of water vapour

Steam injection increases the amount of water in the gas flow and affects combustion because of its impact on gas transport properties. The two common approaches to studying the impact of fluid properties in GT turbine performance are simulation software or models. Fluid properties are found either from polynomial functions or interpolated from fluid tables, the latter is more tedious and it is more common and convenient to use polynomial functions. Typically the GT working fluid consists of varying relative amounts of air, fuel and products of combustion. Two fluid model tables have been generated for this research: natural gas and Jet-A, kerosene (Jet-A, presented in Appendix B). The chemical composition of the fluids was generated using the NASA thermoBuild package, which provides data subsets used in CAE software. The

CAE software can perform calculation within the temperature range from 200K to 2000K. The procedure of using CAE software is presented in [142; 143].

The chemical formulae of the components of the two fuels considered are shown in Table 4-2. Two polynomial functions were generated for  $C_p$ ,  $\gamma$  and  $R$  for each of the two fuels and can be used in the heat transfer model, facilitating the calculation of the effect of WAR on blade creep life.

**Table 4-2: Components natural gas and Jet-A (kerosene) and their formulae**

<b>fuel</b>	<b>Component</b>	<b>Formula</b>
<b>Natural gas</b>	Methane	CH <sub>4</sub>
	Ethane	C <sub>2</sub> H <sub>6</sub>
	Propane	C <sub>3</sub> H <sub>8</sub>
	n-butane	C <sub>4</sub> H <sub>10</sub>
	n-pentane	C <sub>5</sub> H <sub>12</sub>
	Nitrogen	N <sub>2</sub>
<b>Jet-A</b>		C <sub>12</sub> H <sub>23</sub>

The fuel tables generated for this fluid model assume constant gaseous composition of the products of combustion. Since there is no dissociation, the combustion of the products does not change even with change in the temperature as the distributions of moles and consequently mole fractions remain the same at any temperature. These fuel properties were tabulated as function of four variables; temperature, pressure, WAR and FAR (Fuel Air Ratio). These variables were chosen and organised in terms of the range and interval in such a way as to meet the working operation of an industrial GT combustion chamber.

- FAR: if exactly enough air is provided to completely burn all of the fuel, the ratio is known as a stoichiometric mixture [149]. For this work, FAR ranged from a minimal value=0 to a maximum value=0.06 for Natural gas, and from 0 to 0.04 for Jet-A fuel.
- WAR: for this work, WAR ranged from a minimum value of zero to a maximum value of 0.1. The upper limit was imposed because for values higher than that the gas flow cannot be treated as a perfect gas.

- Temperature and pressure distributions were based on the range of the combustion temperatures and pressure for industrial GTs. In this model the temperature ranged between 700K and 2000K in intervals of 50K. The pressure had a minimum value of 10 atmospheres and a maximum value of 30 atmospheres.

For the no dissociation fluid model, it is assumed that all the working fluids are ideal gases and subsequently the fluid properties are function of temperature, pressure, FAR and WAR. The gas constant, R, is a function of FAR and WAR only [149]. In this research NASA's chemical equilibrium with applications (CEA) program was used to generate the tables of the gas properties for both fuels. Polynomial correlation was obtained for Cp,  $\gamma$  and R as function of FAR, WAR, pressure and temperature. The multi regression equation for the gas properties of natural gas is presented in Equation 4-8 and the coefficients for the fluid are presented in Tables 4-3. This equation can be used as input in the heat transfer model to calculate the change in the hot gas properties of the flow when steam is injected into the combustion.

$$\text{Fluid properties } (C_p; \gamma; R) = A + B.X_1 + C.X_2 + D.X_3 + E.X_4 \quad (4-8)$$

Where,  $X_1$ =FAR is the fuel air ratio,  $X_2$ =WAR is the water air ratio,  $X_3$ =P is the gas pressure and  $X_4$ =T is the gas temperature.

**Table 4-3: Coefficients for the calculation of the gas properties of UK Natural Gas.**

	Cp	$\gamma$	R
<b>A</b>	916	1.4	287
<b>B</b>	2741	-0.589	168
<b>C</b>	768	-0.091	102
<b>D</b>	-0.082	1.39E-05	-2.41E-04
<b>E</b>	0.2213	-6.5E-05	3.80E-05

#### 4.5.1 Natural gas properties for different values of WAR

Since there is no dissociation, the combustion products do not change even with changes in inlet temperature. This means that the mean molecular weight of the gases in the products of combustion remains constant regardless of the temperature or pressure. Figures 4-11, 4-12 and 4-13 present the change of

specific heat at constant pressure as function of WAR (0 (dry) to 0.01 (humid)), FAR (0 to 0.06) and temperature (700K to 2000K) for Natural gas, assuming a constant gaseous composition of the products of combustion. The results show an increase in the  $C_p$  for increased WAR, FAR and temperature of the hot gas. For FAR=0.06 and temperature=1300K,  $C_p$  increased from 1423 to 1457 and to 1479 for WAR=0, 0.08 and 0.1, respectively.

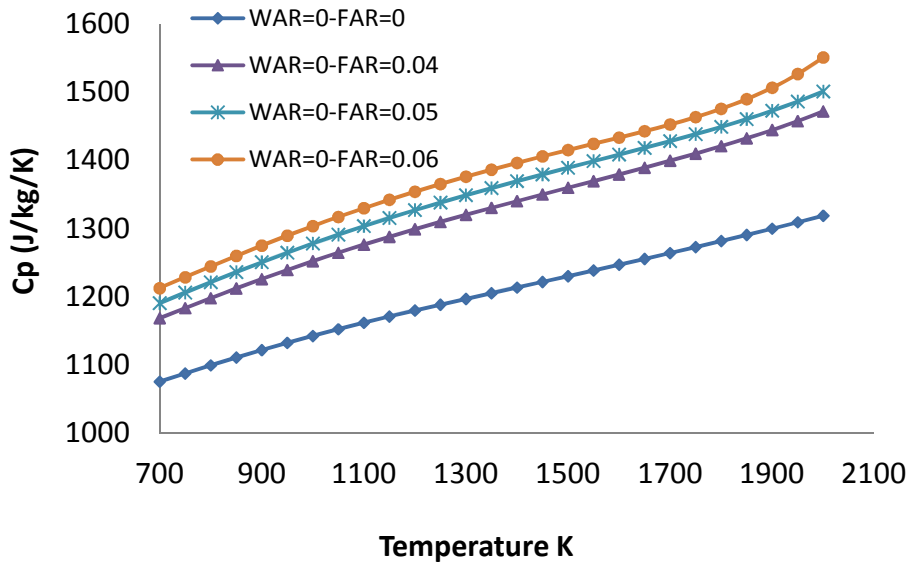


Figure 4-11: Hot gas specific heat at constant pressure for natural gas for WAR=0 and FAR=0, 0.04, 0.05 and 0.06

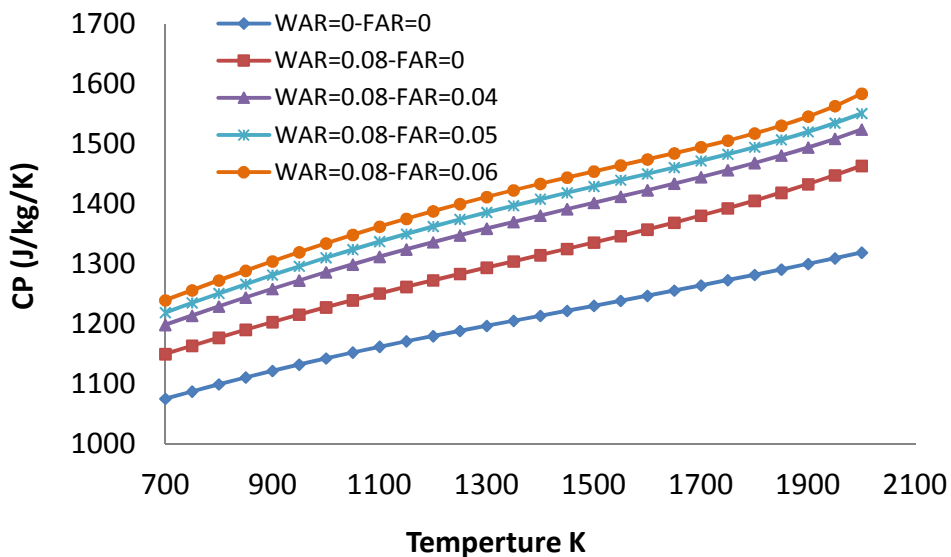
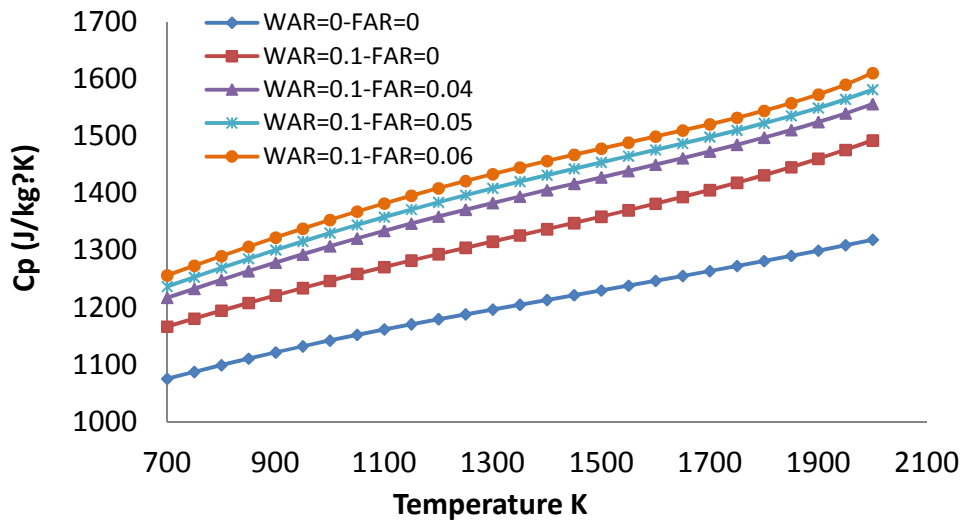


Figure 4-12: Hot gas specific heat at constant pressure for natural gas for WAR=0.08 and FAR=0, 0.04, 0.05 and 0.06





**Figure 4-13: Hot gas specific heat at constant pressure for natural gas for WAR= 0.10 and FAR=0, 0.04, 0.05 and 0.06**

Figure 4-14, 4-15 and 4-16 show the variation of the isentropic coefficient ( $\gamma$ ) as a function of temperature, FAR and WAR for natural gas in the combustion chamber. For a fixed value of WAR and FAR,  $\gamma$ , decreases as the temperature increases, as shown. The variation of  $\gamma$  with temperature is effectively the inverse of the variation of  $C_p$  with increase in temperature. For example, with WAR=0 and FAR=0.06 the value of  $\gamma$  decreased from 1.28 to 1.24 as the TET increased from 1000K to 2000K.

At constant TET and WAR,  $\gamma$  decreased as FAR increased. For example, with TET =1500K and WAR=0, as FAR reduced from 0.04 to 0.06,  $\gamma$  decreased from 1.28 to 1.26.

For constant TET and FAR,  $\gamma$  decreased as WAR increased. For example, for TET = 1500K and FAR=0.04 as WAR increased from 0 (dry) to 0.1(humid),  $\gamma$  reduced from 1.275 to 1.270 approximately. It is clear that the reduction in  $\gamma$  with increase in WAR for a fixed temperature and FAR for a no dissociation fluid model was based on the variation of  $C_p$  (increase with an increase in WAR for a given temperature and FAR) and R as a function of WAR.

The molecular weight of the products (fluid) does not change which means there is a constant gaseous composition of the products of the combustion. As a result R does not change with the change of gas temperature, but does vary

with FAR and WAR. However, for the chemical equilibrium fluid model the level of dissociation is strongly influenced by high temperature [149]. Therefore,  $R$  is function of FAR and WAR for no dissociation fluid. Figures 4-17, 4-18 and 4-19 show the variation of the gas constant as a function of temperature, fuel air ratio and water air ratio for natural gas fuel assuming a constant composition of the gaseous products of combustion (no dissociation).  $R$  increased with increase in either WAR or FAR. For WAR = 0.1,  $R$  increased from 304 to 308 as FAR increased from zero to 0.06. For FAR = 0.06,  $R$  increased from 299 to 308 as WAR increased from zero to 0.1.

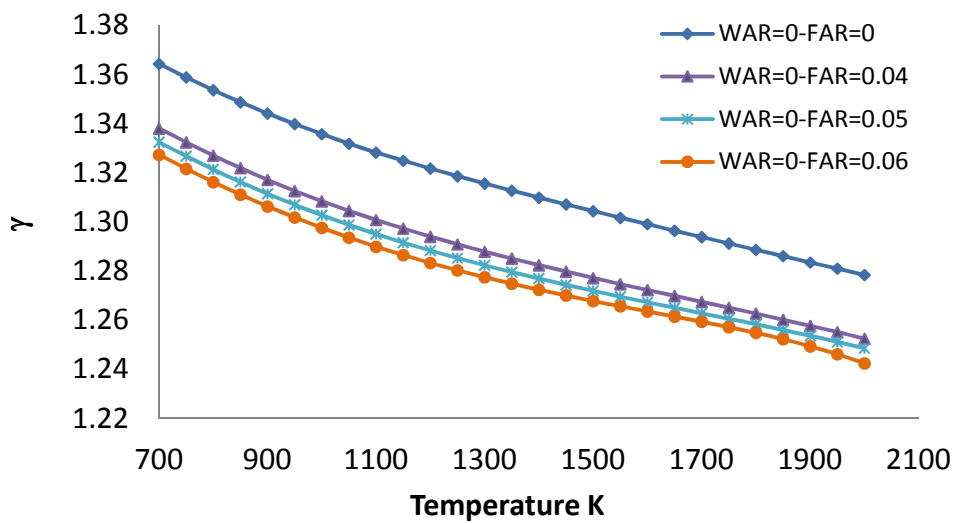


Figure 4-14: Hot gas isentropic coefficient ( $\gamma$ ) for natural gas for WAR=0 and FAR=0, 0.04, 0.05 and 0.06

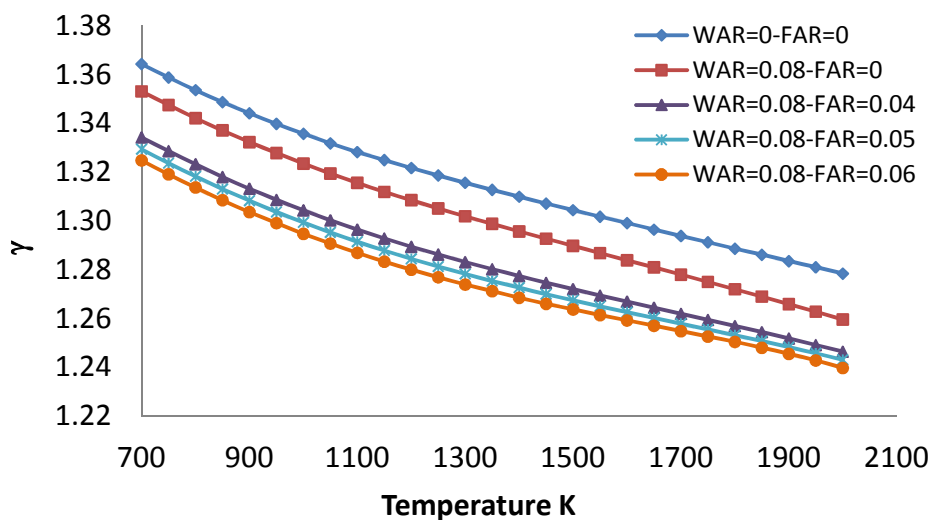


Figure 4-15: Hot gas isentropic coefficient ( $\gamma$ ) for natural gas for WAR=0.8 and FAR=0, 0.04, 0.05 and 0.06

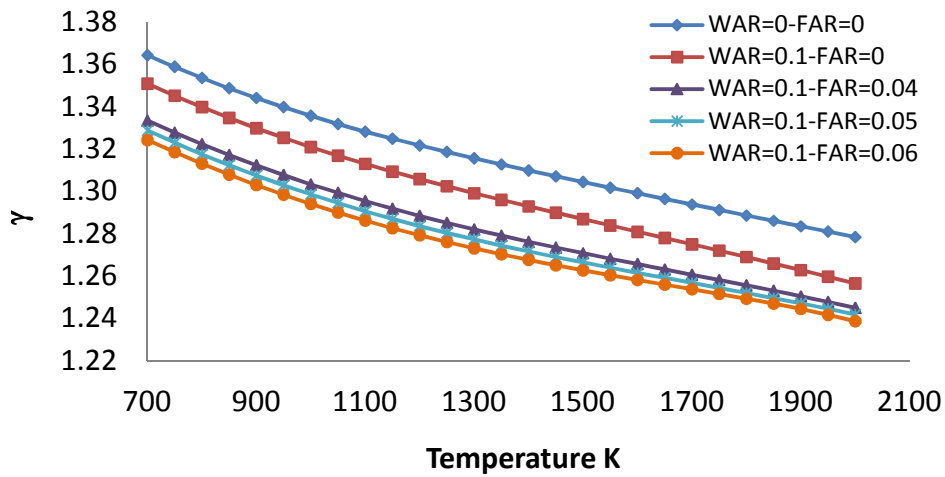


Figure 4-16: Hot gas isentropic coefficient ( $\gamma$ ) for natural gas for WAR=0.1 and FAR=0, 0.04, 0.05 and 0.06

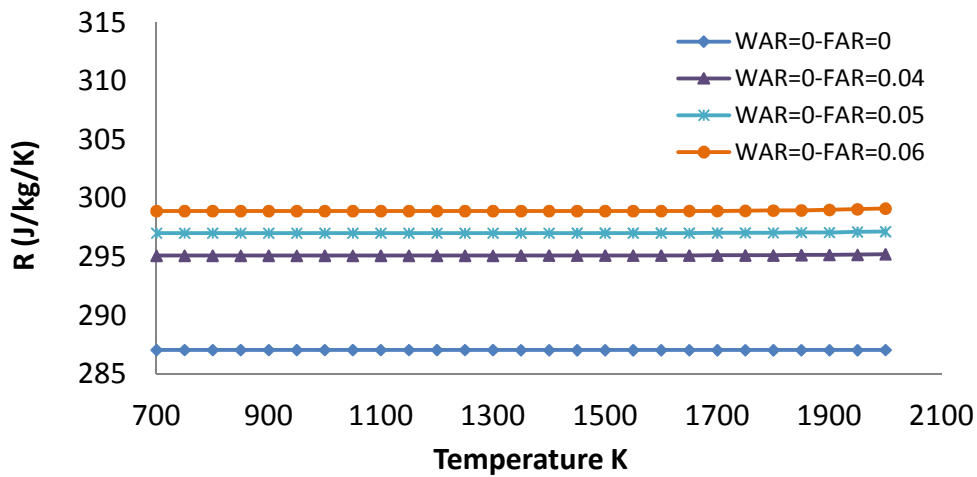


Figure 4-17: Gas constant for hot natural gas for WAR=0 and FAR=0, 0.04, 0.05 and 0.06

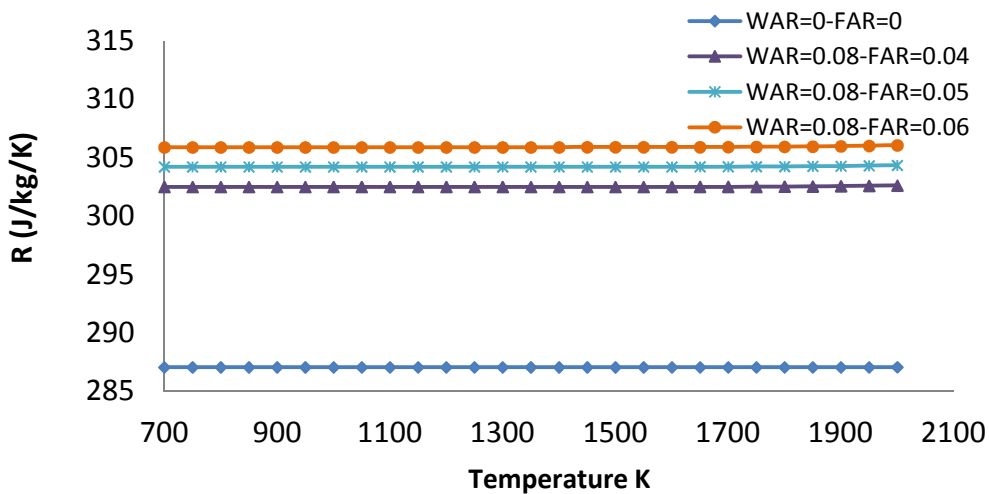
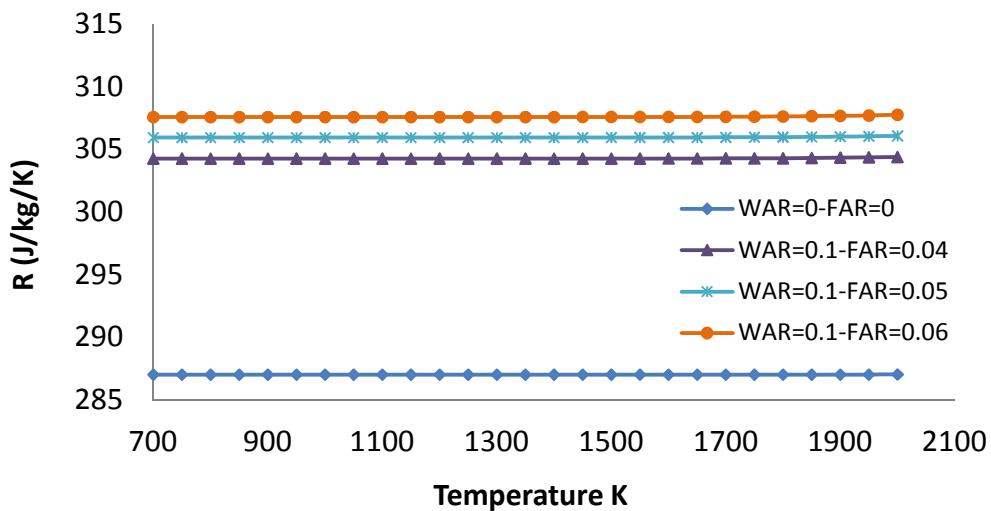


Figure 4-18: Gas constant for hot natural gas for WAR=0.08 and FAR= 0.04, 0.05 and 0.06



**Figure 4-19: Gas constant for natural gas for WAR=0.1 and FAR= 0.04, 0.05 and 0.06**

Vishal [149] shows a comparison of the variation of  $C_p$ ,  $\gamma$  and  $R$  as a function of temperature, FAR and WAR between the Walsh and Fletcher polynomials defined in [141] and the no dissociation fluid model using the CEA [142] software for both Jet-A and natural gas. The results clearly show that the two fluid models are consistent over the temperature range 200K to 2000K.

Figure 4-20 shows  $C_p$  (no dissociation) for Jet-A and natural gas at WAR = 0.1 and FAR = 0.04 for different temperatures. For both fuels  $C_p$  increases with increase in temperature and the difference between the  $C_p$  values of the two fuels is small.

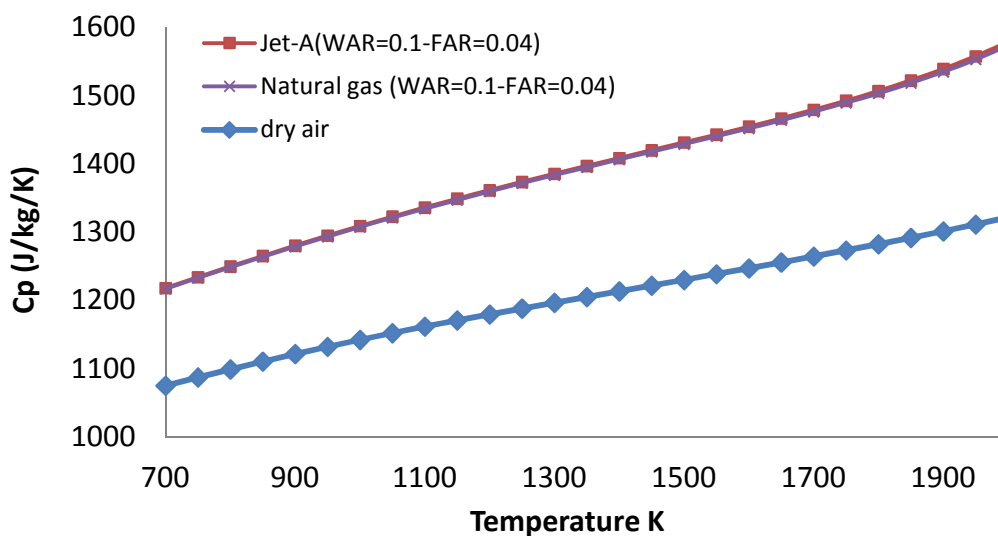


**Figure 4-20: Comparison of no-dissociation  $C_p$  as a function of T, WAR and FAR at p=20atm**

The value of  $\gamma$  decreases as the temperature increases for both fuels (WAR = 0.1 and FAR = 0.04), and  $\gamma$  for Jet-A fuel is consistently less than  $\gamma$  for natural gas, as shown in Figure 4-21. For both fuels the gas constant, R, remains constant as the temperature increases for given values of WAR and FAR, but R was significantly higher for natural gas, as shown in Figure 4-22.

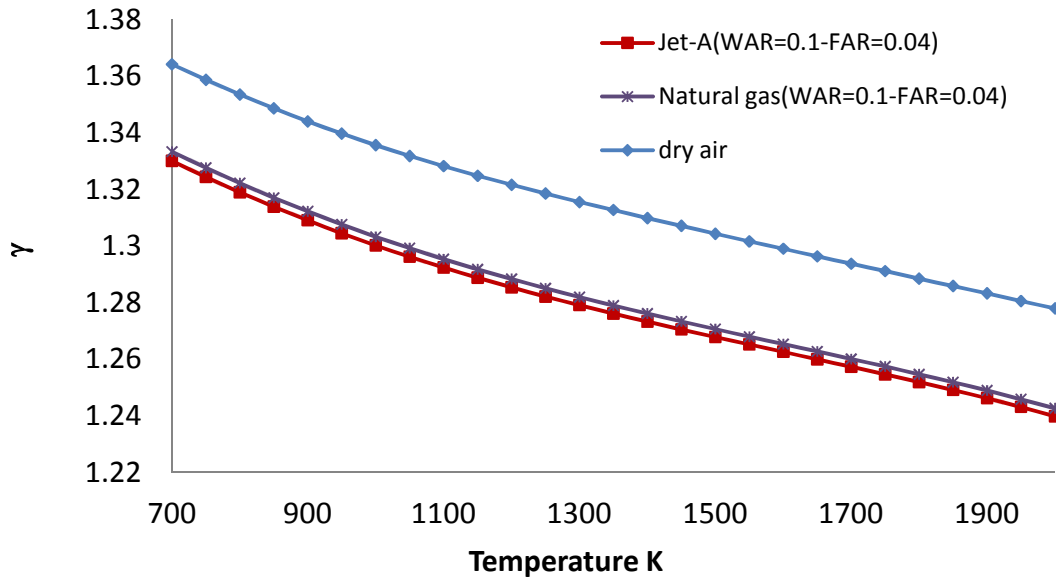


Figure 4-21: Comparison of no dissociation  $\gamma$  as a function of T, WAR and FAR at p=20atm

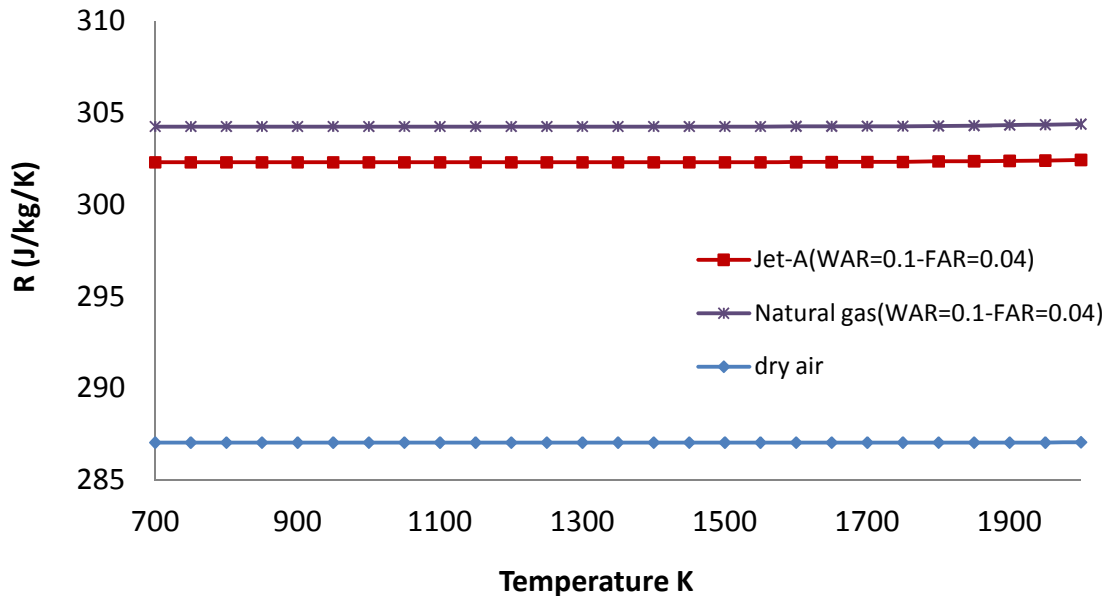


Figure 4-22: Comparison of no dissociation R as a function of T, WAR and FAR at p=20atm

## 4.6 Chapter Conclusions

The presence of water vapour changes the values of the transport gas properties for both the cold side and the hot side gases of the GT engine. The analysis presented here is based on the change of gas properties of dry air and WAR obtained using procedures existing in the literature. The results obtained show the effect of WAR and temperature of the coolant air is for the  $C_p$  and  $R$  to increase, while  $\gamma$  diminishes more slowly, these effects have a significant impact upon the thermodynamic processes throughout the GT engine. The result will be used to demonstrate the effect of the WAR on the heat transfer and blade creep life

This chapter has used the NASA CEA software to generate multi-dimensional fluid model tables for the two fuels; natural gas and Jet-A. These tables were of specific heat at constant pressure, isentropic coefficient and gas constant and were tabulated as function of WAR, FAR, temperature and pressure. The ranges over which the parameters were investigated were selected and organised so as to meet operating conditions of industrial GT combustion chambers. The fuel property data generated are based on a constant gaseous composition and no dissociation in the products of combustion. Since there is no dissociation, the combustion of the products does not change even with change in the temperature.

The results for natural gas shows an increase in  $C_p$  for increased WAR, FAR and temperature of the hot gaseous products of combustion. For a fixed value of WAR and FAR,  $\gamma$  decreases as the temperature increases. Increasing the WAR for constant FAR and TET caused the value of  $\gamma$  to decrease. The gas constant  $R$  does not change with change of gas temperature, but does vary with FAR and WAR. Increase in WAR at different FAR and/or increase in FAR for different WAR increased the value of  $R$ .

The variation of the gas properties  $C_p$ ,  $\gamma$  and  $R$  for the Jet-A fuel at different WAR and FAR (as presented in Appendix B) were similar to natural gas. By increasing the WAR for different FAR the  $C_p$  increased linearly,  $\gamma$  decreased as

the temperature increased whereas for increase in WAR the value of  $\gamma$  decreased. As WAR increased the value of R increased. However for a fixed temperature, as FAR increases the molecular weight of the products of the combustion increase and thus R decreases.

For both fuels, the  $C_p$  increases with increase in temperature and variation of the  $C_p$  for the two fuels was similar. The value of  $\gamma$  decreases as the temperature increased for both types of fuel, but  $\gamma$  for Jet-A fuel decreased slightly more than natural gas as shown in Figure 4-21. For both fuels, the R does not change with change in TET for fixed WAR and FAR, but R was higher for natural gas than for jet-A as shown in Figure 4-22.





## *Chapter five*

### **5 MECHANICAL STRESS MODEL**

A turbine extracts energy from the working fluid and converts it into shaft power. This process requires both a NGV and a rotor component which together comprise the turbine. The blade must be designed to perform the duties required at different operating and environment conditions. Also, the blade should not fail due to over-stressing, high cycle fatigue, thermal fatigue, creep or other failure mechanisms.

The major sources of stress arising in GT blades are:

- Centrifugal inertial load acting on the airfoil section due to the rotation of the airfoil and produced by the mass of blade material which exists outside of that section.
- Gas turbine moment produced by the change in momentum and pressure of the fluid passing across the blades.
- Bending moment produced by the centrifugal load acting at a point which does not act radially above the centroid of the root datum section.
- Shear load arising from the 'untwisting effect' of the loads on the blade..
- Complex loading due to thermal gradients.

In order to perform the creep life calculation, stresses (centrifugal and/or gas bending stresses) on the blade from the hub to tip were considered. The data used in the stress model such as pressure, rotational speed and temperature were generated by Turbomatch. It is assumed in the model that the axial velocity remains constant along the span of the blade and the actions of the forces on the blade (centrifugal loading, static pressure difference and momentum change) act at the blade section centre of gravity (CG). The blade span was divided into sections at intervals of 25% of the span as shown in Figure 5-1. The chord was divided into three: blade TE, blade LE and back of

the blade. It is acceptable to calculate the blade stresses at only these three locations because these are the locations which will, most probably, have the highest tensional or compressible stresses.

The shear stress is definitely much smaller than the centrifugal and the gas bending stresses on the blades, and can be considered insignificant from the point of view of strength. Stresses due to thermal gradients on the turbine blade are often much greater than any of the other forms of stresses and can be very destructive. This type of stress will be considered in the FE analysis using a 3-D turbine blade model.

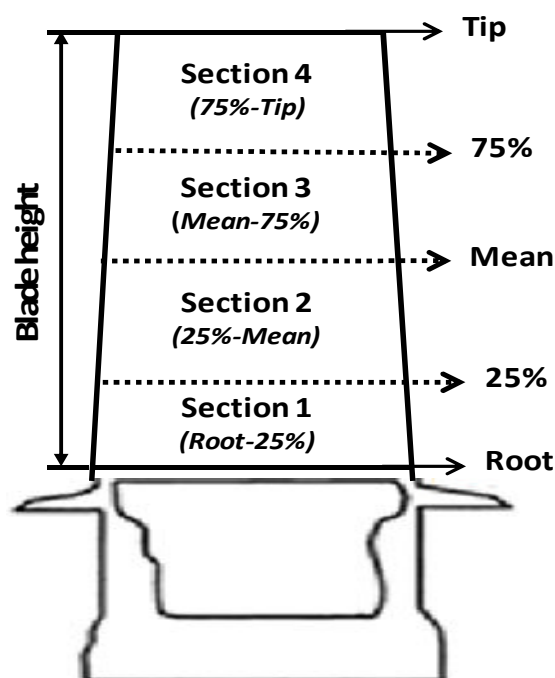


Figure 5-1: Blade sections

## 5.1 Stresses model

This study developed a 2-D stress model where the variations of the blade stresses are predicted at locations along the blade span and chord. The centrifugal stresses caused by engine rotation and the bending stresses caused by the change in gas momentum and the presence of static pressure difference are considered. The blade stress model is based on a number of equations and aims to estimate the maximum stress acting on the HP turbine blade. Figure 5-2 shows the stress model flow chart used in this study.

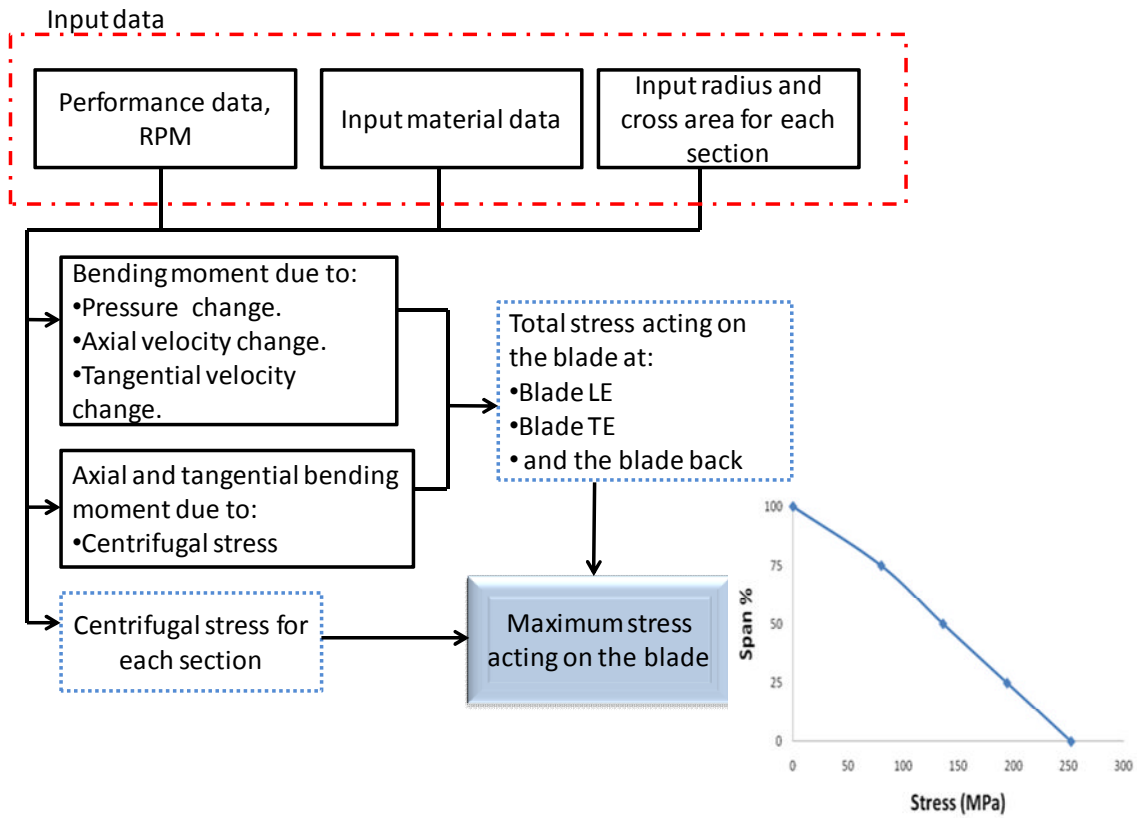


Figure 5-2: Blade stress model flow chart

### 5.1.1 Centrifugal stress model

Centrifugal stresses is the tensile stress act on the blade turbine due to the engine's rotational speed and mass of blade material (mass=density\*mean-cross-sectional-area\*height). Operating in an inertia field, about 50% to 80% of the blade material strength is used to overcome the centrifugal stresses. The centrifugal forces at any blade section is a function of the mass of the blade exterior to that section, the radial distance from the centre of gravity of the material exterior to that section to the centre of rotation and the rotational speed. The centrifugal force of each blade section was calculated for each section,  $CF_{sec}$ , [66; 150]:

$$CF_{Sec} = \rho \times A_{CsAv} \times H_{sec} \times \omega^2 \times r_{cg} \quad (5-1)$$

Where  $\rho$  is the density of the material of the blade,  $A_{AvCs}$  is the average cross sectional area between the top and the bottom of the sections,  $h_{sec}$  is the blade

section height,  $\omega$  is the angular speed, and  $r_{cg}$  is the distance between the rotation axis and the section centre of gravity (cg).

As shown in Figure 5-3 the centrifugal force at the blade tip is due to the mass of the blade shroud, the centrifugal force acting at the blade mean is the vector sum of the centrifugal forces acting on the blade shroud and the blade mean-tip section. The centrifugal force acting at the blade root is the vector sum of the centrifugal forces acting on the blade shroud, the mean-tip section and the root-mean section.

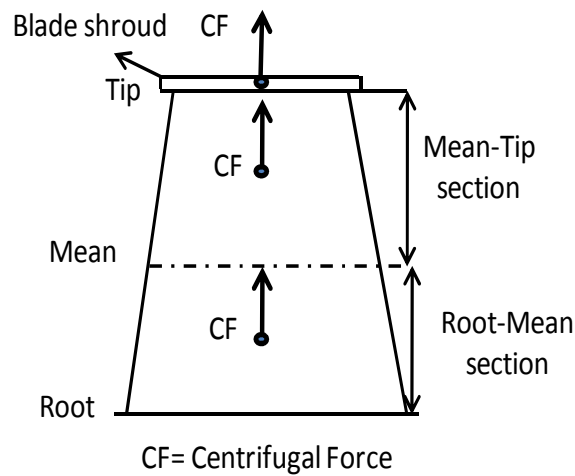


**Figure 5-3: Blade centrifugal forces**

Using Equation 5-2 [66], the centrifugal stress at each section  $\sigma_{CFSec}$  was calculated where  $A_{CS}$  is the cross-sectional area of the corresponding section. The individual stress at each section can be added and the appropriate direct stress obtained.

$$\sigma_{CFSec} = \frac{\sum CF_{Sec}}{A_{CS}} \quad (5-2)$$

### 5.1.2 Gas bending stress model

There is a force on the blades produced by the change in momentum of the gases across the blade, and a second force due to pressure differences as the fluid passes across the blade. The pressure force will act rearward in the turbine

and forward in the compressor with respect to the engine. Due to the blade twist, the ratio between the tangential and the axial component of these gas pressure forces will vary from blade root to blade tip. It is for this reason that the blade is divided into sections, as shown in Figure 5-4, to determine the average velocity change in the tangential and axial directions for each section.

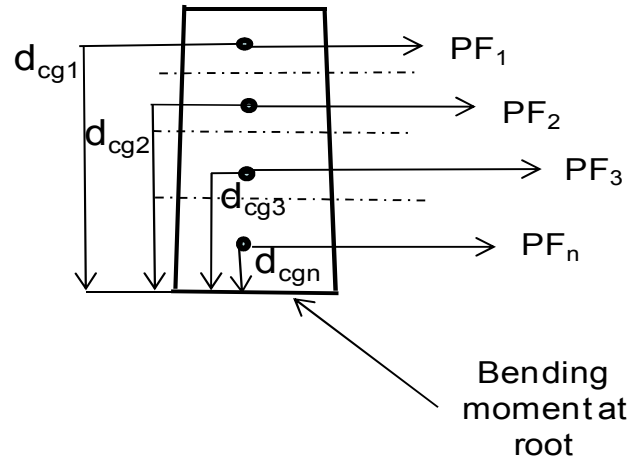


**Figure 5-4: Bending moment at root due to static pressure difference and momentum change**

In order to calculate the bending moment stress due to static pressure difference, the pressure force acting on each blade section,  $PF_{Sec}$  was calculated using Equation 5-3 as shown in Figure 5-4. Once the pressure forces are calculated, the bending moment,  $BMP_{Sec}$  at each blade section can be obtained using Equation 5-4 [66].

$$PF_{Sec} = \frac{A_{AnSec} \times \Delta p_{AvSec}}{N_b} \quad (5-3)$$

$$BMP_{Sec} = \sum (PF_{Sec} \times d_{CGSec}) \quad (5-4)$$

Where  $A_{AnSec}$  is the blade section annulus area,  $\Delta p_{AvSec}$  is the average section static pressure difference,  $N_b$  is the number of blades, and  $d_{CGSec}$  is the distance of the section CG from the blade root, as shown in Figure 5-4.

Turbomatch provides the inlet and outlet properties of the turbine blade as a whole and can also calculate the intermediate properties of multi-stage turbine. The model assumes that the polytropic efficiency,  $\eta_p$  remains constant across

the turbine stages [133] hence is reversely calculated using Equation 5-5. In this equation,  $P_{NGV}$  and  $P_{Out}$  are the turbine inlet and outlet stagnation pressures simulated by Turbomatch,  $\gamma_g$  is the specific heat ratio of the hot gas, and  $\eta_t$  is the turbine isentropic efficiency.

$$\eta_P = \frac{\ln \left( 1 - \eta_t \left( 1 - \left( \frac{P_{NGV}}{P_{Out}} \right)^{\frac{\gamma_g - 1}{\gamma_g}} \right) \right)}{\frac{\gamma_g - 1}{\gamma_g} \ln \left( \frac{P_{NGV}}{P_{Out}} \right)} \quad (5-5)$$

The outlet stagnation pressure of the turbine stage,  $p_{OutStage}$  can be calculated using Equation 5-6 where  $T_{OutStage}$  is the outlet static temperature calculated using Equation 5-7 and  $\%T_{drop}$  denotes the temperature drop percentage of each turbine stage (50%) defined by the Author, and  $T_{drop}$  is the overall temperature drop across the turbine ( $T_{\text{turbine inlet}} - T_{\text{turbine outlet}}$ ).  $P_{NGV}$  in Equation 5-6 and  $T_{NGV}$  in Equation 5-7 are replaced with  $P_{OutStage}$  and  $T_{OutStage}$  from the previous stage.

$$P_{OUTStage} = P_{NGV} \left( \frac{T_{OUTStage}}{T_{NGV}} \right)^{\frac{\gamma_g}{\eta_P(\gamma_g - 1)}} \quad (5-6)$$

$$T_{OutStage} = T_{NGV} - (\%T_{drop} \times T_{drop}) \quad (5-7)$$

Since the focus of creep life prediction is on the HP turbine blade, it is obviously necessary to calculate the gas properties at the inlet of the turbine blade (NGV exit properties). This is because, as the gas flows across the NGV, there is a reduction to the gas properties especially when NGV cooling is present. The calculation process is divided into two parts. In the first part, the NGV exit temperature  $T_{mixing}$  is calculated using the energy balance in Equation 5-8 and as shown in Figure 5-5.

$$T_{Mixing} = T_{NGV} - \frac{NGV_{mass\ frac} \times m_c C p_c}{m_g C p_g} (T_{Co} - T_{Cin}) \quad (5-8)$$

Where  $NGV_{mass\ frac}$  is the mass fraction of the coolant flow that enters the NGV specified by the user (see Equation 4-34),  $m_c$  and  $m_g$  are the coolant and gas mass flows simulated by Turbomatch respectively,  $Cp_c$  and  $Cp_g$  are the specific heats for the cold and hot gas respectively,  $T_{Co}$  is the coolant exit temperature obtained from the blade thermal model, and  $T_{cin}$  is the coolant inlet temperature also simulated by Turbomatch.

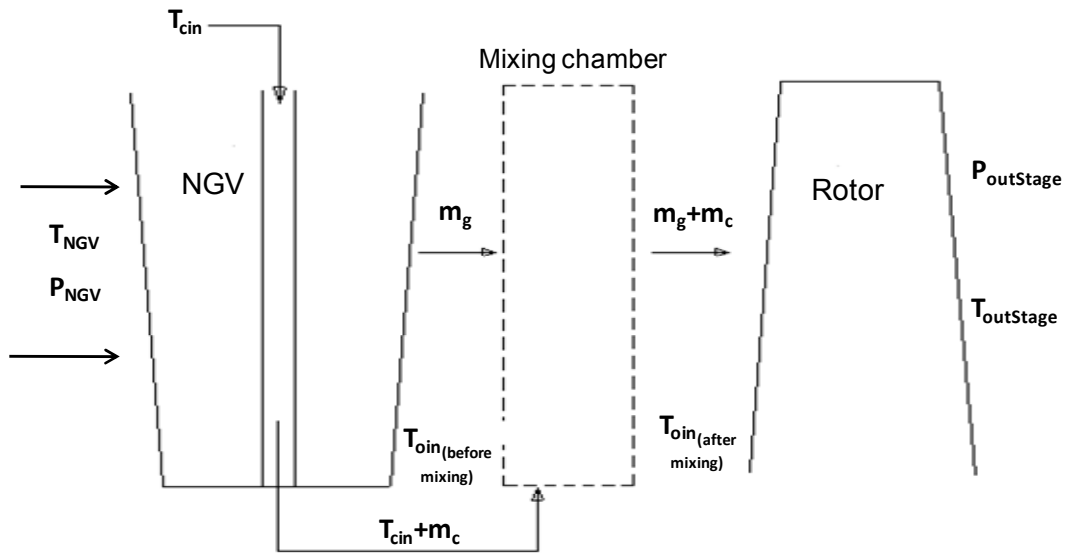


**Figure 5-5: Diagram illustrating the mixing between the core flow and exit cooling**

In the second part, an imaginary mixing chamber as shown in Figure 5-5 is introduced to determine the blade inlet gas temperature with the coolant gas entering the system. It is assumed that all the coolant flow that leaves the NGV will mix together with the core gas flow  $m_g$ . From the thermodynamic mixing chamber relation, the blade inlet gas temperature,  $T_{in}$  is calculated using Equation 5-9.

$$T_{IN} = \frac{m_g Cp_g T_{Mixing} + (NGV_{mass\ frac} \times m_c) Cp_c T_{Co}}{(m_g + (NGV_{mass\ frac} \times m_c)) Cp_g} \quad (5-9)$$

In order to calculate the static pressure difference, the absolute velocities  $V_{Abs}$  of the gas at the inlet and outlet of the blade need to be found by applying Equation 5-10:

$$V_{Abs} = \sqrt{V_{Ax}^2 + V_{Tan}^2} \quad (5-10)$$

Where  $V_{Ax}$  is the blade inlet and outlet gas axial velocity calculated using the Axial Velocity Model, and  $V_{Tan}$  is the blade gas tangential velocity calculated using Equation 5-11 for blade inlet and Equation 5-12 for blade outlet respectively.

$$V_{Tan} = V_{Ax} \times \tan\alpha_o \quad (5-11)$$

$$V_{Tan} = U - W_{Tan} \quad (5-12)$$

Where  $\alpha_o$  is the NGV outlet angle,  $U$  is the blade speed, and  $W_{Tan}$  is the outlet gas relative tangential velocity calculated using Equation 5-13 and  $\alpha_2$  is the blade outlet angle [134].

$$W_{Tan} = V_{Ax} \times \tan\alpha_2 \quad (5-13)$$

Once the velocities are determined, the static temperature  $t$  and pressure  $p$  are calculated using Equations 5-14 and 5-15 respectively. Note that  $(T)$  and  $(P)$  used in Equation 5-14 and 5-15 will depend on whether the calculation is made for the inlet or the exit of the blade (for blade inlet  $T=T_{in}$  and  $P=P_{in}$ , whereas for blade outlet  $T=T_{outstage}$  and  $P=P_{outstage}$ ).

$$t = T - \frac{V_{Abs}^2}{2Cp_g} \quad (5-14)$$

$$p = P \left( \frac{t}{T} \right)^{\frac{\gamma_g}{\gamma_g - 1}} \quad (5-15)$$

The axial velocity model is used to calculate both the inlet and outlet axial gas velocities of the blade. From mass flow continuity [133], we know that the terms  $\frac{W\sqrt{T}}{AP}$  and  $\frac{V}{\sqrt{T}}$  can be expressed in terms of Mach number ( $M$ ), stagnation and static temperature as given Equations 5-16 and 5-17.

$$\frac{W\sqrt{T}}{AP} = M \sqrt{\frac{\gamma_g}{R}} \left( \frac{T}{t} \right)^{\frac{-(\gamma_g+1)}{2(\gamma_g-1)}} \quad (5-16)$$



$$\frac{V}{\sqrt{T}} = M\sqrt{\gamma R} \left(\frac{T}{t}\right)^{-1/2} \quad (5-17)$$

Where  $V$  is the velocity,  $M$  is the Mach number,  $R$  is the ideal gas constant,  $W$  is the inlet mass flow and  $A$  is the cross sectional area through which the gas travels.

In this model, the term  $W\sqrt{T}/(AP)$  is denoted as  $Q1000$  and for each blade inlet and outlet,  $Q1000$  is obtained from the Pressure Bending Moment Model where  $m, T, A,$  and  $P$  in Equation 5-16 are taken as  $m_g, T_{in}$  (for inlet) or  $T_{OutStage}$  (for outlet),  $A_{In}$  (for inlet) or  $A_{Out}$  (for outlet) and  $P_{in}$  (for inlet) or  $P_{OUTStage}$  (for outlet). Note  $A_{In} = \pi(r^2_{tipin} - r^2_{rootin})$  and  $A_{Out} = \pi(r^2_{tipout} - r^2_{rootout})$  are the blade inlet and outlet annulus areas.

Taking the  $Q1000$  values from Pressure Bending Moment Model as target values  $Q1000_{Target}$ , the inlet and outlet  $M$  are estimated and changed iteratively until the values of  $Q1000_{Guess}$  calculated using Equation 5-16 approaches a limiting value. This is done by observing an error value,  $E$  calculated using Equation 5-18 and stopping the iteration process when a designated threshold margin error is achieved. Once the values of inlet and exit  $M$  are determined, using Equation 5-17, the axial velocities are calculated.

$$E = \frac{Q1000_{Target} - Q1000_{Guess}}{Q1000_{Guess}} \times 100 \quad (5-18)$$

Where the error margin used in this work is given in  $-0.005\% < E < 0.005\%$

### 5.1.3 Momentum bending moment model

As the gases travel across the blade, there are forces acting on the blade due to the velocity difference between the inlet and the outlet. These forces are produced by the momentum change of the gases in both axial and tangential directions. A similar approach is adopted In this model for the blade section momentum forces for both axial and tangential directions,  $VF_{Sec}$ , (see Figure 5-

6). The momentum forces acting in both axial and tangential directions were computed using Equation 5-19 and 5-20 respectively [66]:

$$VF_{AxSec} = \frac{m_{Area} \times A_{AnSec} \times \Delta V_{AxSec}}{N_b} \quad (5-19)$$

$$VF_{TanSec} = \frac{m_{Area} \times A_{AnSec} \times \Delta V_{TanSec}}{N_b} \quad (5-20)$$

Where  $m_{Area}$  is the mass flow per unit area of the section annulus,  $\Delta V_{AxSec}$ , is the axial velocity difference and  $\Delta V_{TanSec}$  is the blade section average tangential velocity difference.

Note that the velocity differences calculated for the axial and tangential directions are different. In the axial direction, the velocity along the blade span is constant so the difference in the axial velocity for each blade section is similar and hence does not require any averaging. However in the tangential direction, the velocities at the tip, mid and root positions are different. As a result, the velocity difference for each blade section is taken as the average of the velocity difference of the top and the bottom of each section of the blade. For example, the velocity difference at the root-mid section is the average of the velocity difference at the blade mid-point and blade root.

The momentum bending moments due to the axial and tangential forces at each blade section  $BMV_{Axsec}$  and  $BMV_{Tansec}$  were then calculated using Equation 5-21 and 5-22 respectively [66]:

$$BMV_{Axsec} = \sum(VF_{AxSec} \times d_{CGsec}) \quad (5-21)$$

$$BMV_{Tansec} = \sum(VF_{TanSec} \times d_{CGsec}) \quad (5-22)$$

#### 5.1.4 Maximum stress acting on the blade

In order to obtain the resulting bending moment at the blade direction (about X and Y axis), Equations 5-23 and 5-24 [66] were applied,

$$M_{xx} = (BMP_{sec} + BMV_{AxSec}) \sin \theta + BMV_{TanSec} \cos \theta \quad (5-23)$$

$$M_{yy} = (BMP_{sec} + BMV_{AxSec}) \cos \theta - BMV_{TanSec} \sin \theta \quad (5-24)$$

Where  $M_{xx}$  and  $M_{yy}$  are the blade section resulting bending moments about the x and y axes, and  $\theta$  is the blade section stagger angle.

The conversion of the resulting bending moment from the engine direction (axial and tangential) to the blade direction (X-X and Y-Y) is to allow for the calculation of the resulting bending moment stresses. The bending moment is calculated at three different locations, LE, TE and the back of the blade section using Equation 5-25 [66]:

$$\sigma_{BMsec} = \frac{M_{xx}}{I_{min}} Y + \frac{M_{yy}}{I_{max}} X \quad (5-25)$$

Where  $I_{min}$  and  $I_{max}$  are the maximum and minimum values of the blade section moments of inertia .  $X$  and  $Y$  are the distances from the LE, TE and the back of the blade from the XX and YY axes as shown in Figure 5-6.

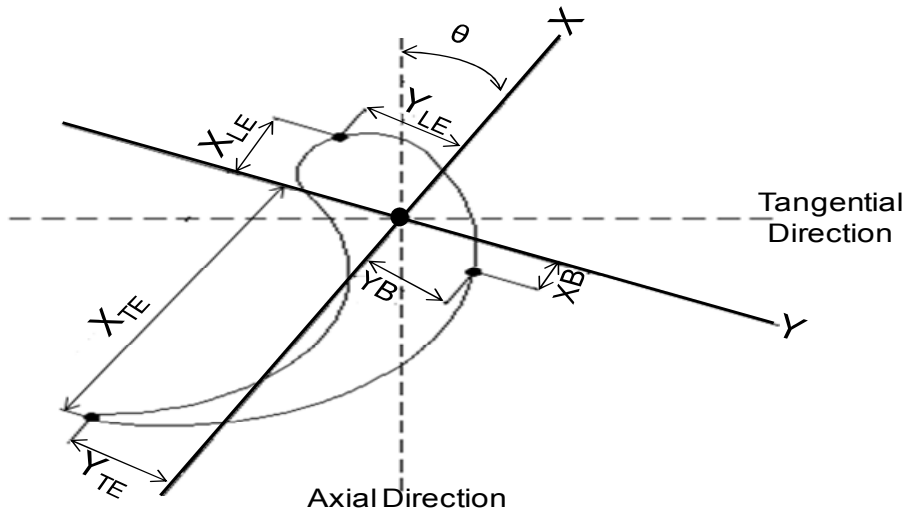


**Figure 5-6: Schematic diagram of the blade and gas flow directions [66].**

Thus due to the moment acting about XX ( $M_{xx}$ ), the LE stress ( $\sigma_{LE}$ ) and TE stress ( $\sigma_{TE}$ ) would both be tensile while stresses on the back of the blade would be compressive. There would also be stresses at the LE and TE arising from

$M_{yy}$  in conjunction with distances  $y$  from the Y-Y axis. Thus, the  $M_{yy}$  stress at the LE would be compressive (-) and at the TE would be tensile (+).

The output of the stress model is the maximum stress at the blade sections when both stresses (centrifugal loading and gas bending moment) were added using total stress Equation 5-26. It is important to note that the location where the maximum stress occurs, either at LE, TE or the blade back largely depends on the operating condition and the geometry of the blade.

$$\sigma_{TotSec} = \sigma_{CFsec} + \sigma_{BMsec} \quad (5-26)$$

The highest stress acting on the blade in the chordwise direction is at the blade root. Whereas the maximum stress at the blade tip is due to the blade tip centrifugal force since there is no bending moment present at this location.

## 5.2 Chapter Conclusions

The stress in the blade at each section can be obtained using the stress model presented in this chapter. A number of the previous work considered only the centrifugal force as the main contributor to the stress in the blade. This is because the values of other sources of stress were considered small compared with the centrifugal stress. However, this assumption always shows that the direct centrifugal stress contributes approximately more than 90% of the total stress. This is quite high compared with the range of between 50% and 80% as recommended in the open literature review. Therefore, in this study the model developed considers the centrifugal and the gas bending stress from the blade root to the tip. The model takes the input data from the performance simulation results and blade sizing model. The centrifugal and the resulting bending moment stress acting on the blade sections were calculated at different operating condition and different values of RH.

The variation of blade metal temperature and maximum stress along the span of the blade has a strong influence on the blade creep life. A small change in these two factors will determine the value and location of the lowest creep life.

Therefore, more consideration needs to be given in component life assessment to the stress values and their locations along the blade in order to identify the position of the minimum creep life.



## *Chapter six*

### **6 HEAT TRANSFER MODEL**

The cooling of high temperature gas turbines has been the subject of intensive work over the past few decades. There are three well known methods for the design the first stage of a HP turbine blade; un-cooled, convection cooled and film cooled. In the early 80's the gas turbine industry developed a turbine blade using both convection and film cooled methods with a thermal barrier coating to reduce the blade metal temperature [4]. The analysis of the temperatures of the cooled blades requires the solution of equations governing heat flow through the solid blade given the internal and external distributions of the boundary gas temperature and heat transfer coefficients [5]. Although analytical solutions are nowadays used for detailed blade design, in earlier years engine companies relied on practical methods for determining the amount of cooling flow required to maintain blade temperature within prescribed metallurgical limits [6].

The determination of the rate of heat transfer from the turbine blade in a cross flow is important in hot section gas turbine life assessment. For design purposes, the rate of heat transfer is normally fixed by semi-empirical correlations expressing Nusselt number in terms of Reynolds and Prandtl numbers. The implementation of such correlations requires knowledge of fluid properties such as density, viscosity, thermal conductivity and specific heat, all which depend on temperature. For gases these properties are normally available only for the dry state, thus the possible effect of the water vapour content of the gas has been overlooked [7].

The aim of this study is to present an analytical model to investigate the influence of humidity on the turbine blade heat transfer and cooling processes which, in turn, affect blade creep life. The model is flexible and capable of assessing the main parameters that influence the blade cooling performance, such as cooling methods, alternative cooling fluids, blade geometry, heat

transfer coefficients, gas properties and material and thermal barrier coating. The whole cooled blade row is regarded as a heat exchanger subjected to a mainstream hot gas flow from the combustion chamber.

## 6.1 Heat Transfer Model and Application

To maintain the turbine blade metal at a low temperature, the heat transferred from the hot stream to the blade is removed by forced convection in the blade channel and carried away by the air coolant (see Figure 6-1). Thus the blade metal is maintained at a low temperature. Chiesa and Macchi [151] considered the blade cooling as a heat exchanger subject to the heat flux  $q_g = h_g \cdot (T_{gr} - T_{bg})$ . Ainley [8] presented basic equations for the heat transfer process obtained by equating the total rate of heat flow into an element to zero. Since the blade cooling process is considered as a heat exchanger with the presence of TBC, the heat transfer model used in this work can be described by the following set of energy equations, 6-1 to 6-4.

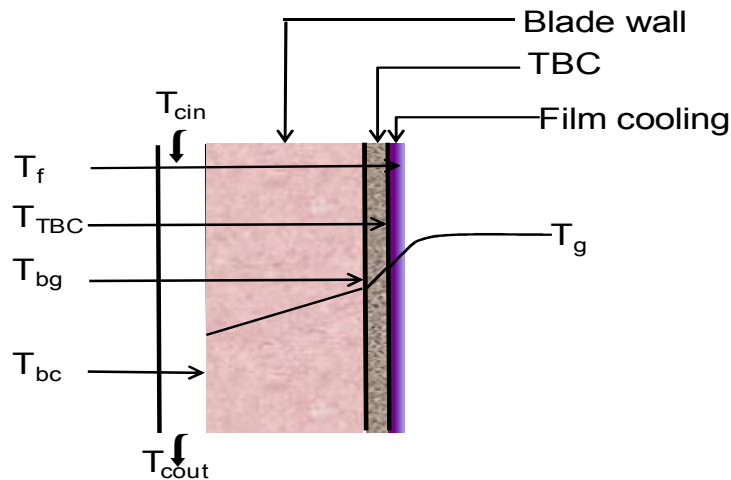


**Figure 6-1: Temperature profile through the blade with film cooling and thermal barrier coating.**

$$dq = h_g A_{gs} (T_{gr} - T_{TBCg}) \quad (6-1)$$

$$dq = k_{TBC} / t_{TBC} A_{gs} (T_{TBCg} - T_{bg}) \quad (6-2)$$

$$dq = k_{bw} / t_{bw} A_{gs} (T_{bg} - T_{bc}) \quad (6-3)$$



$$dq = h_c A_{cs} (T_{bc} - T_{co}) \quad (6-4)$$

The sum of the four energy equations gives the overall heat transfer coefficient of the blade turbine [6; 152].

The integrated analytical procedure and the calculation process in this model are illustrated in Figure 6-2. The model consists of two main sub-models: (i) coolant heat transfer model and (ii) hot heat transfer model. The models receive the aero-thermal input from TURBOMATCH, gas properties with presence of WAR from the gas property model, and the geometrical and material/TBC data are defined by the user.

The output of this model is the blade metal temperature and stress distribution along the blade which will be used as input to the creep life model to calculate blade time to failure. Since the model is analytical, it can take into account the effect of blade geometry and cooling method on the blade cooling performance and blade creep life.

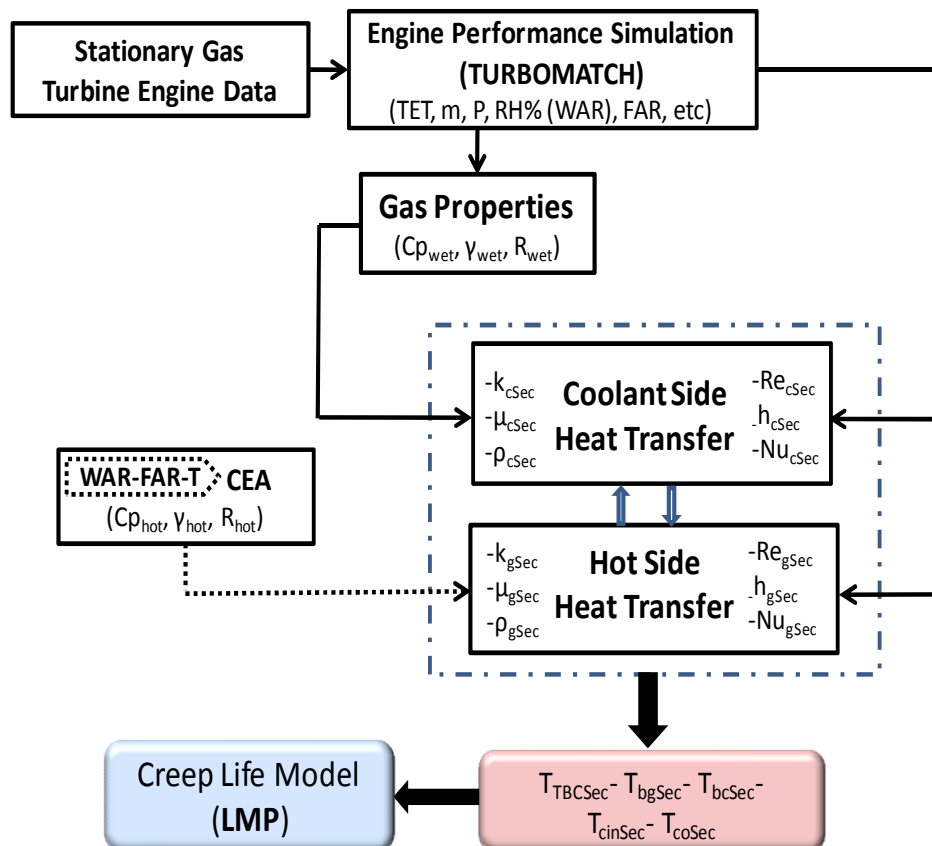


Figure 6-2: Simplified flow diagram of the heat transfer model

This approach deals with convective/film cooling and effect of changing fluid properties on the cooling heat transfer processes of the HP turbine blade, for the purpose of assessing the turbine blade creep life and increasing gas engine availability and reliability. Also, the approach adopted has the ability to analyse alternative cooling medium, humidity (WAR), coolant mass flow, cooling effectiveness, RTDF, blade material, TBC data and other parameters that could affect the heat transfer process. The heat transfer model presented consists of two models; hot side model and cold side model.

### 6.1.1 Coolant Side Heat Transfer

Heat is extracted from the blade inside wall by forced convection increased locally where extra cooling is needed [5]. The cooling system of the blade is defined as its internal geometry and cooling flow extracted from the compressor. Table 6-1 presents the configuration of the cooling system used in this study.

Figure 6-3 presents the process of calculating the coolant heat transfer coefficient in the blade. The figure also shows how the blade was divided to several sections, and the section outlet cooling temperature was used as the next section's inlet cooling temperature.

**Table 6-1: Cooling system data**

	<b>Value</b>	<b>Unit</b>
<b>Height</b>	0.042	m
<b>Chord at mean</b>	0.027	m
<b>Blade mean diameter</b>	0.78	m
<b>Hydraulic diameter</b>	0.0030	m
<b>Number of cooling channels</b>	7	-
<b>Stager angle</b>	35	deg
<b>Air outlet angle <math>\alpha_2</math></b>	60.3	deg
<b>Total coolant bleed</b>	10%	
<b>Prandtl number</b>	0.7	
<b>RTDF</b>	0.07-0.1	
<b><math>\eta_{ad}</math></b>	0.2-0.5	

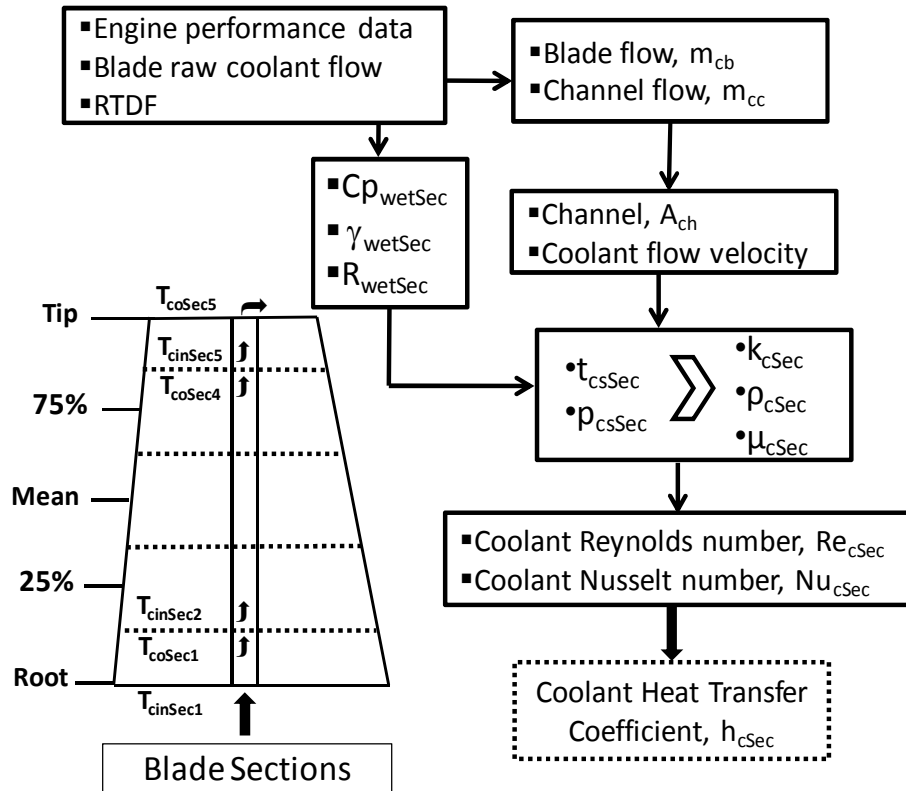


Figure 6-3: Flow chart of process calculating coolant heat transfer coefficient and blade sections

### 6.1.1.1 Coolant Density

The density of the coolant side was calculated using the equation of state and by knowing the static pressure and temperature of the coolant air and gas constant as function of WAR. The density of humid air was calculated as a mixture of ideal gases [153]. According to Dalton's law, the total pressure in a mixture of perfect gases is the sum of the partial pressures of each individual gas in the mixture  $P_{total}=p_d+p_v$ . In this case, the partial pressure of water vapor is known as the vapor pressure. Based on this, the density of humid air is obtained by:

$$\rho_{humid\ air} = \frac{p_d}{R_d * t} + \frac{p_v}{R_v * t} \quad (6-5)$$

The saturation vapour pressure is required to calculate the water vapour pressure. There are many algorithms for determining the saturation vapour pressure, but for this study a simplified equation from the regression of the data is used [154]:

$$p_{sat} = 6.1078 * 10^{\frac{7.5*t-2048.625}{t-35.85}} \quad (6-6)$$

where, the temperature is in Kelvin and the saturation pressure in Pa. The total pressure at the blade inlet is obtained from the simulation performance data.

By knowing the saturation vapour pressure and using the relative humidity, the vapour pressure of water is calculated using the following Equation [155].

$$p_v = RH * p_{sat} \quad (6-7)$$

### 6.1.1.2 Cooling Configuration

The blade cooling system defined as its internal geometry and the cooling flow. The internal configuration of the high pressure turbine blade is often very complex includes cooling channels, passage, ribs, etc. The cross-sectional area of one single channel was calculated by using the channel hydraulic diameter,  $(A_c = \psi_d \cdot \pi \cdot D_h^2 / 4)$ , where  $D_h=0.003m$ . However, the total cross sectional- area of the cooling passages should be within the limit of the blade cross-sectional area and calculated using the number of coolant channels [156; 157]. One single blade has a number of internal uniform circular cooling channels with constant cross-sectional area. The shape factor  $\psi_d$  for this type of channel would be unity, but is greater than unity if the shape non-circular [6; 158]. El-masri [158] calculates the cooling flow for blade on the basis of a constant value for the effectiveness and for film cooled blades, on a correlation for the isothermal effectiveness. In this study, the cooling flow specified in the performance model as percentage of cooled air extracted from the compressor and than the cooling effectiveness calculated in order to calculate the blade metal temperature. The single blade row mass flow, channel mass flow and total effective coolant heat transfer surface area for the coolant side were defined by Equations 6-8 to 6-10:

$$m_{cb} = \frac{M_c}{100} \frac{m_g}{N_b} \quad (6-8)$$

$$m_{cc} = \frac{m_{cb}}{n_{ch}} \quad (6-9)$$

$$A_{cs} = \pi D_h H n_{ch} \quad (6-10)$$

Here  $M_c$  is the coolant bleed % which is based on the coolant mass flow used to cool the blade row. It is assumed that the length of the cooling passages is the same as the blade height.

### 6.1.1.3 Viscosity and Thermal Conductivity of Humid Air

The expressions available for determining the properties of viscosity and thermal conductivity of gas mixtures vary from purely theoretical derivations to direct curve fits of experimental data [159]. Richards and Florschuetz [159] reported different method and results obtained from a survey of the literature regarding the dynamic viscosity and thermal conductivity of humid air. The viscosity of fluid was determined by two methods; one which include the effect of humidity [160] and the second based on the gas temperature only. The viscosity of many fluids doesn't change with pressure but is very sensitive to temperature. In this study the viscosity of the gas at each section of the blade was calculated using Equation 6-11.

The effect of viscosity on the heat transfer is expected to be less significant since the flows inside the cooling channel are turbulent. The results obtained using the Kestin and Whitelaw [160] correlation for the viscosity of a mixture of dry air and water vapour (at WAR=0-0.1) were compared with the results obtained using the alternative Sutherland equation and a good agreement was obtained [161].

$$\mu_{mix} = \frac{\mu_w}{1 + \frac{x_d}{x_w} \frac{\left[1 + \left(\frac{\mu_w}{\mu_d}\right)^{1/2} \left(\frac{MW_w}{MW_d}\right)^{1/4}\right]^2}{2.83 \left[1 + \frac{MW_w}{MW_d}\right]^{1/2}}} + \frac{\mu_d}{1 + \frac{x_d}{x_w} \frac{\left[1 + \left(\frac{\mu_d}{\mu_w}\right)^{1/2} \left(\frac{MW_d}{MW_w}\right)^{1/4}\right]^2}{2.83 \left[1 + \frac{MW_d}{MW_w}\right]^{1/2}}} \quad (6-11)$$

$$\mu_w = (-1.46494887 + 0.037079658 T)10^{-6} \left(\frac{kg}{ms}\right) \quad (6-12)$$

$$\mu_d = (6.0453459 + 0.042489943 T)10^{-6} \left(\frac{kg}{ms}\right) \quad (6-13)$$

Where the  $M_{w_d}$  and  $M_{w_w}$  are the molecular masses of dry air and water vapor respectively,  $x$  is the molar fraction defined as the ratio of the number of moles of water vapor  $n_v$  with respect to the total number of moles of the mixture of humid air  $n_{Ha}$ ,  $x=n_v/n_{Ha}=p_v/p$ .

The viscosity of the water vapour and the dry air was obtained using Equation 6-12 and 6-13 respectively. There is widely used method reported for thermal conductivity of humid air [159; 162]. The thermal conductivity ( $k_{cw}$ ) the humid air for the coolant blade is calculated using Wassiljewa Equation 6-14 proposed in Mason et al. [163]. The  $k_{mix}$  values obtained by this method were also identical to those obtained using NASA CEA (Chemical Equilibrium with Applications) software.

$$k_{mix} = \frac{k_d}{1 + A_{Aw} \frac{x}{1-x}} + \frac{k_w}{1 + A_{Ad} \frac{1-x}{x}} \quad (6-14)$$

The required parameters  $A_{Aw}$  and  $A_{Ad}$  are calculated using the following equation:

$$A_w = 0.28 \left(1 + \frac{M_{wa}}{M_{ww}}\right)^{-0.5} \left[1 + \left(\frac{\mu_d M_{ww}}{\mu_w M_{wa}}\right)^{0.5} \left(\frac{M_{wa}}{M_{ww}}\right)^{0.25}\right]^2 \quad (6-15)$$

The same expression gives  $A_{Ad}$  when subscripts are interchanged.

The required pure component values for the thermal conductivity of the water vapour and dry air was calculated according to the standard values using Equation (third order polynomial) 6-16 and 6-17. Table 6-2 present the Coefficients for the calculation of the thermal conductivities of dry air and water vapour:

$$K_w = A_w + B_w T + C_w T^2 + D_w T^3 \quad (6-16)$$

$$K_d = A_d + B_d T + C_d T^2 + D_d T^3 \quad (6-17)$$

Where the temperature T in K

**Table 6-2: Coefficients for the calculation of the thermal conductivities of dry air and water vapour**

Coefficient for				
	water vapour		Dry air	Units
<b>A<sub>w</sub></b>	31.997566.10 <sup>-3</sup>	<b>A<sub>d</sub></b>	-0.56827429.10 <sup>-3</sup>	W/mk
<b>B<sub>w</sub></b>	-0.13308958.10 <sup>-3</sup>	<b>B<sub>d</sub></b>	0.10805198.10 <sup>-3</sup>	W/mk <sup>2</sup>
<b>C<sub>w</sub></b>	3.8160429.10 <sup>-7</sup>	<b>C<sub>d</sub></b>	-7.3956858.10 <sup>-8</sup>	W/mk <sup>3</sup>
<b>D<sub>w</sub></b>	-2.0.10 <sup>-10</sup>	<b>D<sub>d</sub></b>	3.7302922.10 <sup>-11</sup>	W/mk <sup>4</sup>

#### 6.1.1.4 Coolant Reynolds Number, Nusselt Number and Heat Transfer Coefficient

The cooling flow Reynolds number is calculated from the coolant air density, velocity, viscosity and channel diameter [157]. Coolant velocity inside blade channel was obtained using non-dimensional mass flow (1000Q) and Mach number [139] which are calculated using the iterative process as shown in Appendix C.

Reynolds's number is a ratio of inertia forces to viscous forces. For the coolant side, the coolant channel Reynolds number is calculated using Equation 6-18. Based on this, coolant Nusselt number can be obtained (for turbulent flow) using Equation 6-19 [164]. The Nusselt number is a dimensionless version of the temperature gradient at the surface between the fluid and the metal, and thus it provides a measure of the convection occurring from the blade surface. From the coolant Nusselt number, coolant thermal conductivity and coolant channel diameter, the coolant heat transfer coefficient for the turbine blade can be obtained using Equation 6-20 [165]:

$$Re_{cwSec} = \frac{\rho_{cwSec} \times V_{AbsSec} \times D_h}{\mu_{cwSec}} \quad (6-18)$$

$$Nu_{cwSec} = 0.15 (Re_{cwSec})^{0.8} \quad (6-19)$$

$$h_{cwsec} = Nu_{cwSec} \frac{k_{cw}}{D_h} \quad (6-20)$$

where the thermal conductivity ( $k_{cw}$ ) is for coolant air which was calculated using Wassiljewa Equation proposed in Mason et al. [163].

### 6.1.2 Hot Side Heat Transfer

The external blade geometrical parameters and the gas angles along the spanwise of the blade were obtained from engine performance data and blade sized using constant nozzle method, and the sizing process of first stage of the HP turbine blade presented in [72] and Appendix A. Figure 6-4 shows the stages and processes of calculating the heat transfer coefficient of the hot side and the outlet cooling temperature, as well as the blade metal temperature along the blade span. All the gas properties on the hot side were considered and calculated for a dry hot gas.

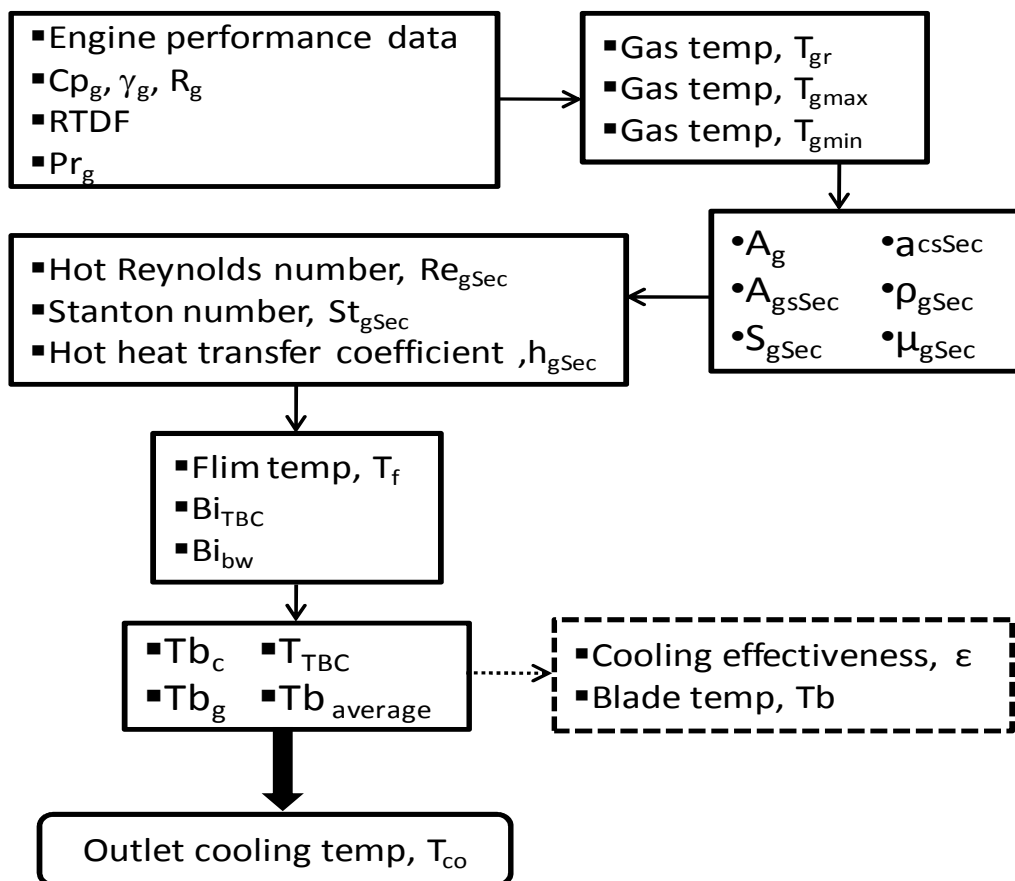


Figure 6-4: process calculating heat transfer of hot side and outlet cooling temperature.



### 6.1.2.1 Gas Recovery Temperature

At low Mach number  $< 0.3$  the difference between  $T_{gst}$ ,  $T_{gtot}$  and  $T_{gr}$  is negligible. However, at higher speeds the conversion of kinetic energy into thermal energy takes place in the boundary layer causing significant temperature change. The effect of such irreversibility taking place within the boundary layer, in accordance with Prandtl's theory, is expressed by the gas recovery temperature factor ( $r$ ) as shown in Equation 6-21. Assuming that the hot gas Prandtl number is the same as for a flat plate and equal to 0.7 [1; 156; 166]. The inlet gas temperature of the turbine blade was determined by considering the mixing effect between the core flow and the coolant flow exiting the nozzle guide vane (NGV) [72].

$$r = \frac{T_{gr} - T_{gst}}{T_{gtot} - T_{gst}} \quad (6-21)$$

Where for a gas with a Prandtl number close to unity, the solution of the energy equation for a turbulent flow gives the gas recovery temperature factor  $r = Pr_g^{1/3}$ . Once the  $r$  factor is known, the gas recovery temperature easily can be obtained by using equation 6-21.

### 6.1.2.2 Radial Distribution of Gas Temperature

The temperature of the hot gas exiting the combustion is far from uniform, due to incomplete mixing. The difference between the maximum and the average gas temperature can be accounted for by introducing radial temperature distribution factor (RTDF). This model used a radial distribution of gas temperature leaving the burner to calculate the temperature variation at each blade section. Taking the RTDF as 0.1 for the nozzle and 0.08 for the first rotor [14; 15; 141; 167; 168], the maximum,  $T_{max}$  and the minimum gas temperature,  $T_{min}$  were calculated using Equations 6-22 [141] and 6-23 respectively [72]:

$$T_{max} = T_{gr} + (T_{REF} * RTDF) \quad (6-22)$$

$$T_{min} = \frac{(5T_{gr} - 2T_{max})}{3} \tag{6-23}$$

Where  $T_{gr}$  is the rotor inlet gas recovery temperature and  $T_{REF}$  is the temperature rise at the burner.

By assuming that the maximum temperature will occur at around 75% of the distance from the root as shown in Figure 6-5,  $T_{75\%}$  the gas temperature at each blade section was predicted. The location of the maximum temperature was based on the fact that the rotation of the turbine blade causes the peak gas temperature to shift from the mid of the span of the blade toward the tip region [169].

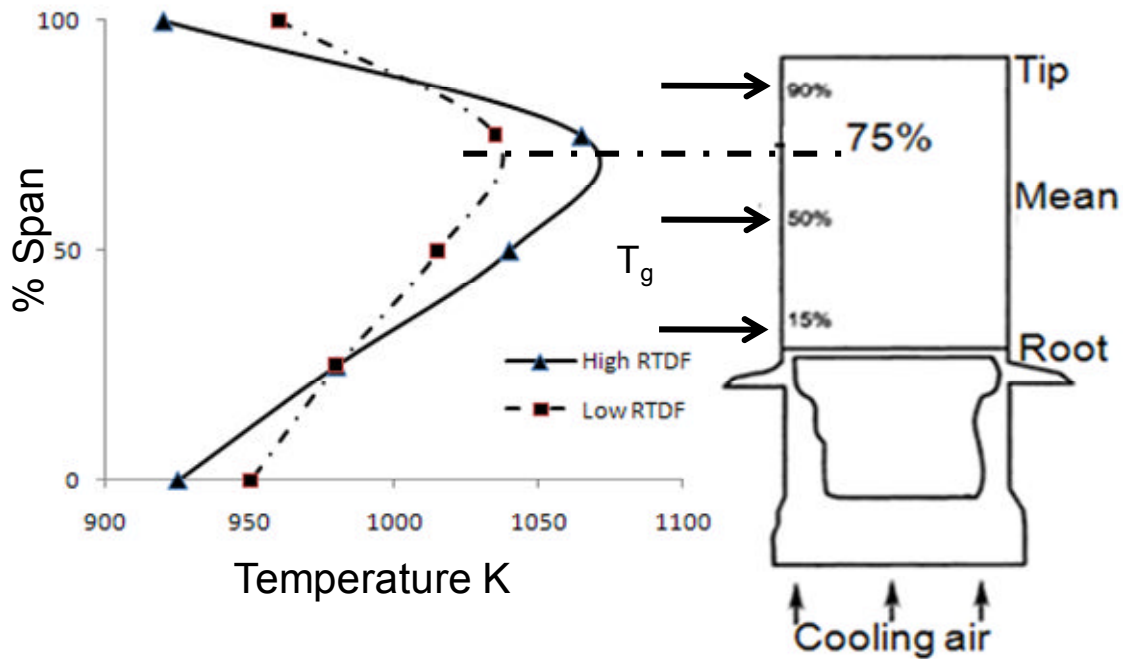


**Figure 6-5: Typical average radial temperature profile at inlet stage turbine rotor blade [169]**

Equation 6-23 was derived through extrapolation of several defined gas temperature points ( $T_{tip}$ ,  $T_{root}$ ,  $T_{75\%}$ ...etc.) along the blade. The assumptions used were: (i) the minimum gas temperatures will occur at the root and the tip of the blade, (ii) the reduction in gas temperature from the maximum temperature,  $T_{75\%}$  to the tip of the blade,  $T_{tip}$  is linear, (iii) the rise in gas temperature from the root,  $T_{root}$  to  $T_{75\%}$  is also linear, and (iv) the average of those defined

temperature points should equal to the rotor inlet temperature,  $T_{IN}$ . In the thermal model a mixing chamber is used in order to calculate the effect of mixing between the core flow and the coolant exiting the blade, as expressed in (chapter 5, Figure 5-5). From energy balance  $\sum m_{in}h_{in} = \sum m_{out}h_{out}$  with the inlet mass flow of the mixing chamber to be  $m_c$  and  $m_g$  and the outlet mass flow of the mixing chamber to be the sum of  $m_c$  and  $m_g$ . This will lead to the prediction of the inlet gas temperature of the rotor.

The values of the NGV metal and rotor inlet gas temperatures were calculated using Equation 6-24 [72].

$$T_{in} = \frac{m_g C_{p_g} T_{in(Be_f)} + m_{cNGV} C_{p_c} T_{CoNGV}}{(m_g + m_{cNGV}) C_{p_g}} \quad (6-24)$$

where  $m_g$  is the gas mass flow,  $C_{p_c}$  and  $C_{p_g}$  are the specific heats of the cold and hot gases respectively,  $T_{in(Be_f)}$  is the rotor inlet temperature before mixing,  $m_{cNGV}$  is the NGV coolant mass flow, and  $T_{CoNGV}$  is the NGV coolant exit temperature. In order to use Equation 6-24,  $T_{in(Be_f)}$  and  $T_{CoNGV}$  are calculated using Equation 6-25 and 6-26 [16]:

$$T_{in(Be_f)} = TET - \frac{m_{cNGV} C_{p_c}}{m_g C_{p_g}} (T_{CoNGV} - T_{cinNGV}) \quad (6-25)$$

$$T_{CoNGV} = T_{cinNGV} + \eta_{conNGV} (T_{NGV} - T_{cinNGV}) \quad (6-26)$$

where  $TET$  is the turbine entry temperature,  $T_{cinNGV}$  is the NGV inlet coolant temperature,  $\eta_{conNGV}$  is the NGV's convection efficiency and  $T_{NGV}$  is the NGV metal temperature. The  $\eta_{conNGV}$  and the  $T_{NGV}$  in Equation 6-24 are determined using Equation 6-27 and 6-28 [16]:

$$T_{NGV} = TET - \varepsilon_{(NGV)} (TET - T_{cinNGV}) \quad (6-27)$$

$$\eta_{conNGV} = \frac{\varepsilon_{(NGV)}}{m^*_{NGV} (1 - \varepsilon_{(NGV)})} \quad (6-28)$$

where  $T_{NGV}$  is the NGV metal temperature,  $\varepsilon_{(NGV)}$  is the NGV's cooling effectiveness assumed 0.6, and  $m^*_{NGV}$  is the NGV coolant non-dimensional mass flow which was assumed to be around  $1/2.5$  of the NGV total coolant mass percentage [5; 157]  $m^*_{NGV} = \frac{1}{2.5} \left( \frac{m_c}{m_g} \right)$ .

### 6.1.2.3 Hot Gas Reynolds Number

Reynolds number of the gas stream for each section of the blade can be expressed in terms of gas flow density, gas absolute velocity (see Appendix C), the blade chord and gas flow viscosity and can be calculated using Equation 6-29 [157]:

$$Re_{gSec} = \frac{\rho_{gsec} \times V_{Abs-gSec} \times C_{Sec}}{\mu_{gSec}} \quad (6-29)$$

The viscosity of the hot fluids was calculated using Sutherland's equation as a function of hot gas temperature [161]. Typical HP turbine values of  $Re_g$  are in the range 0.2-1.5E6, where gives  $St_g=0.0026-0.0062$  and El-Masri [158] assumed  $St_g=0.005$ (constant) to calculate the hot side heat transfer coefficient.

### 6.1.2.4 Stanton Number and Hot Side Heat Transfer Coefficient

The hot heat transfer coefficient ( $h_g$ ) undergoes strong spanwise and chordwise variation, determining its change in chordwise is much beyond the scope of this analysis. Since the  $h_g$  is variable along the flow path, appropriate correlation needs to be used to provide an average heat transfer coefficient at each blade section. For this a purpose a mean value for the gas side heat transfer coefficient  $h_g$  for each blade section can be obtained by calculating the external Stanton number. The external Stanton number is obtained from an empirical relationship for turbulent flow using Equation 6-30 [151]. Also, by neglecting the profile thickness, the blade row throat area can be obtained by using Equation 6-31 [6].

$$St_{gSec} = 0.285 Re_{gSec}^{-0.37} Pr_g^{-2/3} \quad (6-30)$$

$$A_g = \pi D_m H \cos\alpha_2 \quad (6-31)$$

Where the Prandtl Number, Pr for the hot stream is calculated using Equation 6-32:

$$Pr_g = \frac{\mu_g * Cp_g}{k_g} \quad (6-32)$$

The hot side heat transfer coefficient was calculated using Equation 6-33 [6] for each section of the blade, knowing the section Stanton number, specific heat of the gas, gas mass flow through the blade row and the throat section area. All the gas transport properties such as  $\rho$ ,  $\mu$ ,  $C_p$ ,  $\gamma$  and  $k$  were obtained using the multi regression analysis to develop a correlation for the purpose of interpolation as presented in chapter of humidity.

$$h_{gSec} = St_{gSec} \times Cp_g \left( \frac{m_g}{A_g} \right) \quad (6-33)$$

Also, the ratio between the total effective coolant heat transfer surface area and the total hot gas transfer surface area was defined using Equation 6-34 [1].

$$a_{cSec} = \frac{S_c}{S_{gSec}} = \frac{A_{cs}}{A_{gsSec}} \quad (6-34)$$

By knowing the external wetted perimeter for one blade and the height of each blade section, the wetted area of the hot side of the blade can be expressed by [1]:

$$A_{gsSec} = S_{gSec} \bar{H} \quad (6-35)$$

Where  $S_g$  is the hot side parameter =  $2.2 * \text{Chord}$ .

#### 6.1.2.5 Adiabatic Effectiveness

Thermal analysis for the film cooled blade will be the same as that for the convection cooled blade except that the  $T_g$  should be replaced by the  $T_f$  and the external hot-side coefficient  $h_g$  by the one valid in the presence of film cooling  $h_f$ , (in the absence of a correlation for  $h_f$ ). Rohsenow et al. [170] assumed  $h_g$  to be the same as that for the convection cooled blade. The adiabatic wall film temperature  $T_f$  is obtained from the adiabatic wall film effectiveness  $\eta_{ad}$  as

defined by using Equation 6-36 [171]. The  $T_{injSec}$  in this study was assumed equal to the  $T_{cinSec}$  since the air used to cool the blade internally by convection is used to provide the external film. The value of  $\eta_{ad}$  was calculated using means of the semiempirical correlation presented in [172], which suits the injection of film cooling air through a continuous slot over flat plate. However, it is common practice to assume that  $\eta_{ad}$  takes a constant value (0.2-0.5) in the determination of the film cooling temperature, Horlock and Torbidoni [18].

$$\eta_{ad} = \frac{T_{grSec} - T_{fSec}}{T_{grSec} - T_{injSec}} \quad (6-36)$$

The mean value of  $\eta_{ad}$  can be calculated by means of the semi-empirical correlation presented by Goldstein and haaji-sheikh, for the injection of the film cooling air through a continuous slot over flat plates.

#### 6.1.2.6 Thermal Barrier Coating and Wall Biot Numbers

The presence of a thermal barrier coating allows for a reduction in the heat exchange through the blade. Due to their low thermal conductivity, such metal create a barrier to the transfer of heat from the gas stream to the blade metal, thus reducing heat flux and cooling requirements. Also, the external TBC surface can operate at a higher temperature than the blade metal, thus reducing the convective external heat transfer. Biot number is the ratio of conductive resistance to convective resistance. Also, Biot number is looks very similar to Nusselt number but both are different. In Nusselt number,  $K$  is thermal conductivity of fluid where, in Biot it's of solid. The Biot number is a measure of the temperature drop in the blade material and the temperature drop between the material and the fluid. The blade and the TBC Biot numbers are defined by Equations 6-37 and 6-38 respectively. The range of the wall Biot number 0.3-0.8, where Torbidoni and Horlock adopted  $Bi_{bw}=0.25$  [14]. The inclusion of TBC into the cooling model is straightforward. It simply requires adding on more heat resistance to the gas coolant thermal model and the TBC external surface equation can be derived from the heat flux balance as shown in Equation 6-39 [6].

$$Bi_{bwSec} = \bar{h}_{gSec} \frac{t_{bw}}{k_{bw}} \quad (6-37)$$

$$Bi_{TBCSec} = \bar{h}_{gSec} \frac{t_{TBC}}{k_{TBC}} \quad (6-38)$$

$$T_{TBCSec(Ext)} = \frac{T_{cinSec} + \left( Bi_{TBCSec} + Bi_{bwSec} + \frac{h_{gSec}}{a_{cSec} * h_{cSec}} \right) T_{fSec}}{1 + Bi_{TBCSec} + Bi_{bwSec} + \frac{h_{gSec}}{(a_{cSec} * h_{cSec})}} \quad (6-39)$$

### 6.1.2.7 Blade Metal Temperatures

The gas side blade temperature is a very complex function of geometry and flow conditions. To reduce thermal stresses it would be desirable to maintain constant  $T_{bg}$  over the whole blade surface; however this can not be achieved because (i) strong chordwise variations of  $h_g$ , (ii) the blade metal hot side and coolant side temperatures and the coolant flow temperature reach their maximum values at the exit of the cooling channel. The temperature distribution through the blade wall states that, for every blade cross section, the metal temperature is higher on hot side than on the coolant side. Therefore, it is necessary to define the relationship between the distribution of the blade metal temperature  $T_{bg}$  and the distribution of the coolant flow temperature  $T_{co}$ . The blade metal temperatures, hot and cold sides, can be calculated using Equations 6-40 and 6-41 [1].

$$T_{bgSec} = \frac{(1 + Bi_{TBCSec})T_{cinSec} + \left( Bi_{bwSec} + \frac{h_{gSec}}{a_{cSec} * h_{cSec}} \right) T_{fSec}}{1 + Bi_{TBCSec} + Bi_{bwSec} + \frac{h_{gSec}}{(a_{cSec} * h_{cSec})}} \quad (6-40)$$

$$T_{bcSec} = \frac{(1 + Bi_{TBCSec} + Bi_{bwSec})T_{cinSec} + \left( \frac{h_{gSec}}{a_{cSec} * h_{cSec}} \right) T_{fSec}}{1 + Bi_{TBCSec} + Bi_{bwSec} + \frac{h_{gSec}}{(a_{cSec} * h_{cSec})}} \quad (6-41)$$

The outlet coolant gas temperature derived from the energy balance equation and Equation 6-42 is used in this paper. This coolant exit temperature will be used as the inlet temperature to the next section and used to calculate the exit coolant temperature of the next section. Cooling air at temperature  $T_{co}$  is

discharged into the mainstream through the holes in the blade surface to form a cooling film.

$$h_g S_g H (T_f - T_{bc}) = m_{bc} C_{p_c} (T_{co} - T_{in})$$

$$T_{coSec} = \frac{h_g S_g H}{m_{bc} C_{p_{cwSec}}} (T_f - T_{bc}) + T_{ci} \quad (6-42)$$

Blade metal temperature can be considered as the average of metal temperature gas side ( $T_{bg}$ ) and the metal temperature coolant side ( $T_{bc}$ ). Also, the blade metal temperature can be obtained using Equation 6-43, and in order to get  $T_b$  the blade cooling effectiveness should be calculated using Equation 6-44 [14]. The cooling effectiveness ( $\varepsilon$ ) can be determine by knowing inlet blade gas recovery temperature ( $T_{gr}$ ), the desired metal temperature gas side and inlet coolant temperature.

$$T_b = T_{grSec} - \varepsilon_{Sec} (T_{grSec} - T_{cinSec}) \quad (6-43)$$

$$\varepsilon_{Sec} = \frac{T_{grSec} - T_{bgSec}}{T_{grSec} - T_{cinSec}} \quad (6-44)$$

## 6.2 Creep model

The creep life of the blade at each section of interest can be obtained as a function of the blade section stress and the blade metal section temperature using the LMP approach (Equation 6-45) as presented in [72]. Because the maximum metal temperature of the blade and the maximum stresses may occur at different points on the blade span, the blade creep life will be different at each blade section. The lowest creep life of any individual blade section will be considered as the minimum blade life (the blade residual life).

$$LMP = 10^{-3} T (\log t_f + 20) \quad (6-45)$$

The reduction of the blade creep life is presented using a creep factor which measures the consumption of creep life relative to a specific operating condition defined by the end user. The creep factor ( $L_f/L_{fR}$ ) is defined as the ratio between



the actual residual creep life calculated at the corresponding operating condition and the reference residual life at a user defined condition.

### **6.3 Chapter Conclusions**

The cooling of high temperature gas turbines has been the subject of intensive work over the past few decades. There are three well known methods for the design the first stage of a HP turbine blade; un-cooled, convection cooled and film cooled

The determination of the rate of heat transfer from the turbine blade in a cross flow is important in hot section gas turbine life assessment. The rate of heat transfer is normally fixed by semi-empirical correlations expressing Nusselt number in terms of Reynolds and Prandtl numbers. The implementation of such correlations requires knowledge of fluid properties such as density, viscosity, thermal conductivity and specific heat. For gases these properties are normally available only for the dry state, thus the possible effect of the water vapour content of the gas has been overlooked

There has not been a great deal of work done to model the effect of humidity on the heat transfer and cooling processes of a HP turbine blade. The aim of this model is to investigate the influence of humidity on the turbine blade heat transfer and cooling processes which, in turn, affect blade creep life. The model is flexible and capable of assessing the main parameters that influence the blade cooling performance, such as cooling methods, alternative cooling fluids, blade geometry, heat transfer coefficients, gas properties and material and thermal barrier coating. The whole cooled blade row is regarded as a heat exchanger subjected to a mainstream hot gas flow from the combustion chamber.

The approach analysis is based on the relationship between the heat transfer coefficient of the blade and the effect of humidity which in turn determine the blade metal temperature. Thus, it will be possible to recognise the temperature distribution of the blade metal and the coolant flow. The limitations of using water or steam in the blade cooling process are more corrosive than air. Also,

there is probability of condensate that can locally compromise the blade cooling channel functionality.

The model presented here allows a very detailed analysis of blade cooling process includes the effect of cooling configuration and alternative fluids for convective/film cooling techniques.

## *Chapter seven*

### **7 FINITE ELEMENT MODELLING DESCRIPTION**

Abaqus is a commercially available suite of powerful simulation programs, based on the finite element (FE) method, which has the capabilities to solve engineering problems from relatively simple linear analysis to the most challenging nonlinear simulation [173; 174]. Abaqus has been shown to be useful in the investigation of structural problems, heat transfer and thermal stresses analysis. Abaqus CAE (complete Abaqus environment) used in this study allows for the creation of models, assignment of material properties to the geometries, and the application of loads and boundary conditions. Furthermore, options are provided on meshing the geometry and verifying results. Once the model is completed, Abaqus CAE can submit and control the analysis. Lastly, the Abaqus visualization module can be used to interpret the results. The FE analysis completed in this work has been carried out using three stage Abaqus, as shown in Figure 7-1. Namely; preprocessing (input file), simulation (output file) and postprocessing (visualization).

The FE model consists of two interrelated models. The thermal model calculates the temperature distribution in the blade, based on the heat input from the hot gas stream. The mechanical model calculates the stresses in the blade, caused by the externally applied load and the varying temperature distribution. The main objectives of the current study are to determine the blade metal temperature distribution, determine maximum stresses acting on the blade, determine the thermal stresses due to high temperature gradients in a 3-D HP turbine blade and changes in these parameters as a result of change of humidity on the heat transfer.

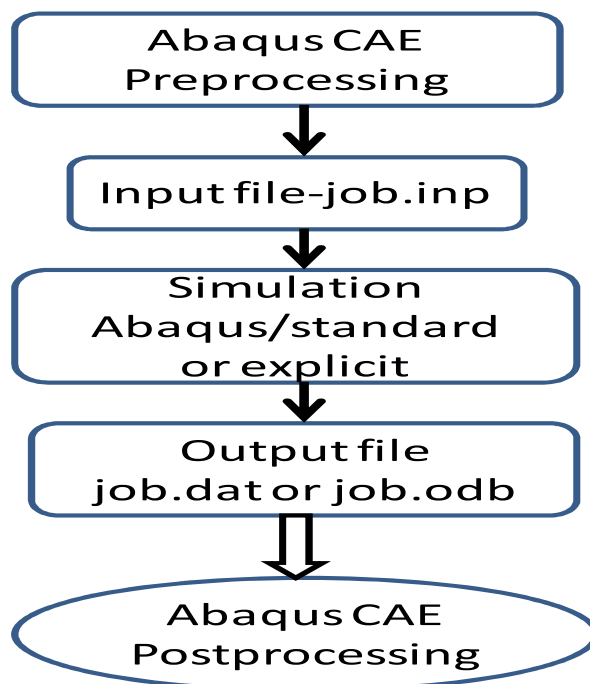


Figure 7-1: Abaqus three stages

## 7.1 Mechanical and Thermal Stress Modelling

In the gas turbine engine, stress develops on the HP turbine blade and disc due to the turbine operating at high rotational speeds and thermal gradients, there will also be pressure loads on the rotor blade. The HP turbine blade is subjected to a flow of hot pressurised gases which force the blade to rotate at a desired speed. In addition, the blade experiences centrifugal forces which impose stress, as well as a bending stress due to the gas pressure on the blade surfaces. Abaqus is used to conduct stress analysis based on the nodal temperature distributions obtained from the heat transfer model, the maximum engine rotational speed and gas pressure

### 7.1.1 Abaqus CATPart Module

This module allows the user to create the part to be investigated or import the geometry from other CAD programs. The first stage of the HP turbine blade study was to investigate the effect of WAR on the heat transfer coefficient and blade metal temperature using a 3-D FE model. The complex 3-D blade profile geometry was designed using CATIA V5R19 software. The CAD part file was saved as .CATPart in order to import in to the ABAQUS 6.9-3 FE software to

carry out the FE thermal and stress analysis. The internal blade cooling system, firtree and shroud also were created in the CATIA model and the boundary conditions of the coolant flow were applied in the Abaqus model. The blade dimensions presented in Table 7-1 were obtained from the blade sizing model in Chapter 3.

**Table 7-1: HP turbine blade dimensions**

	Value	Unit
<b>Height</b>	0.042	m
<b>Chord at mean</b>	0.027	m
<b>Blade mean diameter</b>	0.78	m
<b>Stager angle</b>	35.0	deg
<b>Air outlet angle <math>\alpha_2</math></b>	60.3	deg

The blade solid model was created using CATIA software shown in Figure 7-2, and the Abaqus FE model is shown in Figure 7-3. Internal ribs in the cooling channels and cooling holes have been removed to reduce the complexity of meshing the model. It is thought that the absence of these features would not significantly impact on the thermal and structural analyses.

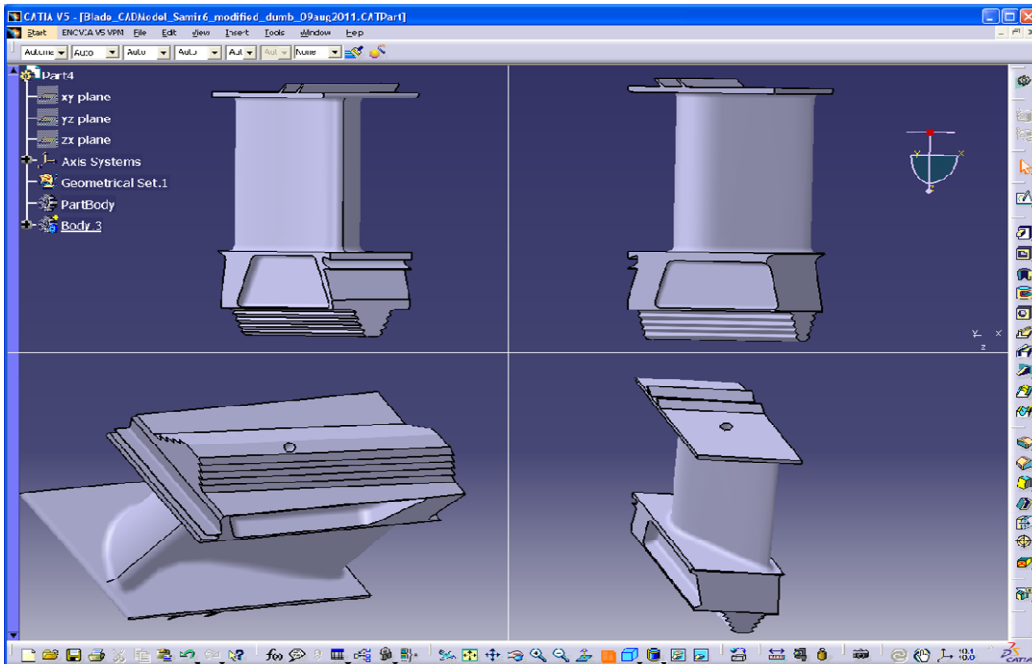


**Figure 7-2: Blade CAD model using CATIA software**

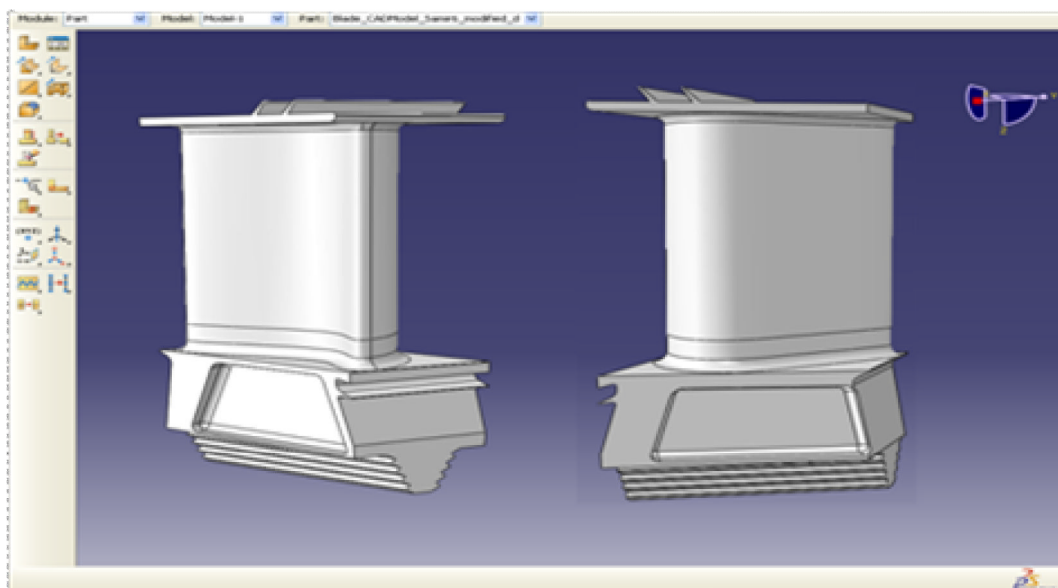


**Figure 7-3: Blade finite element model using Abaqus**

### **7.1.2 Property Module**

In the property module, the author specifies the following properties of the material(s) assigned to regions of the CAD part for the stress analysis:

- Young's modulus,
- Poisson's ratio,
- Density, and
- Thermal expansion coefficient.

An additional thermal conductivity is used as material property for conducting the thermal analysis. Isotropic materials were assumed in this study and elastic behaviour of the materials was also specified. Nimonic alloy was chosen as a valid representative of the material used for land-based HP turbine blades. The Young's modulus, Poisson's ratio and Expansion coefficient were specified as functions of temperature ranging from 20°C to 1200°C as shown in Figure 7-4 [175].

The blade model has two parts. The main part represents the whole blade, while the second part presents the contact surfaces of the shroud and root of the blade. The properties and geometries of the parts were specified by creating a solid homogeneous section for Section-1 (blade) as shown in Figure 7-5, and a membrane for Section-2 (shroud contact surface) as shown in Figure 7-6.

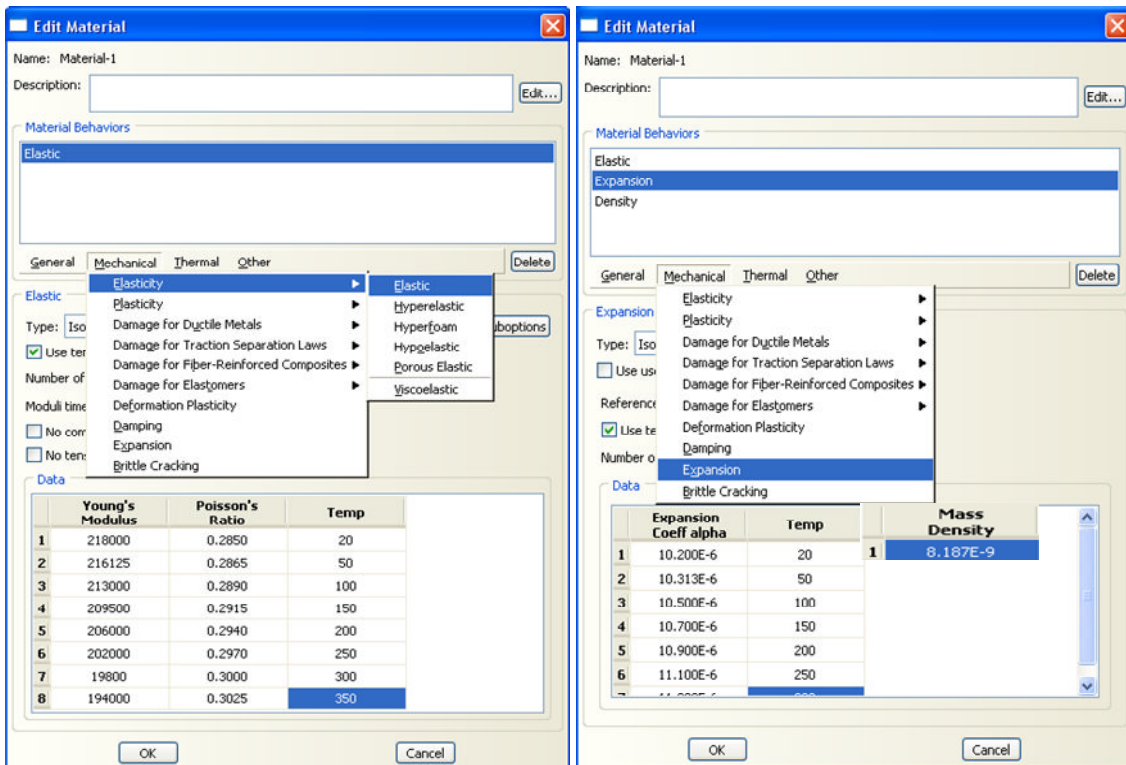


Figure 7-4: Young's modulus, Poisson's ratio, expansion coefficient and material density

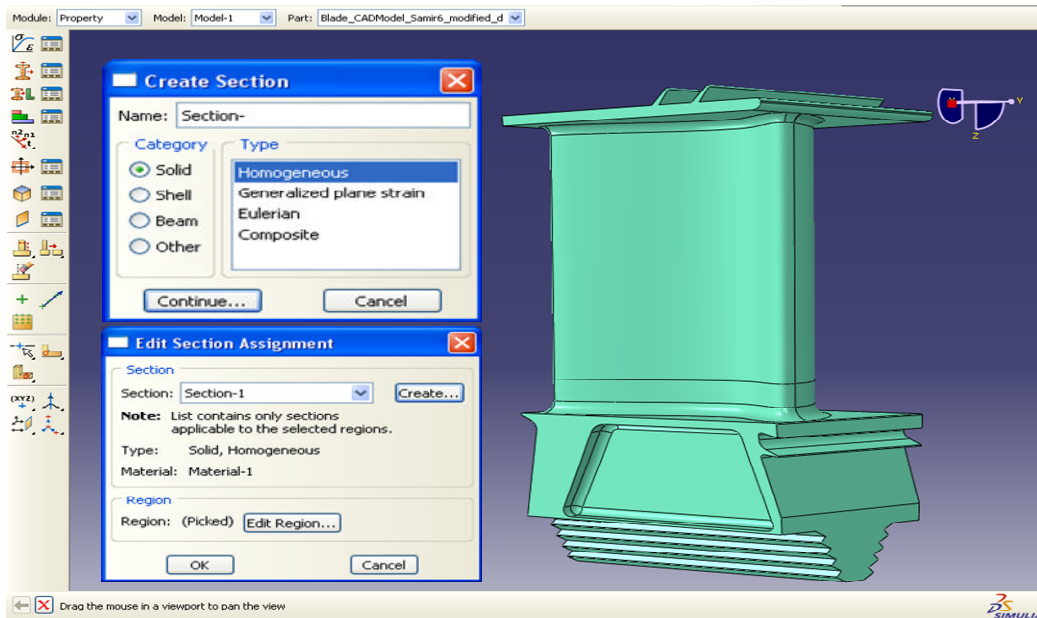


Figure 7-5: Section and section assignment for whole blade

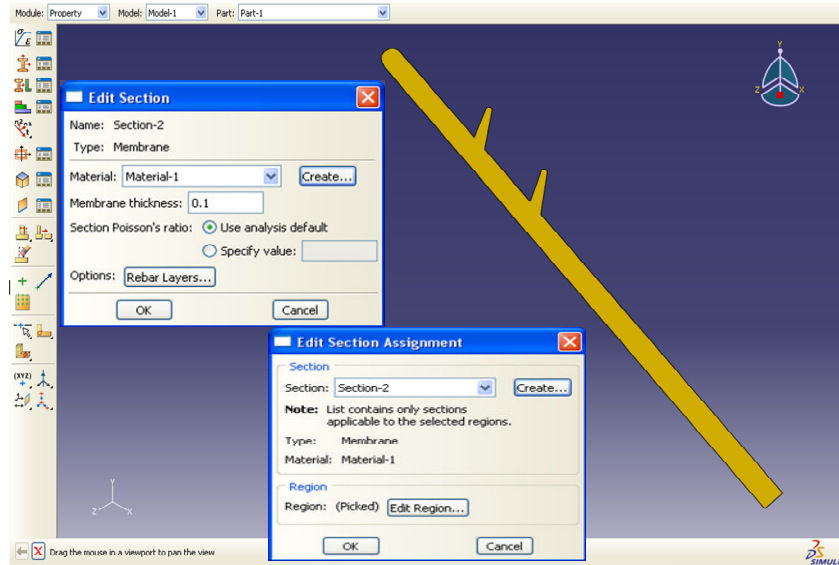


Figure 7-6: Section and section assignment for contact surfaces

### 7.1.3 Mesh module

The Mesh module allows the user to specify the mesh size and element type required for the analysis. A mesh convergence study was carried in this study to assess the right level of mesh to give acceptably accurate results for all cases, as shown in Figure 7-7. The mesh is said to be converged when further mesh refinement produces a negligible change in the solution.

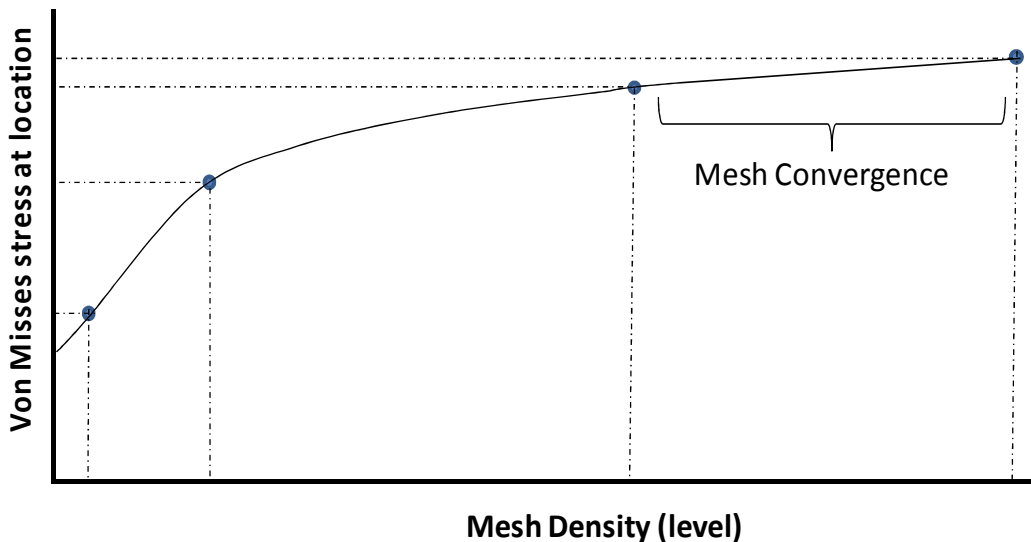


Figure 7-7: Point mesh convergence curve

Abaqus has an element library (e.g. solid, shell, beam, etc.,) which provides a complete geometric modelling capability. Also, elements can be combined to



create the model for the required analysis [173]. In this study, second order tetrahedral (C3D10: A 10-node quadratic tetrahedron) element for the blades was used as shown in Figure 7-8. The very flexible and useful free meshing technique was used for automatically generating the blade mesh on highly irregular geometrical shapes such as firtree and shroud. However, free meshing can result in elements of quality on relatively simple faces. Thus, the mapped meshing technique was used where appropriate to generate elements of high quality on such faces.

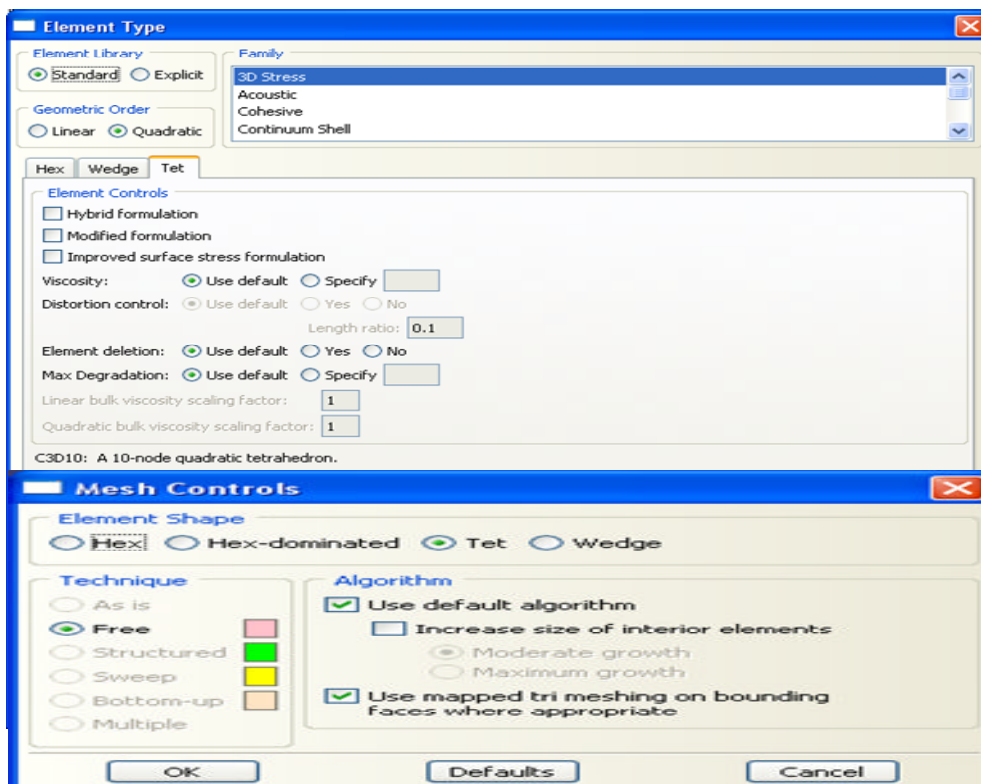


Figure 7-8: Element type and mesh control

The density of the mesh was specified by defining the number of seeds along the edges of the model as shown in Figure 7-9. In the global seed dialog box, the element size was specified as 1.9, the deviation factor as 0.025 and minimum size factor as 0.1. The curvature control allows for seed distribution based on the curvature of the edge, along with the target element size. Specifying a minimum size factor (fraction of the global seed size) prevents Abaqus CAE from creating very fine meshes in areas of high curvature but of little interest. A higher number of elements allows better modelling of the

interface conditions. In region where steep gradients in stress and strain are not expected, a small number of elements was used. The size and number of elements used were dependent upon the solution accuracy required and the computing time necessary for the analysis. The blade FE model consists of 93821 elements of quadratic tetrahedron, type C3D10.

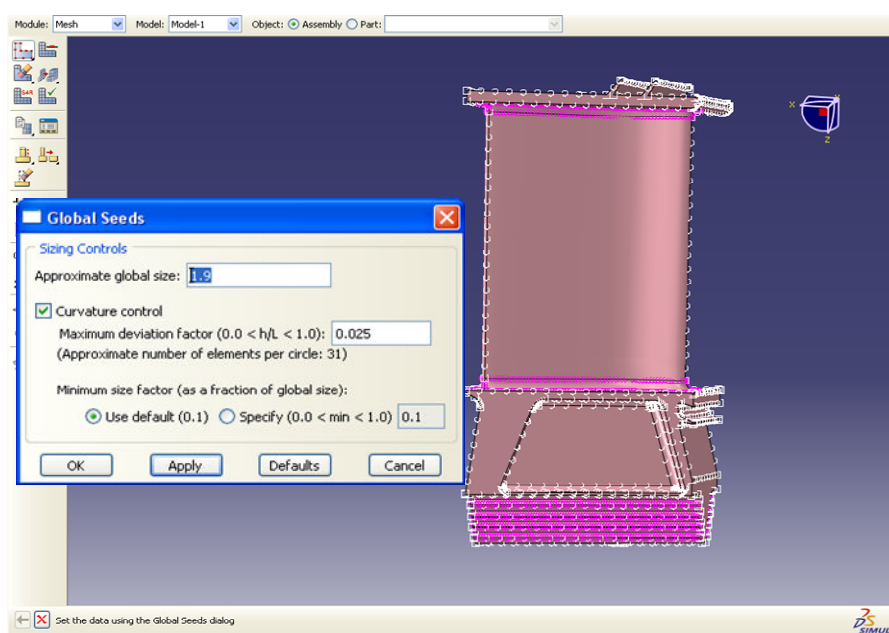


Figure 7-9: Geometry mesh density

#### 7.1.4 Assembly module

The parts were created in a particular coordinate system, and by using the Assembly module instances of the parts were created and positioned relative to each other in a global coordinate system to form the assembly. The dependent type of instance was selected in this model, thus when the user selects a mesh for the original part, Abaqus CAE applies the same mesh to the dependent instances. The advantage of dependent part instances are: i) change the mesh of the original part and Abaqus changes all dependent instances, ii) consumes fewer memory resources iii) the user needs to mesh the part only once.

#### 7.1.5 Step module

The Step module is used to create and configure analysis steps and the associated output of results. The step sequence captures changes in a model

such as variation in loading and boundary condition. Two steps were created in this study;

- Initial step created by Abaqus CAE at the beginning of the analysis
- Steady state operation step, where known load and boundary conditions were applied.

A static-general procedure was defined for the step as shown in Figure 7-10. The step sequence provides a convenient way to capture changes in the boundary conditions and the load applied for different cases. Since the displacements in the model due to the applied load are relatively small during the step, the nonlinear effect (Nlgeom-Off) was negligible.

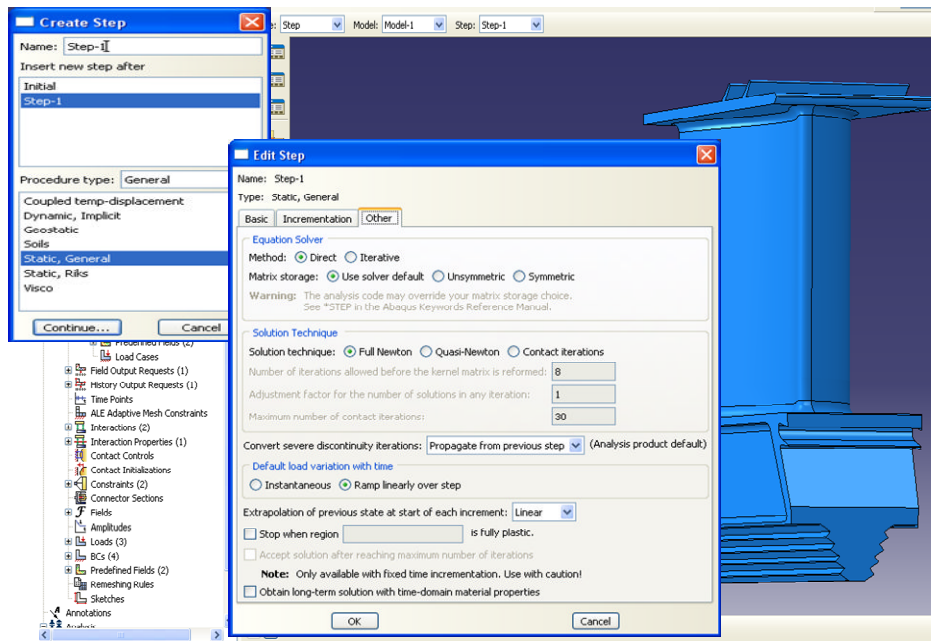


Figure 7-10: Specification of type of stress analysis in the step module

### 7.1.6 Interaction

Abaqus CAE does not recognize mechanical contact between part instances or regions of an assembly unless that contact is specified in the interaction module. In this blade model, the contact between the surfaces at the shroud of the blade with the adjacent blade shroud is defined as being one of small sliding (no friction) for steady state stress analysis as shown in Figure 7-11.

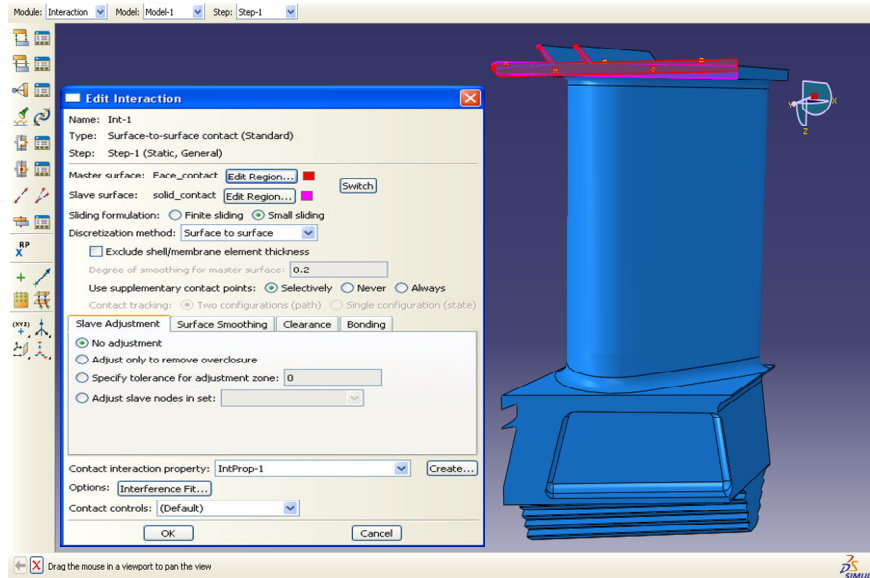


Figure 7-11: Surface to surface contact in the tip and root surface

Contact interaction property was specified for this analysis. This was defined by a tangential behaviour and penalty friction formulation in which the friction coefficient between the contacting surfaces was 0.2.

### 7.1.7 Constraints

The two contact surfaces were tied to simulate the cyclic-symmetry boundary condition. The master and slave surfaces were defined for the solid tip and face tip, before a surface-to-surface discretization method was selected, see Figure 7-12.

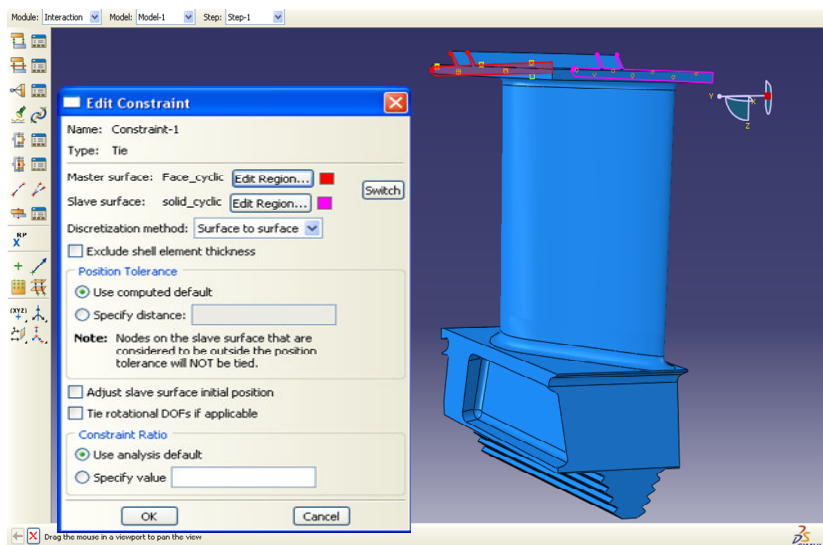


Figure 7-12: Tie constraint to the contacts using a surface to surface discretization method load

### 7.1.8 Load

In this module the load and boundary conditions applied on the blade were specified and implemented in the desired step analysis. The stresses in the gas turbine components were associated with; thermal expansion, rotation speed, and aerodynamic pressure load caused by the variation in pressure between the blade suction and pressure surfaces. The pressure loads were applied on the hot suction side and pressure side of the blade as shown in Figure 7-13. The pressure loads applied were distributed uniformly over both sides of the surfaces. In addition, the rotational (centrifugal) body force was applied on the blade in the radial direction using the angular velocity (radians/time) based on the axis of rotation as shown in Figure 7-13.

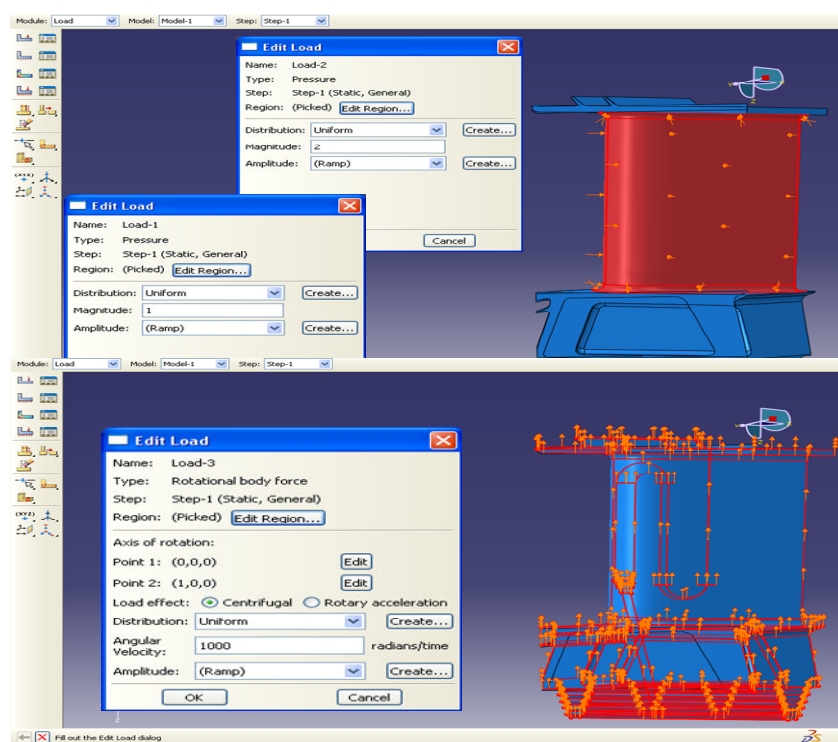


Figure 7-13: Pressure and centrifugal loads applied on the blade

### 7.1.9 Boundary conditions

A boundary condition should be specified in the step in which it is active, and applied to the desired region of the assembly. The analysis step, which activates the boundary condition and mechanical displacement/rotation specified, is selected in the create boundary condition dialog box.

The selection is dependent upon the type of analysis procedures to be performed. A coordinate system was created on the firtree of the blade so as to apply the boundary conditions appropriately. The contact faces of the firtree are restrained normal to the face. Two nodes on firtree on the leading edge side are restrained in the axial direction. Two nodes on firtree on the pressure side are restrained in the circumferential direction. The boundary conditions applied are shown in the Figures 7-14, 7-15 and 7-16.

An initial temperature of 20°C was applied to the model to enable the analysis to obtain easier convergence and give better results. Starting the analysis from 0°C is usually not recommended for high temperature analysis [173; 176]. The detailed steps of defining temperature fields are presented in Abaqus user's manual Section 16.

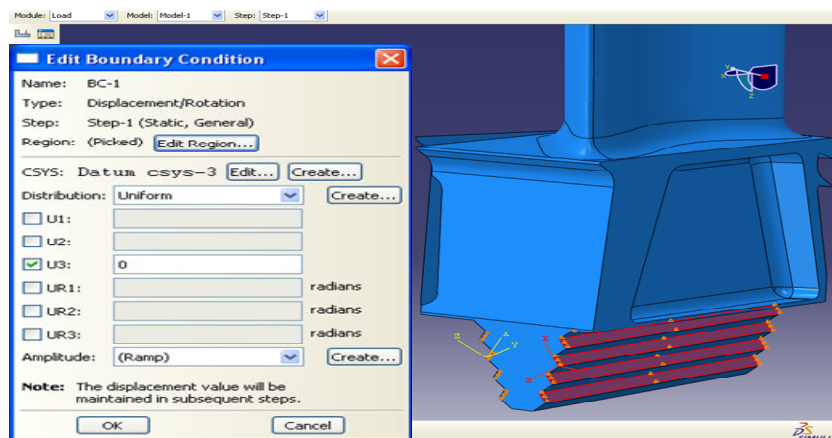


Figure 7-14: Firtree faces constrained normal to contact face

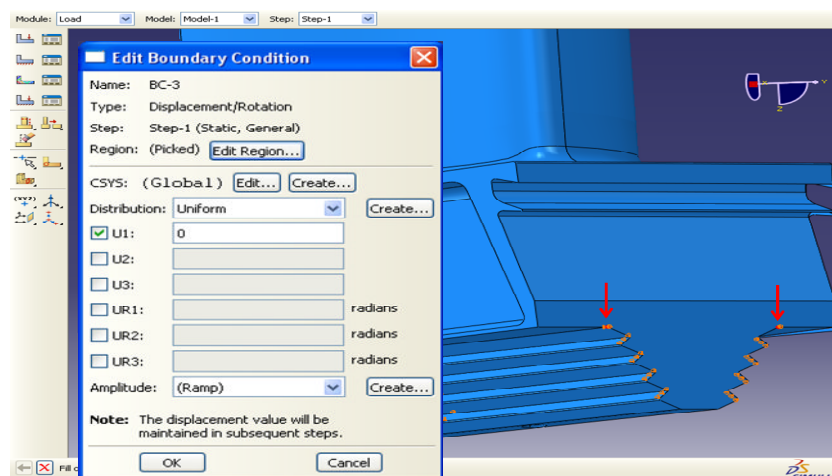


Figure 7-15: Firtree constrained – axial direction

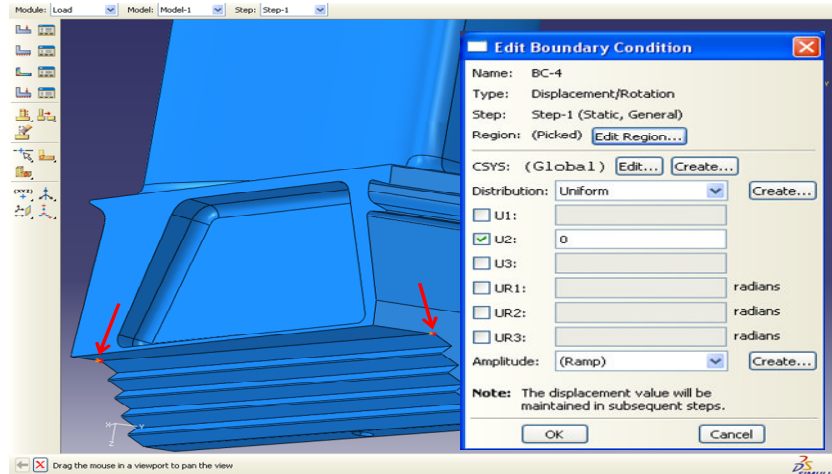


Figure 7-16: Firtree – restrained to circumferential direction

## 7.2 Thermal Modelling

The temperature distribution and thermal gradients across the blade geometry have significant effect on the overall stress in the HP turbine blade. Therefore, a detailed thermal analysis, together with the appropriate boundary conditions is necessary to calculate the blade metal temperature. A turbine entry temperature profile is used to specify the hot gas temperature at each section of the blade height. At these sections, the heat transfer coefficients were calculated based on the performance and aerodynamic data available using the methodology described in Chapter 6.

The results from the analytical heat transfer model (described in Chapter 6) were applied to the three-dimensional blade FE model as thermal boundary conditions. It was necessary to split the blade into a number of sections at various heights, where the corresponding hot gas temperature and heat transfer coefficients were used as boundary conditions as shown in Figure 7-17. A similar methodology was adopted for modelling the blade internal cooling channels, using the HP compressor exit temperature together with the calculated heat transfer coefficients. It is noteworthy that a heat pick-up rate was used as the cooling flow travels along the internal channels, as depicted in Figure 7-18. This model provides a simple and less computationally expensive process that offsets the loss in accuracy, when compared to a CFD analysis.

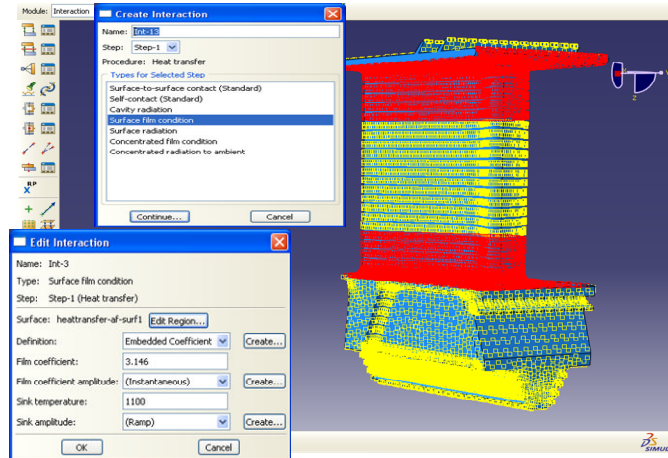


Figure 7-17: FE Hot temperature and hot heat gas transfer coefficient

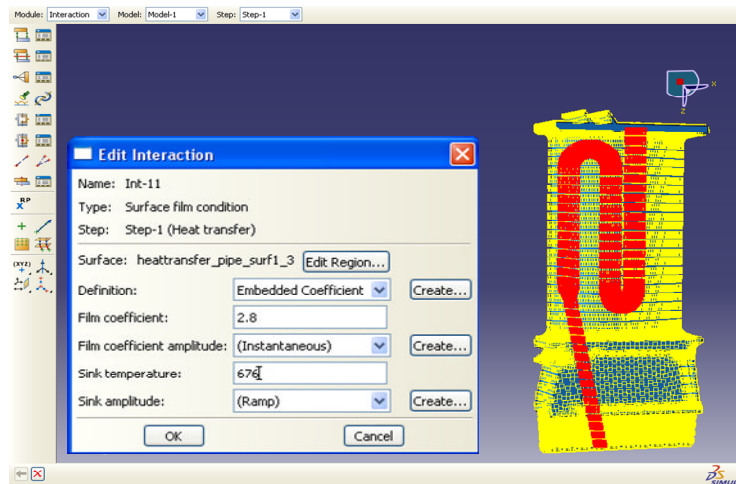


Figure 7-18: FE Coolant air temperature and coolant heat transfer coefficient

### 7.3 Chapter Conclusions

A detailed description of the procedures adopted to carry out the FE analysis of the 3-D HP turbine blade has been presented in sequence using Abaqus software as a simulation program. The blade geometry was imported into Abaqus where the pre-processor tool was used to generate a FE model which consists of the thermal and mechanical sub-models.

Careful consideration was taken when setting the thermal boundary conditions as these have a major effect in determining the blade overall stresses. The radial temperature profile describing the turbine entry temperature at each blade height section together with an analytically calculated heat transfer coefficient was used as external thermal boundary conditions. In addition a representation of the internal cooling flow with the effect of heat pick-up was described.



Engineering judgement was also necessary when setting up the locations for restraining the blade in the axial and circumferential directions together with several surface-to-surface contacts at the root and tip of the blade. Furthermore, a mesh dependency investigation was carried out in order to select a suitable mesh size to produce acceptable results for all cases considered.

The applied pressure loads were set uniformly on the pressure and suction surfaces of the blade. It is recommended to run a three-dimensional CFD simulation to achieve representative 3-D flow behaviour of the aerodynamic parameters such as temperature, pressure and heat transfer coefficient distributions around the blade.



## *Chapter eight*

### **8 FINITE ELEMENT RESULTS**

It is the lengths of exposure times and variations in the stresses and temperatures experienced that are the major factors in shortening the lives of the hot section components of stationary gas turbine. It is necessary to calculate the maximum stress and metal temperature at each point over the blade for use in the creep life calculation. However, there will be thermal stresses in the blade as result of the temperature gradient between the hot side and cooled side which need to be considered in the creep life assessment. 3-D analysis is usually focused on a critical location or critical feature rather than the whole blade. The FE model was used to run a linear static analysis to solve different loading cases; mechanical loads (rotation and gas pressure load), thermal load (heat transfer) and combination of thermal and mechanical load (thermal stress).

This model is used for general lifetime assessment of the blade except shroud and firtree. Due to simplified modelling of the blade – to – blade contact and relatively coarse mesh in the firtree notches, the stress field around the firtree grooves and contact faces was not accurate enough and a special model was needed for shroud/firtree assessment

#### **8.1 Mechanical stresses**

The inner and outer regions of the blade, known as the firtree and the shroud (these regions have limited cooling), create the inner and outer annuli of the gas path and require creep life assessment. In this case the area of interest is only the blade airfoil surface where the stresses are considered jointly with the blade metal temperature to calculate the blade creep life. The stress field around the firtree grooves and contact faces is not accurate enough and thus a special model is needed to assess the life in this area.

The mechanical stresses on the blade were calculated at one operating point for different relative rotational speeds (PCN=1-0.94) to identify the maximum stresses over the first stage HP turbine blade. However, the changes of the PCN result from change in the WAR which in turn changes the compressor inlet mass flow. Abaqus software was used and the blade FE model consists of 93821 modified quadratic tetrahedron elements, type C3D10. The model was first used to calculate the mechanical stresses, using the Turbomatch and analytical results as input data. The loads and boundary conditions used in these analyses are described in the previous chapter. Both the gas loads and centrifugal loads due to the rotational speed of the blade (by defining the angular velocity) were considered in this study.

Figures 8-1 (a, b, c and d) show the equivalent Von Mises stress distribution of first stage HP turbine blade at different operating points (PCN=1, 0.98, 0.94 and 0.92). Figure 8-1 (a) shows the stress distribution along the blade as result of centrifugal force due to blade rotation at PCN=1 (typical of maximum operating condition) with maximum stress at the blade root. However, comparatively large equivalent stress was also observed at the blade root, around the cooling channel and near the curvature of the blade root and shroud. The blade turbine was subjected to tensile stresses due to centrifugal forces (high at the blade root) as well as bending stresses (at middle of the blade) due to the gas pressure.

Centrifugal stresses show the major contribution close to the blade root. Gas bending stresses become more relevant close to the blade tip and near the blade cooling channel. The stresses at that locations were reduced as the engine operating point changed and the PCN reduced as shown in Figures 8-1 (b, c and d). Table 8-1 shows the von Mises stresses at different critical location (I=LE fillet, II=mid 40% span and III= tip 80% span) on the blade airfoil for different PCN. These are critical locations (nodes 7837, 8899 and 9682) due to the design for blade cooling such as root curvature, coolant channel(s) and blade wall thickness. In all cases the mechanical stress was decreased as the engine rotational speed reduced, due to reduction in the centrifugal force and

gas load at each blade section. Turbine blade creep damage usually occurs close to the blade midspan, thus, thermal stress and gas bending stress should be considered.

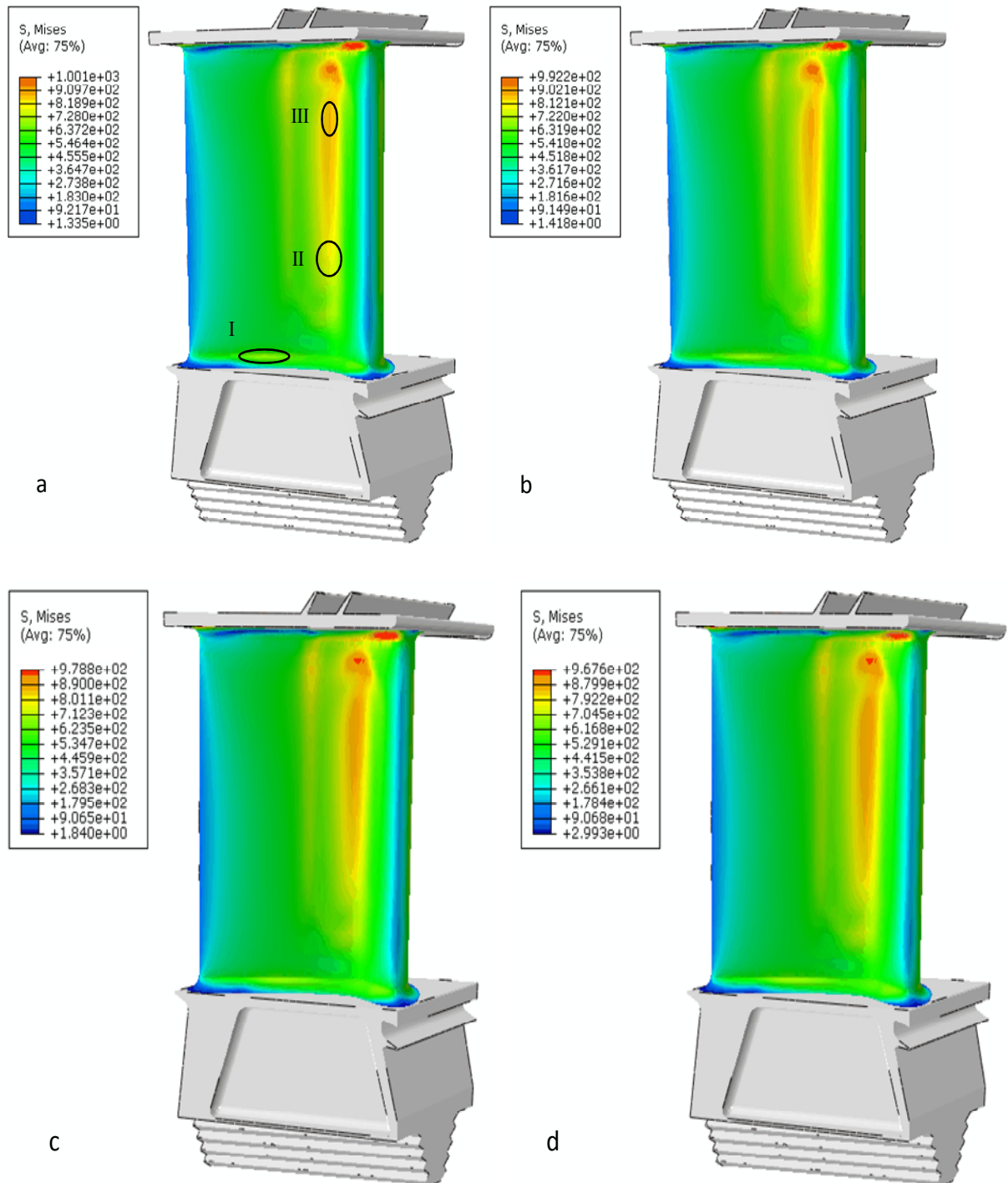


Figure 8-1: Von Mises stress at PCN=1 (a), 0.98 (b), PCN=0.94 (c) and PCN=0.92 (d)

**Table 8-1: Lifting limiting factor-mechanical stresses**

	Life-limiting Locations (nodes)		
	I (7837)	II (8899)	III (9682)
PCN	MPa	MPa	MPa
<b>1</b>	698	793	784
<b>0.98</b>	694	787	779
<b>0.94</b>	650	770	760
<b>0.92</b>	646	764	755

## 8.2 Heat transfer analysis

The thermal model is similar to the structural model but has a single degree of freedom at each node, the temperature. In order to perform the heat transfer analysis of HP turbine blade, it was necessary to evaluate the gas path temperature (TET profile “RTDF=0.8” Figure 6-5) and heat transfer coefficient along the blade airfoil. Therefore, an analytical model was developed using detailed airfoil geometry data, operating parameters and engine performance data obtained from Turbomatch performance software. The results of the analytical model ( $T_g$ -  $h_g$ - $T_{cin}$  and  $h_c$ ) were used as inputs to the FE heat transfer model. The heat transfer coefficient was calculated at various bulk temperatures and as function of change in the gas properties for input into a FE analysis as a variable. Thus, the internal and external heat rates (convection) will vary based on the temperature of the surface of the blade airfoil coolant side and hot side as well as the heat pickup (coolant Cp values) and the flow rate of the cooling air as it passes through the cooling channel.

The first stage of HP turbine blade 3-D temperature distribution is calculated due to the combined effects of the relative external gas temperatures, the RTDF profile, film cooling temperature, TBC and the internal cooling process. First stage HP turbine blade 3-D model of the whole blade is shown in Figure 8-2. This model could thermally expand without constraint and some nodes were constrained to prevent rigid body displacement.

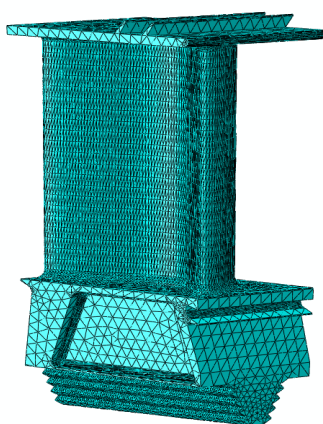


**Figure 8-2: HP turbine blade 3-D finite element model**

It is considered that the gas stream and cooling air temperature and heat transfer coefficient could change as the operating conditions of the gas turbine change in certain ranges and even in steady state operation. In this study, the cooling air temperature and heat transfer coefficient are considered to change at one operating point by change in the WAR in the compressor inlet. Cooling air extracted from the compressor in the gas turbine engine was design to be 7.5% of compressed air in the high pressure turbine and to be supplied to two stages of blades. The flux of cooling air of the first stage of HP turbine was 75% of the extracted air coolant (7.5%) from the compressor. The temperature of the cooling air increased while the air passed through the cooling hole from the bottom to the top.

The steady state temperature distributions along the blade span (pressure side) at different WAR are shown in Figures 8-3 to 8-6 for TET = 1480K. As the WAR increased the blade metal temperature reduced. The figures show that maximum metal temperatures of 980K, 973K, 967K and 964K respectively for WAR = 0.0, 0.04, 0.08 and 0.1. It is evident that the blade LE and mid-airfoil section (60-75% blade span) is the hottest location on the blade surface and that is where the turbine blade creep damage usually occurs. Thermal stress need to be considered in order to calculate the right blade creep life.

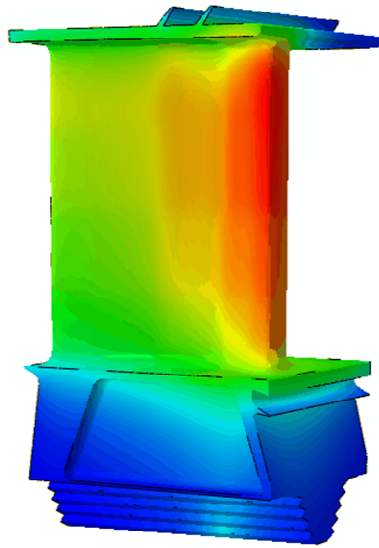
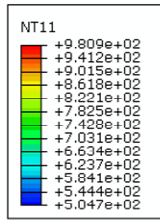


Figure 8-3: TET 1480K and WAR=0.0

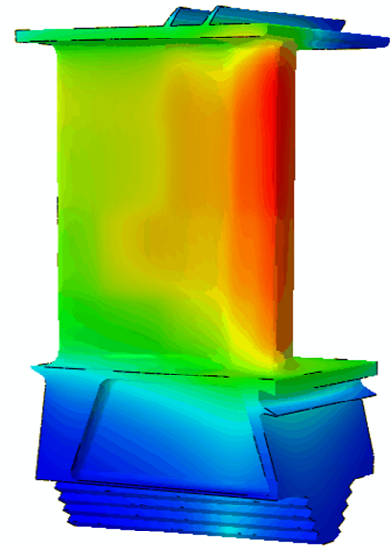
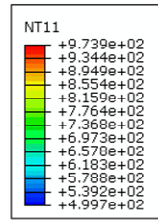


Figure 8-4: TET 1480K and WAR=0.04

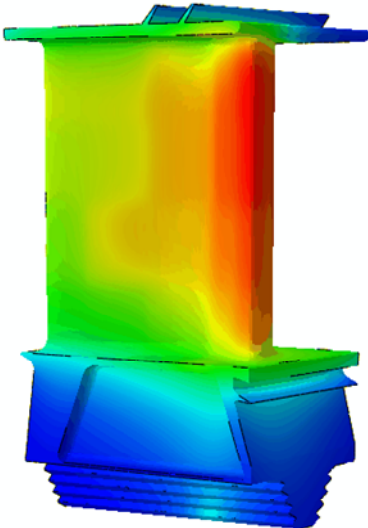
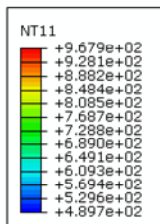


Figure 8-5: TET 1480K and WAR=0.08

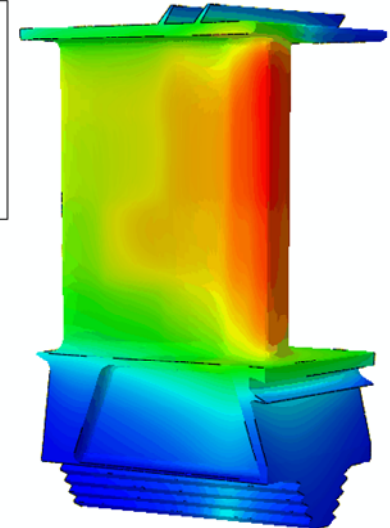
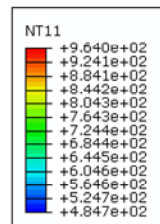


Figure 8-6: TET 1480K and WAR=0.1

From the above results it is seen that the temperature difference between leading edge (LE) and trailing edge (TE) at the blade mean on the pressure side of the blade profile, changes from 964K to 824K to 935K to 805K for WAR = 0.0 and 0.1 respectively. The variation of the blade metal temperature is almost linear from the LE to the TE of the blade. Figure 8-7 shows the blade metal temperature distribution along the chord wise at different blade sections (Root-Mean-Tip), for WAR=0.0 and 1.0. Considerable there is no change in the gas



temperature trend (temperature slope) for the dry and humid air, however, the temperature was dropped when the air is humid (WAR=0.1).

Figure 8-8 contrasts the temperatures of the blade coolant side and hot side along the blade span for WAR=0.0 (dry) and WAR=0.1. It is clear that the temperature increases from root to tip (reaching a maximum near the blade tip). The temperature distribution across any chordwise section occurs because it is relatively difficult to cool the LE and TE as effectively as the mid-chord area of the blade. As the WAR increased the blade metal temperature was reduced at each blade section, because of the increase in the  $C_{p_c}$  which in turn increased the heat transfer coefficient of the coolant air. As the  $C_p$  of the coolant air increased more heat was required to increase the coolant air temperature by 1K. The metal temperature of the coolant side (channel) for WAR=0.0 (dry) and WAR=0.1 at the blade root were 795K and 784K respectively. Whereas, at the hot side for the same WAR values it was 858K (dry) and 850K (WAR=0.1). At the blade tip, the blade metal temperature for the coolant side at WAR=0.0 was 945K, and at WAR=0.1 was 920K, and for the hot side were 982K and 964K respectively.

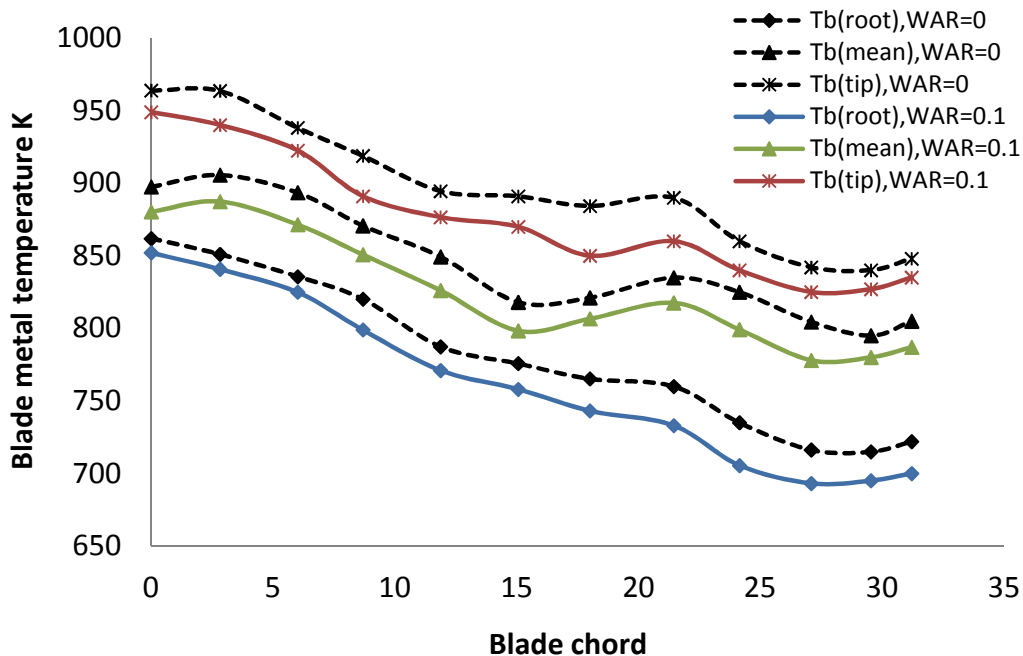
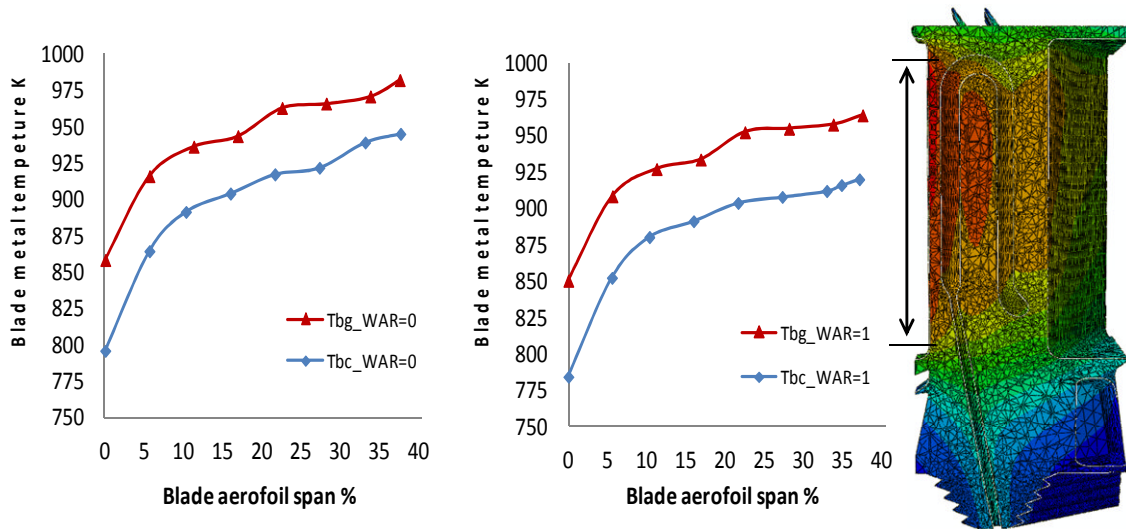


Figure 8-7: Blade metal distribution across the chord wise of the blade at root, mean and tip for different WAR=0.0 (dry) and 0.1



**Figure 8-8: Blade metal distribution on the coolant and hot side of the blade airfoil for WAR=0.0 (dry) and 0.1**

The internal heat transfer coefficient depends strongly on the internal surface, coolant fluid (gas properties) and internal coolant design (coolant configuration). In order to investigate the effect of advanced cooling schemes and coolant heat transfer coefficient ( $h_c$ ) on the blade metal temperature, three different values of  $h_c$  (1000, 2000 and 3000 W/m<sup>2</sup>K) were applied on the internal cooling channel with one air coolant temperature,  $T_{cin}=762$  for operating point main stream gas temperature,  $T_g=1510$ K as presented in Figure 8-9. On a cross-sectional view one can see the internal cooling channel and wall thicknesses. The maximum blade metal temperature on the LE dropped from 1014K for  $h_c=1000$  W/m<sup>2</sup>K to 988K for  $h_c=3000$  W/m<sup>2</sup>K. Also, the contour plots are on different scales which represent the details of the temperature distribution for different coolant schema and  $h_c$ . In all cases the peak temperature are found on the surface of the pressure and section side near to the blade LE, and temperature distribution through the wall thickness is seen on the cross-section view.

Design modification to the HP turbine blade to meet the life could include a reduction in the gas temperature ( $T_g$ ) or increase the internal cooling. The change in the internal cooling can be effected by changing the cooling schemes, including TBC, film cooling, using turbulent air, etc. This study shows that using humid air improves the cooling process by increases the  $Cp_c$  and  $h_c$  which in turn reduce the blade metal temperature and improve the blade creep

life. Knowing the metal temperature and stress at any point on the 3-D blade model, the creep life can be predicted, and the locations of the minimum creep life identified, which in this case is near the blade LE and near the blade coolant channel as well as some areas close to the blade TE and root fillet.

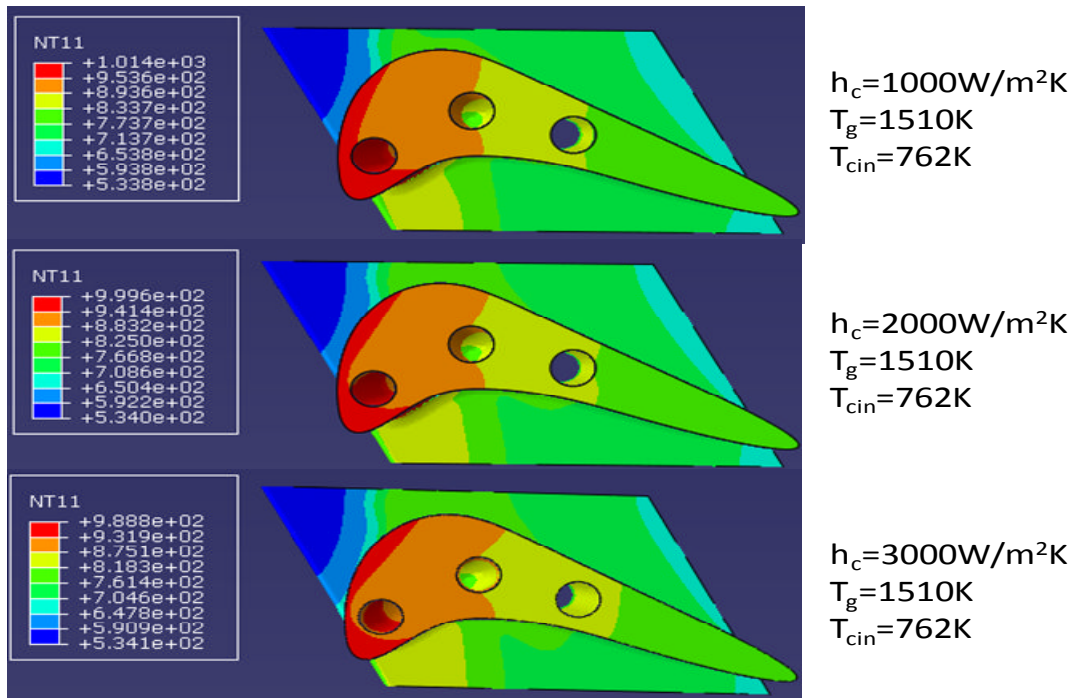


Figure 8-9: Cross-sectional blade metal temperature K distribution for different coolants ( $h_c=1000, 2000$  and  $3000\text{ W/m}^2\text{K}$ )

### 8.3 Thermal stress analysis

The FE model calculates the thermal-mechanical stresses using the nodal temperature distributions and the maximum engine rotational speed as boundary conditions. The von Mises stresses combined thermal stresses (resulting from the temperature gradient) and structural loading (centrifugal stress and pressure load) for change in the WAR from 0.0 to 0.1 as shown in Figures 8-10 to 8-13. These stresses reach quite high levels at the coolant regions of the blade. The results of the thermal model (temperature distribution as shown in Figures 8-3 to 8-6) were used as inputs in the thermal-stress model. This shows that significant variations in temperature occur as result of change in the WAR which led to high thermal-stress near the coolant area. Tensile stress occurred around the cooling channel (cooling holes) and compressive stress occurred on the blade surface. This is because the smaller

thermal expansion around the cooling channel suppressed the larger thermal expansion near the blade surface. The minimum thermal stress at locations near the coolant channel for WAR=0.0, 0.04, 0.08 and 0.1 were 548, 538, 530 and 528 MPa respectively. However, the maximum thermal stress at the same area for the same WAR values were 905 to 873 MPa as shown in Figures 8-10 to 8-13.

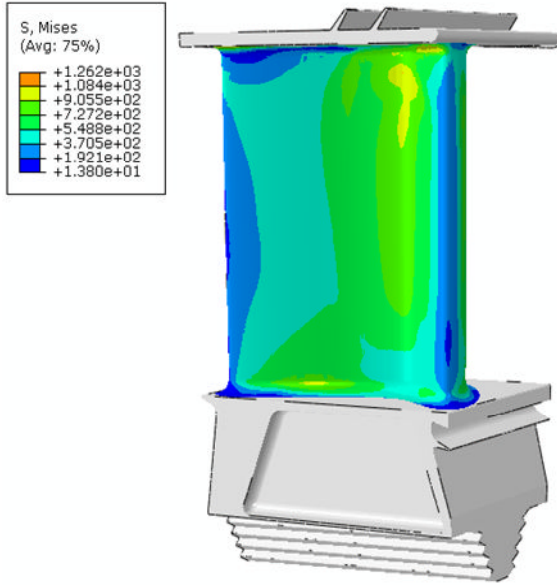


Figure 8-10: Thermal stress (Von Mises) for WAR=0.0

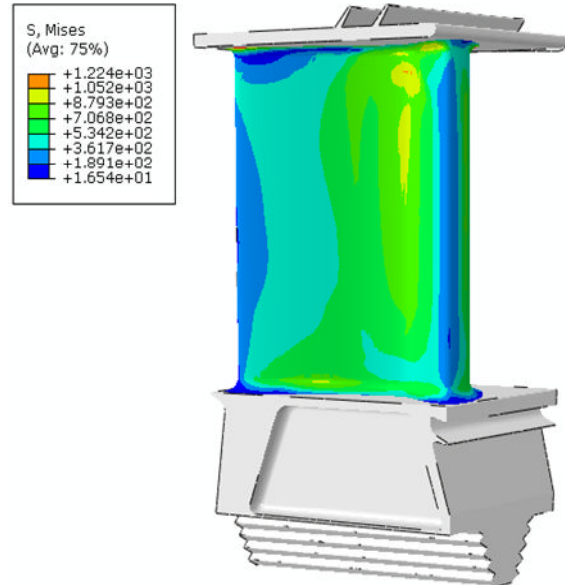


Figure 8-11: Thermal stress (Von Mises) for WAR=0.04

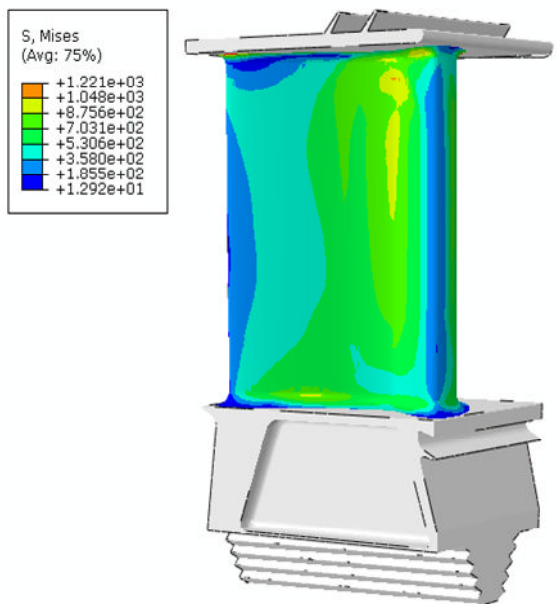


Figure 8-12: Thermal stress (Von Mises) for WAR=0.08

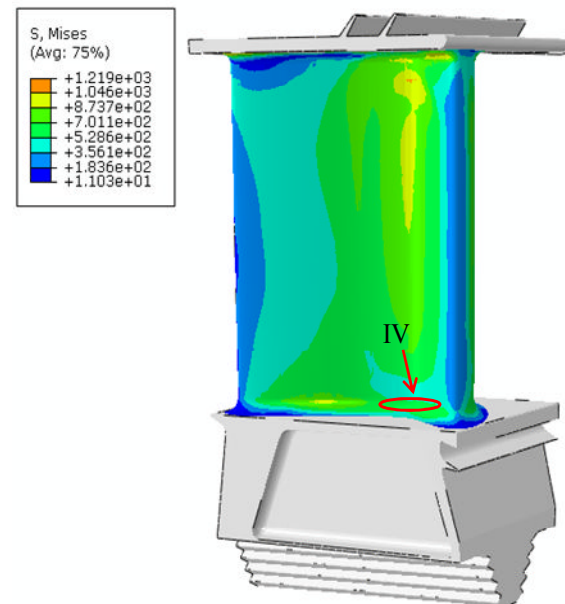


Figure 8-13: Thermal stress (Von Mises) for WAR=0.1

The modulus and thermal expansion coefficient are approximately 150 GPa and  $16.200E-06$  1/K respectively, thus a temperature gradient of 973K at one location results in a stress gradient of 675 MPa which is in agreement with the contour plots at location IV (580 to 670 MPa) as shown in Figure 8-13.

The increase in the coefficient of thermal expansion with temperature means the effects of temperature gradients at high temperatures become more pronounced. The primary loading experienced by the blade section is the centrifugal force based on the rotating mass of the blade, in addition is the thermal loading and the stress caused by the temperature gradient.

The linear FE predicted that none of the blade airfoil regions had undergone any plastic deformation under the loading conditions investigated. Also, the stress distribution was generally quite uniform along the airfoil although, as expected, higher stresses were prevalent in some critical area such as blade root, curvature and near the blade cooling channel.

In the blade situation, the root and tip of the blade will see lower temperatures based on the main stream gas temperature profile. From the results, the stresses in the hotter LE and TE are reduced, resulting in a lower creep life consumption, while the stress in the mid span result in a higher creep rate. It should be noted that the elastic stress throughout the blade resulting from the centrifugal stress varies with the temperature dependence of the modulus of elasticity of the material. It thus appears that fatigue damage is more dominant on the blade LE, and creep damage is most severe on the mid-span of the blade on the pressure side

The blade thermal stress (Von Mises stress) variation at three particular locations, nodes 7682 (root), 9169 (mean) and 9758 (tip) along the blade LE is presented in Figure 8-14. As the WAR increased and the blade metal temperature dropped, it is clear from the results that the thermal stress was reduced at the three nodes along the blade span. The thermal stress at the root (node 7682) for WAR=0.0 was 624 MPa and this dropped to 555 MPa for WAR=0.1. For the blade mid-span (node 9169) the thermal stress was 460MPa at WAR=0.0 and this dropped to 406 MPa at WAR=0.1. The thermal stress at

the blade tip (node 9758) was reduced from 330MPa (dry) to 303MPa (WAR=0.1) as shown in Figure 8-14. Since the engine rotational speed was fixed in this case (PCN=0.97), the thermal stresses produce at the three nodes were as a result of the temperature gradient and not as function of combination of the pressure force and centrifugal stress.

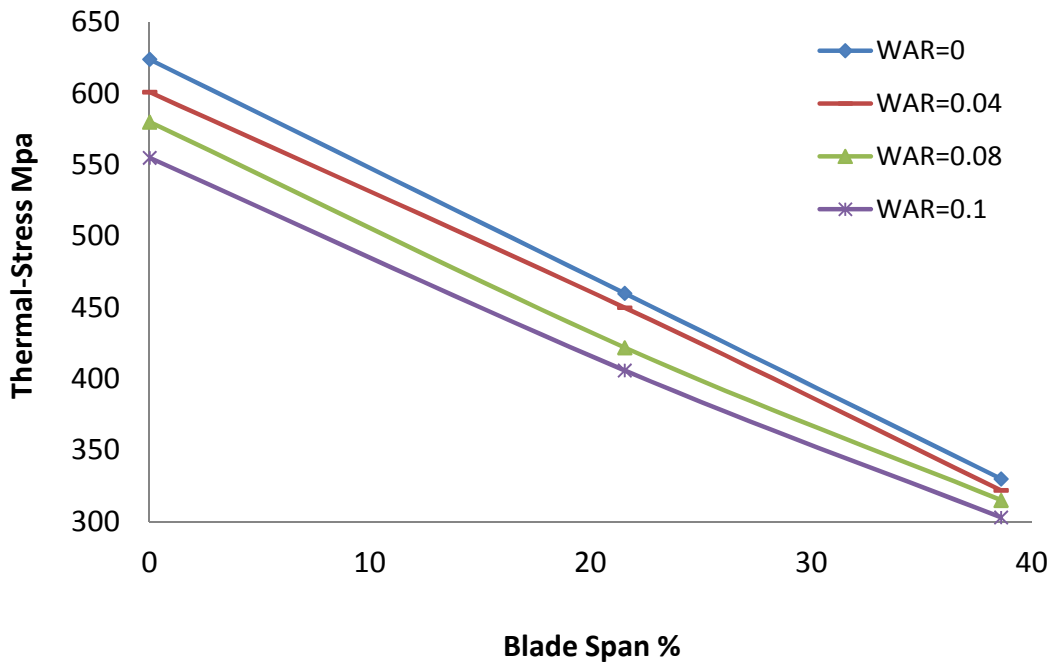


**Figure 8-14: Thermal-stress at the blade LE, nodes 7682 (Root), 9169 (Mean) and 9758 (Tip) for different WAR**

The thermal stresses along the blade chord on the pressure side (25% blade span) for different WAR are shown in Figure 8-15. The results show that the highest thermal stress occurred at a distance of 10% through the blade chord where the first coolant channel is located. The thermal stress was high in that area because of the difference between the coolant air and gas temperatures is quite high compared to other locations. However, the thermal stress was reduced as the WAR increased from WAR=0.0 (dry air) to WAR=1.0 as shown in Figure 8-16. The thermal stresses at the blade LE and TE were low and similar since there is no coolant in that area, and the effect of WAR and temperature gradient very small as shown in Figures 8-3 to 8-6.

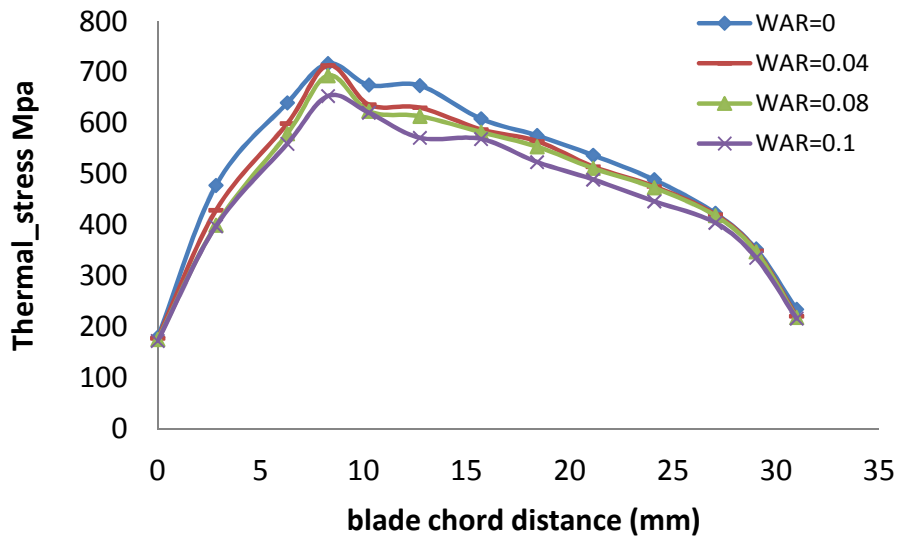


Figure 8-15: Thermal stress on the blade chord (25% blade span) at different WAR

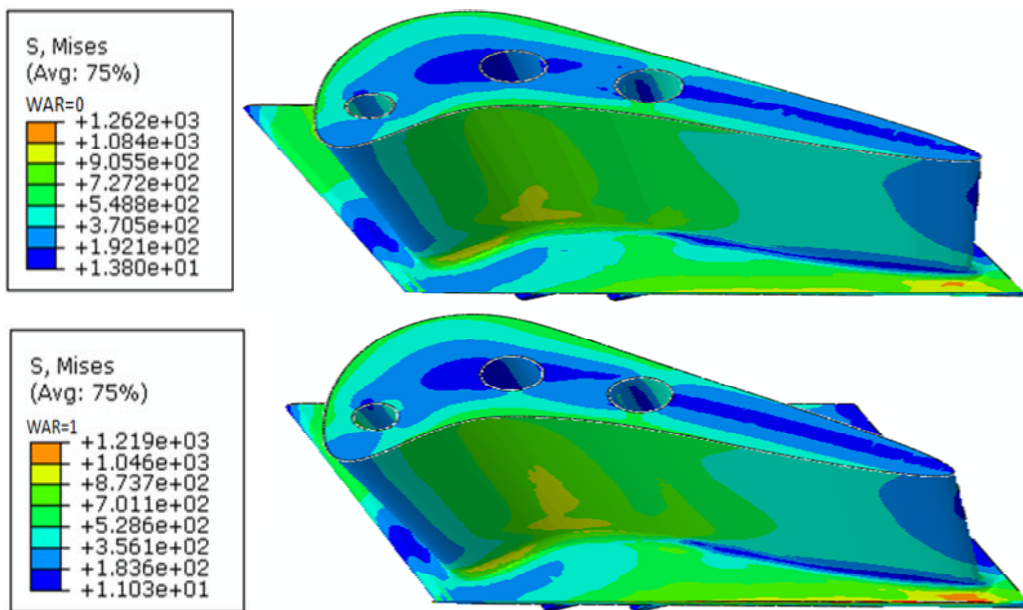
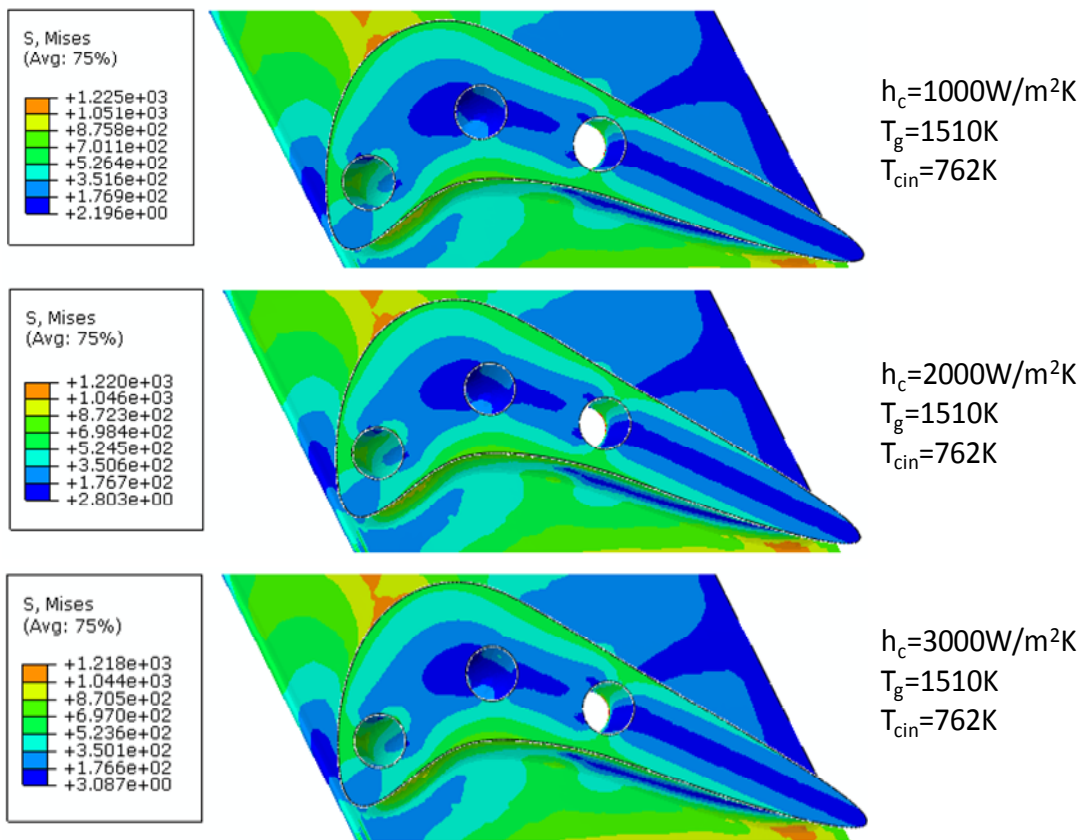


Figure 8-16: Thermal stress FE model on the blade chord (25% blade span) at WAR=0.0 and 0.1

To investigate the potential effect of advance cooling schemes on the thermal stress distribution along the blade span,  $T_{cin}$  was kept constant and  $h_c$  increased from 1000 to 3000 W/m<sup>2</sup>K as shown in Figure 8-17. The PCN and pressure load were fixed and the thermal stress produced was as a function of temperature gradient at the blade cross-sectional area. The cross-sectional view shows the thermal stress around the blade coolant channel and through the blade

thickness. It is clear from these results and the blade metal temperature distribution shown in Figure 8-9, the thermal stress was higher around the surface of the blade and coolant channel near the blade LE. The highest thermal stress around the LE coolant channel dropped from 701 MPa at  $h_c=1000 \text{ W/m}^2\text{K}$  to 697 MPa at  $h_c=3000 \text{ W/m}^2\text{K}$ . This decrease in the thermal stress combined with the reduction in the blade metal temperature will have significant effect on the blade creep life of the hot section component.

The whole stress level increased when the flux of the cooling air increased because of increase of temperature gradient. The thermal stress will decrease when the average temperature ( $\Delta T$ ) between the  $T_g$  and  $T_{in}$  is small (see Figure 8-8) which lead to a decrease of the temperature gradient. The stress at the root was higher because the temperature of the coolant air increased as it ran through the cooling channels, consequently the temperature gradient in the section near the root was larger and decreased along the cooling channel.



**Figure 8-17: Cross-sectional blade thermal-stress distribution (50% blade span) for different coolant schemes ( $h_c=1000, 2000$  and  $3000 \text{ W/m}^2\text{K}$ )**



## 8.4 Model validation

An important point of discussion for this study is the accuracy of the calculated results, which obviously depend on the accuracy of the separate tools and integrated model. The model result should have been validated against experimental data; however, experimental data was not available and the only way to validate the model was to compare the result of the analytical model developed in this work with data available in the open literature.

Since the stress calculated using the analytical model does not include the thermal stress, only the mechanical stresses along the blade span using the devolved analytical mode (A) and 3-D parametric FE model (B) are compared and the results presented in Figure 8-18. The mechanical stress (von Mises) of the 3-D FE model at the blade LE along the blade span is compared with stress obtained using the analytical stress model.

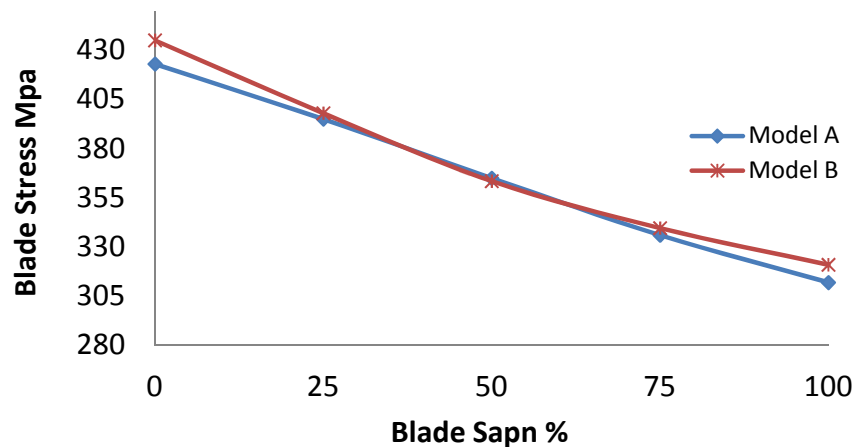


**Figure 8-18: Variation of the mechanical stress along the blade span using analytical model (A) and finite element model (B)**

From the figure above, it is clear that the mechanical stresses of analytical model A were lower compared to FE model B along the entire blade span except at the mid-point where the blade stress value predicted by model B is marginally less than that predicted by analytical model A. The objective of analytical stress model is to understand the effect of the operating conditions and the working environment on the stress distribution of the HP turbine blade. The 3-D FE model analyses were to identify the most critical location on the

blade with changes in the cooling system parameters, in order to focus in creep damage evaluation of the blade. The mechanical stresses predicted by both models were obtained using the same materials and rotational speeds.

The accuracy of the blade metal temperature calculated with the FE model is mainly determined by the accuracy of the heat transfer coefficient calculated in the heat transfer model and main stream gas temperature obtained from the Turbomatch software. One operating point with a given value of WAR was used to compare the results of the analytical model and FE model blade metal temperature distribution along the span.

The FE blade model temperature distribution trend along the blade span and comparable result obtained from the analytical model are shown in Figure 8-19. However, the temperature differences between the two models' predictions will be due to boundary condition assumptions (e.g. cooling configuration, boundary conditions, etc.), in the in the 1-D analytical model (A) and 3-D FE model (B). The accuracy of the FE calculations will largely depend on the accuracy of geometry and size of mesh used, however these can be improved rather easily and therefore are not considered to be serious limitations. Furthermore, in 1-D you would have to describe a cooling effectiveness whereas in 3-D, the temperature distribution is calculated from the heat balance between the hot cooling blade surfaces.

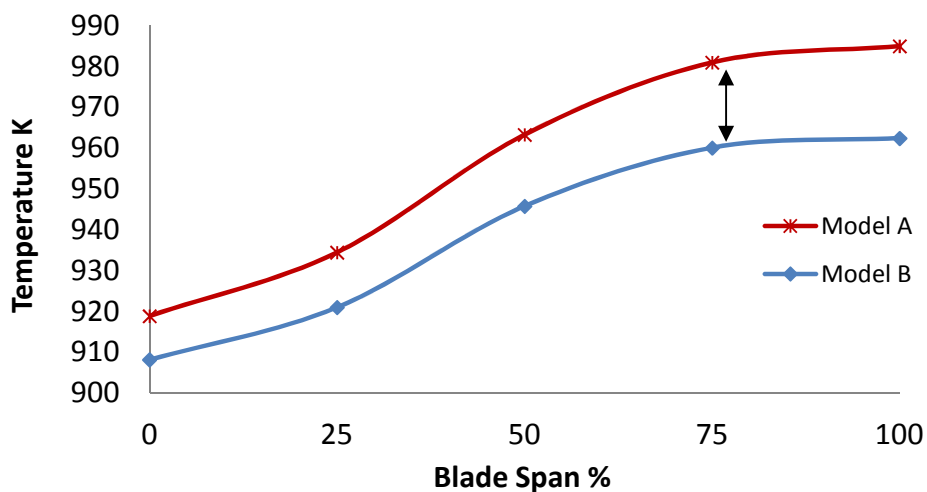


**Figure 8-19: Variation of metal temperature distribution along the blade span using analytical model (A) and finite element model (B)**

## 8.5 Chapter Conclusions

The blade metal temperature and stress is influenced by most of the factors that drive the life of hot section components of stationary gas turbine engines. It is necessary to calculate the maximum metal temperature and stress at each point over the blade in order to calculate the creep life of HP turbine blade. The FE model was used to run a linear static analysis to solve different loading cases; mechanical loads (rotation and gas pressure), thermal load (heat transfer) and combinations of thermal and mechanical load (thermal stress). The result of integrating FE software with other tool and models for life prediction of gas turbine components has been presented. It has been demonstrated that the mechanical and thermal loads of the HP turbine blade can be calculated from the operational data and the creep life prediction can be performed. The accuracy of the integrated tool is obviously dependent on the accuracy of the individual models, and the accuracy of the blade metal temperature distribution with the FE model is mainly determined by the accuracy of the heat transfer coefficient value ( $h_c$ ).

The mechanical stresses on the blade were calculated at one operating point for different rotational speeds ( $PCN=1-0.94$ ) to identify the maximum stresses over the blade. The result reveals that the greatest stresses in the blade come from the rotational load, due to the relatively high operating speed of the turbine. Bending load due to the gas pressure is significantly lower than that produced by rotation. The stress distribution along the blade as result of these loads were a maximum at the blade root. Centrifugal stresses make a major contribution close to the blade root and near the root curvature, while gas bending stresses become more important close to the blade tip and near the blade cooling channel.

Gas stream and cooling air temperatures, and heat transfer coefficient could change as the operating conditions of the gas turbine change, even under steady state operation. In this study, the cooling air temperature and heat transfer coefficient were considered to change the operating point due to change the WAR at the compressor inlet. The steady state temperature

distributions along the blade span at different WAR were obtained using the 3-D FE model. The results show that as the WAR increased the blade metal temperature decreased. The blade LE mid-airfoil section is the hottest location in the blade surface, and where the turbine blade creep damage usually occurs so the thermal stress needs to be considered in order to calculate the correct blade creep life. The effect of advanced coolant design was investigated as change in  $h_c$ . In this study the use of humid air shows an improvement in the cooling process by increases the  $C_p$  and  $h_c$  which in turn reduce the blade metal temperature and thus improve the blade creep life.

The FE model calculates the thermal-mechanical stresses using the nodal temperature distributions and the maximum engine rotational speed as boundary conditions. The von Mises stress under combined thermal and structural loading reduced as the WAR increased from 0.0 to 1.0. These stresses reach quite high levels at the coolant regions of the blade (blade contact with the coolant). The thermal stress linear FE analysis revealed that none of the blade airfoil regions had undergone any plastic deformation under the influence of the loading conditions examined.

The results have been presented in the form of contour maps and temperature profiles to identify the effects of dry and humid air coolant on critical areas of the HP turbine blade in a stationary gas turbine engine. The thermal stress analysis combined with the mechanical stress analysis will yield more valuable information about the actual magnitudes of overall stresses encountered by the turbine blade. Therefore, an attempt has been made in the present work to use FE Abaqus software to obtain the temperature distribution, mechanical stresses and thermal stress at several cross-sectional areas of the stationary gas turbine blade. By knowing these life driving factors, the creep life can be predicted and operation cost reduced.

## *Chapter nine*

### **9 CASE STUDIES**

#### **9.1 Analytical results: effect of operating conditions and design parameters on the blade creep life**

This chapter presents the effects of engine operating conditions and engine component design parameters on the HP turbine blade creep life of stationary gas turbine. The study was carried using Nimonic alloy material at different radial temperature distribution functions (RTDF), turbine entry temperatures (TET) and cooling effectiveness ( $\epsilon$ ). The coolant air considered here is dry air extracted from the compressor to cool the first stage HP turbine blade.

##### **9.1.1 The effect of RTDF on creep life**

In this section, the effect of RTDF on creep life is investigated by changing its values from 10% to 15% and to 20%. During this investigation, TET, relative rotational speed (PCN), and  $\epsilon$  were maintained at 1550K, 0.98 and 0.6 respectively.

The temperature, stress and creep life distribution along the span of the blade at different RTDF values are shown in Figure 9-1 to Figure 9-4. From Figure 9-1, it can be seen that as the value of RTDF is increased from 0.10 to 0.20, the maximum metal temperature increases from 1141K to 1177K at a point 75% along the span of the blade. However, lower RTDF values result in high metal temperature at the root and at the tip of the blade.

Figure 9-2 shows the stress distribution along the span of the blade. Since the stress distribution depends on the PCN alone, changing the values of the RTDF did not change maximum stress.

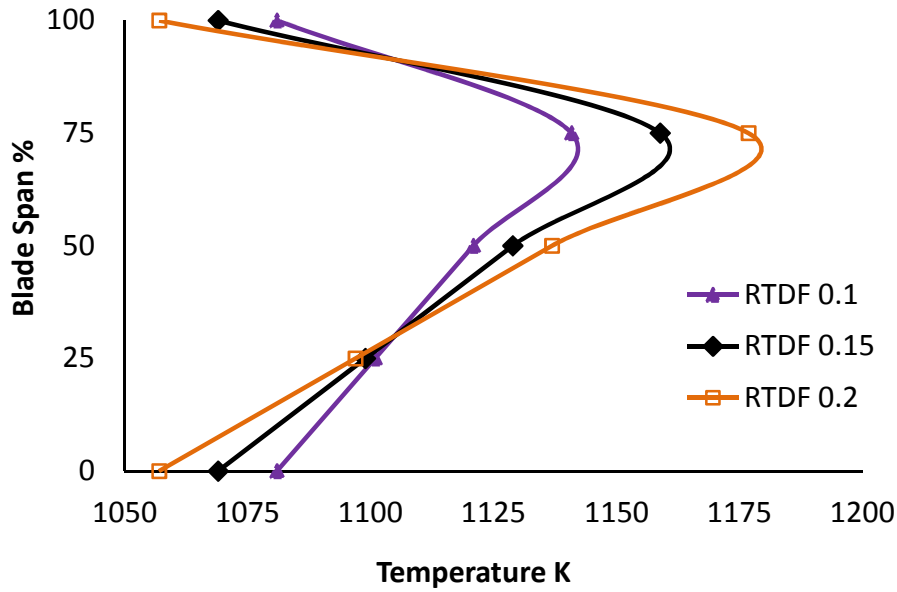


Figure 9-1: Turbine Blade Inlet Temperature Profile along the span of the blade at different values of RTDF

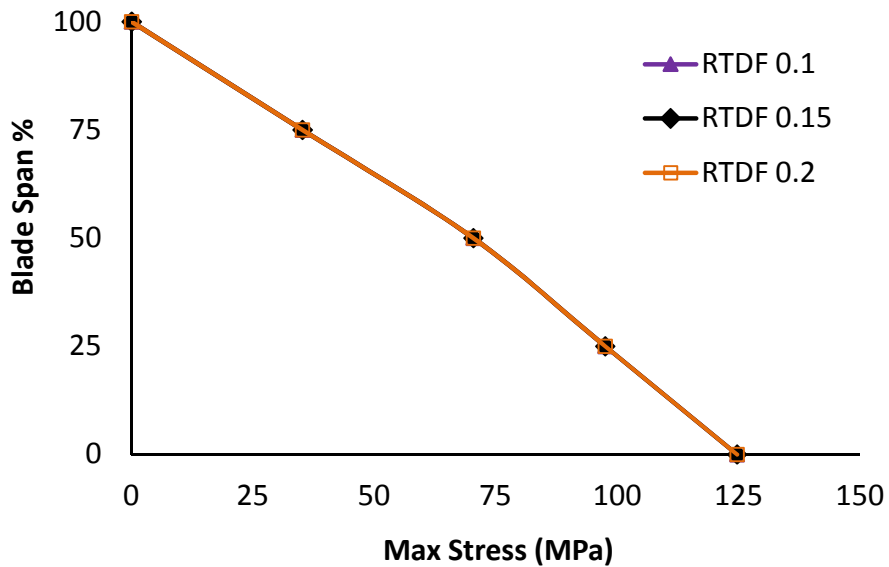


Figure 9-2: Maximum Stress Distribution along the span of the blade at different values of RDTF

Figures 9-3 and 9-4 show creep life variation for RTDF = 0.10, 0.15 and 0.20. The values of creep life in both figures are presented as relative values, expressed as creep factor ( $L_f/L_{fR}$ ) of the creep life at the root. From Figure 9-3, it can be seen that the lowest relative creep life was located at 25% of the span of the blade with a value of 0.97  $L_f/L_{fR}$ . This means that at this location, the blade's

creep life was 3% less than the life at the blade root. The relative creep life increased from a minimum value of 0.97  $L_f/L_{fR}$  at 25% to 2.17  $L_f/L_{fR}$  at the tip. In contrast in Figure 9-4 the lowest relative blade creep life for RTDF 0.15 and 0.20 were located at 75% of the span of the blade with relative values of 0.35  $L_f/L_{fR}$  and 0.09  $L_f/L_{fR}$  respectively. Although the temperature at the root for different RTDF was slightly different, the creep life at the root is the same since at that section of the blade the creep is mainly due to the centrifugal force.

Comparing Figure 9-1, Figure 9-3 and Figure 9-4, it can be seen that for RTDF of 0.10 has a higher metal temperature at the blade root than for RTDF of 0.15 or 0.20. Since the stress and temperature were higher at the blade root as shown in Figure 9-1 and Figure 9-2, the combined effects of the two factors is considered to be the main driving factor producing the lowest life at or near the blade root. In contrast, although the maximum stress for RTDF 0.15 and 0.2 is similar to RTDF 0.10, which is about 124.7MPa at the root, the location of the lowest relative creep life is different from RTDF 0.10. This is because for both RTDFs 0.15 and 0.2, the effect of higher metal temperature at 75% the span of the blade was greater than the effect of maximum stress at the blade root, thus changing the location of lowest relative creep life.

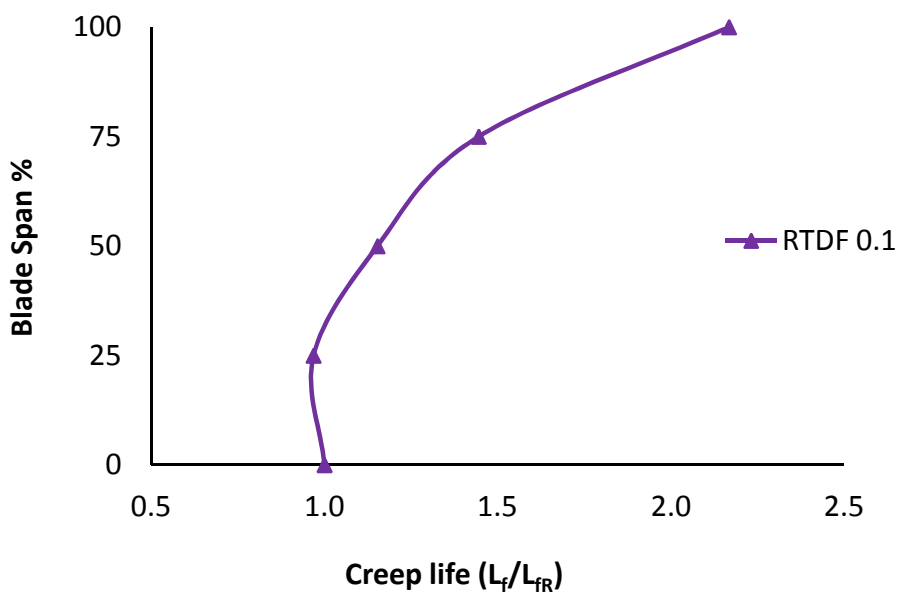
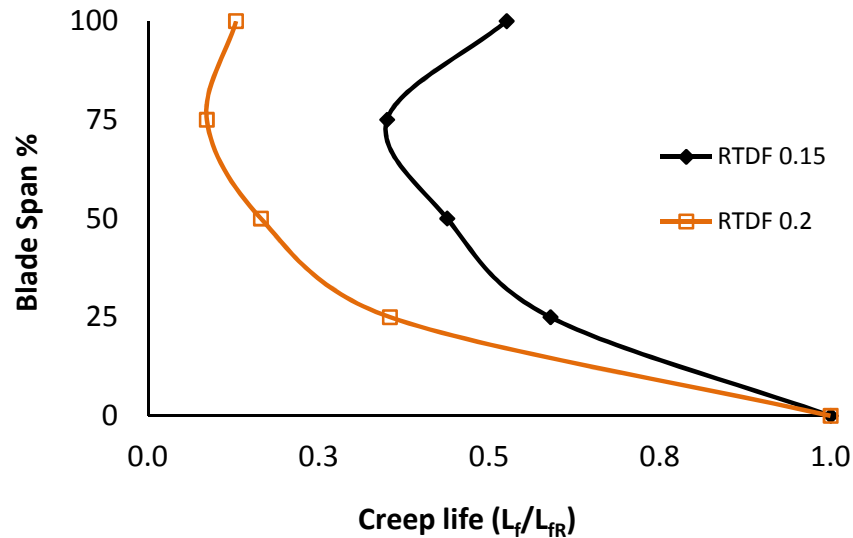


Figure 9-3: Turbine blade creep life along the span of the blade at RTDF=0.10



**Figure 9-4: Turbine blade creep life along the span of the blade at RTDF=0.15 and 0.20**

It is clear from the results that changing the value of the RTDF led to a change in the location of maximum and minimum temperatures along the span of the blade. At the lower RTDF the temperatures at the tip and root are higher than for the higher RTDF. On the other hand the maximum metal temperature which occurred about three-quarters along the span increased with increase in RTDF. It is concluded that more consideration should be given to the selection of the combustor RTDF to better control creep life.

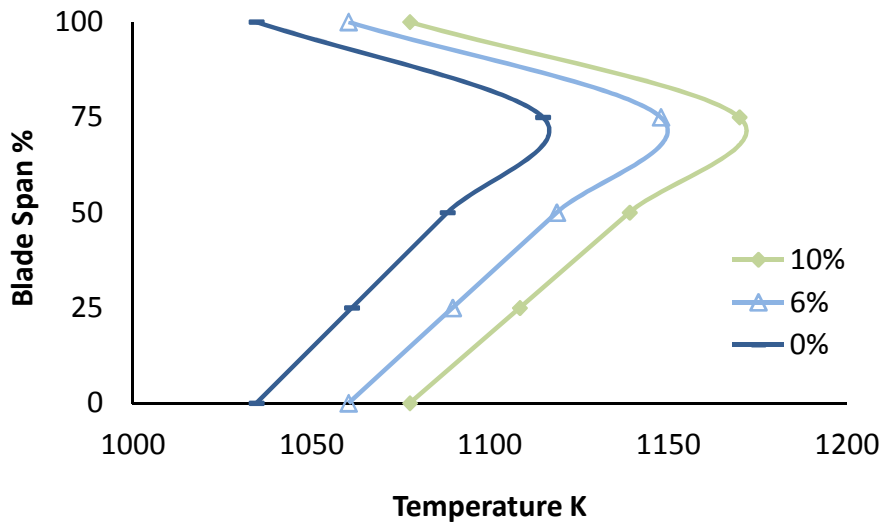
### 9.1.2 The effect of cooling effectiveness on creep life

Blade temperature will be a function of combustor outlet temperature, blade geometry, and cooling effectiveness. The reduction of  $\varepsilon$  could be the result of any combination of the following factors; increase in air cooling temperature, increase in TET or/and degradation in the cooling system [177].

In this investigation, the effect of cooling effectiveness on blade creep life is evaluated. The off-design point selected for consideration was RTDF = 0.15, TET = 1550K and  $\varepsilon = 0.6$ . In the analysis,  $\varepsilon$  was decreased from 0% ( $\varepsilon = 0.6$ ) to 10% ( $\varepsilon = 0.54$ ) in increments of 2% to assess any variation of the blade's creep life from the root to the tip. However to maintain clarity in Figures,  $\varepsilon$  of only 0%, 6% and 10% reduction are shown here.

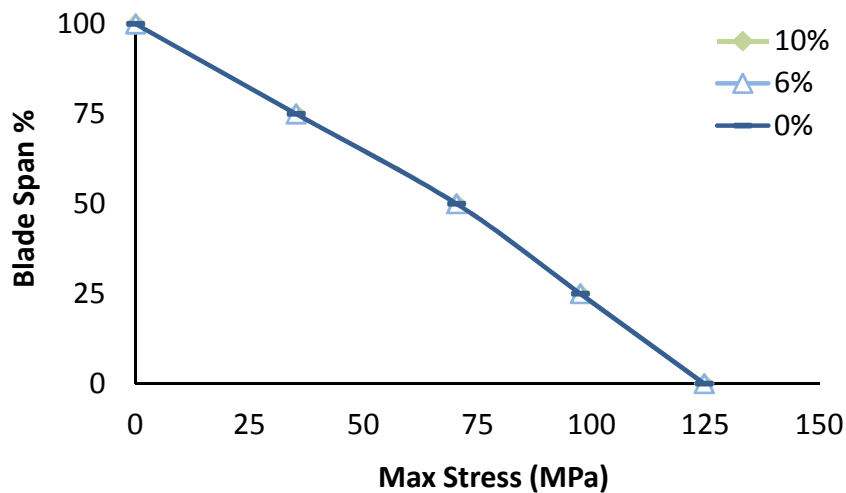


Figure 9-5 shows the temperature, stress and creep life distribution along the span of the blade for different values of  $\epsilon$ . Reducing  $\epsilon$  by 6% increases the maximum metal temperature three quarters the way along the span from about 1116K to 1148K. Reduction of  $\epsilon$  by 10% increased the maximum metal temperature to 1170K as shown in Figure 9-5.



**Figure 9-5: Turbine blade inlet temperature profile along the span of the blade at different reductions in cooling effectiveness**

From Figure 9-6 we see that the maximum stress at 75% of the blade span is 35 MPa for all three values of  $\epsilon$  degradations.



**Figure 9-6: Maximum stress distribution along the span of the blade at different reductions in cooling effectiveness**

Figure 9-7 shows that for all three values of  $\epsilon$  degradations, the shortest creep life is located at 75% of the span of the blade. For  $\epsilon = 0.6$ , the blade creep life at

this point is about half that at the root. Reducing  $\epsilon$  by 10% decreased the blade creep life at the same location to about one-third that at the root. It is clear that reducing  $\epsilon$  increases the maximum blade temperature at 75% of the span of the blade and that, combined with the maximum stress at that region, reduces the blade creep life at that location more than at either the blade root or mean length.

Note that the creep life in Figure 9-7 is given relative to the life at the root of the respective material. However, this does not provide information regarding how it deviates from the chosen reference point. Table 9-1 lists the ratio between the creep life at the blade root of the respective material with the life of the blade root at the reference point. As an example the value of 0.023 means the life at blade root is 2.3% of the life of the reference point's blade root. For this study the reference point chosen is at TET=1500K,  $\epsilon=0.6$  and RTDF=0.15.

**Table 9-1: Creep life ratio at different values of  $\epsilon$**

	Creep life ( $L_i/L_{iR}$ )	
$\epsilon$ (%)	10	0.023
	6	0.055
	0	0.215

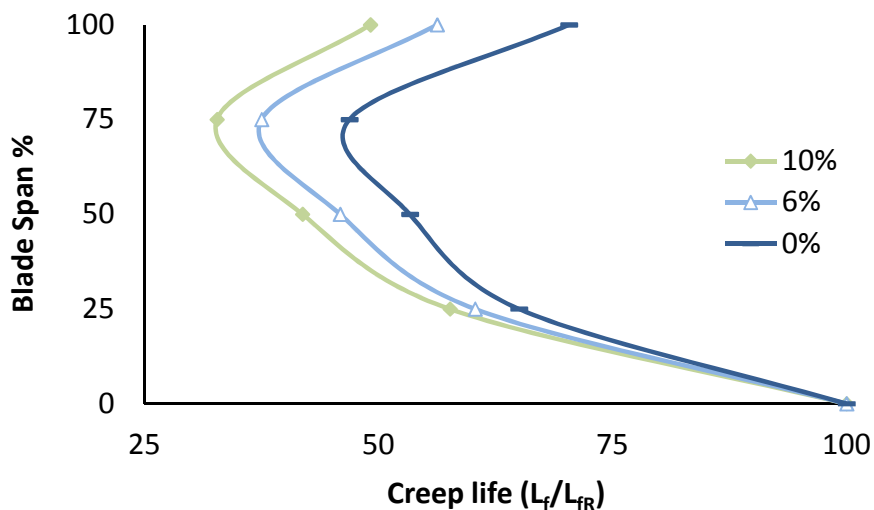


**Figure 9-7: Turbine blade creep life along the span of the blade at different reductions in cooling effectiveness**

Comparing the impact of  $\epsilon$  it is clear that the location and the duration of creep life will be different mainly due to different stresses and temperatures.

### 9.1.3 The effect of TET on creep life

The effect of TET on blade creep life is studied by changing the TET from 1400K to 1600K in increments of 50K. Here, only TET =1400K, 1500K and 1600K are presented to demonstrate the blade's creep life along the span of the blade. The reference off-design point selected in this investigation were RTDF = 0.15 and  $\varepsilon = 0.6$ .

Figure 9-8 shows the temperature distribution along the span of the blade with different TETs. It can be seen that by increasing the TET the maximum blade temperature three-quarters the way along the span increased from 1015K at TET 1400K to 1145K at TET 1600K. However, the minimum temperatures, which occurred at the blade root are 944K at TET 1400K, and 1062K at TET 1600K.

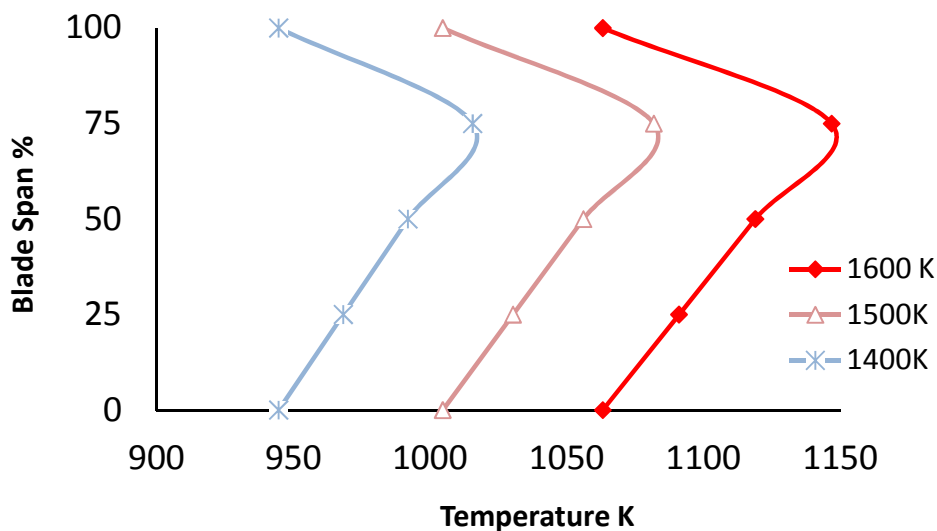


**Figure 9-8: Inlet temperature profile along the span of the turbine blade at different TETs**

Figure 9-9 shows how the maximum stresses along the span of the blade varied as the TET changed. From the figure, the maximum stress at the root increased with temperature, from 96.3MPa at TET 1400K to 128.7MPa at TET 1600K. Three-quarters along the length of the span of the blade the corresponding stresses were 27.2MPa and 36.3MPa. This increase in stress is due to the increase in TET which in turn resulted in increased rotational speed.

Figure 9-10 shows the blade creep life distribution along the span of the blade. The minimum life is found to be three-quarters along the blade. At TET=1400K the creep life at that location is only 0.20  $L_f/L_{fR}$  (20%) of the creep life at the blade root. At TET = 1600K the creep life decreased to 0.52  $L_f/L_{fR}$  (52%) relative to the blade life at the root. Comparing the relative effects of temperature and maximum stress distribution within the blade it is clear that temperature has the greater effect.

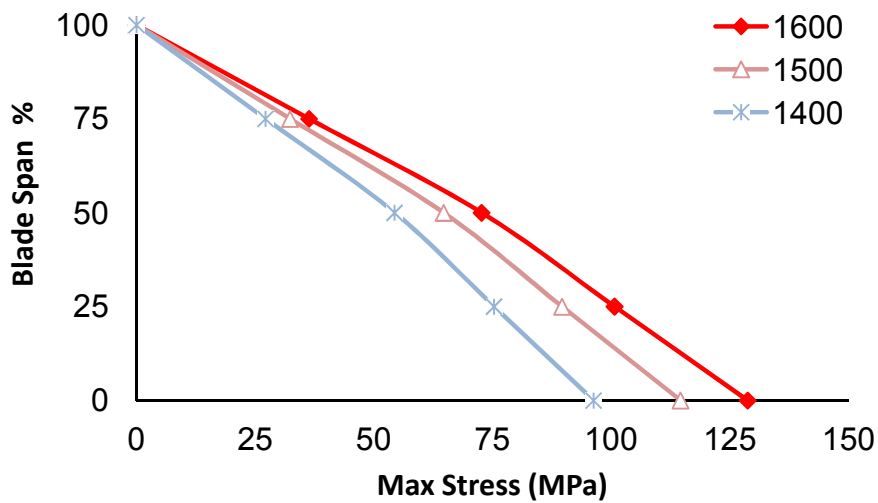


Figure 9-9: Maximum stress distribution along the span of the blade at different TETs

Similar to the results in Section 5.2, Table 9-2 lists the ratio between the creep life at the blade root and the creep life of the reference point at the same blade location for different TET.

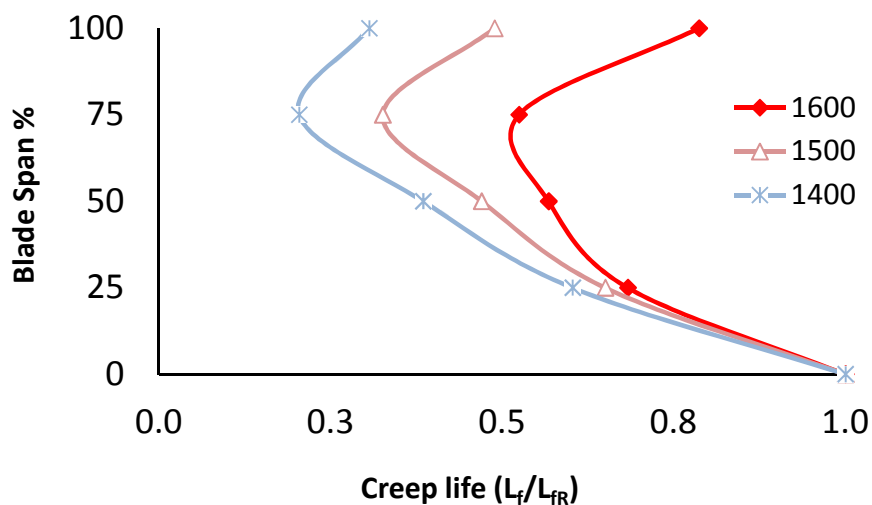


Figure 9-10: Creep life along the span of the turbine blade at different TETs

**Table 9-2: Creep life ratio at different TET**

	Creep life ( $L_f/L_{fR}$ )	
TET(K)	1600	0.041
	1500	1.787
	1400	130

Increasing the TET decreases blade creep life along the span of the blade. However, the location of the minimum life creep will depend on the maximum blade metal temperature, maximum stress and creep behaviour of the material. Small change in the stress value along the span of the blade will move the location of the blade creep life from three-quarters of the blade length to half. The results show that different design parameter combined with a change in operating conditions can significantly affect the creep life of the HPT blade and the location along the span of the blade where the failure could occur.

#### 9.1.4 Effect of compressor degradation on creep life

Compressor fouling is recognized as the most common cause of engine performance deterioration [140]. It manifests as a build up of dirt on the compressor blades, thereby constricting the air flow passage thus reducing mass flow capacity. There is also a reduction in efficiency due to the change in blade aerodynamic profile and increased surface roughness. The reduction in mass flow also leads to lower compressor pressure ratio due to the change in the compressor operating point on its characteristic. The result is a decrease in shaft power and increase in SFC. Operationally, to recover the loss in power, the fuel flow could be increased leading to higher TET and decrease in creep life. In this study, three degradation cases are used to examine the effect of different levels of compressor fouling on creep life [73]. These are: severe fouling, representing the scale of compressor fouling in highly polluted environments; moderate fouling and light fouling as a result of normal usage. Table 9-3 details the percentage drop in mass flow capacity and efficiency for the cases examined. These values are consistent with typical values for compressor fouling [140]. For ease of reference, 3%, 2% and 1% are used to represent severe, moderate fouling and light fouling, respectively.

**Table 9-3: Mass flow capacity and efficiency for different levels of fouling**

Compressor fouling	Change in		
	Mass flow capacity (%)	Isentropic efficiency (%)	Designation
Severe	-6	-3	3%
Moderate	-4	-2	2%
Light	-3	-1	1%

In Figure 9-11 to Figure 9-13 the effect of the different levels of fouling are compared to the baseline conditions. Figure 9-11 shows that compressor fouling has no affect on the location along the blade span of the maximum and minimum creep life. Moreover the shape of the combustor outlet temperature distribution, shown in Figure 9-12 is unchanged. Figure 9-13 also shows that the trend in blade metal temperature remains the same. Hence, the only effect of increasing TET to regain performance due to compressor degradation is the severity in creep life reduction. Figure 9-11 shows clearly the reduction of creep life from a factor of 0.76 to a factor of 0.28 as the severity of fouling increases from 1% to 3% at the blade mean. Performance recovery can be achieved by either regular washing of fouled compressors or by increasing TET (thereby reducing creep life). Economic studies have suggested that compressor washing is the more favoured solution to performance recovery.

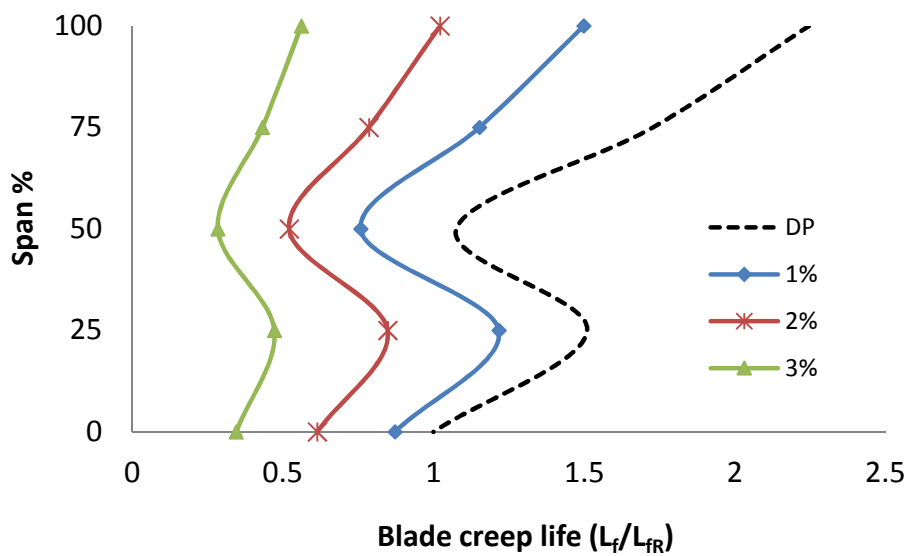


**Figure 9-11: Blade creep life for compressor degradation at  $T_{amb}=288.15K$**

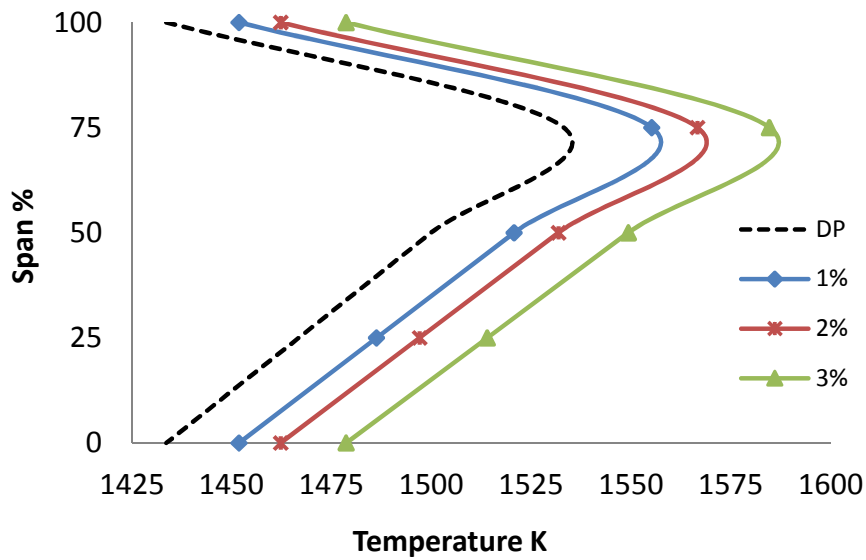


Figure 9-12: Combustor outlet temperature distribution for compressor degradation at  $T_{amb} = 288$

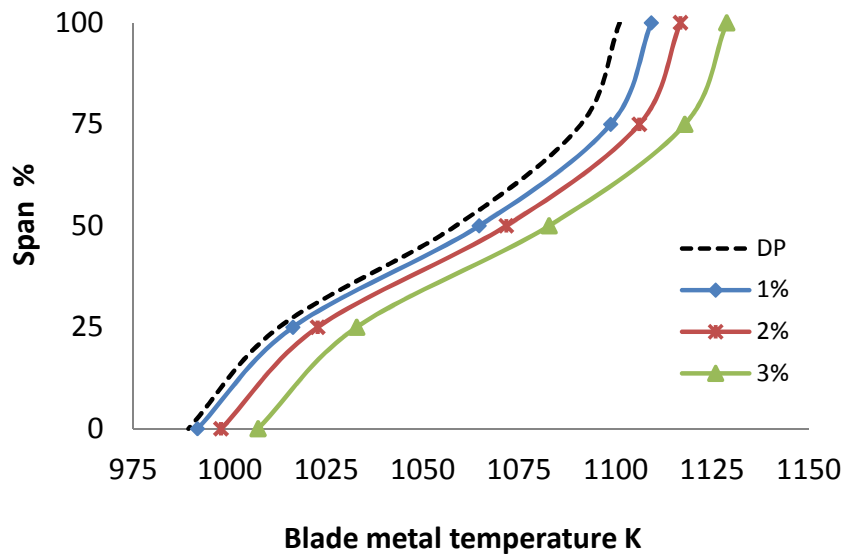


Figure 9-13: Blade metal temperature for compressor degradation at  $T_{amb}=288.15K$

## 9.2 The effect of WAR on the HP turbine blade creep life

For a given off-design point, the WAR varied as dry (0.0), 0.038, 0.051 and 0.07 to evaluate the effect of WAR on the heat transfer. The effect of WAR on the heat transfer coefficient and cooling process along the blade span is presented. The life at each section of the blade span for different operating points was

relative to the life of the selected reference operating point at the blade root. Also, different operating points were also evaluated at different WAR and  $T_{amb}$  to identify the effect of WAR on the creep life at the blade mean. The WAR at each operating point was quantified by the  $T_{amb}$  and relative humidity.

### 9.2.1 Heat transfer and creep life distribution along the blade span

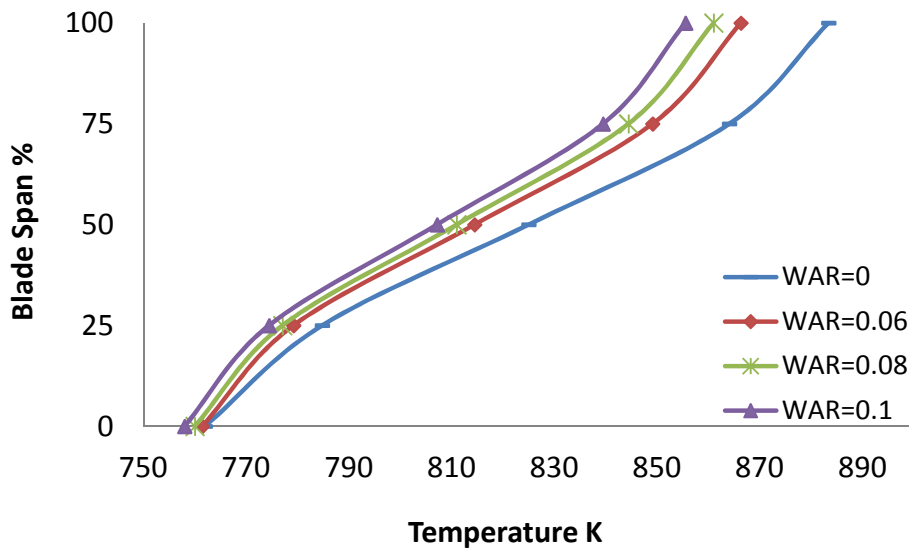
In this section the effect of WAR on the turbine blade heat transfer coefficient and creep life are discussed. The reference point selected for this study is presented in Table 9-4. The off-design point was  $T_{amb}=318.15K$ ,  $TET=1480K$ ,  $T_{cin}=757.5K$ ,  $PCN=0.96$ ,  $RTDF=0.08$  and the WAR was varied from WAR= dry to WAR=0.10. The results presented in this paper are for WAR=dry, 0.06, 0.08 and 0.10.

**Table 9-4: Reference point input data**

<b>Parameter</b>	<b>value</b>
<b>PCN</b>	0.98
<b><math>T_{amb}</math></b>	288.15K
<b><math>T_g</math></b>	1465 K
<b><math>T_{cin}</math></b>	750.0 K
<b>m</b>	80.9 kg/s
<b><math>m_g</math></b>	74.5 kg/s
<b>RTDF</b>	0.08
<b><math>\eta_{ad}</math></b>	0.3
<b>WAR</b>	Dry (0.0)

Figure 9-14 shows the inlet coolant air temperature at each section of the blade span. The outlet coolant of the previous section is used as inlet to the next section. It can be seen that on increasing WAR from dry to 0.10. The blade inlet coolant temperature reduced from 760K to 757K in the blade root and from 825K to 811K in the mean. However, for the same WAR the inlet air coolant temperature increased from the root to the tip as a result of receiving heat from the blade metal by forced convection. In the case of WAR= 0.06 the inlet air coolant temperature at the root was 761K which increased to 866K near the blade tip. The difference between the temperature at the blade tip and blade root decreased as the WAR increased.





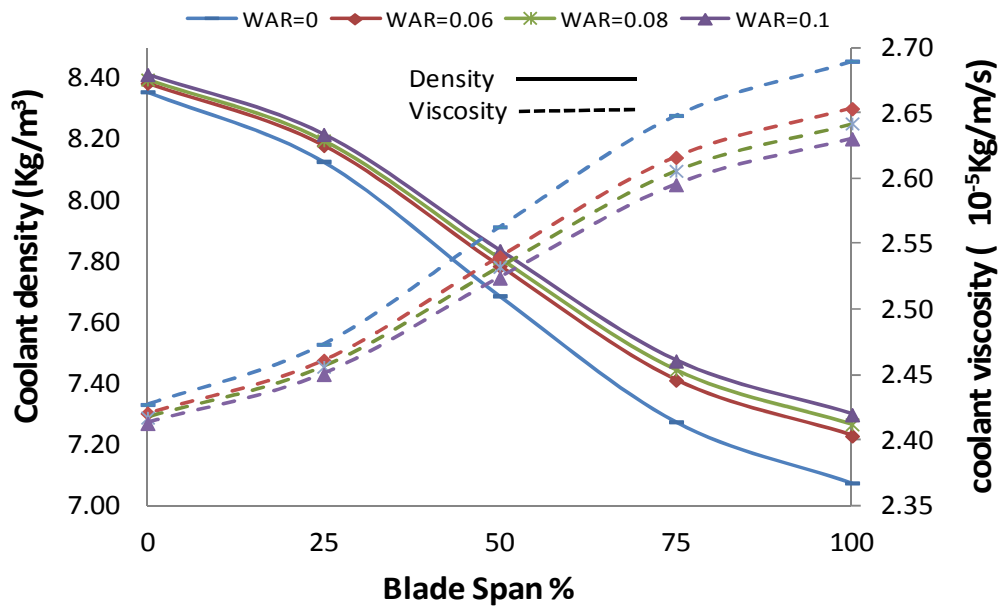
**Figure 9-14: Blade inlet cooling temperature along blade span at WAR = dry (0.0), 0.06, 0.08 and 0.10**

Figure 9-15 shows the change of coolant density and viscosity along the blade span as WAR changed from dry to 0.10. In general, increase in WAR increased the air coolant density for each operating point at given location on the blade. This was because increase in the WAR at each operating point reduced the coolant air temperature. However, along the blade span the coolant density reduced because of the increase in the gas constant of humid air and the air coolant temperature (as shown in Figure 9-14). Also, the effect of temperature on the dry air density was more significant than on humid air, due to which the variation in the density of the dry air from blade root to the tip was higher than for humid air. Near the root, cooling air temperature over the range of WAR is small, hence the density variation at blade root for different WAR is very small. Similarly, above the blade mean, a higher variation in density was noticed between the humid and the dry air.

The coolant air viscosity was reduced when WAR was increased, and for a given WAR, the viscosity increased from the root to the tip. This is mainly due to the increased air coolant temperature along the blade span.

Figure 9-16 shows the distribution of the coolant Reynolds number along the blade span at different WAR (dry to 0.10). Reynolds number was calculated from the coolant air  $\rho$  (which varied with WAR),  $\mu$ ,  $D_h$  and coolant air velocity. At

a given location on the blade, Re was higher for higher WAR. For a given WAR, Re decreased from the root to the tip of the blade. The main reason for this is increase in the coolant air viscosity and decrease in the air density. For all the cases considered, Re was greater than  $4 \times 10^4$ , suggesting turbulent flow conditions. Although the flow mechanism does not change from turbulent to the laminar condition, increase in Re will lead to increase in Nusselt number which in turn will govern heat transfer on the coolant side.



**Figure 9-15: Coolant air density and viscosity along the blade span at WAR = dry (0.0), 0.06, 0.08 and 0.10**

Heat transfer by forced convection is described by the Nusselt number (Nu) which is a function of Reynolds number. Humidity (WAR) affects the heat transfer through a change in the gas composition in these non-dimensional numbers. Figure 9-17 shows the variation of coolant heat transfer coefficient at different WAR along the blade span. As the WAR increased from dry to 0.10 the coolant heat transfer coefficient increased. However, in all cases the coolant heat transfer coefficient decreased along the blade span relative to the root section of the blade. This is mainly because of the change in coolant fluid properties ( $C_p$  and  $R$ ) due to the change in WAR and increase in the coolant inlet temperature (see Table 9-5) from blade root to the tip. The higher the vapour content, the higher its energy content (more heat will be transferred to

the coolant air). The cooling air comes from the compressor discharge, and as this air contains greater water vapour content; it provides higher heat carrying capacity of the cooling flow.

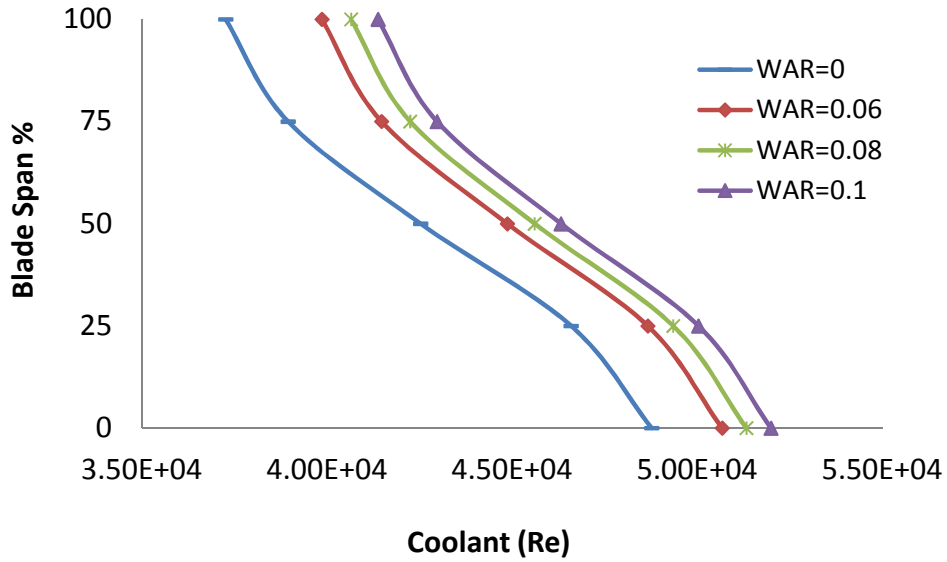


Figure 9-16: Coolant Reynolds Number along the blade span at WAR = dry (0.0), 0.06, 0.08 and 0.10

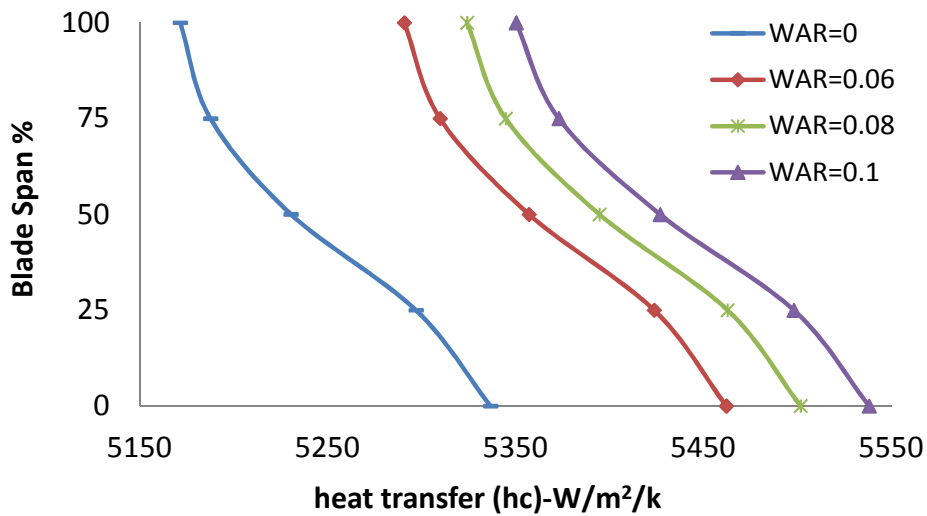


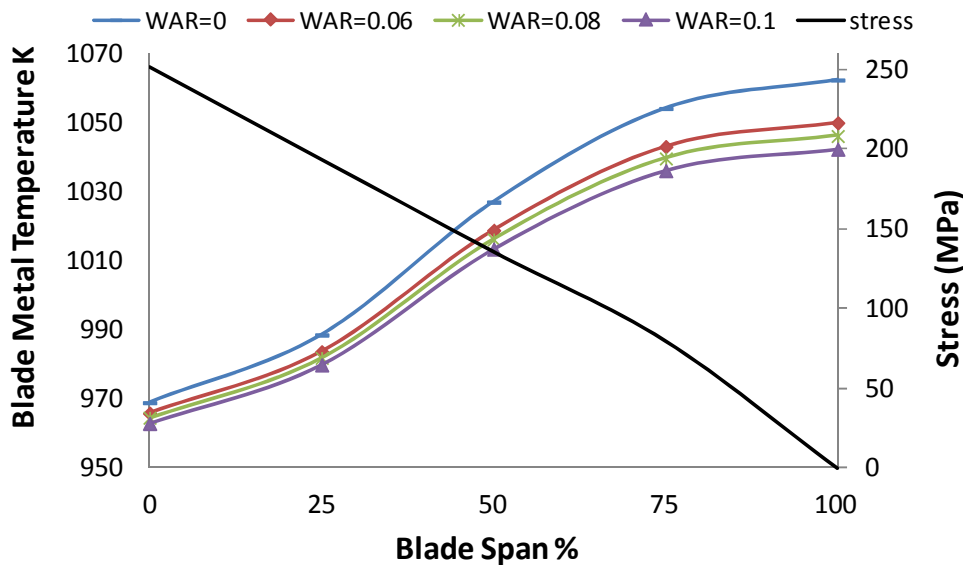
Figure 9-17: Coolant heat transfer coefficient along the blade span at WAR = dry (0.0), 0.06, 0.08 and 0.10

Table 9-5 confirms that change in WAR affects  $\rho$ ,  $\mu$ ,  $C_p$  and  $R$  of the coolant air which in turn affects  $Re$  and  $Nu$ . Any change in the cooling air thermal and flow properties would affect the coolant outlet and blade metal temperatures.

**Table 9-5: Effect of WAR on various parameters along the span**

Parameter	$t_s$	$\rho$	$\mu$	Re	Nu	$T_{cin}$
Hub to tip	↑	↑	↑	↓	↓	↑

Figure 9-18 shows the distribution of blade metal temperature and stress along the blade span. Since the PCN was constant, the stress was constant at each blade section. Therefore, the change of the creep life of the turbine blade at each WAR value was a function of change of the blade metal temperature. In Figure 9-18 the blade metal temperature at each section was reduced as WAR increased from dry to 0.10. The blade temperature at different WAR values was similar at the blade root up to about 25% of the blade span. Also from the root to 25% of blade span the behaviour of Cp was very similar, and hence the effect of humidity on heat transfer was small and the blade metal temperature was less affected by change in WAR. The effect of WAR on the metal temperature became more significant from 25% to blade tip. At 25% of the blade span, the blade metal temperature was 988K at WAR= 0.0 and 979K at WAR= 0.10, whereas at blade mean this temperature was 1025K for WAR= 0.0 and 1012K for WAR= 0.10. This reduction in the blade metal temperatures at each section obtained by increasing the WAR resulted from the change in the coolant heat transfer coefficient and the overall heat transfer.



**Figure 9-18: Blade metal temperatures and stress distribution along blade span at WAR = dry (0.0), 0.06, 0.08 and 0.10**

One reference point was selected (see Table 9-4) in order to compare the blade creep life at an off-design condition to that at the reference operating point. This means that the life obtained at each section as shown in Figure 9-19 was relative to the life at the reference operating point at the blade root. For example, the value of 2.5 at blade mean means the creep life at that section increased to 2.5 times the life of the reference operating point (blade root), whereas the value of 0.8 at the root would indicate a 20% reduction of the component's creep life from its reference operating point.

The results show that at for all the WAR cases considered the life at the blade root was less than the creep reference life, since the ambient temperature and inlet cooling temperature from the compressor of the reference operating point was lower than for the off-design operating points. Also, the creep life for the WAR= dry case ( $T_{amb}$  318.15k) was reduced along the blade span relative to the life at the reference point. On increasing the WAR to 0.06, 0.08 and 0.10, the blade creep life along the blade span increased. It is clear that the increased blade creep life was as a result of reducing the blade metal temperature, and this was achieved by increasing the WAR and the heat transfer capacity of the coolant air flow.

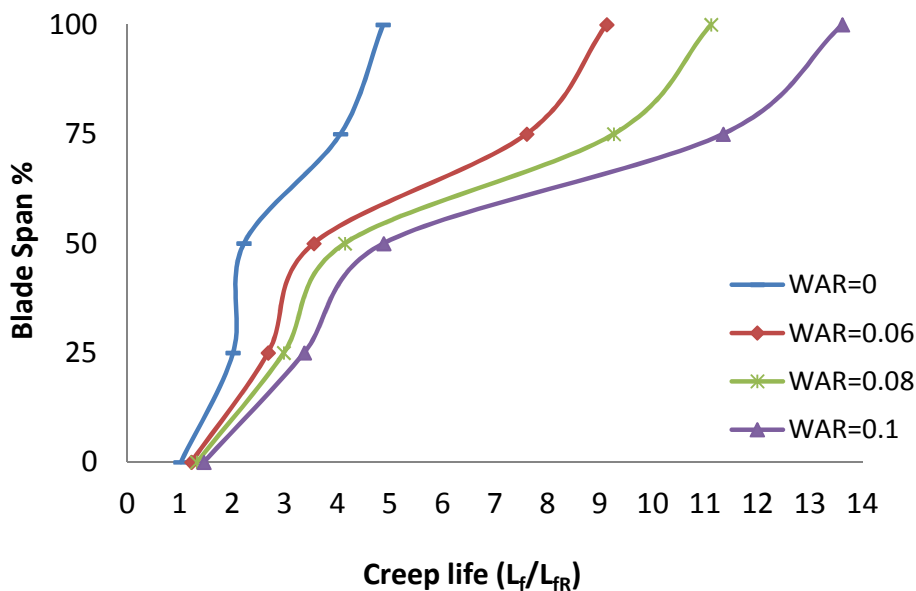


Figure 9-19: Blade creep life ( $L_f/L_{fR}$ ) long the span relative to the blade root at WAR = dry (0.0), 0.06, 0.08 and 0.10

As shown in Table 9-6, at WAR= 0.06 the blade creep life at the mean was 2.98 relative to the reference operating point creep life, and this increased to 4.88 at WAR= 0.10. Also at WAR= 0.10 the creep life at the blade tip increased to 13.3 times the reference creep life.

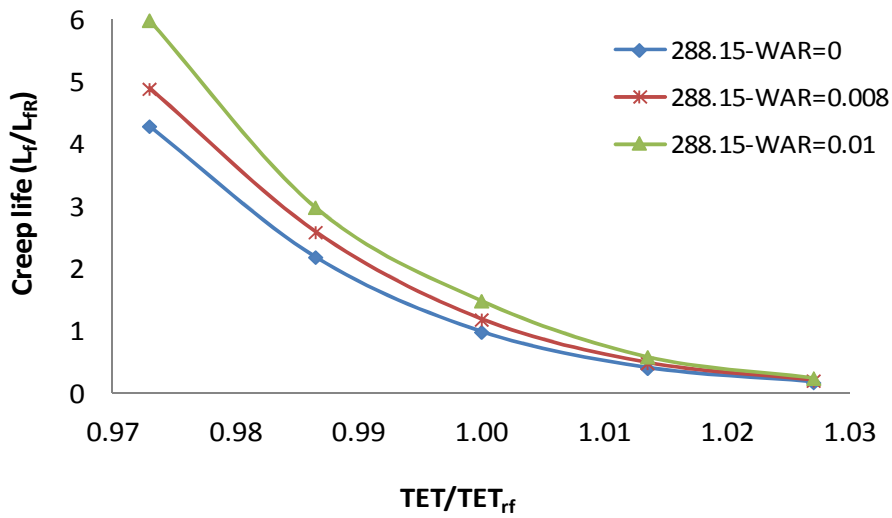
**Table 9-6: Blade creep life with different values of WAR at  $T_{am} = 318.15K$**

WAR	Creep factor ( $L_f/L_{fR}$ )		
	Root	Mean	Tip
Dry (0.0)	1.00	2.22	1.87
0.06	1.22	2.98	9.12
0.08	1.32	3.55	11.1
0.10	1.46	4.88	13.6

It can be concluded that the influence of humidity on turbine blade creep life becomes more important when large variation of WAR is expected. This would more likely in hotter more humid climates and/or when inlet humidification is used to increase gas turbine power output.

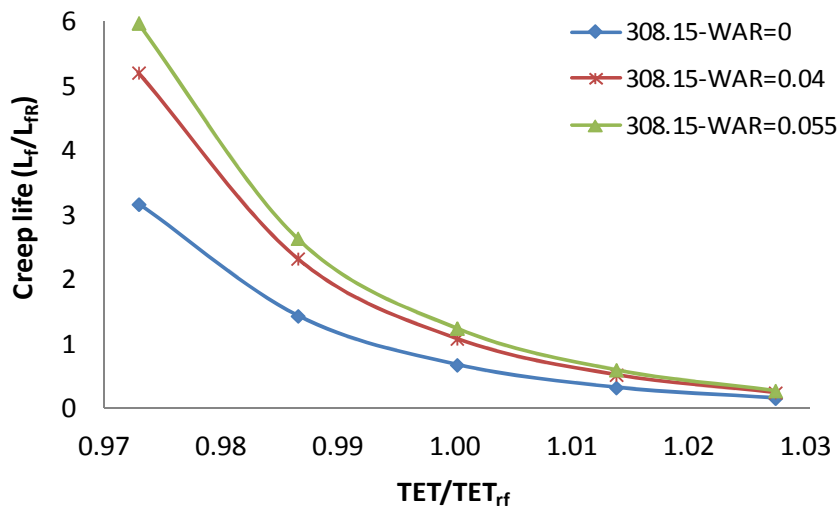
### 9.2.2 Different location and operating point

Gas turbines are sited at different locations and are used for different applications; e.g. aviation, oil and gas, marine and power plants. The effect of creep is highly dependent on the operating conditions of the engine, its mode of operation, the working environment and the properties of critical hot section components. Therefore, creep life at different ambient temperatures and TET were investigated to identify the effect of WAR on the creep life at the blade mean. A reference point was selected at TET=1480K, WAR=0.0 and  $T_{amb} = 288.15K$ . The WAR at each operating point is quantified by the humidity. Figures 9-20 to 9-22 show the change of creep life at different operating points and different ambient temperatures for change in the WAR from dry to 0.10. Figure 9-20 shows the change of creep life ( $L_f/L_{fR}$ ) at  $T_{amb} = 288.15k$  and WAR= dry to 0.01. The result shows that as the WAR increased, the creep life increased. This is the result of reduction in the in the inlet coolant temperature of the HP turbine blade and increase in the heat transfer coefficient as discussed in the previous section.

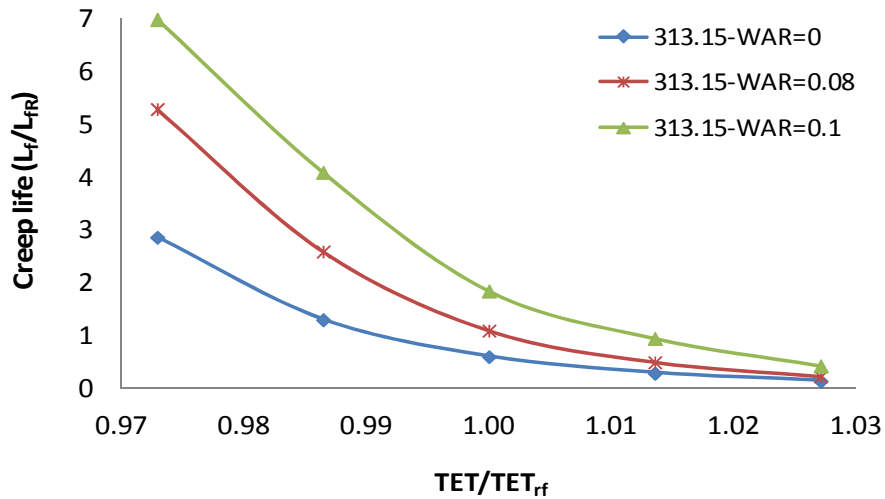


**Figure 9-20: Creep life at the blade mean for different operating points, WAR (dry (0.0), 0.008, 0.01) and  $T_{amb}=288.15K$**

Figures 9-21 and 9-22 show the creep life for  $T_{amb}= 308.15K$  and  $313.15K$ . For  $WAR=0$  the creep life reduced because the inlet mass flow reduced and inlet coolant temperature increased. However, for  $TET/TET_{rf}= 1$  with increase in both  $T_{amb}$  and  $WAR$ ; from  $T_{amb}= 308.15$  and  $WAR=0.04$  to  $T_{amb}=313.15$  and  $WAR=0.08$ , the  $L_f/L_{fR}$  increased from 1.09 to 1.1. Increase in the  $WAR$  from 0.055 to 0.10 for the same  $T_{amb}$  and  $TET/TET_{ef}$  and the  $L_f/L_{fR}$  increased from 1.25 to 1.85. The results also show that operating the GT engine at a lower operating point ( $TET/TET_{ef}= 0.975$ ) in a humid environment ( $WAR= 0.04, 0.055, 0.08$  and  $0.10$ ) improves the blade creep life as shown in Figures 9-21 and 9-22.

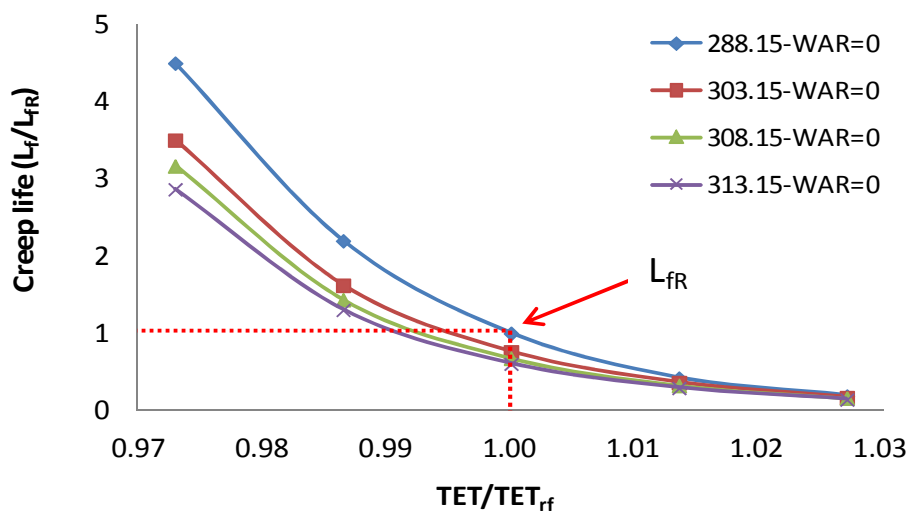


**Figure 9-21: Creep life at the blade mean for different operating points, WAR (dry (0.0), 0.04, 0.055) and  $T_{amb}=208.15K$**



**Figure 9-22: Creep life at the blade mean for different operating points, WAR (dry (0.0), 0.08, 0.10) and  $T_{amb}=313.15K$**

Different operating points for different  $T_{amb}$  and WAR= dry were also studied and the results presented in Figure 9-23. For WAR= dry the blade creep life reduced as the ambient temperature increased, this is because the inlet cooling temperature increased and cooling effectiveness reduced. If the TET is increased above the reference point ( $TET/TET_{rf} > 1$ ) for different  $T_{amb}$ , the effect of  $T_{amb}$  at WAR= 0.0 on blade creep life becomes more significant. Increase in operating TET from the reference point at  $T_{amb}= 288.15K$  to  $313.15K$  will result in a decrease in creep life to 40% of the reference value of the creep life at the blade mean.



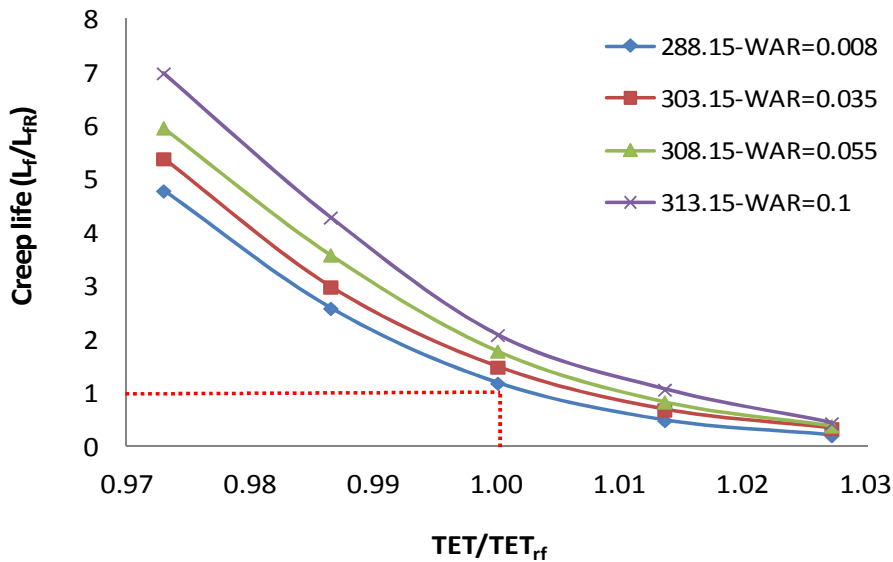
**Figure 9-23: Creep life at the blade mean for different  $T_{amb}$ , TET and WAR= dry (0.0)**



Figure 9-24 shows that when increasing WAR from 0.008 (at 288.15k) to 0.10 (at 313.15k) by increasing the humidity, there is a corresponding increase in blade creep life particularly at lower TET. At WAR= 0.008 (288.15K) the blade creep life factor for  $TET/TET_{rf} = 1$  at the mean and decreased to one fifth (0.20) of the creep life of the reference point. At an operating TET of 1460K, an increase WAR from 0.008 to 0.10, gave a corresponding increase in blade creep life factor from 2.6 fold to 4.3 fold. Increasing the TET to 1500K at WAR= 0.055 reduced the blade creep life to 0.9 of that at the reference point. It is clear from Figure 9-24 that when the  $T_{amb}$  increased the blade creep life increased because of the increase in the WAR and  $C_p$  (coolant) as shown in Table 9-7. The improvement of the blade creep life was achieved by increasing the WAR and  $C_p$  coolant which resulted in more heat being absorbed by the coolant air.

**Table 9-7:  $C_p$  coolant at TET1460K and different WAR**

TET=1460K				
WAR	0.008	0.035	0.055	0.10
$C_p$ (J/kg.K)	1110	1194	1258	1394



**Figure 9-24: Creep life at the blade mean for different  $T_{amb}$ , TET and WAR=0.008, 0.035, 0.055 and 0.10**

Figure 9-25 shows the blade creep life at  $T_{amb} = 288.15K$  and different values of WAR for three operating points: TET= 1480K, 1500K and 1520K. At WAR=dry the blade creep life reduced as the TET increased. However, it is clear from the

results that life improved as WAR increased even if the TET increased (TET=1500K). For WAR= 0.008 and 0.01 the blade creep life increased from 0.5 and 0.63 respectively (the relative life of the blade at WAR=0.0 was 0.4 for the same operating point). Although, in one case the TET increased from 1480K to 1500K at the same  $T_{amb}$ , the blade creep life approached nearly to the reference operating life ( $L_{fR}$ ) by increasing the WAR to only 0.01.

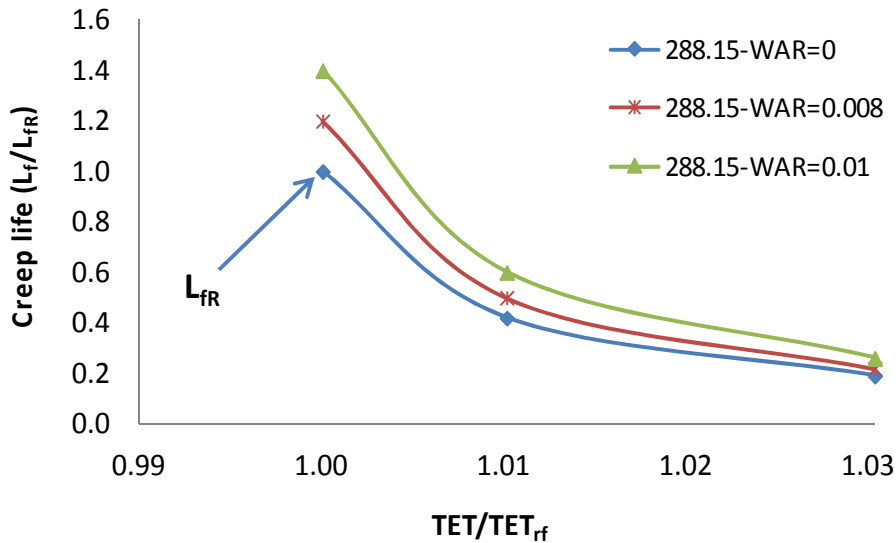


**Figure 9-25: Creep life at blade mean for different TET at WAR= dry (0.0), 0.008, 0.01.  $T_{amb}$  288.15K**

Figure 9-26 shows that at a  $T_{amb}$  of 313.15K, increasing the WAR from dry to 0.10 increased the blade creep life substantially. At WAR= 0.0 the blade creep life was reduced at all operating points because of the increase in the temperature of the cooling air and drop in the cooling effectiveness. However, an increase in the WAR improved the blade creep life at all operating points, compared to  $T_{amb}$ = 288.15K, as shown in Figure 9-25.

On comparing the results plotted in Figure 9-25 and Figure 9-26, it is clear that even if the ambient temperature increased, at higher temperatures the creep life increased due to increase in the WAR. The effect of the increase in the WAR on heat transfer was more significant than the increase in the ambient temperature. This suggests that it is possible to operate the engine even above the reference point just by increasing the WAR.

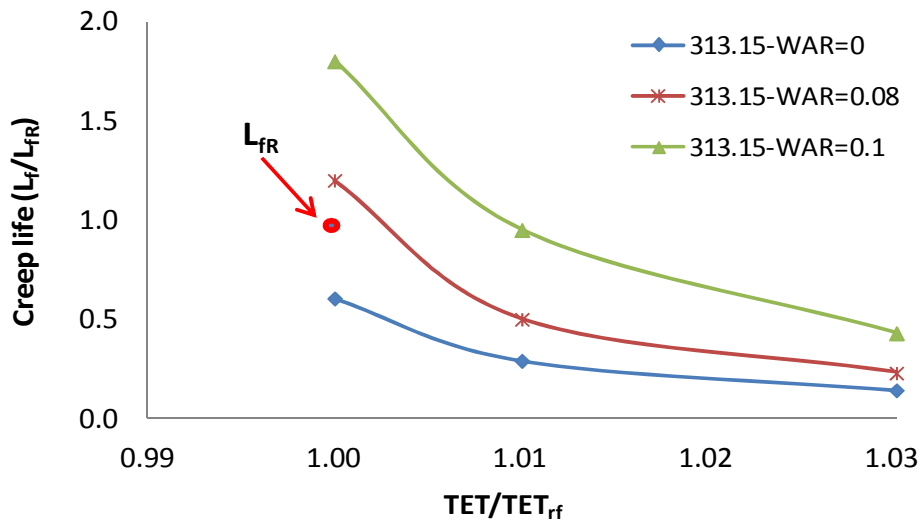


Figure 9-26: Creep life at blade mean for different TET and WAR=0.0, 0.08, 0.10.  
Tamb= 313.15K

### 9.3 Finite element results: effect of humidity on the blade creep life

From the FE model, the temperatures and the mechanical stress are known at each node of the mesh; so for a given value of stress, the Larson Miller parameter (LMP) can be obtained from the LMP creep curve. Hence, the time to failure under any temperature and stress operating conditions can be determined. The blade metal temperature, stresses and creep life at the blade LE at different locations and for different WAR are presented in Tables 9-8 to 9-11. The blade metal temperature at the LE reduced as the WAR increased from dry to 0.10. This resulted to an increase in the life of the blade at the LE as the WAR increased. Also, the average temperature from the root to the tip of the blade at WAR= dry and 0.10 were 57K and 41K respectively. Similarly the mechanical stress was reduced from 484MPa (LMP=21.65) to 215MPa (LMP=24.05). The calculated creep life is presented with reference to the life at a critical point on the LE blade root. The blade metal temperature in all cases increased (root to tip) and reached the maximum at the blade tip. The result shows that the blade creep life at the LE increased from the root to the tip with increase in WAR. At the blade root LE, the stress was higher, while, the temperature was higher above the mid-span of the blade, which shows that the stress (LMP value) controlled the blade creep life at the blade LE.

**Table 9-8: FE model LE blade metal temperature, stress, and creep life for WAR=0**

	T (T)	$\sigma$ (MPa)	LMP	$L_f/L_{fR}$
<b>Tip</b>	975	215	24.05	16.8
↕	973	252	23.58	6.1
	959	290	23.21	5.8
	932	387	22.46	4.5
<b>Root</b>	918	484	21.65	1
$\Delta$	<b>57</b>			


**Table 9-9: FE model LE blade metal temperature, stress, and creep life for WAR=0.06**

	T (T)	$\sigma$ (MPa)	LMP	$L_f/L_{fR}$
<b>Tip</b>	963	215	24.05	33.7
↕	961	252	23.58	10.8
	953	290	23.21	8.3
	928	387	22.46	5.8
<b>Root</b>	914	484	21.65	1.3
$\Delta$	<b>49</b>			

**Table 9-10: FE model LE blade metal temperature, stress, and creep life for WAR=0.08**

	T (T)	$\sigma$ (MPa)	LMP	$L_f/L_{fR}$
<b>Tip</b>	955	215	24.05	55.1
↕	957	252	23.58	16.3
	947	290	23.21	11.8
	923	387	22.46	7.9
<b>Root</b>	909	484	21.65	1.7
$\Delta$	<b>46</b>			

**Table 9-11: FE model LE blade metal temperature, stress, and creep life for WAR=0.10**

	T (T)	$\sigma$ (MPa)	LMP	$L_f/L_{fR}$
<b>Tip</b>	947	215	24.05	89.95
	949	252	23.58	26.2
	941	290	23.21	16.9
	919	387	22.46	9.8
<b>Root</b>	906	484	21.65	2
$\Delta$	<b>41</b>			

The blade metal temperature, stresses and creep life at the blade TE at different locations and for different WAR are presented in Tables 9-12 to 9-15. The results indicate that as the WAR increased the blade creep life at the TE generally increased due to drop in the blade metal temperature. However, along the blade span the blade creep life reduced in all cases of WAR. The creep life was presented with reference to the life at a critical point on the TE blade root. In this case, the average temperature from the root to the tip of the blade at WAR=0.0 and 0.10 were 107K and 90K respectively and the corresponding mechanical stress was reduced from 411MPa (LMP=22.24) to 200MPa (LMP=24.25). At WAR=0.0 the results show that the creep life at blade TE along the span was less than the creep reference life. Thus, the metal temperature and stress are considered to be the main driving factor producing the lowest life at or near the blade tip. Whereas, at WAR=0.08 and 0.10 the blade creep life at the TE was reduced up to 80% of the blade span and then increased slightly near the blade tip. This is because of the reduction in the blade metal temperature as the WAR increased and the average temperature from the root to the tip was less than at WAR=0.0.

The change in the blade creep life at the blade LE and TE results from the change in the blade metal temperature and the LMP value used in the creep life equation; as well as the blade geometry thickness at the LE and TE. The sensitivity of the calculated life for creep life at the blade LE and TE (reference to LE root and TE root) to deviations in stress and temperature is presented in

Figures 9-27 and 9-28. A small deviation in stress and temperature is amplified in the life prediction.

**Table 9-12: FE model TE blade metal temperature, stress, and creep life for WAR=0.0**

	T (T)	$\sigma$ (MPa)	LMP	$L_f/L_{fR}$
<b>Tip</b>	842	200	24.25	0.03
↕	830	225	23.9	0.04
	801	250	23.6	0.16
	759	331	22.88	0.80
<b>Root</b>	735	411	22.24	1.0
$\Delta$	<b>107</b>			

**Table 9-13: FE model TE blade metal temperature, stress, and creep life for WAR=0.06**

	T (T)	$\sigma$ (MPa)	LMP	$L_f/L_{fR}$
<b>Tip</b>	831	200	24.25	0.09
↕	822	225	23.9	0.07
	797	250	23.6	0.22
	756	331	22.88	0.99
<b>Root</b>	733	411	22.24	1.22
$\Delta$	<b>98</b>			

**Table 9-14: FE model TE blade metal temperature, stress, and creep life for WAR=0.08**

	T (T)	$\sigma$ (MPa)	LMP	$L_f/L_{fR}$
<b>Tip</b>	822	200	24.25	0.18
↕	816	225	23.9	0.12
	794	250	23.6	0.30
	754	331	22.88	1.30
<b>Root</b>	730	411	22.24	1.60
$\Delta$	<b>92</b>			

**Table 9-15: FE model TE blade metal temperature, stress, and creep life for WAR=0.10**

	T (T)	$\sigma$ (MPa)	LMP	$L_f/L_{fR}$
<b>Tip</b>	818	200	24.25	0.24
$\updownarrow$	812	225	23.9	0.16
	790	250	23.6	0.41
	751	331	22.88	1.66
<b>Root</b>	728	411	22.24	1.98
$\Delta$	<b>90</b>			

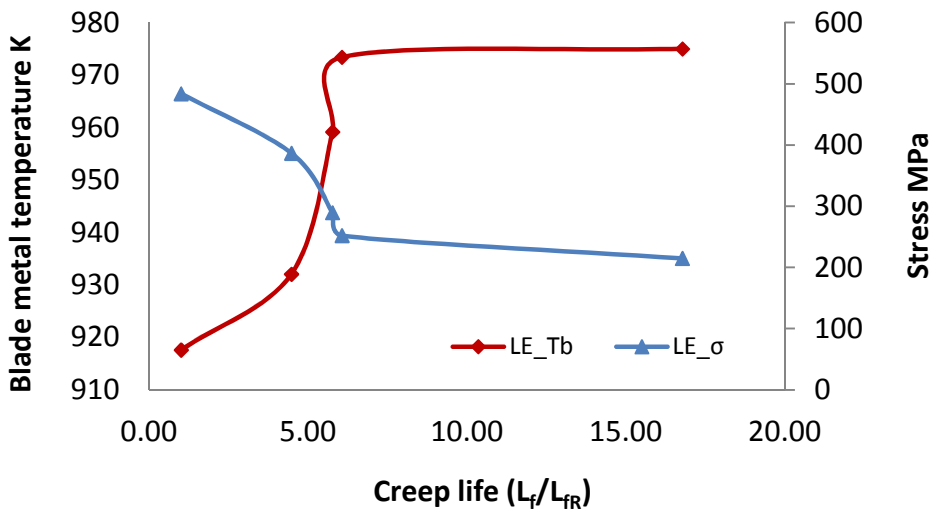


**Figure 9-27: LE metal temperature and stress sensitivity of creep life along the blade span**

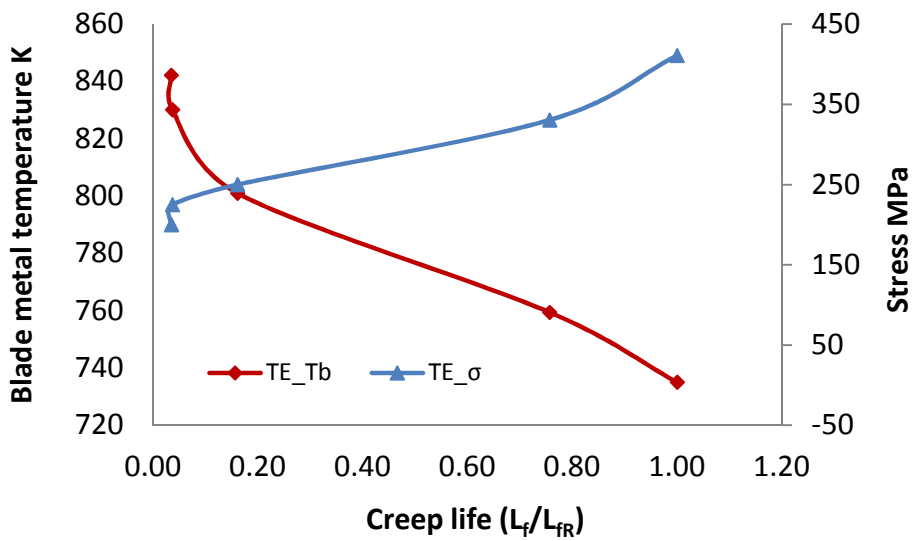


**Figure 9-28: TE metal temperature and stress sensitivity of creep life along the blade span**

At the blade LE and TE the metal temperature increased and the mechanical stresses reduced from the root to the tip. However, the blade creep life from the root to the tip at blade LE increased and at the blade TE is reduced. In the first case, the creep life increased because the stress was driving the reduction in life along the blade span. Whereas, in the second case, the blade creep life was dominated by the increase of temperature. This can be seen from the average temperature from the root to the tip at the blade TE (higher) and the blade LE. In Tables 9-8 to 9-15 variation in LMP values along the blade span (WAR=0.0 to 0.10) at the blade LE and TE has significant effect on the result of creep life.

Tables 9-16 and 9-17 show the blade metal temperature, stress, LMP value and creep life at different critical locations (I=LE fillet, II=middle, 40% span and III= tip, 80% span) on the blade airfoil for WAR=0.0 and 0.10. The stress and blade metal temperature for WAR=0.0 and 0.10 were higher at node 8899 (II) and 9682 (III) compared to the node 7837(I). This because nodes II and III were near to the critical location with higher local gas temperatures (see Figure 6-5). The high stresses in these critical locations due to the design future of the blade coolant such root curvature, coolant channel and blade wall thickness. The blade creep life was presented referred to the design point and increased at nodes 8899 and 9682 for increase in WAR from 0.0 to 0.10 due to the reduction in metal temperature and stress. From the results it can be seen that for WAR=0.0 the creep life was reduced by factors of 0.4 and 0.21 to the reference life at nodes 9682 and 8899 respectively. Increasing the WAR to 0.10 increased the creep life at these nodes (9682 and 8899) by factors of 3.61 and 2.46 respectively to the reference point.

**Table 9-16: Blade creep life at critical location for WAR=0**

Location (node)	T (K)	$\sigma$ (MPa)	LMP	$L_f/L_{fR}$
I (7837)	709	698	20.55	2585
II (8899)	815	793	20.3	0.21
III (9682)	806	784	20.32	0.4



**Table 9-17: Blade creep life at critical location for WAR=0.10**

Location (node)	T (K)	$\sigma$ (MPa)	LMP	$L_f/L_{fR}$
I (7837)	690	646	20.76	31169
II (8899)	784	764	20.36	2.46
III (9682)	779	755	20.38	3.61

## 9.4 Chapter Conclusions

This chapter has investigated the effects of the design parameters and operating conditions on turbine blade creep life. In addition, the chapter highlights how different operating conditions and design parameters can influence the location of the lowest blade creep life along the span of the blade. By understanding the relationship of the design parameters and operating conditions with creep life, both gas turbine designers and users will be able to trade-off between different design options and maintenance decisions.

The effects of using different RTDF, cooling effectiveness, TET and blade turbine materials on the blade creep life were investigated. Changing the value of the RTDF led to a change in the location of maximum and minimum temperatures along the span of the blade. At the lower RTDF the temperatures at the tip and root were seen to be higher than at the higher RTDF. On the other hand the maximum metal temperature which is at 75% along the span of the blade increased with the increase in RTDF. For lower RTDF the lowest creep life was located at the lower section of the blade whereas at higher RTDF it was at around 75% of the span of the blade.

The maximum metal temperatures increased as cooling effectiveness was reduced. However the location of the maximum temperatures remains unchanged. Eshati, [72] has presented results for the change in creep life with use of two Nimonic alloys as turbine blade material. The location of the lowest creep life was seen to change with different material used (75% of the span of the blade for alloy A and 50% of the span of the blade for alloy B). This is mainly due to the difference in the material densities at the same temperature,

which in turn results in different maximum stress values along the span of the blade.

It was found that increasing the TET increased the blade creep life along the span of the blade. However, the location of the minimum creep life depends on the maximum blade metal temperature, maximum stress and creep behaviour of the material.

The variation of blade metal temperature and maximum stress along the span of the blade for all cases has a strong influence on the blade's creep life. Thus, small changes in these two factors will determine the precise value and location of the lowest creep life. Therefore, more consideration should be given during component life assessment to the stresses and temperature values and their locations along the blade, in order to identify the exact location of minimum creep life.

The effects of WAR on the turbine blade heat transfer coefficient and creep life are also presented. The off-design point was selected and the WAR was varied between dry (0.0), 0.06, 0.08 and 0.10. The life at each section of the blade span for different operating points was given relative to the life of the selected reference operating point at the blade root.

It was noticed that on increasing WAR the blade inlet and outlet coolant temperature reduced along the blade span. Also the difference between the temperature at the blade tip and blade root decreased as the WAR increased. As WAR was increased, the coolant density decreased between the blade root and the mean of the blade, but had negligible effect from blade mean up to the tip of the blade. Also, at a given location on the blade, Reynolds number was greater for higher values of WAR, this increased the Nusselt number which governs heat transfer on the coolant side. As the WAR increased from 0.0 to 0.10 the coolant heat transfer coefficient increased. However, in all cases the coolant heat transfer coefficient decreased along the blade span relative to the root section of the blade.

Different operating points were also evaluated at different WAR and  $T_{amb}$  to identify the effect of WAR on the creep life at the blade mean. The WAR at each

operating point was quantified by the  $T_{amb}$  and relative humidity. The results show that increase in WAR increases the blade creep life even if  $T_{amb}$  is increased. The effect of the increase in the WAR on heat transfer was more significant than the increase in the ambient temperature. Also, the result shows that at TET above  $TET_{rf}$  the blade creep life improved with increase in WAR.

FE analysis is coupled with the creep lifing model (LMP) to predict the evolution of metal temperature, stress and creep damage over the entire airfoil. Also, the critical areas susceptible to creep were identified and displayed on a computer screen. In summary, the most critical point on the blade with regard to creep life can be identified in the root LE. This from the lifing point of view would be the predicted life of the whole blade. Nevertheless, the trends in the results show an interesting phenomenon that gives significant insights into blade creep life assessment. It is observed that the blade creep life increased with increase in WAR from the root to the tip at the LE. This is in contrast to a similar critical point in the TE, where the creep life decreases significantly from root to the tip. In the first case, the creep life increased because the stress was driving life reduction along the blade span. Whereas, in the second case, the blade creep life was dominated by the increase of temperature. This is because the average temperature gradient from the root to the tip at the blade TE is higher than at the blade LE, and a small deviation in stress (LMP) and temperature is amplified in the life prediction. The significance of these trends is exemplified in the redesign of blades for improved blade life. The need to consider the final change in temperature and stress gradients as they affect the various blade sections becomes paramount for an optimised design that increases blade creep life and durability.



## *Chapter ten*

### **10 CONCLUSIONS AND RECOMMENDATION FOR FUTURE WORK**

#### **10.1 Conclusions**

Since the first jet engines were put into service, improving engine performance and efficiency have always been major concerns for gas turbine manufacturers and operators and this will continue, requiring engine components to be exposed to ever more extreme mechanical and thermal loads.

In the case of stationary GT engines for mechanical power, creep failure problems are a very common cause of mechanical failure that significantly reduces component life. The magnitude of the adverse effects is highly dependent on the operating conditions of the engine, its mode of operation and also the design parameters and details of the critical hot section components. The design of engine components is determined by both mechanical and aerodynamic requirements. Against this background, the research programme was aimed at achieving a better scientific understanding of the major reasons for creep failure on HP turbine blades to better allow mechanical equipment to run for longer, free of creep failure problems. The outcome could be a substantial saving in operating costs and a considerable improvement in equipment reliability. Therefore, the *aim* of this research was to develop an analytical life model capable of assessing the influence of humidity on the heat transfer and cooling processes on a HP turbine blade taking into account the engine design parameters, operating conditions and working environment. This work contributes to the development of creep life methodology and provides good creep life prediction for HP turbine blades under various gas turbine operating and environmental conditions. The main contribution to knowledge of the current work is the consideration of the effects of humidity on the HP turbine

blade cooling processes and its subsequent impact on the performance and blade creep life of GT engines.

An engine performance model was created using an existing component based engine performance tool developed at Cranfield University; Turbomatch. This tool has the ability to simulate different thermodynamic cycles and processes while analysing the overall performance of the engine including among other things the effects of cooling flows, air and gas mixing, component degradation, variable geometry (including compressors, turbines and exhaust nozzles) as well as extraction of bleed air and shaft power off takes. Output data from the engine performance model (such as temperature, pressure and mass flow rate for each component at inlet and outlet) were then used as inputs into lifing sub-models. Also, the first stage of the HP turbine blade was sized using the constant nozzle method to facilitate estimation of creep life. The design process consists of initial performance engine simulation, inlet/outlet annulus geometry sizing, stage efficiency prediction, rotor inlet velocity, constant NGV blade design calculation and blade design details from root to the tip.

The analytical creep life model considers the change of stress along the blade span, blade trailing and leading edges and back of the blade. However, the blade metal temperature was considered only along the blade span. The model was upgraded to include the change of blade metal temperature through the blade TBC, and blade metal and creep life can be calculated using LMP. However, in this model the thermal stress was not considered, thus a 3-D finite element model was developed to determine the thermal stress of the blade as result of the change of the WAR and heat transfer coefficient.

### **Part I: Effect of operating condition and design parameters on the HP turbine blade creep life**

The work highlights how different operating conditions and design parameters can influence the location of the lowest blade creep life along the span of the blade. By understanding the relationship between the design parameters and operating conditions with creep life, both the gas turbine designers and users

will be able to trade-off between different design options and maintenance decisions.

- The effects of using different RTDF, cooling effectiveness, TET and blade turbine materials on the blade creep life were investigated. Changing the value of the RTDF led to a change in the location of maximum and minimum temperatures along the span of the blade. Maximum metal temperature which is located at 75% of the blade span increased with increase in RTDF. The lowest creep life was located at the lower section of the blade for lower RTDF, whereas at higher RTDF it was at around 75% of the span of the blade.
- The maximum metal temperatures increased as cooling effectiveness was degraded (reduced). However the location of those temperatures remains unchanged, but the location of the lowest creep life changed as different material was used. This is mainly due to the difference in material densities at the same temperature, which in turn results in different maximum stress values along the span of the blade.
- For all cases the variation of blade metal temperature and maximum stress along the span of the blade has a strong influence on the blade's creep life and small change in these two factors will significantly affect the value and location of the lowest creep life. Thus, more consideration should be given during component life assessment to stresses and temperature values and their locations along the blade to identify the location of minimum creep life.

## **Part II: Effect of humid on the HP turbine blade creep life**

The presence of water vapour changes the values of the gas transport properties for both the cold side and the hot side gases of the GT engine. Little work has been done to model the effect of humidity on coolant heat transfer and cooling processes of HP turbine blades. The analytical creep life model was upgraded to investigate the influence of WAR on the turbine blade heat transfer and cooling process which affects the blade creep life of industrial gas turbines. This approach deals with convective/film cooling with TBC and is based on an engine performance model, heat transfer model (hot side and cold side), and

the change of properties of moist air as a function of WAR. The changes of fluid properties due to the presence of water vapour are not only considered through a variation of the  $C_p$ ,  $\gamma$  and  $R$ , but also the variation of density, Reynolds number, Nusselt number and other related parameters.

The whole cooled blade row is regarded as a heat exchanger, and with the presence of TBC is subjected to mainstream hot gas flow from the combustion chamber. Also, the temperature variation due to the heat transfer along the metal blade span is considered. The creep life of the blade at each section of interest can be obtained as a function of the blade section stress and the blade metal section temperature using the LMP approach. Heat transfer depends on the parameters governing fluid flow conditions (density, viscosity,  $Re$ , temperature, structure of turbulence, body geometry, etc) and heat transfer ( $k$ ,  $C_p$ ,  $Nu$  etc). The condition and properties of the layers between the coolant fluid and hot gas flow determine the rate at which heat is transferred.

- The off-design point was selected and the WAR was varied between 0.0 (dry) to 0.1. The life at each section of the blade span for a different operating point was expressed relative to the life of the selected reference operating point at the blade root.
- It was observed that on increasing WAR: the blade inlet and outlet coolant temperatures reduced along the blade span; the difference between the temperature at the blade tip and the blade root decreased; and the coolant density decreased between the root and the tip of the blade. Also, at a given location on the blade, Reynolds number was greater for higher values of WAR, thus increasing the Nusselt number which governs heat transfer on the coolant side. As the WAR increased from dry to 0.1 the coolant heat transfer coefficient increased. However, in all cases the coolant heat transfer coefficient decreased along the blade span relative to the root section of the blade.
- The blade metal temperature at each section was reduced as WAR increased which resulted in increased blade creep life. This was achieved because increase in WAR increased the  $C_p$  of the coolant and the heat transfer capacity of the coolant air flow.



- Different operating points were evaluated at different WAR and  $T_{amb}$  to identify the effect of WAR on the creep life at the blade mean. The WAR at each operating point was quantified by the  $T_{amb}$  and relative humidity. The results show that increase in WAR increases the blade creep life even if  $T_{amb}$  is increased. The effect of the increase in the WAR on heat transfer was more significant than the increase in the ambient temperature. Moreover, the result shows that at TET above the  $TET_{rf}$  the blade creep life improved with increase in WAR. This suggests that it is possible to operate the engine above the reference point just by increasing the WAR.
- The study indicates the importance of accounting for changes in humidity on the life of the HP turbine blades of an industrial gas turbine engine. The life savings in terms of maintenance scheduling and costs for users in parts of the world which are affected by hot/humid conditions could be considerable over the life cycle of a HP gas turbine engine.

### **Part III: Finite element results: effect of humidity on the blade creep life**

The creep life model and heat transfer model are integrated with the finite element 3-D first stage HP turbine blade model to run a linear static analysis to solve different loading cases; mechanical loads (rotation and gas pressure load), thermal load (heat transfer) and combination of thermal and mechanical load (thermal stress). The results of integrating FE software with other tools and models for life prediction of gas turbine components have been presented. It has been demonstrated that the mechanical and thermal loads of the HP turbine blade can be calculated from the operational data and creep life prediction can be performed. However, the accuracy of the integrated tool is obviously dependent on the accuracy of the individual models, and the accuracy of the blade metal temperature distribution with the FE model is mainly determined by the accuracy of the heat transfer coefficient value ( $h_c$ ).

- The mechanical stresses on the blade were calculated at one operating point for different rotational speeds (PCN=1 to 0.94) to identify the maximum stresses over the blade. The results reveal that the greatest stresses in the blade are from rotational load, owing to the relatively high

operating speed of the turbine. Bending load due to the gas pressure is significantly lower than those produced by rotation. The stress distribution along the blade as result of these loads were a maximum at the blade root. Centrifugal stresses show the major contribution to be close to the blade root and near the root curvature, while gas bending stresses become more relevant close to the blade tip and near the blade cooling channel.

- The steady state temperature distributions along the blade span at different WAR were obtained using a 3-D FE model. The results show blade LE and mid-airfoil section is the hottest location on the blade surface and that is where the turbine blade creep damage usually occurs, but as WAR increased the blade metal temperature reduced. It follows that thermal stress need to be considered in order to calculate the right blade creep life and the effects of advanced coolant design investigated and presented at different  $h_c$ . In this study using humid air improved the cooling process by increases the  $C_p$  and  $h_c$  which in turn reduce the blade metal temperature and improved blade creep life
- The FE model calculates the thermal stresses using nodal temperature distributions and the maximum engine rotational speed as boundary conditions. The thermal von Mises stresses under combined thermal and structural loading were reduced as the WAR increased from dry to 1. These stresses reach quite high levels at the coolant regions of the blade. The thermal stress linear FE analysis revealed that none of the blade airfoil regions had undergone any plastic deformation under the influence of the loading conditions examined.
- FE analysis was coupled with the creep lifing model (LMP) to predict the evolution of metal temperature, stress and creep damage over the entire airfoil. Also, the critical areas susceptible to creep were identified and displayed. In summary, the most critical point on the blade with regard to creep life can be identified as the root of the LE. From the lifing point of view this determines the life of the whole blade. Nevertheless, the results reveal an interesting phenomenon that gives a significant insight into blade creep life assessment. It was observed that the blade creep life increases with

increase in WAR from the root to the tip at the LE. This is in contrast to a similar critical point in the TE, where the creep life decreases significantly from root to the tip. In the first case, the creep life increased because stress was reduced along the blade span. Whereas, for the TE, the blade creep life was dominated by the increase of temperature. This is because the average temperature gradient from the root to the tip at the blade for the TE was higher than at the blade LE. A small deviation in stress (LMP) and temperature is therefore amplified in the life prediction. The significance of these trends will be embodied in the redesign of blades for improved blade life. The need to consider the final change in temperature and stress gradients as they affect the various blade sections becomes paramount for an optimised design that increases the blade creep life and durability.

- The comparison of the mechanical stresses along the blade span between the developed analytical model (A) and 3-D parametric FE model (B) reveal that the mechanical stresses of model A were slightly lower at the root and tip sections along the blade span. This difference, which is less than 5%; is mainly due to the fact that model A considers the stress only in the principal axis of rotation, whereas model B accounts for the stress components in all directions on the blade material. Therefore the analytical model (A) presents a suitable approximation of the main stresses on the blade; and can give acceptable results for blade creep life assessment. In general the temperature differences between the 2-D and 3-D models will be influenced by the state of the boundary layer from LE to TE (either laminar or turbulent). In this case, the temperature differences between model A and model B are mainly due to the surface area, metal thickness and temperature and heat transfer coefficient distribution around the pressure and suction surfaces of the blade. These are better described in 3-D FE model. Furthermore, in 1-D you would have to describe a cooling effectiveness whereas in 3-D, the temperature distribution is calculated from the heat balance between the hot cooling blade surfaces.

It can be concluded that the developed creep life model is capable of assessing the main parameters that influence blade cooling performance, such as cooling

methods, alternative cooling fluids, blade geometry, heat transfer coefficients, gas properties, materials and TBCs. In addition, the method will assist users in the selection of the most cost effective engine and will help them to make appropriate inspection and/or maintenance decisions to minimise operating costs while giving the best engine availability.

The thermal stress analysis with the mechanical stress analysis will yield more valuable information about the actual magnitudes of overall stresses encountered by the turbine blade. Therefore, an attempt was made in the present work to use FE Abaqus software to obtain the temperature distribution, mechanical stresses and thermal stress at several cross sections of the stationary gas turbine blade. By knowing these life driving factors, the creep life can be predicted and operation cost reduced. However, a limitation of the integrated creep life model is that it cannot use the thermal stress results in the LMP to calculate the blade creep life as the creep rupture data generated during the material test does not consider both the stress due the thermal gradient and the range of thermal stress values.

## **10.2 Recommendations**

The aim and objectives outlined in this work have been successfully achieved. However, there are some aspects that could be improved upon in future work. The following are recommendations to improve the creep life analytical model and the FE model:

- One of the assumptions made in the effect of WAR in the heat transfer model was that the blade metal temperature changed along the blade span and through the blade wall. Therefore, the heats transfer model could be improved to consider the temperature distribution chordwise in the blade.
- The whole blade cooling process is regarded as a heat exchanger subjected to mainstream hot gas flow. Analysis usually requires detailed information of the geometry of the blade as well as the flow conditions, which are typically not available at the conceptual design stage. Expensive experimental tests and more computation could be used; making the process both time-consuming and laborious. Other simpler heat transfer techniques could be

used to model the blade. One interesting approach would be to model the LE area as a semi-cylinder and the rest of the blade (TE area) as a flat plate subject to mainstream hot gas flow; using analogies for the heat transfer for flow over a cylinder and flat plate previously published in [152; 166; 178]. This kind of model would be necessary for developing a method for life assessment of turbine blade, using the blade span and chord as the basic details required.

- Although the creep failure mechanisms are dominant in stationary GTs, other failure mechanisms such as fatigue and oxidation could be integrated with the creep failure mechanism using different coolant fluids (dry, humid air and steam) in the lifing model. This could be done by applying a linear summation rule for the total damage due to creep, fatigue and oxidation. Another way, (which seems more robust, particularly for transient applications), is to use a thermo-mechanical damage model that couples the effect of the three main damage mechanisms. Some of the models that could be considered include [179-182] amongst others.
- This model is capable of assessing the life of hot section components and there could be further modifications of the model to make it applicable to life estimation of other components such as the compressor.

Linear static analysis of the 3-D FE model was integrated with the analytical lifing model in order to analyse the thermal and stress loads at different WAR as well as to identify the critical areas or feature susceptible to creep on the blade.

- The boundary condition (parameters) such as  $T_g$ ,  $T_{cin}$ ,  $h_c$ , and  $h_g$  were used in the blade FE model along the blade span as obtained from the performance model and the heat transfer model. 3-D CFD analysis could enhance the thermal analysis (blade metal temperature) and thermal stress predictions along the blade span and chordwise. Localised stresses along these parts could be accounted for, thus providing a more accurate creep life estimation. This would be computationally costly and the trade between complexity, cost and accuracy required should be considered carefully.

- The area of interest in this study was only the blade airfoil. The simplified modelling of blade – to – blade contact and the relatively coarse mesh used in the shroud/firtree notches, mean the stress field around firtree grooves and contact faces would be relatively inaccurate and a special model is needed for shroud/firtree life assessment.
- The FE model could be upgraded to include the film cooling configuration and TBC to give more accurate information about the actual magnitudes of overall temperature distributions and thermal stresses (using humid air cooling) on the pressure side and suction side of the turbine blade. This could be easier to implement through the model suggested above (the LE area as semi- cylinder and TE area as flat plate).

## REFERENCES

- [1] Consonni, S. (1992), *Performance prediction of gas/steam cycles for power generation*, PU/CEES Report No.269, A dissertation Presented to the Faculty of Princeton University in Candidacy for the Degree of Doctor of Philosophy, Princeton University.
- [2] Meherwan, P. B. (2006), *Gas Turbine Engineering Handbook*, Third Edition ed, Gulf Professional Publishing.
- [3] Zhimin, L., Mavris, D. N. and Volovoi, V. V. (2001), "Creep Life Prediction of Gas Turbine Components Under Varying Operating Conditions", *ASME International Joint Power Generation Conference*, June 4-7, New Orleans, Louisiana, USA.
- [4] Koff, B. L. (2003), "Gas Turbine Technology Evolution-A Designer's Perspective", *AIAA/ICAS International Air and Space Symposium and Exposition: the Next 100Y*, 14-17 July 2003, Dayton, Ohio.
- [5] Holland, M. J. and Thake, T. F. (1980), "Rotor Blade Cooling in High Pressure Turbine", *Journal of Aircraft*, vol. 17, no. 6, pp. 412-418.
- [6] Torbidoni, L. and Horlock, J. H. (2005), "A New Method to Calculate the Coolant Requirements of a High-Temperature Gas Turbine Blade", *Journal of Turbomachinery*, vol. 127, no. 1, pp. 191-199.
- [7] Still, M., Venzke, H., Durst, F. and Melling, A. (1998), "Influence of Humidity on the Convective Heat Transfer from Small Cylinders", *Experiments in Fluids*, vol. 24, no. 1, pp. 141-150.
- [8] Ainley, D. G. (1957), *Internal Air-Cooling for Turbine Blades a General Design Survey*, 3013, Aeronautical Research Council Reports and Memo, London.
- [9] Halls, A. G. (1967), "Air Cooling of Turbine Blades and Vanes an account of the history and development of gas turbine cooling", *Aircraft Engineering*, vol. 39, no. 8, pp. 4-14.
- [10] Horlock, J. H. (1998), "Heat exchanger performance with water injection (with relevance to evaporative gas turbine (EGT) cycles)", *Energy Conversion and Management*, vol. 39, no. 16-18, pp. 1621-1630.
- [11] Horlock, J. H., Watson, T. D. and Jones, V. T. (2001), "Limitations on Gas Turbine Performance Imposed by Large Turbine Cooling Flows", *Journal of Engineering for Gas Turbine and Power*, vol. 123, no. 3, pp. 487-494.
- [12] Jordal, K., Torbidoni, L. and Massardo, F. A. (2001), "Convective Blade Cooling Modelling for the Analysis of Innovative Gas Turbine Cycles", *Proceedings of ASME Turbo Expo, GT2001-0390*, June 4-7, 2001, New Orleans, Louisiana, USA, ASME.
- [13] Young, B. J. and Wilcock, C. R. (2002), "Modeling the Air-Cooled Gas Turbine: Part 1-General Thermodynamics", *Journal of Turbomachinery*, vol. 124, no. 2, pp. 207-213.

- [14] Young, J. B. and Wilcock, R. C. (2002), "Modeling the Air-Cooled Gas Turbine: Part 2-Coolant Flows and Losses", *Journal of Turbomachinery*, vol. 124, no. 2, pp. 214-222.
- [15] Torbidoni, L. and Massardo, F. A. (2004), "Analytical Blade Row Cooling Model for Innovative Gas Turbine Cycle Evaluations Supported by Semi-Empirical Air-Cooled Blade Data", *Journal of Engineering for Gas Turbines and Power*, vol. 3, no. 126, pp. 498-506.
- [16] Horlock, J. H. and Torbidoni, L. (2006), "Turbine Blade Cooling: The Blade Temperature Distribution", *Journal of Power and Energy*, vol. 220, pp. 343-353.
- [17] Mathioudakis, K. and Tsalavoutas, T. (2002), "Uncertainty Reduction in Gas Turbine Performance Diagnostics by Accounting for Humidity Effects", *Journal of Engineering for Gas Turbines and Power, ASME*, vol. 124, pp. 801-808.
- [18] Meacock, A. J. and White, A. J. (2006), "The Effect of Water Injection on Multispool Gas Turbine Behavior", *Journal of Engineering for Gas Turbine and Power*, vol. 128, no. 1, pp. 97-102.
- [19] Brun, K., Kurz, R. and Simmons, H. R. (2006), "Aerodynamic Instability and Life-Limiting Effects of Inlet and Interstage Water Injection into Gas Turbine", *Journal of Engineering for Gas Turbine and Power*, vol. 128, no. 3, pp. 617-625.
- [20] Szargut, J., Skorek, J. and Szczygiel, I. (2000), "Influence of Blade Cooling on the Efficiency of Humid Air Turbine", *International Journal of Applied Thermodynamics*, vol. 3, no. 1, pp. 21-26-26.
- [21] Sanjay, Singh, O. and Prasad, B. N. (2009), "Comparative performance analysis of cogeneration gas turbine cycle for different blade cooling means", *International Journal of Thermal Sciences*, vol. 48, no. 7, pp. 1432-1440.
- [22] AGARD-332 (1995), *Recommended Practices for the Assessment of the Effects of Atmospheric Water Injection on the Performance and Operability of Gas Turbines Engines*, 332.
- [23] Amell, A. A. and Cadavid, F. J. (2002), "Influence of the relative humidity on the air cooling thermal load in gas turbine power plant", *Applied Thermal Engineering*, vol. 22, no. 13, pp. 1529-1533.
- [24] Albeirutty, M. H., Alghamdi, A. S. and Najjar, Y. S. (2004), "Heat transfer analysis for a multistage gas turbine using different blade-cooling schemes", *Applied Thermal Engineering*, vol. 24, no. 4, pp. 563-577.
- [25] Marcus, E. B. S. (2008), *A PARAMETRIC PHYSICS BASED CREEP LIFE PREDICTION APPROACH TO GAS TURBINE BLADE CONCEPTUAL DESIGN* (unpublished PhD thesis), Georgia Institute of Technology.
- [26] Carter, T. J. (2005), "Common failures in gas turbine blades", *Engineering Failure Analysis*, vol. 12, no. 2, pp. 237-247.



- [27] Zhuang, W. Z. and Swansson, N. S. (1998), *Thermo-Mechanical Fatigue Life Prediction A Critical Review*, DSTO-RR-0609.
- [28] Kurz, R. and Brun, K. (2001), "Degradation in Gas Turbine Systems", *Journal of Engineering for Gas Turbines and Power*, vol. 123, no. 70, pp. 70-77.
- [29] Zwebek, A. I. and Pilidis, P. (2004), "Degradation Effects on Combined Cycle Power Plant Performance---Part III: Gas and Steam Turbine Component Degradation Effects", *Journal of Engineering for Gas Turbines and Power*, vol. 126, no. 2, pp. 306-315.
- [30] Naeem, M., Singh, R. and Probert, D. (2001), "Consequences of Aero-Engine Deteriorations for Military Aircraft", *Applied Energy*, vol. 70, no. 2, pp. 103-133.
- [31] Harrison, G. F., Tranter, P. H., Shepherd, D. P. and Ward, T. (2004), "Application of multi-scale modelling in aeroengine component life assessment", *Materials Science and Engineering A*, vol. 365, no. 1-2, pp. 247-256.
- [32] George, Y. L. (2007), *High Temperature Corrosion and Materials Applications*, ASM International, USA.
- [33] Sourmail, T. (2004), *Coatings for High Temperature Applications*, available at: <http://www.thomas-sourmail.org/coatings/single-page.html> (accessed November, 2008).
- [34] Dibbert. A (2006), "Extending Gas Turbine Life", *Turbomachinery International*, vol. 47, no. 2, pp. 36-37.
- [35] Stephenson, D. J. and Nicholls, J. R. (1995), "Modelling the influence of surface oxidation on high temperature erosion", *Wear*, vol. 186-187, no. Part 1, pp. 284-290.
- [36] MW Industries. , *Fatigue life Estimates Using Goodman Diagrams*, available at: <http://www.mw-ind.com/TechTips/?TipNO=19> (accessed January, 2009).
- [37] Viswanathan, R. (1989), *Damage Mechanisms and Life Assessment of High-Temperature Components*, ASM INTERNATIONAL, Metals Park, Ohio.
- [38] Mestaneke, P. (2008), "Low Cycle Fatigue Analysis of a Last Stage Steam Turbine Blade", *Applied and Computational Mechanics*, vol. 2, pp. 71-82.
- [39] Viswanathan. R and Stringer. J (2000), "Failure Mechanisms of High Temperature Components in Power plants", *Journal of Engineering Materials and Technology*, vol. 122, no. 3, pp. 246-255.
- [40] Holcomb, G. R. (2000), "Hot corrosion in a temperature gradient", *Materials and Corrosion*, vol. 51, no. 8, pp. 564-569.

- [41] Wellman, R. G. and Nicholls, J. R. (2004), "High Temperature Erosion-Oxidation Mechanisms, Maps and models", *Wear*, vol. 256, no. 9-10, pp. 907-917.
- [42] Eliaz, N., Shemesh, G. and Latanision, R. M. (2002), "Hot corrosion in gas turbine components", *Engineering Failure Analysis*, vol. 9, no. 1, pp. 31-43.
- [43] Weber, B., Jin, H., Pistor, R. and Lowden, P. (2005), "Application of an Integrated Engineering Approach for LM1600 Blade Life On-Line Assessment", *16th Symposium on industrial application of gas turbines (IAGT)*, 12-14, October, Canada.
- [44] Prakash, D. G. L., Walsh, M. J., Maclachlan, D. and Korsunsky, A. M. (2009), "Crack Growth Micro-Mechanisms in the IN718 Alloy Under the Combined Influence of Fatigue, Creep and Oxidation", *International Journal of Fatigue*.
- [45] Bernstein, H. (2006), "Materials Issues for Users of Gas Turbines", *35th Turbomachinery Symposium, ASMW IGTI Lecture, Turbomachinery Laboratory Technical Paper, ASME*, Turbomachinery Laboratory, Texas A&M University, College Station, Texas.
- [46] Penny, R. K. and Marriott, D. L. (1995), *Design for Creep*, 2nd, Chapman and Hall.
- [47] Webster, G. A. and Ainsworth, R. A. (1994), *High Temperature Component Life Assessment*, Chapman & Hall.
- [48] Dieter, G. E. (1988), *Mechanical Metallurgy*, McGraw-Hill Book Company, UK.
- [49] Metallurgical Consultants. , *Creep and Stress Rupture*, available at: <http://www.materialsengineer.com/CA-Creep-Stress-Rupture.htm> (accessed July, 2008).
- [50] Naem, M., Singh, R. and Probert, D. (1998), "Implications of engine deterioration for creep life", *Applied Energy*, vol. 60, no. 4, pp. 183-223.
- [51] Cane, B. J. and Aplin, P. F. (1994), "Creep Life Assessment Methods", *Journal of Strain Analysis*, vol. 29, no. 3, pp. 225-232.
- [52] Bagnall, S. (2008), *Fatigue Life Prediction in Turbine Components*, 52.
- [53] Li, J. and Dasgupta, A. (1993), "Failure-mechanism models for creep and creep rupture", *Reliability, IEEE Transactions on*, vol. 42, no. 3, pp. 339-353.
- [54] Altenbach, H. and Naumenko, K. (2007), *Modeling of Creep for Structural Analysis*, Springer Berlin Heidelberg New York.
- [55] Marahleh, G., Kheder, A. R. I. and Hamad, H. F. (2006), "Creep-Life Prediction of Service-Exposed Turbine Blades", *Materials Science*, vol. 42, no. 4, pp. 476-481.
- [56] Bunker, R. S. (2006), "Cooling Design Analysis", In *The Gas Turbine Handbook*, The National Energy Technology Laboratory, USA, pp. 296-308.

- [57] Frank, J. C. (2006), "Heat Transfer Analysis", in *The Gas Turbine Handbook*, The National Energy Technology Laboratory, USA, pp. 389-409.
- [58] Wilcock, R. C., Young, J. B. and Horlock, J. H. (2005), "The Effect of Turbine Blade Cooling on the Cycle Efficiency of Gas Turbine Power Cycles", *Journal of Engineering for Gas Turbines and Power*, vol. 127, no. 1, pp. 109-120.
- [59] Kays, W. M. and London, A. L. (1998), *Compact Heat Exchangers*, 3rd ed, Krieger Publishing Company.
- [60] James, G. V. (1983), *Feasibility of Water Injection into the Turbine Coolant to Permit Gas Turbine Contingency Power for Helicopter Application*, TM-83043, NASA, Arizona, March 1983.
- [61] Cleeton, J. P. E., Kavanagh, R. M. and Parks, G. T. (2009), "Blade cooling optimisation in humid-air and steam-injected gas turbines", *Applied Thermal Engineering*, vol. 29, no. 16, pp. 3274-3283.
- [62] Eno, D. R., Young, G. A. and Sham, T. L. (2008), "A Unified View of Engineering Creep Parameters", *Proceedings of PVP2008, ASME Pressure Vessels and Piping Division Conference*, July 21-31, 2008, Chicago, Illinois, pp. 1.
- [63] Bueno, L. O. and Sordi, V. L. (2008), "Creep behaviour of Fe–Mn–Al steel from 500 °C to 800 °C: Part 2: Aspects of rupture strength and parametric analysis", *Materials Science and Engineering: A*, vol. 483-484, pp. 560-563.
- [64] DiMelfi, R. J. (1978), "Comments on: "Understanding the Larson-Miller parameter", by F. T. Furillo, S. Purushothaman and J. K. Tien (1)", *Scripta Metallurgica*, vol. 12, no. 4, pp. 327-329.
- [65] Razak, A. M. Y. (2007), *Industrial Gas Turbine: Performance and Operability*, Woodhead Publishing Limited, Abington Hall Cambridge, England.
- [66] Cookson and Haslam, A. S. (2008), *Mechanical Design of Turbomachinery* (unpublished MSc Lecture Notes), Cranfield University.
- [67] Monkman, F. C. and Grant, N. J. (1965), "An Empirical Relationship between Rupture Life and Minimum Creep Rate", *Deformation and Fracture at Elevated Temperatures*, MIT Press, .
- [68] Tinga, T., De Wolf, W. B., Visser, W. P. J. and Woldendorp, S. (2001), "Integrated Lifting Analysis of a Film-Cooled Turbine Blade", *RTO-AVT Symposium on Monitoring and Management of Gas Turbine Fleets for Extended Life and Reduced Costs* NATO Research and Technology, Manchester, UK.
- [69] Betten, J., Sklepus, S. and Zolochovsky, A. (1999), "A Microcrack Description of Creep Damage in Crystalline Solids with Different Behaviour in Tension and Compression", *International Journal of Damage Mechanics*, vol. 8, no. 3, pp. 197-232.

- [70] Chaboche, J. L. (1987), "Continuum damage mechanics: Present state and future trends", *Nuclear Engineering and Design*, vol. 105, no. 1, pp. 19-33.
- [71] Cane, B. J. (1982), "Remaining creep life estimation by strain assessment on plant", *International Journal of Pressure Vessels and Piping*, vol. 10, no. 1, pp. 11-30.
- [72] Eshati, S., Abdul Ghafir, F. M., Laskaridis, P. and Li, Y. G. (2010), "Impact of Operating Conditions and Design Parameters on Gas Turbine Hot Section Creep Life", *Proceedings of ASME Turbo Expo 2010: Power for Land, Sea and Air, GT2010-22334*, June 14-18, 2010, Glasgow, UK.
- [73] Eshati, S., ABU, A., LASKARIDIS, P. and HASLAM, A. (2011), "Investigation into the Effects of Operating Conditions and Design Parameters on the Creep Life of High Pressure Turbine Blades in A Stationary Gas Turbine Engine ", *10th International Symposium on Compressor and Turbine Flow Systems-Theory and Application Areas* Lodz, 26 - 28 October, 2011.
- [74] Wood, M. I. (1999), "Gas Turbine Hot Section Components: the challenge of "residual life" assessment", *Journal of Power and Energy*, vol. 214, no. 3, pp. 193-201.
- [75] Dedekind, M. O. (1994), "Implementation of creep-fatigue model into finite element code to assess cooled turbine blade", *International Journal of Pressure Vessels and Piping*, vol. 59, no. 1-3, pp. 13-19.
- [76] DiCristoforo, P. E. and Elledge, M. (2004), "Stress Redistribution for Increased Creep Life in the GE MS6001 B Second-Stage Blade", *Journal of Engineering for Gas Turbines and Power*, vol. 126, no. 1, pp. 127.
- [77] Naeem, M. (2009), "Implications of day temperature variation for an aero-engine's HP turbine-blade's creep life-consumption", *Aerospace Science and Technology*, vol. 13, no. 1, pp. 27-35.
- [78] Cerri, G., Gazzino, M. and Borghetti, S. (2006), "Hot Section Life Assessment by a Creep Model to Plan Gas Turbine Based Power Plant Electricity Production", *3rd international conference, The Future of Gas Turbine technology*, 11-12, 2006, Brussels, Belgium.
- [79] Assoul, Y., Benbelaid, S., Zeravcic, V. S., Bakic, G. and Dukic, M. (2008), "Life Estimation of First Stage High Pressure Gas Turbine Blades", *Scientific Technical Review*, vol. LVIII, no. 2, pp. 8-13.
- [80] Abdul Ghafir, M. F., Li, Y. G., Singh, R., Huang, K. and Feng, X. (2010), "Impact of operating and health conditions on aero gas turbine hot section creep life using a creep factor approach (GT2010-22332)", *Proceedings of ASME Turbo Expo 2010: Power for Land, Sea and Air*, Glasgow, UK.
- [81] Cerri, G., Gazzino, M., Botta, F. and Salvini, C. (2008), "Production Planning with Hot Section Life Prediction for Optimum Gas Turbine Management", *International Journal of Gas Turbine, Propulsion and Power Systems*, vol. 2, no. 1, pp. 9-16.

- [82] Mohamed, W., Eshati, S., Pilidis, P., Ogaji, S. O. T. and Laskaridis, N.,P. A. (2011), "A method to evaluate the impact of power demand on HPT blade creep life", *Proceedings of ASME Turbo Expo 2011: Power for Land, Sea and Air-GT2011-45092*, June, 6-10, Vancouver, Canada.
- [83] Hagmeijer, R., De Boer, A., Tinga, R., Ten Hoeve, H. J., Huisman, H. N., Kok, J. C., Kool, G. A., Koolloos, M. F. J., Visser, W. P. J., Woldendorp, S. and DE wolf, W. B. (May 2000), *Towards integrated analysis of gas turbine components for life prediction*, NLR-TP-2000-196, National Aerospace Laboratory NLR.
- [84] Tinga, T., Visser, W. P. J., DE wolf, W. B. and Broomhead, M. J. (2000), *Integrated Lifting Analysis Tool for Gas Turbine Components*, NLR-TP-2000-049, National Aerospace Laboratory NLR.
- [85] Rosario, D. A. (2002), "Life Assessment of Critical Boiler and turbine components Using EPRI's Creep-Fatigue Pro Software", *EPRI International Conference on Advances in Power Plant Life Assessment*, March 11-13, 2002, Orlando, Florida.
- [86] Aghaie-Khafri, M. and Hajjavady, M. (2008), "The effect of thermal exposure on the properties of a Ni-base superalloy", *Materials Science and Engineering: A*, vol. 487, no. 1–2, pp. 388-393.
- [87] Aghaie-Khafri, M. and Noori, M. (2011), "Life prediction of a Ni-base superalloy", *Bulletin of Materials Science*, vol. 34, no. 2, pp. 305-309.
- [88] Kaftelen, H. and Baldan, A. (2004), "Comparative creep damage assessments using the various models", *Journal of Materials Science*, vol. 39, no. 13, pp. 4199-2461.
- [89] Evans, M. (2004), "A Comparative Assessment of Creep Property Predictions for a 1CrMoV Rotor Steel Using the CRISPEN, CDM, Omega and Theta Projection Techniques", *Journal of Materials Science*, vol. 39, no. 6, pp. 2053-2071.
- [90] Ibanez, A. R., Saxena, A. and Kang, J. (2006), "Creep Deformation and Rupture Behaviour of Directionally Solidified GTD 111 Superalloy", *Strength, Fracture and Complexity*, vol. 4, no. 12, pp. 1010-1020.
- [91] Bagnoli, K. E., Cater-Cyker, Z. and Budiman, B. S. (2007), "Evaluation of the theta projection technique for estimating the remaining creep life of GTD-111DS turbine blades: GT2007-28345", *presented at the ASME Turbo Expo 2007: Power for Land, Sea and Air*, Motreal, Canada.
- [92] Baldan, A. and Tascioglu, E. (2008), "Assessment of  $\theta$ -Projection Concept and Fracture Cavitation", *Journal of Materials Science*, vol. 43, no. 13, pp. 4592-4606.
- [93] Miodownik, A., Li, X., Saunder, N. s. and Schille, J. P. (2003), "Modelling of Creep in Nickel Based Superalloys", *Sixth International Charles Parsons Turbine Conference*, Dublin, Ireland.

- [94] Sheperd, D., Ward, T. J., Wisbey, A., Vermeulen, B. and Boyd Lee, A. (2004), "Life extension methods in aero-engines", *Operation Maintenance and Materials Issues-OMMI*, vol. 3, no. 1, pp. 1-15.
- [95] Robinson, E. L. (1938), "Effect of temperature variation on the creep strength of steels", *Trans. ASME*, vol. 60, pp. 253-259.
- [96] Cunha, F. J., Dahmer, M. T. and Chyu, M. K. (2006), "Thermal-Mechanical Life Prediction System for Anisotropic Turbine Components", *TRANSACTIONS- AMERICAN SOCIETY OF MECHANICAL ENGINEERS JOURNAL OF TURBOMACHINERY*, vol. 128, no. 2, pp. 240-250.
- [97] Rinaldi, C., Bicego, V. and Colombo, P. P. (2006), "Validation of CESI blade life Management System by Case Histories and in Site NDT", *Journal of Engineering for Gas Turbines and Power*, vol. 128, no. 1, pp. 73-80.
- [98] Knowles, D. M. and MacLachlan, D. W. (2004), "The effect of material behaviour on the analysis of single crystal turbine blades: material model development", *Current Applied Physics*, vol. 4, no. 2-4, pp. 300-303.
- [99] Qi, W. and Bertram, A. (1999), "Anisotropic continuum damage modeling for single crystals at high temperatures", *International Journal of Plasticity*, vol. 15, no. 11, pp. 1197-1215.
- [100] Qi, W., Brocks, W. and Bertram, A. (2000), "An FE-analysis of anisotropic creep damage and deformation in the single crystal SRR99 under multiaxial loads", *Computational Materials Science*, vol. 19, no. 1-4, pp. 292-297.
- [101] MacLachlan, D. and Knowles, D. (2000), "Creep-behavior modeling of the single-crystal superalloy CMSX-4", *Metallurgical and Materials Transactions A*, vol. 31, no. 5, pp. 1401-1411.
- [102] MacLachlan, D. W. and Knowles, D. M. (2001), "Modelling and prediction of the stress rupture behaviour of single crystal superalloys", *Materials Science and Engineering: A*, vol. 302, no. 2, pp. 275-285.
- [103] Karaivanov, V. G., Mazzotta, D. W., Chyu, M. K., Slaughter, W. S. and Alvin, M. A. (2008), "Three-Dimensional Modeling of Creep Damage in Airfoils for Advanced Turbine System", *Proceeding of ASME Turbo Expo 2008: Power for Land, Sea and air*, 9-13, June, Berlin, Germany.
- [104] Vladimirov, I. N., Reese, S. and Eggeler, G. (2009), "Constitutive modelling of the anisotropic creep behaviour of nickel-base single crystal superalloys", *International Journal of Mechanical Sciences*, vol. 51, no. 4, pp. 305-313.
- [105] Meric, L., Poubanne, P. and Cailletaud, G. (1991), "Single crystal modeling for structural calculations: part I-model presentation", *J. Eng. Mater. Technol.*, vol. 113, pp. 162-170.
- [106] MacLachlan, D. W. and Knowles, D. M. (2002), "The effect of material behaviour on the analysis of single crystal turbine blades: Part I ? Material model", *Fatigue & Fracture of Engineering Materials & Structures*, vol. 25, no. 4, pp. 385-398.

- [107] Maclachlan, D. W. and Knowles, D. M. (2002), "The effect of material behaviour on the analysis of single crystal turbine blades: Part II ? Component analysis", *Fatigue & Fracture of Engineering Materials & Structures*, vol. 25, no. 4, pp. 399-409.
- [108] ASHBY, M. F. and DYSON, B. F. (1986), "Creep Damage Mechanics and Micromechanisms", *Advanced Fracture Research - Proceedings International Conference on Fractures (6th)*, vol. 6, no. 1, pp. 3-30.
- [109] DYSON, B. F. (2000), "Use of CDM in Materials Modeling and Component Creep Life Prediction", *Journal of Pressure Vessel Technology*, vol. 122, no. 3, pp. 281-296.
- [110] International Atomic Energy Agency (IAEA, Training course report , 2005), *Non-destructive testing for plant life assessment*, IAEA-TCS-26, IAEA, Vienna International Centre.
- [111] Saniie, J., Panda, B., Wang, T. and Nagle, D. T. (1990), "Life Assessment of Creep Degraded Super Alloy Materials Using Ultrasound", *Ultrasonics Symposim, Proceedings, IEEE 1990*, Vol. 2, 4-7 Dec, Honolulu, HI, USA, pp. 987-990.
- [112] Pitkänen, J., Hakkarainen, T., Jeskanen, H., Kuusinen, P., Lahdenperä, K. and Särkiniemi, P. (2000), "NDT methods for revealing anomalies and defects in gas turbine blades", *15th World Conference on Non-Destructive Testing*, Rome.
- [113] AUERKARI, P., PITKÄNEN, J., PIHKAKOSKI, M., MUURINEN, L., KEMPPAINEN, M. and KANGAS, P. (2002), "Maintenance of gas turbine-impact and implication for NDT", *Insight*, vol. 44, no. 9, pp. 568-571.
- [114] Kumar Raja, P., Ganesan, V., Saravanan, T., Bagavathiappan, S. and Balasubramaniam, K. (2009), "Detection of micro-crack in the HP turbine blades using phase array and radiography techniques and enhancement of radiographic images by image processing", *National Seminar and Exhibition on Non-Destructive Evaluation*, Tiruchy, India.
- [115] Abbasi, W. and Rahman, S. (Dec 2-4, 2008), "NDE Inspections and Lifetime Assessment of Turbine Equipment", *Power-Gen International-Siemens Energy*, Orlando, Florida.
- [116] Vagn, H. J. (1998), "Non-destructive metallography used on-site, possibilities and experience", *7th European Conference on Non-Destructive Testing*, Copenhagen.
- [117] Zuljan, D. and Grum, J. (2005), "Non-destructive metallographic analysis of surface and microstructures by means of replicas," in *The 8th International Conference of the Slovenian Society for Non-Destructive Testing*, *The 8th International Conference of the Slovenian Society for Non-Destructive Testing*, September 1-3, Slovenia.
- [118] Neubauer, B. and Wedel, U. (1983), "Restlife estimation of creeping component by means of replicas", *Advances in Life Prediction Methods*, *American Society of Mechanical Engineering*, New York, pp. 307.

- [119] Viswanathan, R. (1988), "Residual life techniques for plant life extension", *Materials Science and Engineering: A*, vol. 103, no. 1, pp. 131-139.
- [120] Gooch, D. J. (1988), "Plant-life extension-remanent-life assessment of high-temperature components", *Power Engineering Journal*, vol. 2, no. 6, pp. 323-331.
- [121] Brett, S. and et al. (2005), *Residual life assessment and microstructure*, AC/MC/93, ECCO, Italy.
- [122] Vaezi, M. and Soleymani, M. (2009), "Creep Life Prediction of Inconel 738 Gas Turbine Blade", *Journal of Applied Sciences*, vol. 9, no. 10, pp. 1950-1955.
- [123] Zhimin, L., Dimitri, N. M. and Vitali, V. V. (2001), "Creep Life Prediction of Gas Turbine Components under Varying Operating Conditions", *Proceeding of IJPGC'01: ASME International Joint Power Generation Conference*, 4-7, June, New Orleans, Louisiana, USA, pp. 1.
- [124] Zhimin, L., Vitali, V. and Dimitri, N. M. (2002), "Probabilistic Remaining Creep Life Assessment for Gas Turbine Components under Varying Operating conditions", *43rd AIAA/ASME/ASCE/AHS/ASC Structures, Structural Dynamics, and Materials Conference*, 22-25, April, Denver, Colorado.
- [125] Wallace, J. M. and Dimitri, N. M. (2003), "Creep Life Uncertainty Assessment of a Gas Turbine Airfoil", *Proceeding of 4<sup>th</sup> AIAA Non-Deterministic Approaches Forum*, 7-10, April, Norfolk Virginia.
- [126] Zhao, J., Li, D., Zhang, J., Feng, W. and Fang, Y. (2009), "Introduction of SCRI model for creep rupture life assessment", *International Journal of Pressure Vessels and Piping*, vol. 86, no. 9, pp. 599-603.
- [127] Zhao, J., Han, S., Gao, H. and Wang, L. (2004), "Remaining Life Assessment of a CrMoV Steel Using the Z-Parameter Method", *International Journal of Pressure Vessels and Piping*, vol. 81, pp. 757-760.
- [128] Harris, J. (2001), "Fuzzy Logic Methods in Fatigue and Creep", *The Journal of Strain Analysis for Engineering Design*, vol. 36, no. 4, pp. 411-420.
- [129] Koul, A., Bhanot, S., Tiku, A. and Junkin, B. (2008), "Improving Component Life Prediction Accuracy and Reliability Through Physics Based Prognosis-A Probabilistic Turbine Blade Case Study", *Proceedings of ASME Turbo Expo 2008: Power for Land, Sea and air GT2008*, June 9-13, Berlin.
- [130] Koul, A. K., Tiku, A., Shankar, S. and Zhao, J. (2010), "Probabilistic creep life prediction of turbine disc-GT2010-22169", *Proceeding of ASME Turbo Expo 2010*, Glasgow, UK.
- [131] Liu, Z., Mavris, D. and Volovoi, V. (2001), "Creep life prediction of gas turbine components under varying operating conditions", *ASME International Joint Power Generation Conference*, Louisiana, USA.



- [132] Liu, Z., Volovoi, V. and Mavris, D. (2002), "Probabilistic Remaining Creep Life Assessment for Gas Turbine Components under Varying Operating Conditions", *43rd AIAA/ASME/ASCE/AHS/ASC Structures, Structural Dynamics, and Materials Conference*, Denver, Colorado.
- [133] Liu, Z. and Mavris, D. (2004), "A Methodology for Probabilistic Creep-Fatigue Life Assessment of Hot Gas Path Components", *presented at the 45th AIAA/ASME/ASCE/AHS/ASC Structures, Structural Dynamics and Materials Conference*, Palm Springs, California.
- [134] Frovola, O., Roos, E., Maile, K. and Muller, W. (2011), "Representation of the heat specific creep rupture Behaviour of 9%Cr steels using neural networks", *Transactions on Machine Learning and Data Mining*, vol. 4, no. 1, pp. 1-16.
- [135] Gupta, V. K., Kwatra, N. and Ray, S. (2007), "Artificial neural network modeling of creep behavior in a rotating composite disc", *Engineering Computations*, vol. 24, no. 2, pp. 151-164.
- [136] Jeong, H. and Kim, D. -. (2002), "Estimation of Creep Voids Using a Progressive Damage Model and Neural Networks", *Research in Nondestructive Evaluation*, vol. 14, no. 1, pp. 33-45.
- [137] Sakai, T., Ogata, T., Nomoto, A. and Watanabe, K. (2000), "Elasto-Plastic and Creep Analysis of A First Stage Blade in A Land Based Gas Turbine Under Steady State Operating Conditions", *Proceeding of ASME Turbo Expo 2000*, 8-11, May, Munich Germany.
- [138] Vassilios. (2008), *Gas Turbine Performance Simulation and Diagnostics-Turbomatch Manual* (unpublished Course Notes).
- [139] Ramsden. (2008), *Gas Turbine Fundamentals and Turbomachinery* (unpublished MSc Lecture Notes, Cranfield University), Cranfield University.
- [140] Saravanamuttoo, H., Rogers, G., Cohen, H. and Straznicky, P. (2009), *Gas Turbine Theory*, Prentice Hall imprint, Great Britain.
- [141] Walsh, P. P. and Fletcher, P. (2004), *Gas Turbine Performance*, second edition ed, Blackwell Science.
- [142] Gordon, S. and McBride, B. J. (1994), *Computer program for calculation of complex chemical equilibrium and applications: part I Analysis*, NASA RP 1311, National Aeronautics and Space Administration.
- [143] McBride, B. J. and Gordon, S. (1996), *Computer Program for Calculation of Complex Chemical Equilibrium and Applications: Part II*. NASA RP 1311, National Aeronautics and Space Administration.
- [144] Becker, A. (2006), *Engine Company Evaluation of Feasibility of Aircraft Retrofit Water-Injected Turbomachines*, NASA/CR-2006-213871, NASA, Hanover.
- [145] Daggett, D. L. (2004), *Water Misting and Injection of Commercial Aircraft Engines to Reduce Airport NOx*, NASA/CR-2004-212957, NASA Center for Aerospace Information.

- [146] Uzoigwe, I. G. (2011), *The effect of steam injection on the creep life of high pressure turbine blade* (unpublished MSc thesis), Cranfield University.
- [147] Tsilingiris, P. T. (2008), "Thermophysical and transport properties of humid air at temperature range between 0 and 100 °C", *Energy Conversion and Management*, vol. 49, no. 5, pp. 1098-1110.
- [148] Soares, C. (2007), *Gas Turbines : A Handbook of Air, Land and Sea Applications*, Elsevier / Butterworth-Heinemann, Amsterdam.
- [149] Vishal, S. (2008), *Advanced Performance Simulation of Gas Turbine Components and Fluid Thermodynamic Properties* (unpublished PhD thesis), Cranfield University.
- [150] James, M. G. (2004), *MECHANICS OF MATERIALS*, Sixth Edition ed, Bill Stenquist.
- [151] Chiesa, P. and Macchi, E. (2002), "A Thermodynamic Analysis of Different Options to Break 60% Electric Efficiency in Combined Cycle Power Plants", *Proceeding of ASME Turbo Expo, GT-2002-30663*, June 3-6, Amsterdam, The Netherlands.
- [152] Frank, P. I. and David, P. D. (2002), *Fundamentals of Heat and Mass Transfer*, Fifth Edition ed, John Wiley & Sons, USA.
- [153] Frank, E. J. (1995), *Techniques and Topics in Flow Measurement* CRC Press, Boca Raton. Florida.
- [154] Tetens, O. (1930), "Uber einige meteorologische Begiffe.Z.", *Geophys*, vol. 6, pp. 297-309.
- [155] Perry, H. R. (2007), *Perry's Chemical Engineering Handbook*, 8th Edn ed, McGraw-Hill, New York.
- [156] Yunus, A. C. and Afshin, J. G. (2010), *Heat and Mass Transfer: Fundamentals and Applications*, 4th ed, McGraw-Hill Education - Europe.
- [157] Rubini. (2008), *Turbine blade cooling* (unpublished MSc Lecture Notes), Cranfield University.
- [158] El-Masri, M. A. (1986), "On Thermodynamics of Gas-Turbine Cycles: Part 2---A Model for Expansion in Cooled Turbines", *Journal of Engineering for Gas Turbines and Power*, vol. 108, no. 1, pp. 151-159.
- [159] Richards, D. R. and Florschuetz, L. W. (1984), *Forced Convection Heat Transfer to Air/Water Vapor Mixtures*, 3769, NASA Natinal Aeronautics and Space Administration.
- [160] Kestin, J. and Whitelaw, J. H. (1964), "The viscosity of dry and humid air", *International Journal of Heat and Mass Transfer*, vol. 7, no. 11, pp. 1245-1255.
- [161] Genick Bar-Meri. (2008), *Basics of Fluid Mechanics*.
- [162] Melling, A., Noppenberger, S., Still, M. and Venzke, H. (1997), "Interpolation Correlations for Fluid Properties of Humid Air in the

- Temperature Range 100 °C to 200 °C", *Journal of Physical and Chemical Reference Data*, vol. 26, no. 4, pp. 1111-1123.
- [163] Mason, E. A. and Saxena, S. C. (1958), "Approximate Formula for the Thermal Conductivity of Gas Mixtures", *Physics of Fluids*, vol. 1, no. 5, pp. 361-369.
- [164] Cheesewright, R., Heggs, P. J., Martin, B. W., Parry, W. J. and Ralston, T. (1992), *Forced Convection Heat Transfer in Straight Tubes, Part 1: Turbulent flow*, ESDU 92003, The Institution of Chemical Engineers.
- [165] Lakshminarayana, B. (1996), *Fluid Dynamics and Heat Transfer of Turbomachinery*, John Wiley & Sons, New York.
- [166] Holman, J. P. (1997), *Heat Transfer*, 8th ed, McGraw-Hill, New York.
- [167] Colantuoni, A., Colella, L., Di Nola, D. C. and Marotta, D. (1993), *Aero-Thermal Design of A Cooled Transonic NGV and Comparison with Experimental Result*, AGARD-CP-527, Antalya, Turkey.
- [168] Guenette, G. R., Pappas, G. and Epstein, A. H. (1993), "The Influence of Non-Uniform Spanwise Inlet Temperature on Turbine Rotor Heat Transfer", *AGARD Heat Transfer and Cooling in Gas Turbine*, 12th-16th October, 1992, Antalya, Turkey.
- [169] Je-Chin, H., Sandip, D. and Srinath, V. E. (2000), *Gas Turbine Heat Transfer and Cooling Technology*, Taylor & Francis.
- [170] Rohsenow, W. M., Hartnett, J. P. and Ganic, E. N. (1985), *Handbook of Heat Transfer Fundamentals*, 2nd ed, McGraw-Hill Book Co, New York.
- [171] De Wolf, W. B., Woldendorp, S. and Tinga, T. (2001), "Analysis of combined convective and film cooling on an existing turbine blade", *RTO-AVT Symposium Heat Transfer and Cooling in Propulsion and Power Systems*, May, 2001, Loen, Norway, NATO Research and Technology Organisation.
- [172] Goldstein, R. J. and Haji-Sheikh, A. (1967), "Prediction of Film Cooling Effectiveness", *Proceedings of Japanese Society of Mechanical Engineering, SEMI-International Symposium*, Vol. 2, JSME, Tokyo, pp. 213-218.
- [173] Abaqus-CAE, *Abaqus Version 6.7-Tutorials, Getting Startes with Abaqus*, DS Dassault Systemes.
- [174] Manjunath. (2009), *Finite-Element Project: Abaqus Tutorial*.
- [175] Nimonic Alloy. , *Special Metals*, available at: <http://www.specialmetals.com/products/index.php> (accessed October, 2008).
- [176] Gokhale, N. S., Deshpande, S. S., Bedekar, S. V. and Thite, A. N. (2008), *Practical Finite Element Analysis*, First Edition, Finite to Infinite, India.
- [177] Gomes, E. E. B. (2007), *Operational optimisation of gas turbine distributed generation systems in a competitive electricity market* (PhD thesis), Cranfield University.

- [178] Frank, M. W. (1988), *Heat and Mass Transfer*, Addison-Wesley, USA.
- [179] Sehitoglu, H. (1990), "Thermo-mechanical fatigue of mar-m247: Part 2-life prediction", *Journal of Engineering Materials and Technology*, vol. 112, pp. 80-89.
- [180] Miller, M. P., McDowell, D. L., Oehmke, R. L. T. and Antolovich, D. D. (eds.) (1993), *Life Prediction Model for Thermomechanical fatigue Based on Microcrack Propagation*, ASTM STP 1186 ed, American society for testing and materials.
- [181] Miller, M. P., McDowell, D. L. and Oehmke, R. L. T. (1992), "A Creep-Fatigue-Oxidation Microcrack Propagation Model for Thermomechanical Fatigue", *Journal of Engineering Materials and Technology*, vol. 114, no. 3, pp. 282-288.
- [182] Zamrik, S. Y. and Renauld, M. L. (2000), "Thermo-mechanical out-of-phase fatigue life of overlay coated in-738lc gas turbine material", *In Thermo-Mechanical Fatigue Behavior of Materials, ASTM*, vol. 3, pp. 119-137.
- [183] Ainley, D. G. and Mathieson, G. C. R. (1951), *A Method of Performance Estimation for Axial-Flow Turbines*. 2974, British Aeronautical Research Council, London.
- [184] David, K. H. (2008), *Performance Limits of Axial Turbomachine Stages* (MSc thesis), Massachusetts Institute of Technology.
- [185] Mattingly, J.D., ( 2006), *Elements of Propulsion - Gas Turbines and Rockets*, American Institute of Aeronautics and Astronautics, Inc, AIAA.
- [186] Wilson, D. G. (1998), *The Design of High-Efficiency Turbomachinery and Gas Turbines*, 2nd ed, Prentice Hall, Upper Saddle River, NJ.
- [187] Glassman, A. and J. (1994), *Turbine Design and Application*, NAS 1.71:LAR-15058-1, Glenn Research Center.
- [188] Chu, J. (2009), *Gas Turbine Technology: Preliminary Design of the Fan and Life Estimation of the HP Turbine (1st Stage) Disk and Blade of a 130-Seat Airliner* (unpublished MSc thesis), Cranfield University.

## APPENDICES

### Appendix A Blade sizing model

#### A.1 Blade sizing

- The design process is as shown in Figure A-1
- The inlet and outlet gas path values at the DP are presented in Table A-1.

**Table A-1: Engine simulation at design point output**

	Values	Unit
<b>Non-dimensional speed (PCN)</b>	1	-
<b>Compressor efficiency</b>	88.2	%
<b>Turbine efficiency</b>	88.5	%
<b>Compressor inlet mass flow</b>	82.5	<i>kg/s</i>
<b>Compressor inlet stagnation temperature</b>	288.15	<i>K</i>
<b>Compressor inlet stagnation pressure</b>	1.0083E+05	<i>Pa</i>
<b>Compressor outlet stagnation temperature</b>	745	<i>K</i>
<b>Compressor outlet stagnation pressure</b>	2.33E+06	<i>Pa</i>
<b>NGV inlet stagnation temperature</b>	1505	<i>K</i>
<b>NGV inlet stagnation pressure</b>	2.15E+06	<i>Pa</i>
<b>Rotor outlet stagnation temperature</b>	1065	<i>K</i>
<b>Rotor outlet stagnation pressure</b>	408.7	<i>Pa</i>
<b>Coolant mass flow rate</b>	6.033	<i>kg/s</i>
<b>Coolant outlet stagnation temperature</b>	745	<i>K</i>

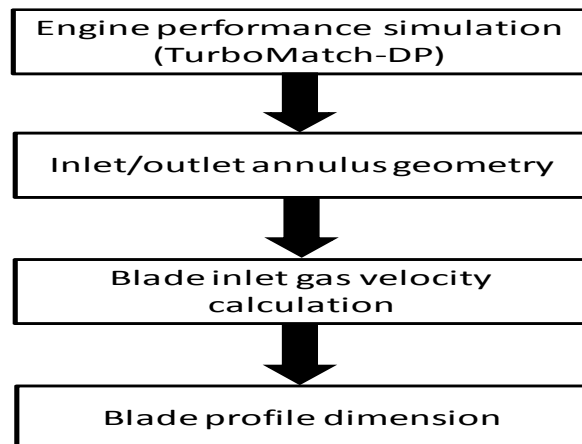


**Figure A-1: HP turbine first stage blade design process**

### A.2 Turbine blade cooling technology

- Figure A-2 presents the rotor inlet temperature capability as a function of the cooling effectiveness using single crystal materials [4]. Therefore, based on the TET; the  $\epsilon$  for this blade size model is assumed to be around 0.55 to 0.6.

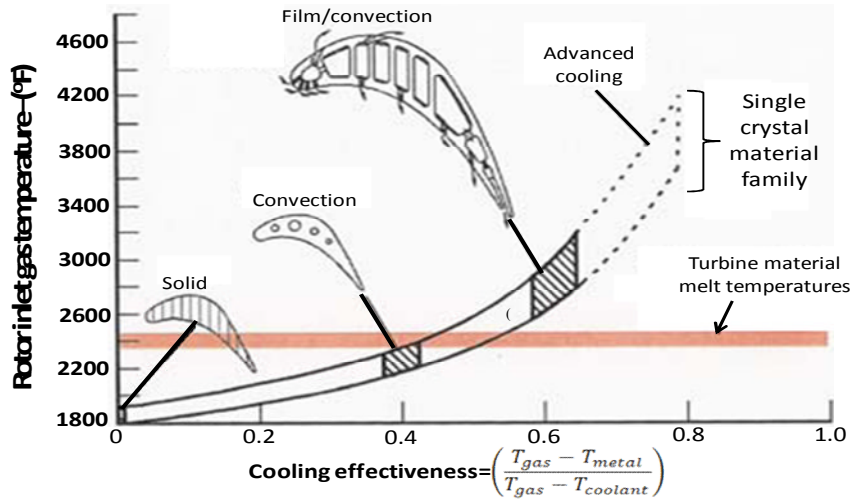


Figure A-2: Estimated Cooling Effectiveness [4]

### A.3 Model description

- Figure A-4 illustrates typical velocity triangles at the inlet and exit of the turbine rotor blades.
- The developed turbine model is based on a mean line analysis for constant nozzle flow along the blades.

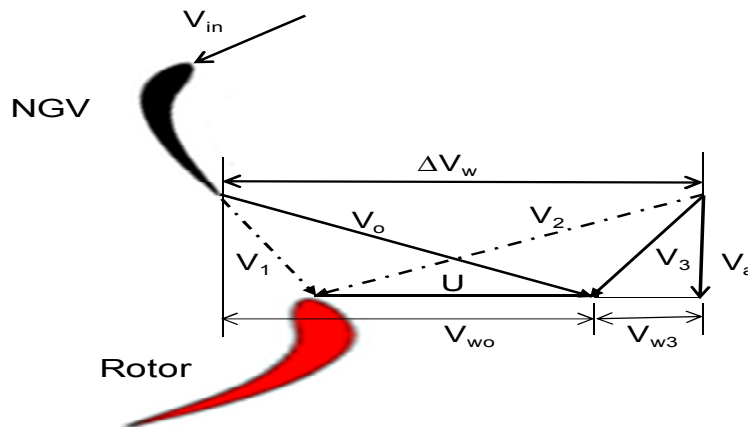


Figure A-4: HP turbine stage velocity triangles

#### A.3.1 Specific heat at constant pressure and polytropic efficiency

- The gas properties used during the velocity triangles calculation were obtained by using Equations A-1 to A-4, and turbine polytropic efficiency was obtained using Equation A-5.

$$\text{Ratio of specific heats, } \gamma_g = \frac{\ln\left(\frac{P_{oout}}{P_{oNGV}}\right)}{\ln\left(\frac{P_{oout}}{P_{oNGV}}\right) - \ln\left(1 - \frac{\Delta T}{\eta_t T_{oNGV}}\right)} \quad \text{A- 1}$$

$$\text{specific heat, } Cp_g = \frac{\gamma_g R}{\gamma_g - 1} \quad \text{A- 2}$$

$$\text{Ratio of specific heats, } \gamma_c = \frac{\ln\left(\frac{P_{oComOut}}{P_{oComIn}}\right)}{\ln\left(\frac{P_{oComOut}}{P_{oComIn}}\right) - \ln\left(\eta_c \frac{\Delta T}{T_{oComIn}} + 1\right)} \quad \text{A- 3}$$

$$\text{specific heat, } Cp_c = \frac{\gamma_c R}{\gamma_c - 1} \quad \text{A- 4}$$

$$\text{Polytropic efficiency, } \eta_p = \frac{\ln\left(1 - \eta_t \left(1 - \left(\frac{P_{oOut}}{P_{oNGV}}\right)^{\frac{\gamma-1}{\gamma}}\right)\right)}{\frac{\gamma-1}{\gamma} \ln\left(\frac{P_{oOut}}{P_{oNGV}}\right)} \quad \text{A- 5}$$

Where  $\gamma$  is ratio of the major specific heats,  $R=287$  ( $\text{J}\cdot\text{kg}^{-1}\cdot\text{K}^{-1}$ ),  $P_o$  is the total pressure (Pa),  $\Delta T$  is the component temperature drop (K) and  $\eta$  is component efficiency.

### A.3.2 Overall specification

- Since the HP turbine is a two stage turbine, it was assumed that the temperature drop was half-way between the two stages. Knowing the stage temperature drop and  $C_{Phot}$  the stagnation enthalpy  $\Delta H=C_{Phot}\cdot\Delta T$  can be obtained. Equations A-6 and A-7 were used to calculate the HP turbine temperature drop and turbine power.

$$\text{Temperature drop, } \Delta T = T_{oNGV} - T_{oOut} \quad \text{A- 6}$$

$$\text{HP Power} = mCp_g\Delta T \quad \text{A- 7}$$

Where  $T$  is temperature (K),  $m$  inlet mass flow (kg/s), and  $C_p$  specific heat at constant pressure ( $J \cdot kg^{-1} \cdot K^{-1}$ )

- It is essential to know the values of  $V/\sqrt{T}$  and Mach number as well as the non-dimensional mass flow  $W\sqrt{T}/AP$ ; these should be calculated for isentropic expansion of the gas from the stagnation pressure, and stagnation temperature [183]. Equations A-8 to A-10 were used to calculate static temperature, static pressure and  $V/\sqrt{T}$ .

$$T/t = 1 + \left( \left( \frac{\gamma - 1}{2} \right) M^2 \right) \quad \text{A- 8}$$

$$P/p = \left( 1 + \left( \frac{\gamma - 1}{\gamma} \right) M^2 \right)^{\frac{\gamma}{\gamma - 1}} \quad \text{A- 9}$$

$$V/\sqrt{T} = M \left[ \sqrt{\gamma R} / \left( 1 + \frac{\gamma - 1}{\gamma} M^2 \right) \right] \quad \text{A- 10}$$

Where  $T$  is total temperature (K),  $t$  is static temperature (K),  $P$  is total pressure (Pa),  $p$  is static pressure (Pa),  $M$  is mach number,  $\gamma$  is ratio of major specific heats and  $R$  is gas constant=287 J/kg.K.

### A.3.3 Inlet annulus geometry

- The inlet annulus area of the first stage HP turbine was obtained by using Equation A-11, blade height Equation A-12 and blade tip root diameter Equations A-13 and A-14.

$$\text{Inlet annulus area, } A = \frac{1000m\sqrt{T_{In}}}{1000QP_{In}} \quad \text{A- 11}$$

$$\text{Blade height, } h = \frac{A}{\pi D_{mean}} \quad \text{A- 12}$$

$$\text{Blade tip diameter, } D_{tip1st} = D_{mean} + h \quad \text{A- 13}$$

$$\text{Blade tip diameter, } D_{root1st} = D_{mean} - h \quad \text{A- 14}$$

Where  $m$  is compressor inlet mass flow (kg/s),  $T_{in}$  is turbine inlet temperature (K),  $P_{in}$  is turbine inlet total pressure (Pa),  $A$  is the HP turbine inlet annulus area ( $m^2$ ),  $D_{mean}$  is blade diameter at the mid of the span (m) and  $h$  is the blade height (m).



- The value of the blade root tip ratio in this blade design process was obtained using Equation A-15.
- The blade hub to tip ratio should be between 0.5 and 0.9 to prevent high tip clearance loss and decrease secondary flow. Also, low blade hub to tip ratio increases the blade stress at the blade root as a result of increase of blade height [141][139; 184].

$$\text{Root to tip ratio} = \frac{D_{tip1st}}{D_{root1st}} \quad \text{A- 15}$$

#### A.3.4 Stage efficiency prediction at mean height

- In order to calculate the stage load and flow coefficient the blade speed at the mean blade height is calculated using Equation A-16, knowing HP turbine speed and mean blade diameter mean.

$$\text{Blade speed at mean height, } U_{mean} = \frac{RPM \pi D_{mean}}{60} \quad \text{A- 16}$$

Where RPM is HP turbine speed and D is blade diameter (m).

- The performance and the efficiency of the axial turbine stage can be described in terms of two non-dimensional parameters: the stage loading coefficient and the flow coefficient. For most engines stage a typical load value is between 1.3 and 2, with higher values for the front stages.
- $\Delta H/U$  is a measure of the energy exchange, per unit mass flow for a given blade speed (U). The number of stages is a compromise between achieving low loading and good efficiency, or high loading and low cost and weight [139]. The stage loading was calculated using the following equation:

$$\text{Stage load, } \left( \frac{\Delta H}{U^2} \right) = \frac{C_p \Delta T_{stage}}{U^2} \quad \text{A- 17}$$

Where  $C_p$  is the gas specific heat at constant pressure (J/kg.K),  $\Delta T_{stage}$  is stage temperature drop (K) and  $U$  blade speed (m/s).

- Equation A-18 is used to obtain the turbine inlet axial velocity. Figure A-5 shows the turbine velocity triangles at mid radius of the blade.

$$\text{Inlet axial velocity, } V_{AxIn1st} = \frac{V}{\sqrt{T}} \sqrt{T_{InNGV}} \quad \text{A- 18}$$

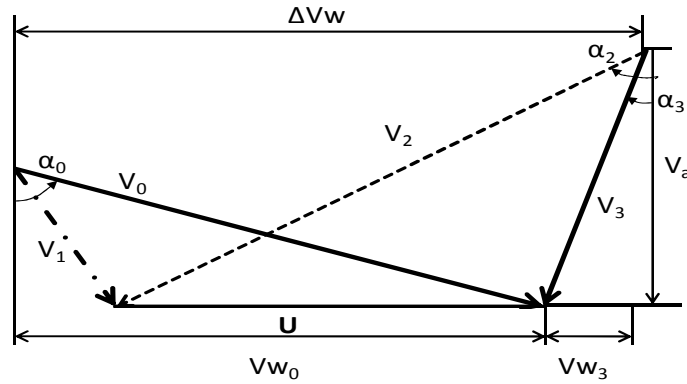


**Figure A-5: Turbine velocity triangles at mid radius of the blade span**

- The flow coefficient is a measure of the mass flow passing through a stage at a given blade speed. For a given stage loading the corresponding pitch line flow coefficient for optimum efficiency can be obtained from the correlation presented in a SMITH CHART minus 2% [49; 139; 184]. Figure A-6 shows turbine efficiency correlation (Smith chart).

$$\text{Flow coefficient, } V/U = \frac{V_{AxIn1st}}{U_{mean}} \quad \text{A- 19}$$

Where  $C_p$  is the gas specific heat at constant pressure (J/kg.K),  $\Delta T_{stage}$  is stage temperature drop (K),  $T$  temperature,  $U$  blade speed (m/s) and  $V$  is axial velocity (m/s).

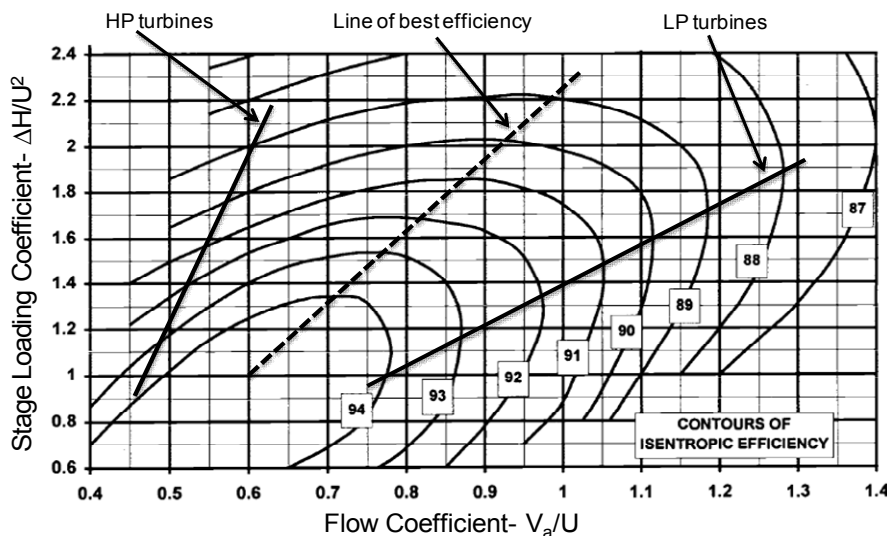


**Figure A-6: Turbine efficiency correlation (SMITH CHART) [139; 184; 185]**

### A.3.5 Outlet stage data and annulus geometry

- Using Equations A-20 to A-29, the first stage HP turbine outlet stagnation temperature and pressure, air outlet angle and velocity triangles at the blade mean can be calculated.

$$\text{Rotor outlet temperature, } T_{rotorOut} = T_{ONGV} - \Delta T_{stage} \quad \mathbf{A-20}$$

Where,  $T_o$  is NGV inlet temperature (K),  $\Delta T$  is total temperature drop across the stage (K).

- The blade total whirl velocity calculated using Equation A-21.

$$\text{Total whirl velocity, } \Delta V_{W(mean)} = \frac{\Delta H}{U^2} \frac{U}{\Omega} \quad \mathbf{A-21}$$

Where  $\Delta H/U^2$  is a non-dimensional stage load coefficient,  $U$  is blade speed (m/s) and  $\Omega$  is a non-dimensional stage work done factor and assumed to be 0.98 [139].

- The blade outlet whirl velocity at the blade mean is obtained using Equation A-22. The mean blade speed is subtracted from the blade total whirl velocity and since the blade reaction is 50% at the blade mean, the result is divided by two.

$$\text{Outlet whirl velocity, } V_{w3(mean)} = \frac{\Delta V_{Wmean} - U_{mean}}{2} \quad \mathbf{A-22}$$

- Equation A-23 gave the stage pressure ratio,  $\Gamma_p$ , using the stage temperature drop, stage isentropic efficiency (from Smith Chart) and NGV inlet temperature.

$$\text{Stage pressure ratio, } \Gamma_p = \frac{1 - \Delta T}{(\eta_{isent} T_{In})^{\frac{\gamma}{\gamma-1}}} \quad \mathbf{A-23}$$

- From stage pressure ratio and stage inlet stagnation pressure,  $P_{oNGV}$ , the rotor outlet stagnation pressure can be obtained from Equation A-24.

$$\text{Rotor outlet stagnation pressure, } P_{oOut} = \Gamma_p + P_{oNGV} \quad \mathbf{A-24}$$

- The rotor outlet (1000Q) is obtained from Equation A-25. The rotor outlet axial velocity can be calculated using Equation A-26.

$$\text{Rotor outlet non – dim mass flow, } 1000Q = \frac{1000 m \sqrt{T_{oOut}}}{P_{oOut} A_{Out}} \quad \text{A- 25}$$

$$\text{Rotor outlet axial velocity, } V_{AxOut} = \frac{V}{\sqrt{T}} T_{oOut} \quad \text{A- 26}$$

Where m is compressor inlet mass flow (kg/s),  $T_{oOUT}$  is rotor outlet temperature (K),  $A_{OUT}$  is stage annulus outlet area ( $m^2$ ) and  $P_{oOUT}$  rotor outlet stagnation pressure (Pa).

- The whirl exit angle is obtained using Equation A-27.

$$\alpha_{3mean} = \tan^{-1} \frac{V_{W3}}{V_a} \quad \text{A- 27}$$

- The rotor exit absolute velocity can be obtained using Equation A-28.

$$\text{Rotor exit absolute velocity, } V_3 = \frac{V_{Axout}}{\cos \alpha_3} \quad \text{A- 28}$$

- Equation A-29 was used to obtain  $V/\sqrt{T}$  parameter and then the rotor exit Mach number was found.

$$V_3/\sqrt{T_{oOut}} = \frac{V_3}{\sqrt{T_{oOut}}} \quad \text{A- 29}$$

### A.3.6 Rotor inlet axial velocity

- Blade convection effectiveness and NGV metal temperature were calculated using Equations A-31 and A-32.
- 10% of the total inlet mass air flow is used to cool the hot section components. The HP turbine uses 7.058% of the core flow to cool the first and second stage. The first stage of the HP turbine uses 60% of the core flow to cool the NGV and rotor, 2/3 of that core flow is used to cool the NGV and 1/3 is used to cool the rotor.
- The NGV air cooling percentage,  $\phi$  can be obtained by knowing the non-dimensional coolant mass flow and the constant K. For typical modern turbines K is of order 2% to 3% [157]. Rearranging the NGV cooling equation the non-dimensional coolant mass flow can be obtained using Equation A-30.

$$\text{Non – dimensional coolant mass flow, } m^* = \frac{\varphi}{K} \quad \text{A- 30}$$

Where,  $\varphi$  is percentage of air cooling in the NGV,  $K$  is a constant and assumed in this calculation to be 0.025.

- The convection effectiveness can be obtained using Equation A-31.

$$\text{Convection effectiveness, } \eta_{con} = \frac{\varepsilon_{st1}}{m^* - (\varepsilon_{st1} m^*)} \quad \text{A- 31}$$

- Using Equations A-32 to A-34 the NGV metal temperature, NGV air cooling exit temperature and NGV mass fraction can be calculated.

$$\text{NGV metal temperature, } T_{NGV} = T_{oNGV} - (\varepsilon_{st1} - T_{cIn}) \quad \text{A- 32}$$

$$\text{Coolant exit temperature, } T_{cOut} = T_{cIn} + \eta_{con} (T_{NGV} - T_{cIn}) \quad \text{A- 33}$$

$$\text{NGV mass fraction} = \frac{\%coolant \text{ 1stNGV}}{\%coolant \text{ from core flwo enter HPT}} \quad \text{A- 34}$$

Where,  $T_{oNGV}$  is NGV inlet stagnation temperature (K),  $T_{coolIN}$  is air cooling temperature (K) and  $\varepsilon$  is non-dimensional stage cooling effectiveness.

- Using Equations A-35 and A-36 the rotor inlet stagnation pressure and temperature are obtained, and the rotor inlet non-dimensional mass flow and inlet axial velocity using Equations A-37 and A-38.

$$\begin{aligned} \text{Rotor inlet stagnation temperature, } T_{oInst1} \\ = \frac{T_{oNGV} - (NGV_{massfraction} m_c C p_c)(T_{cOut} - T_{cIn})}{m^* C p_g} \end{aligned} \quad \text{A- 35}$$

$$\begin{aligned} \text{Rotor inlet stagnation pressure, } P_{oIn} \\ = NGV_{pressure \text{ recovery}} P_{oNGVst1} \end{aligned} \quad \text{A- 36}$$

$$\text{Rotor inlet nondim mass flow, } 1000Q = \frac{1000 m \sqrt{T_{oInst1}}}{P_{oInst1} A_{In}} \quad \text{A- 37}$$

$$\text{Rotor inlet axial velocity, } V_{AxRotorInst1} = \frac{V}{\sqrt{T}} \sqrt{T_{oInst1}} \quad \text{A- 38}$$

Where,  $NGV_{pressure\ recover}$  is assumed to be 99%, which means a 1% pressure loss in the NGV,  $m_c$  is air cooling mass flow (kg/s),  $m$  is inlet total mass flow (kg/s).

### A.3.7 HP turbine fixed nozzle design

- The stator outlet flow angle  $\alpha_o$  is obtained using Equation A-39 and is assumed constant from the root to the tip of the blade.

$$\alpha_o(\text{constant through root to tip}) = \tan^{-1} \frac{V_{W0}}{V_{AxRotorIn}} \quad \text{A- 39}$$

- The rotor inlet absolute velocity ( $V_o$ ) can be obtained using Equation A-40. The rotor outlet absolute velocity is calculated by knowing the rotor outlet whirl and axial velocities and using Equation A-41.

$$V_o = \frac{V_{AxRotorIn}}{\cos \alpha_o} \quad \text{A- 40}$$

$$V_3 = \sqrt{(V_{W3})^2 + (V_{AxRotorOut})^2} \quad \text{A- 41}$$

- The rotor inlet and outlet relative velocity can be obtained using Equations A-42 and A-43, while the rotor inlet and outlet flow angles are calculated using Equations A-44 and A-45.

$$V_1 = \sqrt{(V_{W0} + U)^2 + (V_{AxRotorIn})^2} \quad \text{A- 42}$$

$$V_2 = \sqrt{(V_{W3} + U)^2 + (V_{AxRotorOut})^2} \quad \text{A- 43}$$

$$\alpha_1 = \cos^{-1} \frac{V_{AxRotorIn}}{V_1} \quad \text{A- 44}$$

$$\alpha_2 = \cos^{-1} \left( \frac{V_{AxRotorOut}}{V_2} \right) \quad \text{A- 45}$$

Where,  $V_{W0}$  is rotor inlet whirl velocity,  $U$  is blade speed (m/s),  $V_{ax}$  is rotor inlet axial velocity and  $V_{w3}$  is rotor outlet whirl velocity.

- The acceleration values for both blades can be obtained using Equations A-46 and A-47.

$$\text{Nozzle acceleration} = \frac{V_0}{V_{AxNGVinst1}} \quad \text{A- 46}$$

$$\text{Rotor acceleration} = \frac{V_2}{V_1} \quad \text{A- 47}$$

- To calculate the reaction from the root to the tip, the  $V_{w2}$  is calculated using Equation A-48 and then the reaction values obtained from the hub to tip using Equation A-49.

$$V_{W2} = V_2 \sin\alpha_2 \quad \text{A- 48}$$

$$\text{Reaction} = \frac{V_{W2} - V_{W1}}{2U} \quad \text{A- 49}$$

Where  $V_2$  is rotor outlet relative velocity as shown in Figure 4-4,  $\alpha_2$  is rotor outlet flow angle,  $V_{w1}$  is rotor whirl inlet velocity minus blade speed ( $V_{w0}-U$ ) and  $U$  is blade speed (m/s).

### A.4 Blade design strategy

In the open literature some published material and procedures have been presented on how to carry out blade design [140; 183; 186] [187]. The contribution in this stage is to the detailed design of the first stage blade of the HP turbine. Figure A-7 shows a typical turbine blade profile.

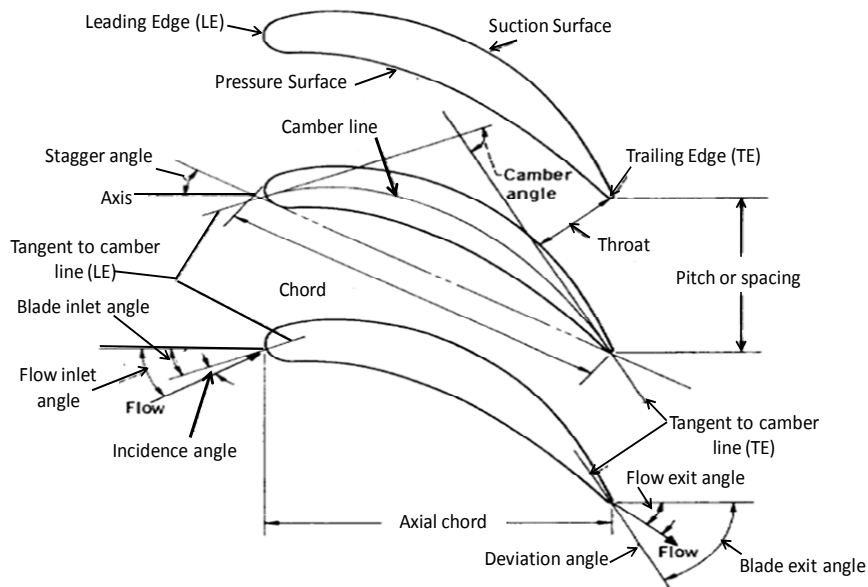


Figure A-7: A typical turbine blade profile [187]

#### A.4.1 First stage blade design details

- The minimum loss solidities could be well correlated by assuming that the Zweifel loading coefficient ( $\psi_T$ ) had a constant value of 0.8 [184; 188].
- Knowing the blade inlet and outlet flow angles and Zweifel loading coefficient the space chord ratio ( $s/c$ ) can be obtained using Equation A-50.

$$\frac{s}{c} = \frac{\psi_T}{2 \cdot \tan \alpha_1 (\cos \alpha_2)} \quad \text{A- 50}$$

- From the user's manual of the engine selected the blade height to chord ratio was scaled and found to be equal to 1.46. Also, Saravanamuttoo [140] has stated that the value of  $h/c$  would certainly be satisfactory if greater than 1 and less than 4.
- The blade chord and space chord ration can be obtained using Equation A-51 and A-52.

$$\text{Blade chord, } c = \frac{h}{h/c_{ratio}} \quad \text{A- 51}$$

$$\text{Space/pitch, } s = c \cdot s/c_{ratio} \quad \text{A- 52}$$

- The stagger angle ( $\xi$ ) of the HP turbine rotor is assumed to be  $35^\circ$  based on the discussion with the axial turbine designer at Cranfield University.
- The axial chord and axial solidity were found from Equation A-53 and A-54

$$\text{Axial chord, } b = c \cdot \cos \xi \quad \text{A- 53}$$

$$\text{Axial solidity} = \frac{b}{s} \quad \text{A- 54}$$

Where  $\xi$  is the stagger angle

- For the preliminary design, a ratio of the blade spacing to the surface curvature of up to 0.75 is acceptable. A range that appears to give favourable shaped blades is  $0.25 < (s/e) < 0.625$  [186].
- In this study  $s/e$  was assumed 0.2 to achieve a good degree of surface curvature on the blade convex surface and accelerate the air downstream of the blade throat.



$$\text{Surface curvature at throat, } e = \frac{s}{s/e} \quad \text{A- 55}$$

- The angle of induced incidence is calculated using Equation A-56.

$$\text{Induced incidence, } \theta_{ind} = 14 \left( 1 - \left( \frac{\alpha_1}{70} \right) \right) + 9 \left( 1.8 - \left( \frac{c}{s} \right) \right) \quad \text{A- 56}$$

- The opening or throat area is calculated using the correlation presented in [186] for flow outlet angle calculations at Mach number  $0 < M < 0.5$ . The equation was rearranged and used to obtain the value of  $o/s$  as shown in Equation A-57.

$$\frac{o}{s} = \cos \left( 10 + \frac{6}{7} \right) \alpha_2 - \left( 4 \frac{s}{e} \right) \quad \text{A- 57}$$

- Regarding the blade outlet angle, it has been common practice to take the gas angle as being equal to the blade angle defined by  $\cos^{-1}(\text{opening/pitch})$ . Equation 4-58 was used to calculate the blade outlet angle. The relation between the relative gas outlet angle  $\beta_3$  and the blade angle is presented in Figure A-8 and defined by Equation A-58.

$$\text{Blade outlet angle, } \beta_2 = \cos^{-1}(o/s) \quad \text{A- 58}$$

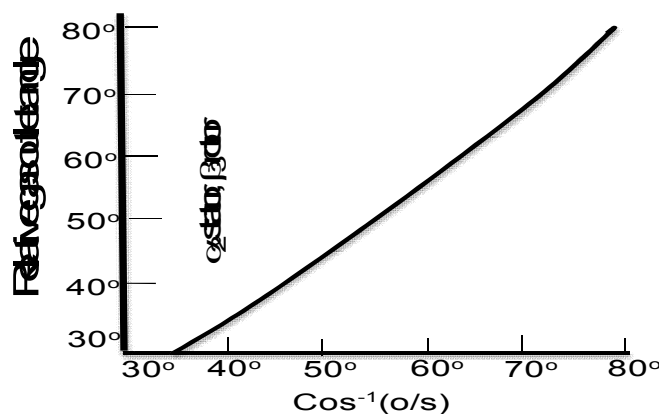


Figure A-8: Relation between gas and blade outlet angles [140].

- By using Equation A-59 the blade deviation angle can be obtained.

$$\text{Deviation angle, } \delta = \beta_2 - \alpha_2 \quad \text{A- 59}$$

- Knowing stagger angle, throat, pitch and axial solidity, the TE intercept can be calculated using Equation A-60. The blade leading edge radius is often specified to be a given proportion of the blade spacing. Typical values fall between  $0.05*s$  and  $0.10*s$ . by using Equation A-61 the LE radius can be calculated.

$$TE \text{ intercept} = \left( \frac{0.02 \left( \frac{b}{s} \right)}{(o/s) \cos \xi} \right) s \quad \mathbf{A-60}$$

$$LE \text{ radius} = 0.1 \times s \quad \mathbf{A-61}$$

## Appendix B Humidity

### B.1 Jet-A fuel properties for different values of FAR and WAR

- The results of the investigation into the gas properties of the gaseous products of combustion ( $C_p, \gamma$ , and  $R$ ) of Jet-A fuel at different values of TET, WAR and FAR are presented in Figures B-1 to B-9. The multi regression equation for the gas properties of Jet-A fuel is presented in Equation B-1 and the coefficients for the fluid are presented in Tables B-1.

$$\text{Fluid properties } (C_p; \gamma; R) = A + B.X_1 + C.X_2 + D.X_3 + E.X_4 \quad (\text{B-1})$$

Where,  $X_1$ =FAR is the fuel air ratio,  $X_2$ =WAR is the water air ratio,  $X_3$ =P is the gas pressure and  $X_4$ =T is the gas temperature.

**Table B-1: Coefficients for the calculation of the gas properties of Jet-A (kerosene).**

	<b>Cp</b>	$\gamma$	<b>R</b>
<b>A</b>	908	1.4	287
<b>B</b>	1863	-0.57	-8.95
<b>C</b>	1201	-0.15	156.5
<b>D</b>	-0.08	1.34E-05	-2.54E-04
<b>E</b>	0.223	-6.66E-05	3.74E-05

- $C_p$  increased more or less linearly with increase with TET, WAR and/or FAR. As would be expected there was a strong similarity to the results obtained for natural gas.
- The trend of the isentropic coefficient ( $\gamma$ ) curve was similar to that obtained for natural gas:  $\gamma$  decreased with increase in any of TET, WAR and/or FAR.
- $R$  does not change with temperature and only very slightly with change in FAR. However,  $R$  increased with WAR, as WAR increased from 0 (dry air)

to WAR=0.10 (humid air) for different values of FAR and TET, R increased from approximately 287 to 303.

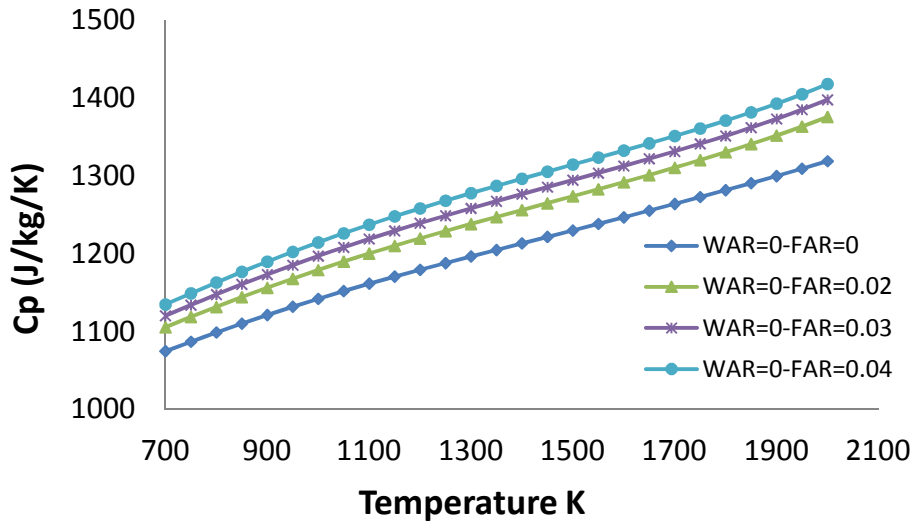


Figure B-1: Hot gas specific heat at constant pressure of WAR=0 and different FAR=0, 0.02, 0.03 and 0.04 (Jet-kerosene)

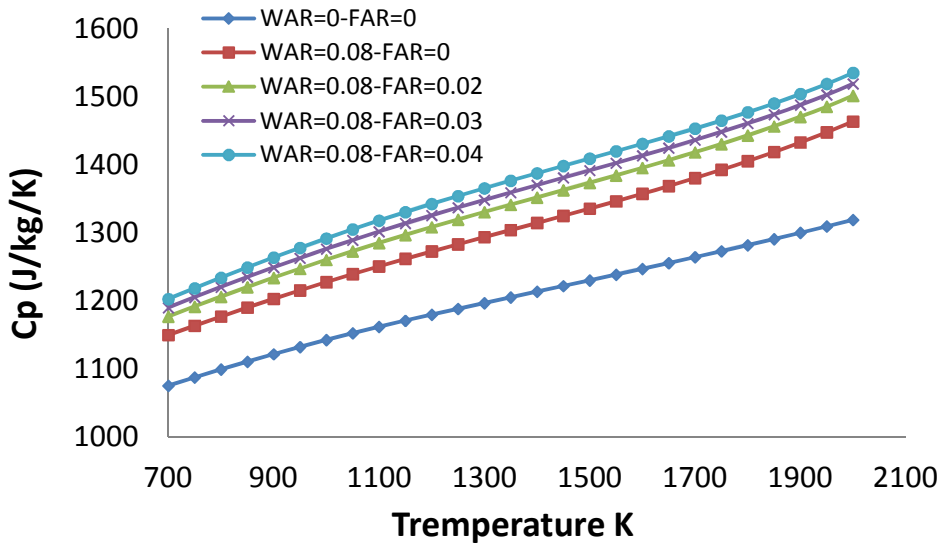


Figure B-2: Hot gas specific heat at constant pressure of WAR=0.08 and different FAR=0, 0.02, 0.03 and 0.04 (Jet-kerosene)

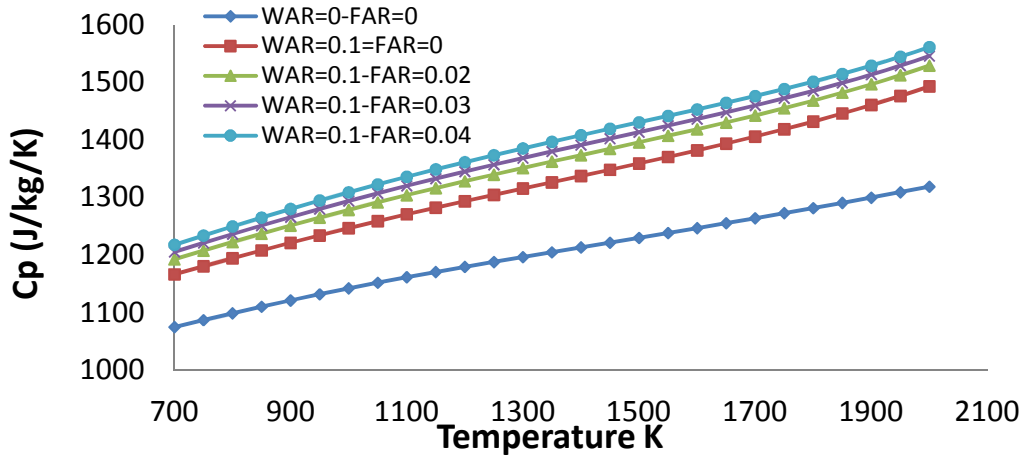


Figure B-3: Hot gas specific heat at constant pressure of WAR=0.1 and different FAR=0, 0.02, 0.03 and 0.04 (Jet-kerosene)

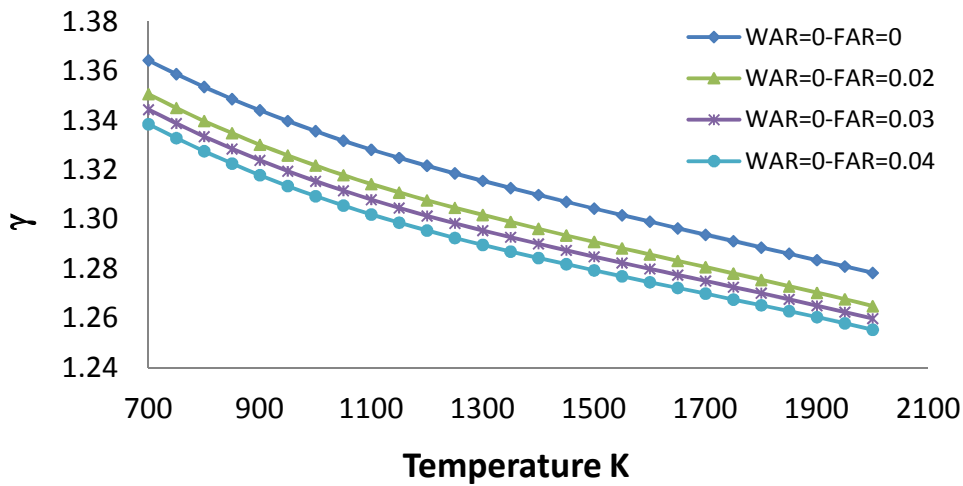


Figure B-4: hot gas isentropic exponent of WAR=0 and different FAR=0, 0.02, 0.03 and 0.04 (Jet-kerosene)

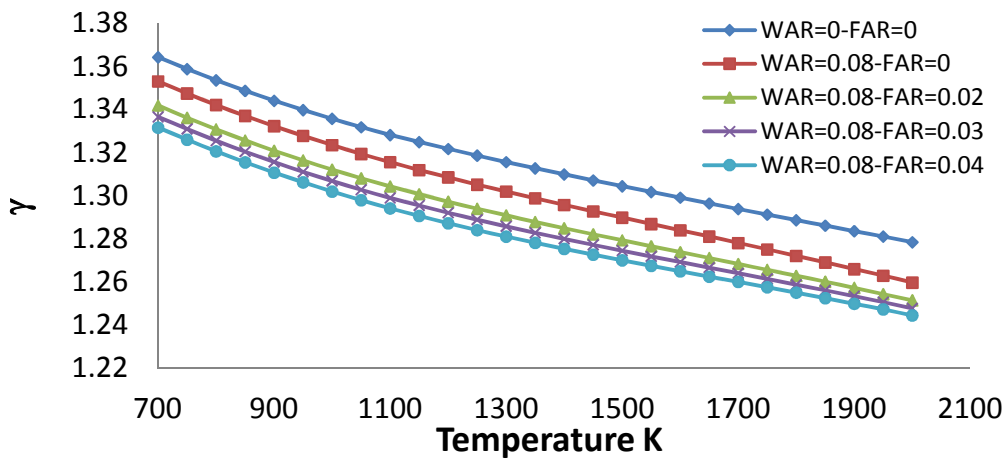


Figure B-5: hot gas isentropic exponent of WAR=0.08 and different FAR=0, 0.02, 0.03 and 0.04 (Jet-kerosene)

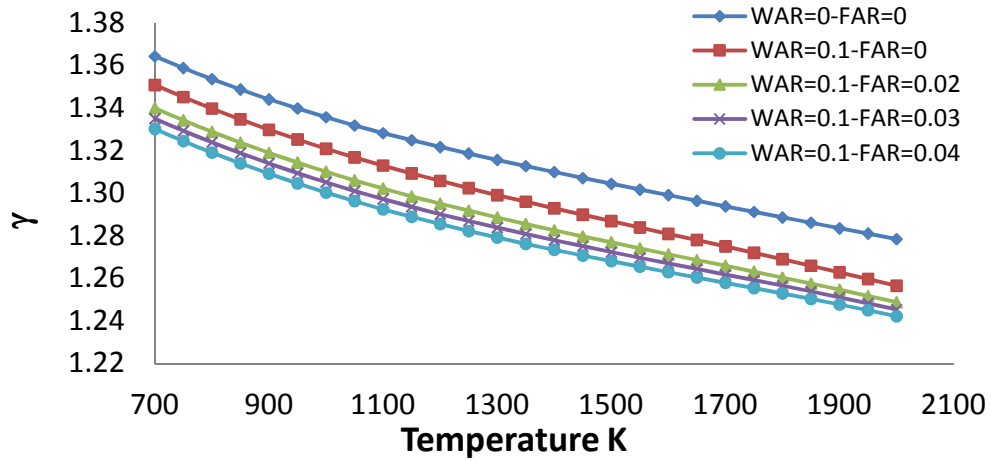


Figure B-6: hot gas isentropic exponent of WAR=0.01 and different FAR=0, 0.02, 0.03 and 0.04 (Jet-kerosene)

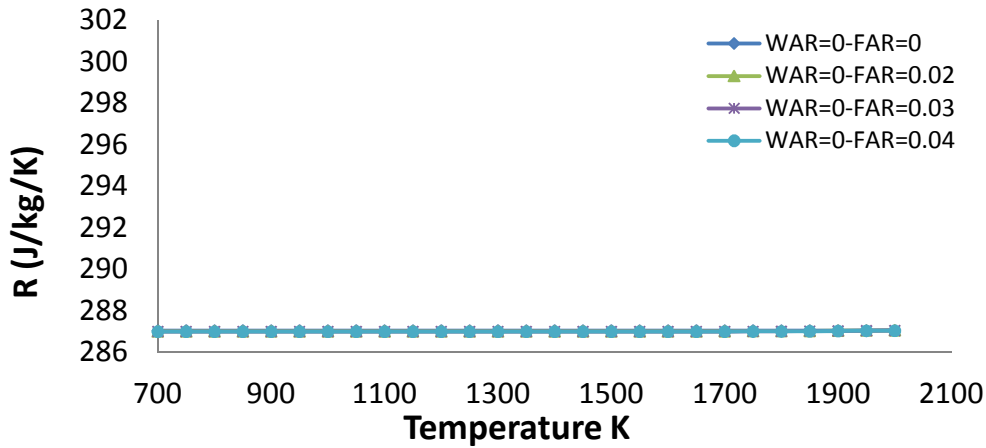


Figure B-7: Hot gas constant of WAR=0 and FAR=0, 0.02, 0.03 and 0.04 (Jet-A kerosene)

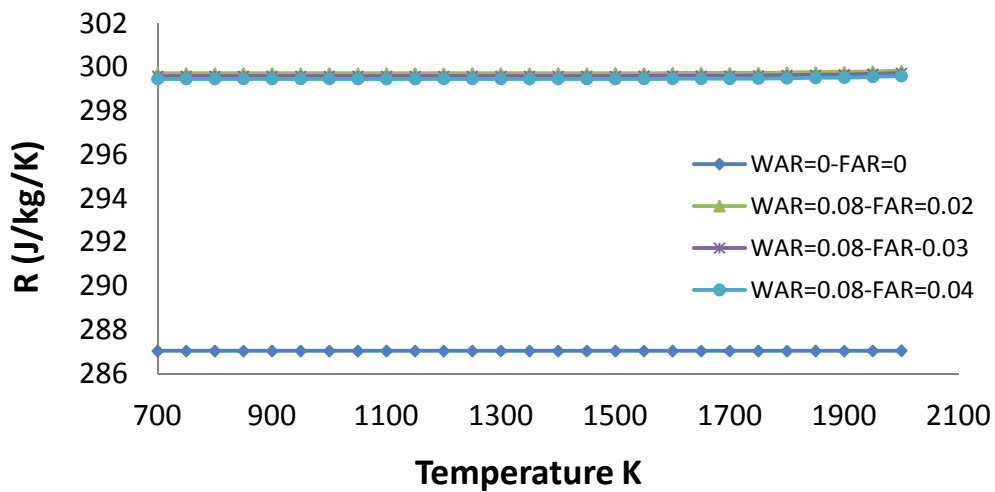
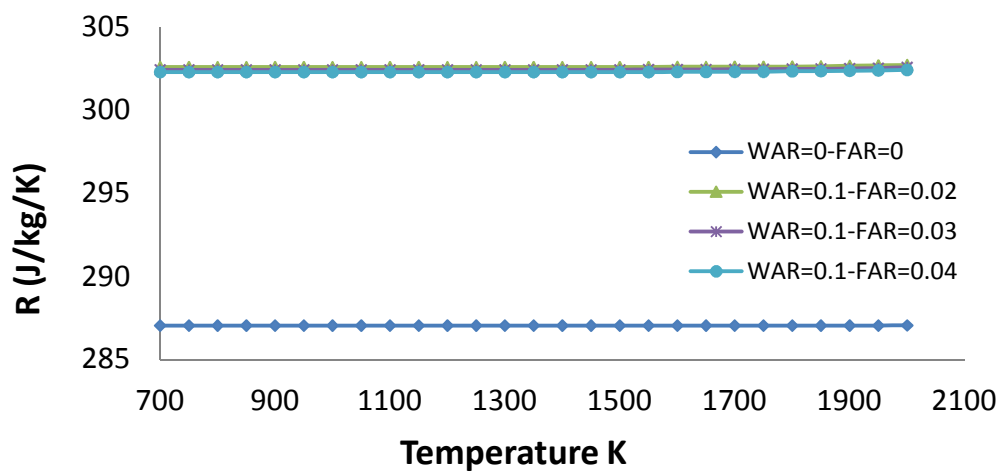


Figure B-8: Hot gas constant of WAR=0.8 and FAR=0, 0.02, 0.03 and 0.04 (Jet-A kerosene)



**Figure B-9: Hot gas constant of WAR=0.10 and FAR=0, 0.02, 0.03 and 0.04 (Jet-A kerosene)**

## Appendix C Gas absolute velocity

$$1000Q = (m_{cc} \times \sqrt{T_{cin}}) / (A_{ch} \times P) \quad (C-1)$$

$$1000Q = M \times \sqrt{\frac{\gamma}{R}} \times \left(1 + \frac{\gamma - 1}{2} \times M^2\right)^{-\frac{\gamma+1}{2 \times \gamma - 1}} \quad (C-2)$$

$$T/t = 1 + \frac{\gamma - 1}{2} \times M^2 \quad (C-3)$$

$$P/p = T/t^{\left(\frac{\gamma}{\gamma-1}\right)} \quad (C-4)$$

$$V / \sqrt{T_{cin}} = M \times \sqrt{\frac{\gamma}{R}} \times \sqrt{\frac{1}{T/t}} \quad (C-5)$$

$$V = M \times \sqrt{\frac{\gamma}{R}} \times \sqrt{\frac{1}{T/t}} \times \sqrt{T_{cin}} \quad (C-6)$$

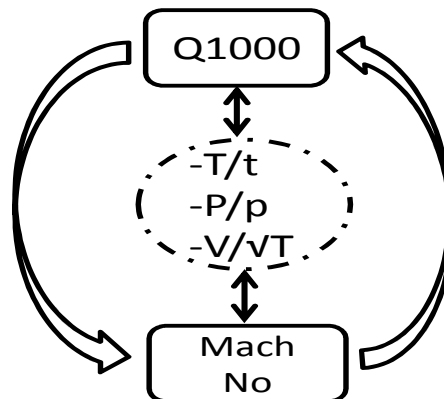


Figure Appendix C: illustrate the iterative process of calculating the coolant gas velocity